



BRNO UNIVERSITY OF TECHNOLOGY

VYSOKÉ UČENÍ TECHNICKÉ V BRNĚ

CENTRAL EUROPEAN INSTITUTE OF TECHNOLOGY BUT

STŘEDOEVROPSKÝ TECHNOLOGICKÝ INSTITUT VUT

SMART NANODEVICES

CHYTRÉ NANONÁSTROJE

NANOSCALED POLYPYRROLE FOR SENSING GASEOUS ANALYTES AND VOLATILE ORGANIC COMPOUNDS

NANO-POLYPYRROL PRO DETEKCI PLYNNÝCH ANALYTŮ A TEKAVÝCH ORGANICKÝCH LÁTEK

DOCTORAL THESIS

DIZERTAČNÍ PRÁCE

AUTHOR

AUTOR PRÁCE

Milena Šetka, M.Sc.

SUPERVISOR

ŠKOLITEL

doc. Ing. Jana Drbohlavová, Ph.D.

CO-SUPERVISOR

ŠKOLITEL SPECIALISTA

Dr. Stella Vallejos Vargas

Abstract

Polypyrrole (PPy) is a hetero-cyclic conductive polymer (CPs) with chemical structure based on the existence of conjugated electrons between alternating single and double bond system. This polymer has occupied the attention of many scientists from different research disciplines due to its outstanding properties such as good electrical conductivity, relatively high environmental stability, and facile and diversified synthesis methods. The aim of this research was to study the sensing behavior of PPy. Therefore, the gas sensing performances of PPy nanostructures were verified to ‘gas molecules of high importance’ including acetone, ammonia, ethanol, ethylene and toluene.

In this work, PPy in the form of nanorods (NRs) and nanoparticles (NPs) was prepared using electrochemical and chemical synthesis approaches, respectively. Additionally, the modified PPy structures were developed by functionalization of PPy NPs with catalytic particles of gold (Au), silver (Ag) and cadmium-telluride (CdTe). Many complementary analytical techniques (microscopic and spectroscopic) were used for the investigation of morphology, composition and structure of the synthesized materials. Moreover, spectroscopy techniques such as Raman and X-Ray Photoelectron Spectroscopy (XPS) were employed for *in-situ* gas sensing tests, which confirmed the potential of PPy NRs and PPy NPs to be used as gas sensitive materials.

In order to developed the gas sensor device, the PPy based materials were integrated into chemo-resistive and Love mode surface acoustic wave (L-SAW) transducing platforms. The gas sensing test of chemo-resistive sensors based on PPy NRs revealed negligible response to nitrogen dioxide and ammonia due to complicate architecture of those sensors. The measuring of response of non-modified and modified PPy NPs chemo-resistive sensors was complex due to their extremely high resistance in $G\Omega$ range. However, multi-guiding L-SAW sensors based on bare PPy NPs and modified with Au NPs and Ag NPs, and CdTe quantum dots (QDs) manifested the response to low concentration of all tested target gas molecules including ammonia, acetone, ethanol, ethylene and toluene at room temperature (RT). Generally, the L-SAW sensors with modified sensing layers established enhanced sensing performances over non-modified sensors. The performance of the L-SAW sensor primarily depends on the operating frequency and the choose of sensitive layer in the active region of the sensor. Thus, among the tested sensing layers for the target gases, modified PPy layer with Ag NPs and/or Au NPs can be selected as the best option for the detection of acetone.

The developed PPy based L-SAW sensors are simple and cost effective devices with improved sensing properties such as high sensitivity and low limit of detection (LOD) which make them potential candidates in future systems for air quality control, food quality control or disease diagnosis via exhaled breath.

Key words

Polypyrrole, surface acoustic wave, gas sensors, volatile organic compounds.

Abstrakt

Polypyrol (PPy) je heterocyklický vodivý polymer s chemickou strukturou založenou na existenci systému konjugovaných elektronů mezi střídajícími se jednoduchými a dvojnými vazbami. Díky svým vynikajícím vlastnostem jako je dobrá elektrická vodivost, relativně vysoká stabilita prostředí a zároveň i jednoduchost a variabilita metod jeho přípravy, přilákal tento polymer pozornost mnoha vědců z různých vědních disciplín. Cílem výzkumu v této dizertační práci byla studie senzoričského chování PPy. Za tímto účelem byla ověřena účinnost nanostruktur PPy při detekci vybraných „vysoce důležitých molekul plynů“ včetně acetonu, amoniaku, etanolu, etylenu a toluenu.

V této práci byl připraven PPy ve formě nanotyčinek (NRs) pomocí elektrochemické syntézy a také ve formě nanočástic (NPs) chemickou cestou. Dále byly připraveny modifikované PPy struktury, a to funkcionalizací PPy NPs katalytickými částicemi zlata (Au), stříbra (Ag) a teluridu kadmennatého (CdTe). Pro charakterizaci morfologie, složení a struktury připravených materiálů bylo použito několik komplementárních analytických (mikroskopických i spektroskopických) technik. Navíc byly využity techniky jako Ramanova a rentgenová fotoelektronová spektroskopie (XPS) pro in-situ test detekce plynů, které potvrdily potenciál připraveného materiálu, tedy PPy NRs i PPy NPs, pro využití v senzorech plynů.

Za účelem výroby senzoru plynů byl připravený PPy materiál integrován do dvou typů převodníkových platforem: chemorezistivní a na bázi povrchové akustické vlny v tzv. Love módu (L-SAW). Test detekce plynů pro chemorezistivní senzory s PPy NRs ukázal pouze zanedbatelnou odpověď těchto senzorů pro oxid dusičitý a amoniak z důvodu jejich komplikované architektury. Změření odzvy tvou typů chemorezistivních senzorů-nemodifikovaného i modifikovaného PPy NPs nebylo možné z důvodu extrémně vysoké odporu v řádu GΩ. Nicméně multivodivé L-SAW senzory založené na holých PPy NPs či PPy NPs modifikovaných Au či Ag NPs a nebo CdTe kvantovými tečkami (QDs) vykazovaly odezvu pro nízké koncentrace všech testovaných velmi důležitých molekul plynů při pokojové teplotě (RT). Obecně měly L-SAW senzory s modifikovanou citlivou vrstvou vyšší citlivost než senzory s nemodifikovanou PPy citlivou vrstvou. Účinnost L-SAW senzoru primárně závisí na pracovní frekvenci a na výběru citlivé vrstvy v aktivní oblasti senzoru. Z otestovaných typů vrstev senzoru vůči jednotlivým plynům, modifikovaná PPy NPs s Ag NPs i Au NPs se javí jako nejlepší varianta pro detekci acetonu.

Připravené L-SAW senzory na bázi PPy jsou jednoduchá a cenově přijatelná zařízení s vylepšenými detekčními vlastnostmi jako je vysoká senzitivita a nízký limit detekce (LOD), což je řadí mezi potenciální kandidáty v budoucích systémech pro kontrolu kvality vzduchu, potravin a rovněž pro diagnostiku nemocí z dechu.

Klíčová slova

Polypyrol, povrchová akustická vlna, plynové senzory, volatilní organický látky.

Bibliographic citation

Milena Šetka. Nanoscaled polypyrrole for sensing gaseous analytes and volatile organic compounds. Doctoral Thesis. Brno University of Technology, Central European Institute of Technology. Brno, 2020. Supervisor Jana Drbohlavová.

Declaration

I hereby declare that this doctoral dissertation is my own original work which has been done under the supervision of doc. Ing. Jana Drbohlavová, Ph.D. and Dr. Stella Vallejos Vargas. I have duly acknowledged all the sources of information which have been used in the thesis.

Brno

.
(author's signature)

To my parents, Danica and Janko

Acknowledgment

The PhD journey is long and demanding that one cannot endure it alone. I would like to acknowledge the arms that held mine during this adventure. Thank you all helping me get to this point in my life and career.

First, I would like to thank to my supervisors, doc. Ing. Jana Drbohlavová, Ph.D. and Dr. Stella Vallejos Vargas, for their endless support, encouragement, immense knowledge and friendship. Your exemplary attitude and enthusiasm in working environment as well as in private life are inspiring for me. There were times when it was difficult and challenging, but your mindset and positive demeanor helped me to met some unknown parts of myself and go further.

Throughout my entire PhD I had the privilege to work in different institutions with an amazing set of collaborators. I own to all of you huge thank for the opportunity to collaborate, and I would like to acknowledge that this work was not possible without your assistance. My first two internships were at Universitat Rovira and Virgili, Tarragona, Spain and I would like to thank to prof. Eduard Llobet and all nice people from MINOS group. It was such a pleasure to work with you and I spent a nice times with you. My special thank goes to Dr. Daniel Matatagui Cruz who supervised my work during the internship at Universidad Nacional Autónoma de México (UNAM), Mexico City, but also he was very helpful and his advices were precious all time afterward. Apart, I have expanded my expertise thanks to him, also I will never forget his nice hospitality in Mexico. I also had the fortune to participate at two more internships at Institute de Microelectronica de Barcelona (IMB-CNM, CSIC), Barcelona, Spain mentored by Stella. I will always be grateful for her mentorship and guidance how to chose the right direction in order to archived my goals. From her I not only received the best possible research guidance, but also I learned to appreciate the much larger life beyond research, and my nice summers in Spain are special thanks to her. Also, I had help from great senior researchers, Isabel and Eduard, during my stay in Barcelona.

As my PhD was a real journey with a lot of movements between my base institution of Central European Institute of Technology (CEITEC) and many other places, it gave me an opportunity to meet many colleagues and particularly amazing people who made this experience memorable. Thus, I would like to thank to Celia, Eric, Fabio, Lukas, Martha, Michele, Milica, Ondrej, Raul, Stefano and Tomas. I know, I needed a lot of help, and you know that you will have special place in my life all time long.

I also would like to sincerely acknowledge the funding who supported my doctoral studies, namely, CEITEC Ph.D. Scholarship, Erasmus + and Free Movers program, Internal Grant Agency of Czech Republic and Czech Science Foundation (GAČR) via Grant No. 20-20123S.

Finally, I would like to thank to all my friends which I met on this journey and my lifelong friends, my ŽFK TMF, for their continued love, laughter, indescribable moments and adventures. My biggest support since day one in my life is my family, thanks Mum, Dad, Natasa, Sanja and Radenko for your unconditional love. Additionally, I would like to thank to Zdenek for seeing this through with me. Volim vas puno and no matter how far apart we are, our bond is forever.

Contents

| | |
|--|------------|
| Abstract | i |
| Declaration | iii |
| Acknowledgements | v |
| 1 Introduction | 1 |
| 1.1 Motivation | 1 |
| 1.2 Aims of the thesis | 2 |
| 1.3 Structure of thesis | 2 |
| 2 Literature review | 4 |
| 2.1 Classification of sensing materials | 4 |
| 2.1.1 Metal oxides | 5 |
| 2.1.2 Conductive polymers | 6 |
| 2.2 Introduction to gas sensors | 9 |
| 2.2.1 Transducing principles | 10 |
| 2.2.2 SAW sensors | 12 |
| 2.3 Gaseous analytes | 15 |
| 2.3.1 Gases and VOCs in exhaled breath | 15 |
| 2.3.2 Gases and VOCs in air quality monitoring | 17 |
| 2.3.3 Gases and VOCs in food quality monitoring | 17 |
| 2.3.4 Gases and VOCs of high importance | 17 |
| 2.3.4.1 Acetone | 17 |
| 2.3.4.2 Ammonia | 18 |
| 2.3.4.3 Ethanol | 18 |
| 2.3.4.4 Ethylene | 19 |
| 2.3.4.5 Toluene | 19 |
| 3 Methods | 20 |
| 3.1 Synthesis | 20 |
| 3.2 Material characterization | 21 |
| 3.2.1 Microscopy Techniques | 21 |
| 3.2.2 Spectroscopy Techniques | 23 |
| 3.2.3 Mass Spectrometry | 25 |
| 3.3 Gas sensors fabrication and characterization | 25 |
| 3.3.1 L-SAW sensors fabrication | 26 |
| 3.3.2 Electrical characterization of L-SAW sensors | 26 |
| 3.3.3 Gas characterization of L-SAW sensors | 27 |
| 4 Polypyrrole in gas sensing | 29 |
| 4.1 Motivation | 29 |
| 4.2 Outputs | 29 |
| 4.3 Conclusions | 30 |
| 4.4 Articles | 30 |
| 4.4.1 Journal Article 1 | 30 |
| 4.4.2 Journal Article 2 | 30 |

| | | |
|----------|---|------------|
| 4.4.3 | Conference article 1 | 30 |
| 5 | Love wave sensors based on polypyrrole modified with catalytic metal nanoparticles | 78 |
| 5.1 | Motivation | 78 |
| 5.2 | Outputs | 78 |
| 5.3 | Conclusions | 79 |
| 5.4 | Articles | 79 |
| 5.4.1 | Journal article 3 | 79 |
| 5.4.2 | Journal article 4 | 79 |
| 6 | Love wave sensor based on polypyrrole modified with CdTe quantum dots | 100 |
| 6.1 | Motivation | 100 |
| 6.2 | Outputs | 100 |
| 6.3 | Conclusions | 100 |
| 6.4 | Articles | 101 |
| 6.4.1 | Journal Article 5 | 101 |
| 7 | Summary of results and conclusions | 121 |
| | List of abbreviations | 124 |
| | Bibliography | 126 |
| | List of publications | 138 |
| A | Polypyrrole nanoparticles as chemo-resistive sensors | 139 |
| B | Other collaborative journal papers | 142 |

Chapter 1

Introduction

1.1 Motivation

The development and investigation of gas sensors become the subject of great importance because of their potential implementation in various areas such as environment monitoring, food quality, and health diagnosis [1, 2, 3]. Many efforts have been devoted in developing of gas sensing materials with high sensing capabilities to target analytes. Nanomaterials have undoubtedly gained the most of the attention among scientists as gas sensors functional layers, due to their high surface to volume ratios and unique chemical or physical gas adsorption capabilities resulting in enhanced sensitivity [4]. Moreover, nanoscale morphology gives possibility for easy surface modifications of the active layer of gas sensor using a relatively simple and cost effective fabrication methods [2].

Among different materials, inorganic materials, such as metal [2] and metal oxides (MOX) [5, 6] represent the most widespread sensing layers for gas sensors. Mostly, from the group of MOX, semiconductor oxides (e.g., WO_3 , ZnO , SnO_2 , In_2O_3 , etc.) have been extensively investigated [7]. In addition, the doping of host sensing material with nanostructures of noble metals have been reported to increase its chemical activity and enhance the sensing properties of gas sensors. Among the metallic elements employed for gas sensors are palladium (Pd) [8], platinum (Pt) [9], Au [10], Ag [11], etc. Another category used for gas sensors are carbon based materials, thanks to their high quality crystal lattices and high carrier mobility (e.g. ballistic charge transport) [12]. The most frequently studied carbon nanomaterials in gas sensors application are namely carbon nanofibres, carbon nanotubes, graphene and reduced graphene oxide [13].

From organic materials, CPs represent an important class for next generation of chemical gas sensors [14, 15]. CPs either individually or in a hybrid form, i.e., in the combination with other materials such as various noble metals (e.g., Ag [16, 17], Au [18], Pd [19]), MOX (e.g., ZnO [20], SnO_2 [21]), carbon-based materials (e.g., carbon nanotubes [22, 23] or various forms of graphene [24, 25]) were used for the development of the sensing layers. CPs such as PPy [26, 27], polyaniline (PANI) [28, 29], polyacetylene (PA) [30, 31], polythiophene (PTh) [32], and poly(3,4 ethylenedioxythiophene) (PEDOT) [33, 34] are considered as most promising materials for gas sensing applications. Among hetero-cyclic CPs, PPy captured the wide attention of the scientific community due to its facile and diversified synthesis methods, its good electrical conductivity and relatively high environmental stability. Therefore, it has been used not only in gas sensing but also in electrodes for batteries [35], supercapacitors [36] and biosensing [37].

Metal and MOX gas sensors require very high operating temperatures (from 200 °C [38, 39] up to 400 °C [40, 41], or even higher [42]) which turn into high power consumption. This is a primary issue, especially for the autonomy of portable battery-powered devices. To overcome this problem, it is necessary to accomplish sensitive layers from novel materials, which allow sensing of the gaseous analytes at RT. In particular, the main advantage of the above mentioned CPs is their capability of working at RT, which make them outstanding candidates compared to most MOX. The creation of composite materials by functionalization of CPs with e.g., catalytic metals or MOX showed better gas sensing performances compared with the single component, especially higher response, lower LOD and faster response [43].

The monitoring of the gases and volatile organic compounds (VOCs) in exhaled breath has gained a considerable scientific, clinical, and research attention due to its potential in enabling the non-invasive observation of the biochemical processes of the human body. Specific gases and VOCs can be considered as relevant biomarkers related to different diseases especially variety of pulmonary diseases (chronic

obstructive pulmonary disease, lung cancer, asthma, cystic fibrosis, respiratory tract infection), and other diseases such as colorectal cancer, breast cancer, and they could aid the early diagnosis of those diseases [44, 45, 46, 47, 48, 49].

Apart from the breath analysis, specific gases and VOCs are classified as air pollutants and they are considered as essential parameters for assessing the air quality in indoor and outdoor environments (e.g., emission from industrial processes, traffic activity, waste treatment and disposal, tobacco smoking, etc.) [50]. Moreover, detection of different gases and VOCs is used for food quality analysis in order to determine the freshness and spoilage of food [51].

The detection of analytes such as ammonia, acetone, ethanol, ethylene and toluene in very small amounts, in the sub-ppm range, is of great significance for assessment of potential environmental pollution, human health risks, diseases diagnosis and food spoilage. Nowadays, the detection of those target gases in the breath analysis, food and/or air quality requires large and expensive laboratory equipment such as gas-chromatographers, ion-mobility spectrometers and mass spectrometers [51, 52, 53, 54, 55]. Recently, the gas sensors also have found a new potential in such applications, where development of novel sensing materials and their utilization for the detection of the gaseous markers have attracted wide attention among many researchers. This attractive research direction could have a huge social impact with the possibility of the costs reduction, and affecting, in turn, the quality of life.

Therefore, my dissertation topic was focused on developing of a micro scalable gas sensor to enable monitoring of low concentration levels of the target analytes defined above which are relevant in air and food quality control or disease diagnosis. Keeping in mind the main advantage of CPs (working at RT), the sensing properties of PPy and its combinations with other decorative/functional materials were examined, discussed, and compared in this work.

1.2 Aims of the thesis

The main aim of this thesis is to develop sensor devices based on a unique combination and integration of nanostructured PPy sensing materials and transducing techniques. The performance of this device was verified by monitoring low concentrations of specific gases and VOCs including acetone, ammonia, ethanol, ethylene and toluene, which are classified as relevant markers involved in breath analysis, food quality analysis and/or environment monitoring.

To achieve this goal, the thesis is divided into the following specific objectives:

1. Synthesis of nanoscaled functional films (e.g., NRs, NPs) based on PPy via chemical and/or electrochemical methods.
2. Study of composition and structure of the synthesized PPy materials as well as investigation of their chemical activity and potential to be used as sensing material.
3. Surface modification of the nanoscaled PPy with different catalytic metals (e.g., Au, Ag) or QDs (e.g., cadmium based core/shell structures) followed by determination of chemical composition of those inorganic-organic composites.
4. Gas sensing tests of both non-modified and surface modified PPy films to target gases and VOCs through measurements of variation in electrical conductivity or changes in surface acoustic wave (SAW) characteristics due to analyte sorption.

1.3 Structure of thesis

The development and progress of this thesis are described and discussed in the following structure:

Chapter 2 reviews the state of the art related to the diversity of gas sensing materials and their performances, the transducing technologies in gas sensor devices, as well as the origin and classification of specific gaseous markers. As MOX and CPs have been the main materials selected for my PhD research, their properties are broadly reviewed and studied in this chapter.

Chapter 3 describes the principles of techniques used for the synthesis of PPy based gas sensing materials, determination of structural and morphological characteristics of those materials, and gas sensing test of developed sensors.

Chapter 4 expands the state of the art related specifically to PPy and its role in gas sensing. Therefore, this chapter presents the recent progress in PPy based gas sensors with different morphology and their sensing capability towards different gases and VOCs. Additionally, this chapter shows the results associated to specific objective 1 and 2, in which the synthesis of PPy NPs and NRs was achieved via chemical and electrochemical approaches and complemented with their morphological and compositional studies. The sensing activity of PPy NRs and NPs to ammonia (classified as relevant marker in breath, food and environment analysis) is investigated by *in-situ* analysis using Raman and XPS.

The results from this research are presented in the following articles:

- **Journal Article 1.** *Nanostructured polypyrrole-based ammonia and volatile organic compound sensors*, M. Šetka et. al., *Sensors*, 17, 28, 2017, doi: 10.3390/s17030562. (Section 4.4.1)
- **Journal Article 2.** *Raman and XPS studies of ammonia sensitive polypyrrole nanorods and nanoparticles*, M. Šetka et. al., *Scientific Reports*, 9, 10, 2019, doi: 10.1038/s41598-019-44900-1. (Section 4.4.2)
- **Conference article 1.** *Gold/polypyrrole nanorods for gas sensing application*, M. Šetka et. al., *Proceedings of SPIE (Smart Sensors, Actuators, and MEMS VIII)*, Barcelona, 2017, doi: 10.1016/j.matpr.2019.10.067. (Section 4.4.3)

Chapter 5 reports on the synthesis and processing conditions of PPy films modified with catalytic Au NPs and/or Ag NPs. Those films are implemented into L-SAW transducing platforms and their sensing properties are tested towards specific gases and VOCs (selected in Section 2.3.4) in the low concentration range (ppb-ppm). The presented results are related to specific objective 3 and 4, and they are summarized in following articles:

- **Journal Article 3.** *Love wave sensors based on gold nanoparticle-modified polypyrrole and their properties to ammonia and ethylene*, M. Šetka et. al., *Sensors and Actuators B: Chemical*, 304, 2019, doi: 10.1016/j.snb.2019.127337. (Section 5.4.1)
- **Journal Article 4.** *Love wave sensors with silver modified polypyrrole nanoparticles for VOCs monitoring*, M. Šetka et. al., *Sensors*, 20, 5, 2020, doi: 10.3390/s20051432. (Section 5.4.2)

Chapter 6 describes the morphological and chemical properties of inorganic-organic composite films formed of PPy NPs and CdTe QDs. The gas sensing test of L-SAW sensors based on this CdTe/PPy layer is validated towards target VOCs (acetone, ethanol and toluene). The obtained results are discussed in following article:

- **Journal Article 5.** *Cadmium telluride /polypyrrole nanocomposite based Love wave sensors for monitoring of acetone in ppb range*, M. Šetka et. al. (submitted to *Sensors and Actuators B: Chemical*). (Section 6.4.1)

Chapter 7 presents the summary and comparison of the critical sensing features of all developed PPy based sensors in this thesis. The conclusions of this research are included in this chapter.

Appendix A includes the results related to initial gas test of chemo-resistive sensors based on non-modified and modified PPy NPs.

Appendix B reports the development of MOX nanostructures and their investigation for gas sensing of specific markers. The results related to MOX were obtained in collaboration with CEITEC and IMB-CNM, CSIC, and they are summarized in following articles:

- **A Journal Article 1:** *AACVD synthesis and characterization of iron and copper oxides modified ZnO structured films*, M. Claros, M. Šetka et. al., *Nanomaterials*, 10, 3, 2020, doi: 10.3390/nano10030471. (Appendix B)
- **A Journal Article 2:** *Cerium oxide-tungsten oxide core-shell nanowire-based microsensors sensitive to acetone*, M. Tomić, M. Šetka et. al., *Biosensors*, 8, 4, 2018, doi: 10.3390/bios8040116 (Appendix B)

Chapter 2

Literature review

2.1 Classification of sensing materials

This sub-chapter introduces a various type of gas sensitive materials and discusses their advantages, disadvantages, and performance parameters.

The gas sensing materials are a key component which play a critical role in the performance of gas sensors. According to their nature, all gas sensors can be classified into three groups: MOX [56], CPs [14] and carbon based materials [13, 57], as it is shown in Figure 2.1. In general, the main requirements of gas sensing material are the ability to show a high sensitivity and selectivity in contact with target species. Additionally, the sensing layer is supposed to interact reversibly and reproducibly with the specific analyte of interest, and show a strong stability in a harsh environment conditions such as high temperature and/or high relative humidity (RH). From the economical point of view, the molecular recognition layer should be widely available, simply and inexpensively synthesized, compatible and easily implemented with a specific transducing platforms.

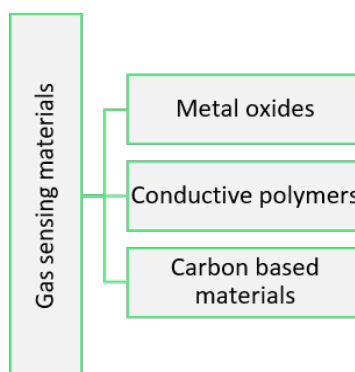


Figure 2.1: Classification of gas sensitive materials.

All mentioned types of gas sensing materials showed the markedly different sensing characteristics with the competing advantages over each other due to different nature of analyte adsorption process and sensing mechanism between specific material and target analyte [4]. The summary of advantages and limits of gas recognition materials is presented in Table 2.1. Generally, the particular drawbacks for single sensing materials, namely, high operating temperature and low selectivity for MOX, poor chemical stability and deficient selectivity for CPs, and poor reproducibility, long term stability and high cost of carbon based materials, can restrict their practical application.

In order to conquer the above mentioned specific issues, several possibilities have been suggested as an alternative strategies for enhancement of gas sensing performances by many researchers [43, 58, 59, 60]:

- the functionalization and doping of host recognition materials with other components,
- creation of hetero-junctions (interface between two dissimilar semiconductor materials with different band gap),
- and utilization of inorganic/organic hybrid materials.

Table 2.1: Summary of Gas Sensitive Materials. The data is adapted from [61].

| Type of material | Advantages | Limiting factors |
|------------------------|--|--|
| MOX | Small size Low cost Short response time Long-lasting life Simple circuit | Poor specificity and selectivity High operating temperature Affected by humidity and poisoning Non-linearity at high temperature High energy consumption |
| CPs | Strong sensitivity Room operating temperature Strong biomolecular interactions Various preparation processes | Long response and recovery time Low selectivity Easy affected by humidity |
| Carbon based materials | High sensitivity Strong adsorption capacity Stable and suitable for mixing with other materials Quick adsorption capacity | High cost Complicated production Non-uniform standard Complex mechanism |

Additionally, the gas sensing properties can be enhanced by morphological and dimensional control, specifically by structuring materials to 0 dimensional (D) (e.g., NPs and QDs), 1D (e.g., nanofibers, nanotubes, NRs, and nanowires), 2D (e.g., thin films, nanosheets and nanoplates) and 3D (e.g., hierarchical structures assembled from NPs, NRs, nanosheets, etc.). These forms with the high surface area may provide more active sites for the sorption of gas [60].

2.1.1 Metal oxides

Semiconductor MOX nanostructures and thin films have been widely adopted for detection of different gases and VOCs. Those structures are mostly implemented into chemo-resistive transducing platforms [62], but also they find application in the field of SAW [63] or optical sensors [64]. There are two main types of semiconducting MOX based sensors, n-type (whose majority carrier are electrons) and p-type (whose majority carrier are holes).

Both, n-type (e.g., ZnO, WO₃, etc.) and p-type (e.g., CuO, NiO, etc.) oxides were tailored to various shapes (e.g., NRs, nanowire, nanotubes etc.) with different aspect ratio (μm - nm scale) and used as the recognition layer for gas sensors [65]. Figure 2.2 illustrates the predominant composition of MOX used in gas sensing.

Those materials have been synthesized using various synthesis routes based on wet processing, solid-state processing and vapor-phase processing [65]. In general, the MOX gas sensors showed enhanced sensing properties with high sensitivity towards many analytes including specific gases and VOCs (selected in Section 2.3.4) [66]. However, the main drawback of those sensors which restricts their development is a high operational temperature (even up to 500 °C). Thus, high cost and complicated configuration of those sensors is noticed in comparison to others system working at RT.

Selected semiconductor MOX nanostructures were examined in this thesis in collaboration with CEITEC and IMB-CNM, CSIC. Namely, columnar ZnO nanostructures were synthesized and their surface was modified with CuO and Fe₂O₃. The investigation of their morphology, chemical composition and wettability properties was analysed, because these parameters are essential factors for the selection of further application of materials. The results showed that the modification of ZnO with iron or copper oxides enhances the hydrophobic behaviour of modified structures. This feature is very important for gas sensing applications, as the surfaces with increased hydrophobicity can lead to lower adsorption of water on active sites and avoid humidity interference with the detection of gas. The results are published in a journal article, *AACVD synthesis and characterization of iron and copper oxides modified ZnO structured films* [216].

The formation of hetero-junctions by coupling of two different n-types and/or n and p-type of MOX have been reported in the literature as a new strategy for improvement of gas sensing performance [60, 68]. Therefore, the gas sensing studies of the composite MOX structure, namely cerium oxide-tungsten oxide core-shell nanowires (n-n hetero-junctions) were also explored in this

thesis. The results are summarized in a journal article, *Cerium oxide-tungsten oxide core-shell nanowire-based microsensors sensitive to acetone* [67]. Indeed, the structures with hetero-junctions demonstrated an increased response and sensitivity in comparison to non-modified tungsten oxide wires or cerium oxide porous films based sensors. The gas sensing test of those sensors to specific gases and VOCs (ethanol, acetone, toluene, carbon monoxide and hydrogen) was carried out at the temperature range between 150-400 °C. Those studies confirmed the above mentioned requirements (in terms of high operation temperature) of MOX based sensors and shifted the focus of this thesis to exploration of properties of CPs in gas sensing.

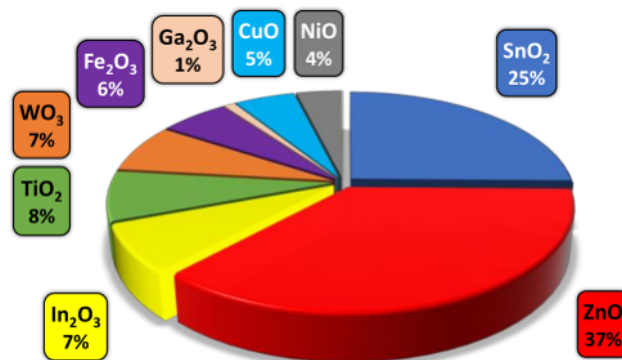


Figure 2.2: A survey of the most applicable gas sensitive MOX reported in the literature (Web of Science database from 1998 to 2018). The image is adopted from [67].

2.1.2 Conductive polymers

Polymers are organic materials and most of them belongs to the category of insulators since they are made by covalent bonds without free movable charge carriers (electrons or ions). However, CPs are a specific category of synthetic polymers which opened a new era in science and technology due to their distinctive electrical and optical properties which are similar to those of semiconductor MOX or even metals. CPs, namely PA, were discovered by Heeger, MacDiarmid and Shirakawai in 1977 and authors were awarded the Nobel Prize in Chemistry in 2000 [69]. The structure of PA is shown in Figure 2.3. CPs found extensive application in the field of rechargeable batteries, electrochromic display devices, polymeric light emitting diodes, photovoltaic devices, biosensor and gas sensor [14, 70, 71, 72].

The conductivity of CPs originates from highly delocalized electrons between the conjugated polymer backbone (alternating single bonds (σ) and double bonds (π)) and the dopant (negatively charged species). The delocalized π -electrons freely move along the entire chain of polymer and the dopant removes an electron from a delocalized bonding arrangement, creating a hole. Afterwards, an electron from neighbouring molecule jumps and fits that hole generating a new hole and allowing charge to flow through the polymer chain [69]. Therefore, the choice of dopant and doping level determine the conductivity of CPs [74].

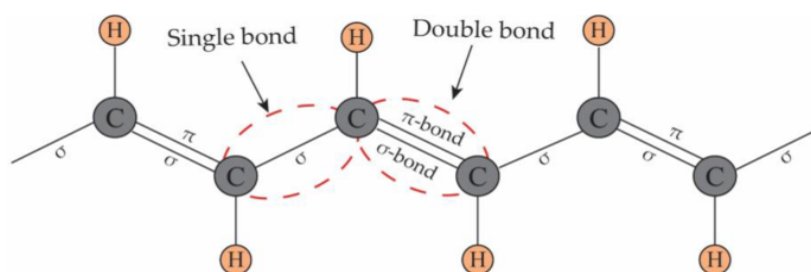


Figure 2.3: The structure of PA: the backbone contains conjugated double bonds, where π bonds move along the carbon chain. The image is adopted from [73].

CPs undergo oxidation and reduction processes which are dependent on the use of p-type and n-type dopants, respectively. During the oxidation, electrons are extracted from the highest occupied molecular orbital (HOMO) of the valence band, while electrons are transferred to the lowest unoccupied molecular

orbital (LUMO) of the conduction band during the reduction. The charge carriers in the form of polarons, bipolarons or an equilibrium between those two are created during the redox processes. A polaron is defined as a radical ion (spin $\frac{1}{2}$) associated with a lattice distortion and localized electronic levels within the band gap after removal of an electron. A bipolaron is defined as a pair of like charges (dication) associated with a strong local lattice distortion after removal of second electron where the decrease in the energy gap occurred [73, 75]. The electronic band structures of an undoped polymer, polaron and bipolaron are shown in Figure 2.4.

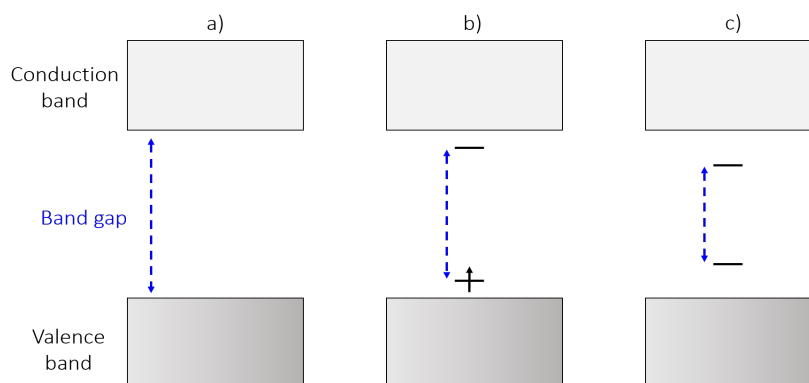


Figure 2.4: Electron band structure of: (a) undoped polymer (insulator), (b) polaron and (c) bipolaron.

Most of nanostructured CPs with different morphology (e.g., 0D, 1D, or 3D) have been synthesized by oxidative polymerization between corresponding monomer and an oxidizing agent using chemical or electrochemical techniques [76]. A different synthesis conditions and approaches induce the differences in the morphology and structure of CPs, which are unquestionably a crucial factors affecting their physical and chemical properties. Various synthesis strategies have been used for CPs fabrication, which can be categorized under two main approaches: template based synthesis (hard templates) and template free approaches (soft templates) [71, 77, 78, 79]. A schematic illustration of CPs synthesis process using the hard and soft templates is shown in Figure 2.5.

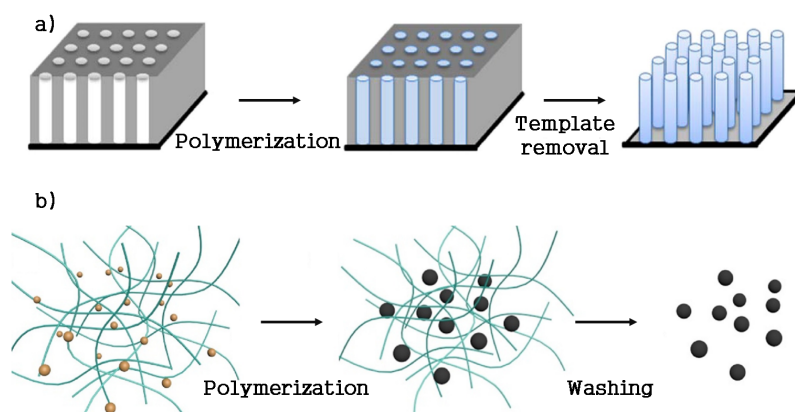


Figure 2.5: Schematic illustration of polymerization of CPs using: anodic aluminum oxide (AAO) hard template (a) and self assembly process (b). The images are adopted from [84, 85].

1. The template based synthesis used a physical template to guide grow of nanostructures in designed shapes and sizes. The most common hard templates are nano sized channels such as AAO and particle track-etched membranes (e.g., polycarbonate or polyester) [80, 81]. Those type of synthesis routes are effective for controlling of homogeneity, length, and diameter of nanostructures, while their main disadvantage is a post-synthesis removal of the template.
2. The soft template approaches are a relatively simple and cheap fabrication process where polymerization of CPs is based on self assembly of various types of surfactants micelles [81, 82, 83]. Those methods do not require a template or potentially harsh post-synthesis treatment.

The CPs have been used as the sensitive layers of gas sensors since early 1980s. They have been in the spotlight of research investigations particularly thanks to their conductivity and operation at RT, but also due to easy synthesis, chemical and structural diversity, and flexibility. CPs such as PPy, PANI, PTh, and PEDOT, and their derivatives have been the most studied candidates for sensing layers [86, 87, 88]. The interaction between those CPs and chemical species of interest can cause a change in electrical, piezoelectric or optical properties of the active layer. Therefore, the CPs have found application in chemo-resistive [89, 90], mass [91, 92] and optical gas sensors [93, 94]. The structure of typical CPs used in gas sensing is presented in Figure 2.6.

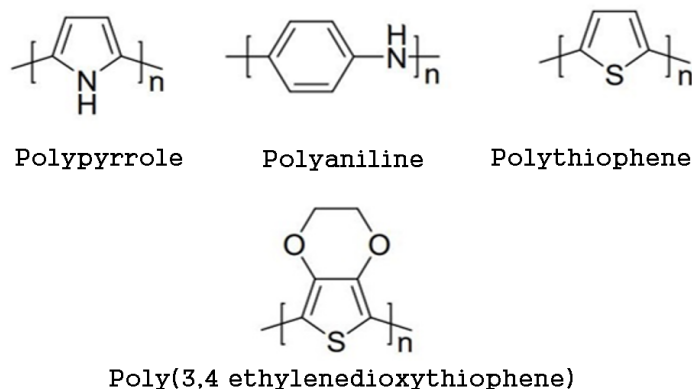


Figure 2.6: Chemical structure of polypyrrole (PPy), polyaniline (PANI), polythiophene (Pth) and Poly(3,4 ethylenedioxythiophene) (PEDOT).

The most widely used gas sensors based on PPy, PANI, PTh and PEDOT are chemo-resistors and their sensing performances to different gases (e.g., ammonia, nitrogen dioxide, carbon dioxide etc.) and VOCs (e.g., methanol, ethanol, acetone, etc.) were intensively investigated [14, 95, 96, 97]. Ammonia have been very often studied as the target species of those sensors and the responses to this analyte are compared and presented in Table 2.2.

Table 2.2: Summary of sensing properties of various CP chemo-resistive based sensors to ammonia. Response of sensor is defined as $R = R_g/R_a$, where R is response of sensors, and R_a and R_g are resistance in air and gas, respectively. The response of sensor (R) is defined for the tested concentration (C).

| Type of CPs | Modification | Morphology | R | C (ppm) | Ref. |
|-------------|-------------------------|---------------|-----|---------|-------|
| PPy | - | Film | 1.1 | 20 | [99] |
| | - | Thin film | 1.5 | 50 | [100] |
| | SnO ₂ | Nanofiber | 2.8 | 2.5 | [89] |
| | Reduced graphene oxide | Film | 1.1 | 1 | [101] |
| PANI | - | Film | 1.6 | 50 | [102] |
| | - | Nanofibrous | 2.4 | 10 | [103] |
| | SnO ₂ | Porous sphere | 5.4 | 10 | [90] |
| | Quasi-graphite capsules | 3D hollow | 1.1 | 5 | [104] |
| PTh | - | Film | 1 | 100 | [105] |
| | Reduced graphene oxide | Fiber | 2.2 | 10 | [106] |
| PEDOT | - | Film | 1 | 500 | [107] |
| | Graphene | Film | 1 | 50 | [107] |
| | - | Nanotube | 1.0 | 20 | [108] |
| | Ag | Film | 1.3 | 15 | [109] |

In general, all tested sensing CP materials showed the positive response to ammonia. However, the ratio of response magnitude to concentration value of PPy and PANI based sensors is slightly higher compared to other mentioned polymers. These observations were reported in the review paper about “*Conducting Polymers as Chemiresistive Gas Sensing Materials*” [86]. The enhanced responses of PPy

and PANI may be partially assigned to their particular morphology, but also to the doped states (especially their nature and concentration) which affect the degree of oxidation and control the electrical conductivity in polymers [98]. The sensors based on hybrids of PPy, PANI, PTh and/or PEDOT with another material (e.g. MOX, noble metals or carbon based materials such as graphene) showed increased sensing properties over bare materials. As mentioned above, this can be related to the creation of functionalized material which possesses a new or improved electronic, magnetic, and optical properties in comparison with non-modified CPs.

Consequently, it was demonstrated that either in single or modified form, various type of CPs can be successfully used for gas sensing. Despite their great advantages such as RT operation, high sensitivity and short response time, some functional issues such as poor selectivity and modified sensor response in humid atmosphere have been found challenging [110]. The development of nanocomposite material with favourable properties and chemical versatility may help to overcome those limitations, and hence, promote an effective detection of specific gases and VOCs [96, 111]. Thus, the interest in future investigation and development of hybrid materials (especially PPy and PANI) with the desired properties is expected in the field of gas sensors.

In this context, the work in this thesis was focused on the studies of non-modified and modified PPy nanostructures and their integration into sensing devices for the detection of target gases and VOCs.

2.2 Introduction to gas sensors

This sub-chapter introduces the general working principles of gas sensors with different transducing principles. This section is focused specifically on chemo-resistive and surface acoustic wave (SAW) sensors. A chemical gas sensor can be described as a device that transforms chemical information into an analytically useful signal (e.g., electrical, optical), which can be measured and quantified directly or indirectly, see Figure 2.7. The receptor (i.e., gas sensitive material) and transducer are two main parts of chemical sensors. The transformation of chemical information into a form of energy is responsibility of the receptor, while the transducer converts that energy into analytical signal [112].

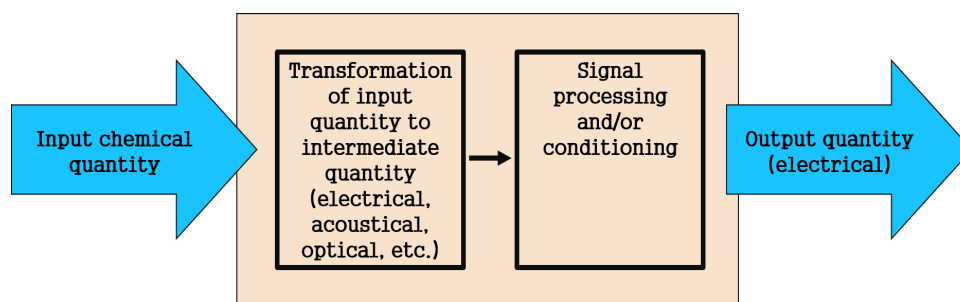


Figure 2.7: The schematic diagram of chemical gas sensor which produce an electrical signal as results from the interaction between some chemical species (input signal) and sensitive layer [113].

The main functional characteristics of gas sensors include sensitivity, selectivity, response time, recovery time, and reversibility [114]. Depending on the type of transducing mechanism, these parameters may vary a lot and have a significant influence on the final feature of the sensor. The meaning of each parameter is specified below:

- **Sensitivity** of sensor measures a magnitude of output signal which is produced as the response to an input quantity of given magnitude. Generally, the response of gas sensors is expected for the tested analyte concentration in range of ppm or even ppb.
- **Selectivity** can be defined as the ability of sensor to respond primarily to only one species in the presence of other analytes. However, complete selectivity of gas sensor is usually desired but very often hard to achieve.
- **Response time** is defined as the necessary time to reach 90 % of the total value of measured electrical change.
- **Recovery time** is defined as the time required for measured signal to return to 90 % of the original value, when sensor exposure is switched from the target gas to carrier gas (synthetic air or some halogen gas). Both, response and recovery times should be as fast as in units of seconds.

- **Reversibility** is the ability of a sensor to recover, or return to its original background/baseline condition, after exposure to an analyte.

Apart of the mentioned sensors characteristic and their desired magnitudes, there is also a need for production of simple, inexpensive and low-power devices in order to fulfill the economical requirements.

2.2.1 Transducing principles

Gas sensors can be classified according to the method for monitoring of gas-solid interactions (type of transducing mechanism), and they can be divided in following groups shown in Table 2.3.

Table 2.3: The classification of gas sensors based on the transducing mechanism.

| Principle | Groups | Measured quantity |
|-------------------|----------------|-------------------------|
| Electrochemical | Conductometric | Conductivity/resistance |
| | Amperometric | Current |
| | Potentiometric | Voltage |
| Electromechanical | Optical | Absorption/emission |
| | Gravimetric | Mass |
| | Calorimetric | Thermal conductivity |

Electrochemical gas sensors can be divided into three main classes according to the operating principle: **conductometric**, **amperometric** and **potentiometric** sensors. The current generated by reaction of an analyte at an electrode surface is measured as the signal of amperometric sensor. The signal is usually measured at a fixed electrode potential. The potentiometric sensors measure the change in potential on an electrode under zero current. The conductometric sensors are devices that transduce the measured physical parameter into a change in conductivity (conductance is the reciprocal of resistance) [115]. Those sensors are popularly called **chemo-resistors**, and their working principle is described below.

The operating principle of chemo-resistive gas sensors is based on the change in their electrical conductivity caused by a reaction between gaseous chemical species and receptor (sensing material). The reaction between gas and sensitive layer is believed to occur by the adsorption of oxygen in the surface, leading to an increase or decrease of electrical resistance of the sensitive layer after the exposure to an oxidative or reductive target gas, respectively (considering an n-type semiconductor) [116]. Typically, these sensors are designed from two parts:

1. electrodes (mostly interdigital) which are patterned on an insulating substrate (silicon, alumina),
2. and a conductive sensing layer (e.g. MOX, CPs and/or carbon based materials) which is embedded to electrodes.

The sensors are usually connected to direct current (DC) bridge configuration. During the measurements, DC voltage is applied to the electrodes and the electrons are traveling in the sensitive layer between two electrodes. When the target gaseous analyte is adsorbed at the sensitive layer, the change in electrical resistance occurs and this change is monitored as a sensor response. Chemo-resistive gas sensors are the most frequently reported in the literature among sensors from electrochemical group. The working principle of those sensors is shown in Figure 2.8.

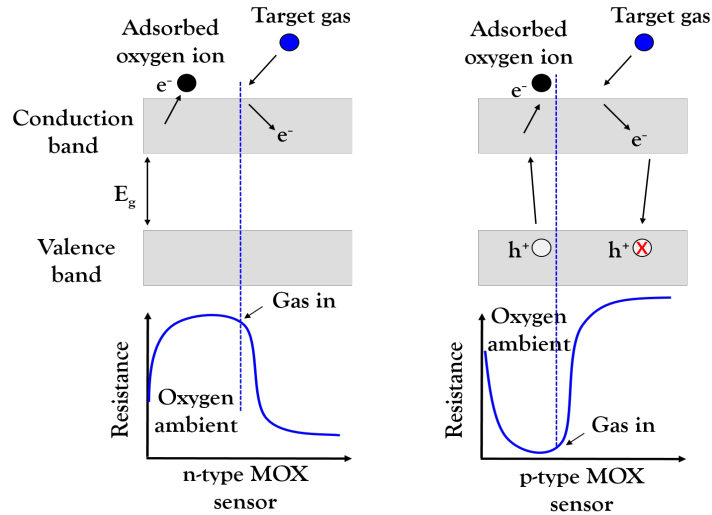


Figure 2.8: The working principle of chemo-resistive gas sensors; In the presence of air, oxygen gas is adsorbed on the surface of the sensing material, and the interaction between oxygen molecules and MOX forms charged oxygen species by capturing electrons from the conduction band, leading to a change in conductivity of the MOX. When the sensors is exposed to a reducing gas, the gas may react with the adsorbed oxygen ion and the resistivity is decreased for an n-type MOX sensors (left) due to electron transfer into the conduction band. The opposite holds for a p-type MOX sensors (right). The image is adapted from [117].

Gravimetric gas sensors rely on disturbance and changes in the mass of sensitive layer during the interaction with analysed gases. The mass vibrations (changes) on the mechanical resonator (piezoelectric substrate) are caused by the absorption of a gas on sensitive layer which induce a shift in the operating frequency of resonator. The resonator motion (displacement, rotation, strain) is converted into the electrical signal which is measured as the sensor response [118]. The working principle of those sensors is showed in Figure 2.9. Commonly, three types of the piezoelectric transducers are known in the field of the gas sensors, including cantilevers, bulk acoustic wave (BAW) resonators (e.g. quartz crystal microbalance (QCM)) and SAW based devices. Cantilevers are micro-machined elastic beams that can reversibly bend under applied stress (adsorbed mass). The propagation path of acoustic wave occurs through a bulk of structure and near the surface of piezoelectric material in BAW and SAW sensors, respectively. It has been found that sensitivity of SAW gas sensors is higher compared to the corresponding gas sensors based on BAW, which is related to the operation of SAW devices at higher frequency and propagation of the wave close to sensing surface in those sensors [63, 119].

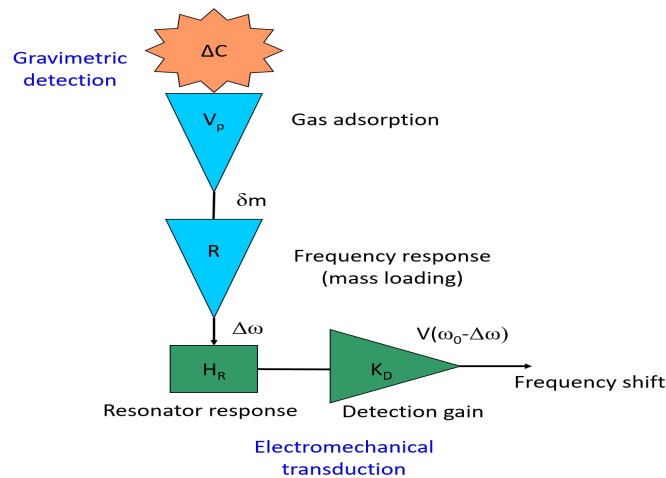


Figure 2.9: Schematic illustration of the working principle of gravimetric sensors. The gas with the concentration (δC) is adsorbed in the volume (V_p) of the sensitive layer causing a mass variation δm of the resonator, which induces a shift of its resonance frequency. The resonator motion is then translated into an electrical signal. The image is adopted from [118].

Optical gas sensors are based on classical spectroscopy principles encompassing a range of techniques such as measurement of absorbance, fluorescence, reflectance, refractive index and surface plasmon resonance. When the sensitive material is exposed to an electromagnetic radiation, the radiation interferes with a sample and changes its optical parameters. That change is detected and measured by an optical detector such as such as a photodiode, thermopile, etc. The shift in the signal (e.g., absorbed, reflected or transmitted light) when sensing material is exposed to a gas is calculated as the response of gas sensor [110]. The working principle of the optical sensor based on surface plasmon resonance is shown in Figure 2.10.

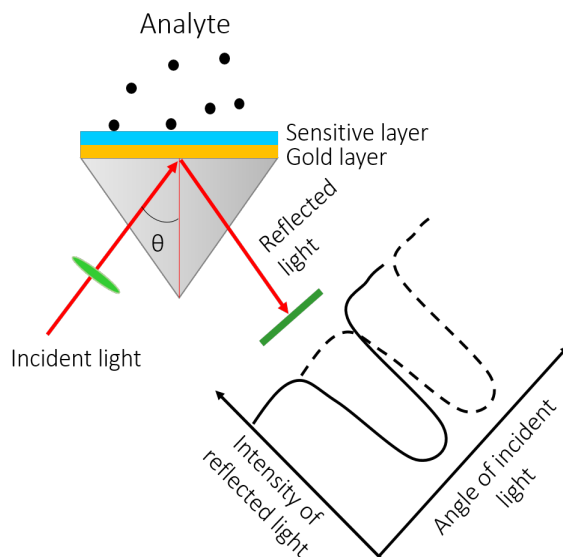


Figure 2.10: Schematic illustration of the working principle of the optical gas sensor based on surface plasmon resonance. The image is modified from [120].

The principle of calorimetric gas sensors is based on the creation of temperature variation (enthalpy generated by a catalytic exothermic reaction) which is measured as the response of sensor. Pellistors (based on catalytic and thermal conductivity) are the most common devices [110].

2.2.2 SAW sensors

The existence of SAW was firstly demonstrated by Lord Rayleigh in 1885 so those type of waves are very often called **Rayleigh wave**. Rayleigh waves propagate along a free surface or on the boundary between two materials with the particle motion in longitudinal and transverse directions which follows a retrograde elliptical path. The most of wave energy is localized in the near surface region of an isotropic solid and the amplitude of wave is decreasing with depth [121]. The Rayleigh waves are studied by seismologists as they exist in earthquakes.

Later in 1911, the **Shear Horizontal (SH) SAW** were investigated by Augustus Love. Those waves exist in the surface layer when the shear wave velocity of the upper layer is less than that of the lower layer. Those waves are often called **Love waves**. The waves are trapped in the upper layer and the particle motion is parallel to free surface and perpendicular to the direction of propagation [121]. The propagation path of Rayleigh and Love waves is shown in Figure 2.11 a and b, respectively.

Since interdigital transducers (IDTs) were introduced for transmitting and receiving SAW (White and Voltmer, 1965) [121], SAW devices have been widely employed in electronic systems and sensors. The utilization of SAW (e.g., Rayleigh and Love waves) in sensor application have been showed as beneficial due to a surface confinement of energy which makes the waves extremely sensitive to any surface perturbations. The SAW could be excited and detected by IDTs on the surface of piezoelectric crystals. When a radio frequency voltage is applied between the electrodes, the periodic electric field is produced on the crystal and SAW is generated. As the SAW propagates, any change on the surface layers or the nearby environment can affect the characteristics of propagation path and change the velocity or amplitude of the wave. Those changes in velocity can be monitored by measuring the frequency or phase characteristics of the sensor [113].

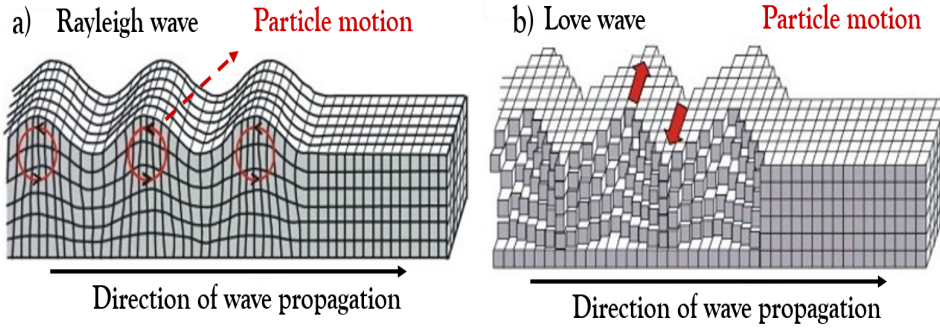


Figure 2.11: The schematic illustration of propagation path of Rayleigh (a) and Love (b) waves. Both types of wave have horizontal propagation from left to right. Rayleigh waves contain both vertical and radial motion, whereas Love waves have purely transverse motion. The image is adopted from [122].

The SAW gas sensors are composed of:

- piezoelectric substrate,
- IDTs,
- wave guiding layer (in the case of Love wave),
- and sensitive layer.

The structure of the SAW sensor with the guiding and sensitive layer on the top of piezoelectric substrate is presented in Figure 2.12.

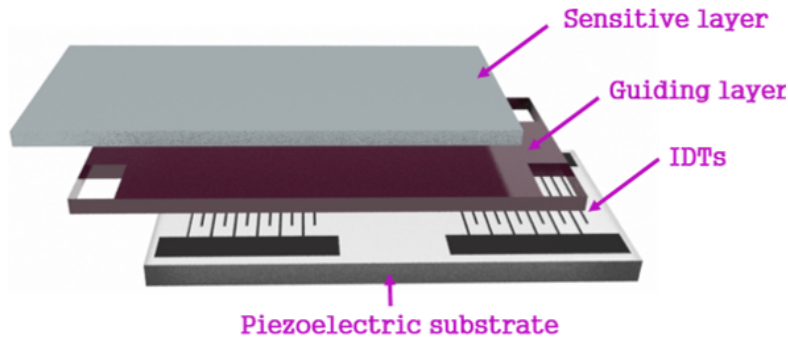


Figure 2.12: The structure of L-SAW sensor contains of piezoelectric structure, IDTs, guiding and sensitive layer. When the wave is guided through both, guiding and sensitive layer, that structure is known as multi-guiding.

The piezoelectric crystals such as quartz, lithium niobate (LiNbO_3), lithium tantalite (LiTaO_3), gallium arsenide (GaAs), zinc-oxide (ZnO) are the most common materials used for the generation of SAW. The crystal cut and its orientation are critical parameters which have an influence on polarization of wave and determination of type of SAW such as Rayleigh, SH, Love, Leaky, Stoneley, or Lamb. For instance, materials such as ST-X quartz¹, 128° Y-X LiNbO_3 and 64° Y-X LiNbO_3 are very often used for the generation of Rayleigh waves, while in the case of Love waves, ST- 90° X quartz, 41° YX LiNbO_3 and 36° Y-X LiTaO_3 are frequently implemented. Electromechanical coupling coefficient (K^2) and temperature coefficient of frequency (TCF) are key parameters which need to be considered for the selection of the piezoelectric substrate. K^2 represents the efficiency of converting electrical energy into mechanical energy. TCF determines the change in length of a material for a given temperature change and how quickly the period of IDTs changes as a function of temperature. The piezoelectric crystal with the large K^2 and zero TCF provides the wave with low attenuation and appropriate velocity, respectively [124, 125, 126]. The properties of different piezoelectric crystals are shown in Table 2.4.

¹Rotated Y-cut with rotation angle of $42^\circ 75'$, propagation in X direction [123]

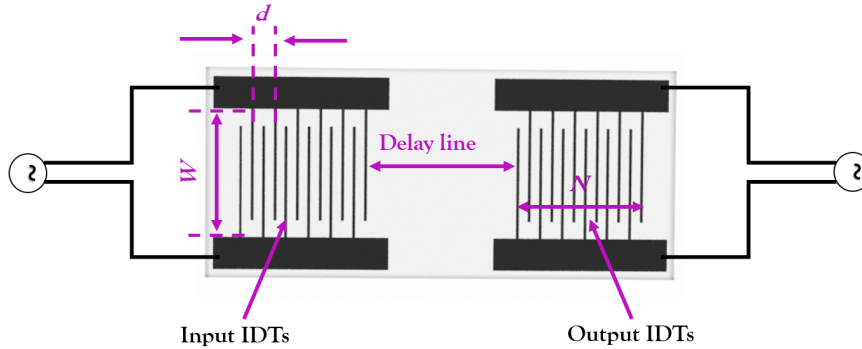
Table 2.4: Summary of the properties of different piezoelectric crystals used for SAW sensors.

| Type of crystal | Type of wave | K^2 (%) | TCF (ppm/C) | Velocity (m/s) |
|-----------------------------|------------------|-----------|-------------|----------------|
| ST-X Quartz | Rayleigh or Love | 0.11 | 0 | 3159 |
| 128° Y-X LiNbO ₃ | Rayleigh | 5.6 | 75 | 3992 |
| 64° Y-X LiNbO ₃ | Rayleigh | 11.3 | 80 | 4743 |
| 41° Y-X LiNbO ₃ | Love | 17.2 | 75 | 4792 |

A delay line configuration which consists of two ports of IDTs at the certain separation, is the most frequently used in the design of SAW sensors. The SAW is generated at the input port of electrode, it is propagated through the delay line (sensing area), and after delay of some finite time, it is received by output IDTs and converted into an electrical signal. The IDTs are periodic metallic (e.g., aluminium, Au) electrodes with high electrical conductivity and good mechanical adhesion, deposited on the piezoelectric substrate using a lithographic pattern [127]. The geometry of IDTs such as electrode width, periodicity (d), number of finger pairs (N) and acoustic aperture (W) significantly affect the operating frequency of the sensor. The operational frequency of SAW devices can be set in a wide frequency range (MHz–GHz) [128]. The IDTs operate most efficiently when the SAW wavelength (λ) matches the IDTs periodicity (distance between the two consecutive fingers). The operation frequency (f) is function of wave velocity (v) and periodicity, and it is defined as:

$$f = \frac{v}{d} \quad (2.1)$$

The schematic of SAW delay line is showed in Figure 2.13.

**Figure 2.13:** Schematic illustration of the SAW delay line with input and output IDTs on piezoelectric substrate.

The utilization of wave guiding layer over the piezoelectric substrate with patterned IDTs is needed for the transmission of Love wave (this is not a case for Rayleigh waves). The Love waves are guided close to the sensing surface by confining the wave energy in thin guiding layer. The guiding layer slows the velocity of wave with respect to the piezoelectric substrate and make the surface highly sensitive to small perturbation. Materials such as polymers, silicon dioxide (SiO₂), ZnO have been used as guiding layers. The materials with a low shear velocity and low insertion loss seem to be the most promising as the guiding layers [129].

The SAW gas sensors are coated with sensing layer (molecular recognition layer) which need to have a high sorption capacity to target gases. When gas interacted with the sensitive layer, it causes a change in wave velocity and amplitude which are detected as a shift in resonant frequency of the sensor. The changes in SAW propagation can be caused by three distinct ways of sensing principle [126]:

- *Mass effect* – the change in mass of sensing layer due to the adsorption of gas species on the surface causes the decrease in velocity and resonant frequency of the SAW sensor. The relationship between the frequency shift (Δf) and the mass loading is given by [113]:

$$\Delta f = (k_1 + k_2) f_0^2 h \rho \quad (2.2)$$

where k_1 and k_2 are substrate material constants, f_0 is unperturbed oscillation frequency of the sensor, h and ρ are a thickness and density of the sensing film, respectively.

- *Acoustic-electric effect* – the change of electric properties (conductivity/resistance) of sensitive layer due to the adsorption of gas molecules directly affects the SAW velocity. The decrease in resistance of sensing film results in the decrease of SAW velocity and vice versa. The relationship between the frequency shift and the electric loading is given below [113]:

$$\Delta f = -f_0 \frac{K^2}{2} \Delta \left(\frac{1}{1 + \left(\frac{V_0 C_s}{\sigma_s} \right)^2} \right) \quad (2.3)$$

where K^2 is electromechanical coupling coefficient, V_0 is unperturbed SAW velocity, C_s is capacitance per unit length and σ_s is the sheet conductivity of the sensing film.

- *Visco-elastic effect* – the elasticity of sensitive layer can be influenced by the adsorption of gas molecules causing the tension in the layer. This strain is partly transferred to the substrate and it affects the wave propagation and increases the resonant frequency of sensor. The relationship between the frequency shift and the electric loading is given by [113]:

$$\Delta f = C_e f_0^2 \Delta \left(\frac{4h\mu}{v_0^2} \left(\frac{\lambda + \mu}{\lambda + 2\mu} \right) \right) \quad (2.4)$$

where C_e is the elasticity constant of the substrate material, λ and μ are the shear modulus and Lamb constant of the sensitive layer, respectively.

A wide range of the materials (e.g., MOX, polymers, carbon based materials) have been used for successful gas recognition and detection using SAW system. The properties of each type of sensing materials are already discussed in Section 2.1. The different techniques such as spin coating, spray coating, sputtering, drop casting, electrospraying or Langmuir–Blodgett approach have been used for the deposition of sensitive layer on SAW sensors. In general, except of sensing material nature, a good control of thickness, uniformity, viscosity and adhesion of film to the piezoelectric substrate is required in order to obtain reliable and stable SAW sensor performances [63, 126].

In summary, the important characteristics of SAW gas sensor, such as sensitivity, selectivity, LOD, repeatability, and stability depend critically on the physical and chemical properties of sensing layer, device design, operation frequency and environmental conditions such as temperature and RH. In principle, SAW gas sensors offer ultra-high sensitivity, fast response, suitable size and structure, and ability to work in wireless mode [130, 131]. Therefore, PPy based L-SAW sensors were chosen and investigated as the suitable candidates in this thesis.

2.3 Gaseous analytes

This sub-chapter introduces the origin and classification of specific gases and VOCs with high impact for various applications, including breath analysis, food quality analysis and air quality control. The gaseous analytes classified as ‘gas molecules of high importance’ were used for the validation of PPy based sensors in this thesis.

2.3.1 Gases and VOCs in exhaled breath

A damage of cells in human body which is known as an oxidative stress is caused by the disordered equilibrium between free radicals such as reactive oxygen species (e.g., $O_2\cdot$, $\cdot OH$, $NO\cdot$, H_2O_2 , etc.) and antioxidant defense system [132, 133]. Free radicals are molecules with unpaired electron formed exogenously (mutagens produced by radiation, pollutants or drugs) and endogenously (by-products of normal metabolism, chronic infection by viruses, bacteria, or parasites, etc.) [134]. Toxicity of free radicals contributes to proteins and DNA damage, inflammation, tissue damage or even cell death by oxidation of cellular lipids (lipid peroxidation). These processes are connected with production of chemically diverse group of biomolecules in human body (by-products such as peroxides, alcohols, aldehydes, ketones, etc.) which can trigger the development of many diseases and serve as diagnostic and prognostic biomarkers [44, 135, 136]. Some of those releasing biomarkers are exhaled in the breath

and they are defined as breath biomarkers. Figure 2.14 shows the schematic illustration of processes involved in the formation of breath biomarkers.

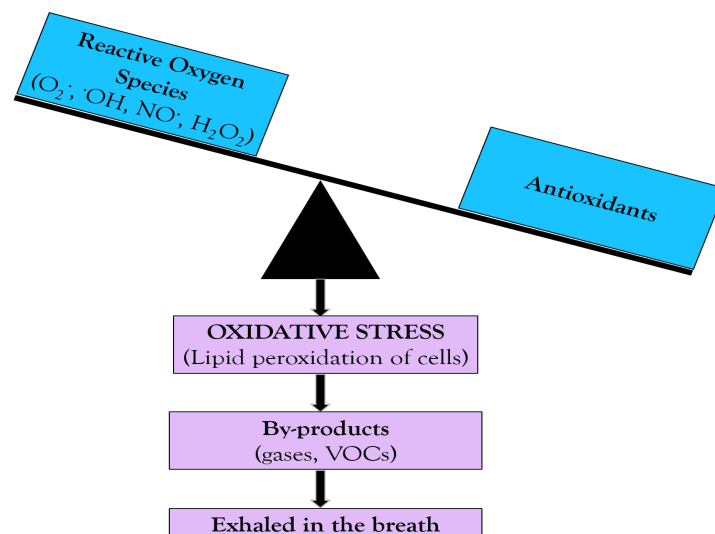


Figure 2.14: The mechanism leading to excretion of biomarkers in the exhaled breath caused by the damage of cells (oxidative stress).

The composition of exhaled breath is complex, it is a mixture of various gases (e.g., nitrogen, oxygen, carbon dioxide, carbon monoxide, water vapour, etc.) and traces of VOCs [137, 138]. The origination of exogenous VOCs in a body is from an external source such as environmental exposure, diet, medication or they can be released by bacteria in the airways. These molecules are expressed in exhaled breath after circulation and/or internal metabolism. The endogenous VOCs in breath arise from the respiratory tracks after passing a blood–air barrier and they are related to any metabolic or pathologic processes in the body [139, 140, 141]. The number of exogenous VOCs in exhaled breath exceeds the amount of endogenous ones (even some of them can be overlapping) [142], and only a small number of endogenous VOCs (specific biomarkers) are of high interest in the medical field. The schematic illustration of VOCs pathways in human body is shown in Figure 2.15.

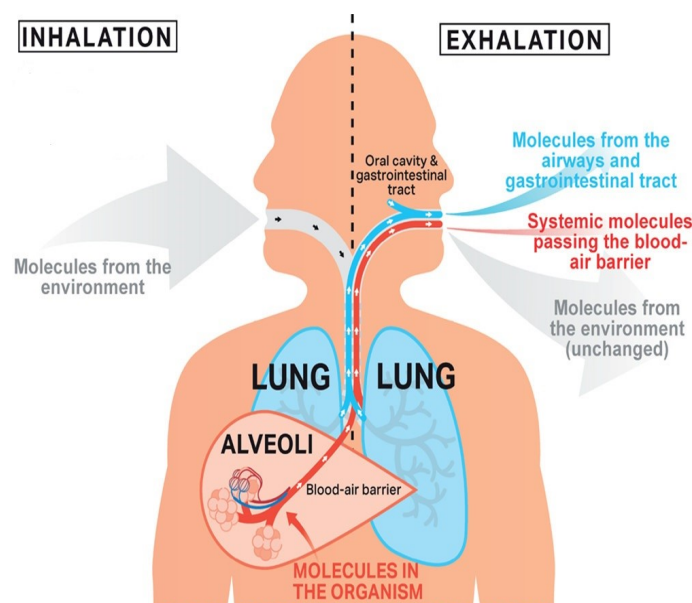


Figure 2.15: A pathway of exhaled molecules in human body. The composition of the exhaled breath includes: the molecules of the environmental origin (major), the molecules of airways and gastrointestinal tract origin (minor) and molecules related to metabolic or pathologic process (molecules which jump over the blood–air barrier, minor). The image is adopted from [139].

The VOCs profile in exhaled breath is also very complex, it includes a different type of molecules with different concentrations range (ppm-ppb), which may vary depending on state of health, life-style, age, gender and smoking habits. The different compound classes including hydrocarbons (alkanes/alkenes/alkynes, benzyl, and phenyl hydrocarbons), oxygen-containing compounds (alcohols, aldehydes, ketones), esters, sulfur-containing compounds and nitrogen containing volatiles have been identified in the exhaled breath [44, 143, 144, 145]. Even though there is a high number of publications related to breath analysis [53, 139, 142, 146], a definite list of VOCs compounds in breath is still not available, which is more probably caused by the large variation of results [144]. However, the analytes such as acetone, ammonia, ethanol, ethylene and toluene are within those which are important in breath analysis, thus, each of them is individually discussed in Section 2.3.4.

2.3.2 Gases and VOCs in air quality monitoring

Specific gases and VOCs are categorized as harmful substances with toxic, carcinogenic, or mutagenic effect which may have a short term and/or long term negative impact on the environment and human health [50]. The tropospheric ozone (as a part of photochemical smog formed by the reaction of sunlight, air containing hydrocarbons and nitrogen oxides) and secondary organic aerosols are primary environmental issues induced by increased concentration of specific gases and VOCs in ambient [55]. These molecules can be emitted either from natural (e.g., emission from vegetation and sea) or anthropogenic (e.g., industrial processing, transportation, biomass burning) sources [147]. In general, chronic health problems caused by exposure to specific gases and VOCs can be classified as either non-carcinogenic or carcinogenic. The main non-carcinogenic chronic effects are irritation, sensory effects, damage to the liver, kidneys and central nervous system, asthma and other respiratory effects, while the main carcinogenic effects include lung, blood (leukaemia and non-Hodgkin lymphoma), liver, kidney and biliary tract cancer [50, 148]. Different world organizations, such as American Conference of Governmental Industrial Hygienists (ACGIH) sets the occupational threshold limit values (TLV) for short and long time weighted averages for various gases and VOCs which have impact on health and environment. The detection of acetone, ammonia, ethanol and toluene is of high importance in this field, and so their TLV values are included in Section 2.3.4.

2.3.3 Gases and VOCs in food quality monitoring

Controlling the food quality is very important as it allows to prevent the microbial spoilage of a product, and hence its waste and economic loss. It also helps to protect customer health, keep its satisfaction with a product and the brand. The complex physical and chemical changes caused by microbial or enzymatic action, lipid oxidation, and other biochemical reactions are involved in a degradation and spoilage processes of food [149, 150]. During the storage of food, the metabolic decomposition of main food ingredients like proteins, fat and carbohydrates occurs usually by enzymes and bacteria, producing an odor composed from different gases and VOCs, which gets more and more intense with the decrease of food freshness. For instance, protein can be decomposed into amines, nitrogen and sulphur based components, etc.; the fat can be decomposed into different low molecular weight compounds such as aldehydes and ketones, etc.; while the carbohydrates can be decomposed into alcohols, ketones, aldehydes, and carboxylic acid gases [51, 151]. The released gases have been considered as quality indicators of different type of food such as meat, fish, fruits, etc., and can be used to determine food freshness and spoilage. The analytes such as ammonia, acetone, ethanol and toluene belong to this group.

2.3.4 Gases and VOCs of high importance

As it is already described in the section above, the profile of gases and VOCs which are classified as markers for different applications (e.g., breath analysis, air or food quality monitoring) is wide and complex. In order to design a sensor for multiple applications, it is necessary that the selected gases and VOCs of interest are overlapping. Thus, some gases and VOCs including acetone, ammonia, ethanol, ethylene and toluene are classified as the target gases in this thesis, as their detection has a great impact in various applications.

2.3.4.1 Acetone

Acetone (C_3H_6O) has a sweetish taste with a characteristic odor of decaying apple and it has been found in different concentration levels in the exhaled breath of almost every person. During the history, acetone

has been known as a breath biomarker for diabetes mellitus, however, only acetone cannot be used to diagnose and monitor diabetes. The increased acetone levels in the range of 0.22 to 9.41 ppm [152] have been found in the breath of diabetic patients [152, 153], but also in the breath of lung cancer patients (112–2654 ppb) in comparison with healthy people (42–753 ppb) [154]. The reported acetone concentrations can vary from disease to disease and from patient to patient and it can be affected by several factors such as age, food consuming (fasting), medicines, addiction behaviour, lifestyle, and/or profession [155]. For instance, overnight fasting and/or a ketogenic diet (low carbohydrate diet) can raise the levels of acetone in the exhaled breath in healthy individuals [156]. Thus, there is a need for additional studies and combination of acetone with other breath biomarkers which may help to indicate glycaemia [152, 155, 156].

The increased concentration of acetone vapours has been also reported in indoor air. It can originate from different solvents such as furniture polish, cleaning products (e.g., bleach, laundry detergent, etc.), nail polish remover, floor glue, and oil paint [157, 158]. Breathing of acetone in moderate to high amounts for a short time can cause an irritation of nose, throat, lungs and eyes. It can also cause headaches, dizziness, confusion, a faster pulse, nausea, vomiting, effects on the blood, passing out and possible coma, and a shorter menstrual cycle [159]. ACGIH sets the occupational TLV for acetone to 250 ppm, considering 8-h time-weighted averages.

Also, acetone is one of ketone that is present as an aroma compound in many foods and used as the quality marker. For instance, it was identified as a good marker to characterize the freshness of various type of fish (e.g., tuna, salmon, cod) due to its accumulation during fish spoilage [51]. Moreover, acetone was identified in contaminated apples and used as marker of high bacterial content [160].

2.3.4.2 Ammonia

Ammonia (NH_3) is classified as a toxic air pollutant with an unpleasant odour that can harm the human body, namely causing the damage to the respiratory tract, eyes, and skin, inflammation or inhibition of the cell growth [161]. The presence of ammonia in atmosphere originates from different sources like chemical or automotive industry, agricultural sector, farming, etc. [162]. The concentration of this gas in natural atmosphere is very low (sub-ppb levels), while for instance its concentration can reach more than 10 ppm near intensive farming areas. The concentration of 50 ppm is tabulated as lower limit of human ammonia perception by smell, nevertheless, ammonia may cause irritation to respiratory system, skin and eyes even at lower concentration [163]. TLV value for ammonia is set to be 25 ppm (based on 8-hour time weighted average) by ACGIH.

In human body, ammonia is processed in the liver, kidneys and skeletal muscles. The ammonia path through a body of healthy individuals is followed by its conversion into urea in the liver and urea is then transported through the bloodstream and excreted into urine by the kidneys. The excessive level of ammonia in blood is noted in the patient with kidney dysfunction due to an impaired removal of waste products (e.g., urea) from the blood. The surplus ammonia molecules as well as other nitrogen-containing volatile compounds can diffuse into the lungs and be found in higher concentrations (92–4240 ppb) in the breath of patients with chronic kidney disease in comparison to healthy controls (43.2–830 ppb), and serve as the relevant biomarker of renal disease [164, 165].

Total volatile basic nitrogen (TVB-N) content is an important indicator for evaluation of meat freshness. Ammonia is one of the main component of TVB-N, its levels increase with a spoilage by either bacterial or enzymatic degradation and it can be used as a marker of meat freshness [166, 167].

2.3.4.3 Ethanol

Ethanol ($\text{C}_2\text{H}_6\text{O}$) is a volatile alcohol which is extensively used in a broad range of industries such as biomedical, chemical, food, pharmaceutical, etc. The accurate detection of ethanol is very important and necessary in various applications, including the quality of alcoholic beverages (e.g. wine, beer) [168], quality control of food [169], indoor air quality [158], breath analysis (e.g. breath alcohol test of drivers, clinical diagnosis) [154, 170].

Ethanol is an important marker used for monitoring of fermentation processes during the alcoholic beverages production and determination of characteristics of final products (e.g., aroma, flavour, quality, etc.) [168, 171]. Additionally, ethanol is also used for the estimation of food spoilage, namely, it was used as effective index for freshness characterization of peach [172]; the increased concentration of ethanol was found in the various types of fish (e.g., whiting, mackerel, cod) after storage for 10 days and used to determine the spoilage stages of fish [150].

Ethanol is presented in a relatively low concentration around 200 ppb in human breath of healthy individuals. Its level in the breath is significantly increased after alcohol consumption, thus, ethanol is used as the marker of drunkenness level of drivers [173]. Also, the increased concentration of ethanol has been found in the breath of lung cancer patients (13–1520 ppb) in comparison with healthy subjects (4–480 ppb) [154]. Before the ethanol values in exhaled breath are linked to specific pathological processes and this volatile is used as a biomarker, it is necessary to take into account other sources of ethanol in breath. Hence, the increased ethanol concentration may be affected by its production by mouth flora or gut microflora after consumption of sugars [173], and/or by its contribution in the inhaled ambient air [174].

Considering effect of the inhaled vapours of ethanol on human health, the concentration of ethanol (observed in industrial fields with fermentation and distillation) can cause irritation of the skin, inflammation of the nasal mucous membrane and conjunctiva, while at high levels, it can cause even alcohol poisoning [170]. 1000 ppm is the maximum permitted concentration of ethanol vapour in the work place (defined by ACGIH).

2.3.4.4 Ethylene

Ethylene (C_2H_4) is a gaseous plant hormone which plays a crucial role in many phases of plant biology, such as growth, development, pathogen infection, fruit ripening, storage of fruit [175, 176]. It is generated in the plants during their maturity. In the agricultural and food industry, ethylene concentration in range of ppb-ppm levels has been used as a maturity index to determine the time of harvest. During post-harvest in storage room and transportation chains, the control of ethylene concentration is necessary, as the specific concentration of this gas can be either beneficial or deleterious for different types of fruits. For instance, climacteric fruits (e.g., banana, kiwi, avocado) are usually artificially ripened by ethylene in order to extend their shelf-life and ensure shelf-maturity; however, the excess concentration of ethylene can increase its auto-catalytic production in the fruit and cause accelerated maturation, senescence and even spoilage [177]. The sensitivity between ethylene concentration and fruit ripening varies in the storage conditions, namely, 10 ppm of ethylene is used to induce ripening of bananas [178], while continues exposure to 10 ppb of ethylene can affect mandarin quality [179].

Ethylene contained in the human breath is considered as a biomarker of oxidative stress. The production of ethylene in the body is connected with the oxidative degradation (lipid peroxidation) of polyunsaturated fatty acids caused by reactive oxygen species. Ethylene is highly volatile gas which is not significantly metabolized by the body and not soluble in body fat, thus its diffusion into bloodstream after generation is rapid. After its transportation to the lungs, it is excreted in the expired breath. Thus, ethylene in the exhaled breath can be considered as a novel biomarker of the infection and oxidative stress with potentially important clinical implications [180, 181, 182]. The low concentration of ethylene is found in the breath of healthy humans (around 6.3 ppb), while its concentration is increased in the breath of patient with renal failure (around 150 ppb) [164, 183].

From an environmental point of view, ethylene is considered a precursor pollutant being involved in the creation of ozone at ground level, which is seriously harmful for human health [184]. Ethylene in the atmosphere originates mostly from natural sources (emissions from vegetation) and anthropogenic sources (emission from incomplete engine combustion, industry, cigarette smoke, natural gas leaks) [185]. The ACGIH lists ethylene as a simple asphyxiate gas.

2.3.4.5 Toluene

Toluene (C_7H_8) is an aromatic hydrocarbon, classified as a chronic toxicant which causes eye, nose, and throat irritation, drowsiness and dizziness in low concentrations (below 100 ppm), while a neurological damage and dysfunction of the central nervous system (e.g. moderate performances of short-term memory, attention and concentration, visual scanning, perceptual motor speeds, colour vision and auditory capacity) is a principal health outcome of exposure to high concentration of toluene [186, 187, 188]. For instance, the concentration of toluene exceeding 200 ppm can cause a fatigue, headache, paresthesias, and slowed reflexes, while confusion develops at levels of 600 ppm or above, and euphoria appears as levels near 800 ppm [188]. The principal sources of toluene in the environment originate from evaporation and combustion of various industrial products (e.g., petrol, paint, adhesives, coating, tobacco smoke, etc.). ACGIH limits the TLV of toluene to 20 ppm. In the human breath, toluene is considered among the VOCs with exogenous origin and it has been reported very often as a marker of smoking habits. The average concentration in the breath of smokers (9–153 ppb) is significantly higher compared to non-smoker breath [173, 189, 190].

Chapter 3

Methods

3.1 Synthesis

The thesis objective related to the synthesis of sensing materials consists of the growth of different PPy nanostructures and their doping and/or surface functionalization. In order to achieve this goal, PPy was synthesized in the form of NRs and NPs. PPy NPs were modified with the colloids of Au and Ag, and CdTe QDs. This sub-chapter includes the general description of synthesis principles used for the creation of those materials, while the specific synthesis conditions are included in the corresponding articles in Chapter 4, Chapter 5 and Chapter 6.

Generally, the used synthesis approaches are based on a wet chemical synthesis and/or electrochemical synthesis. Wet chemical synthesis routes deal with chemical reactions in the solution phase using precursors at proper experimental conditions. Electrochemical synthesis is based on using an appropriate electrolyte solution (monomer and an oxidizing agent) under constant applied voltage or current in an electrochemical cell. The schematic illustration of these synthesis process is shown in Figure 3.1.

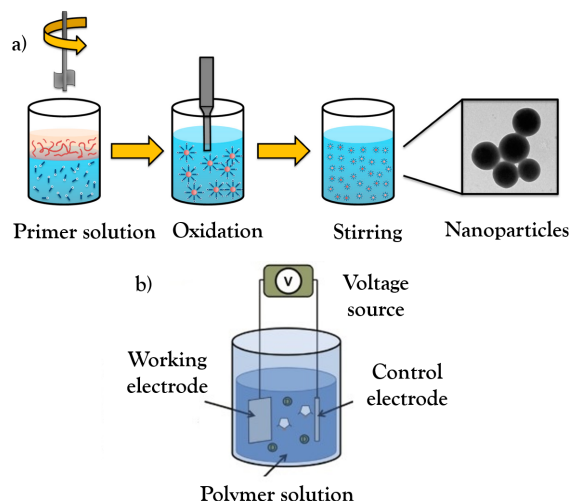


Figure 3.1: Schematic illustration of (a) wet chemical synthesis and (b) electrochemical synthesis process. The images are adopted from [191, 192].

PPy NPs were prepared via a wet chemical synthesis and without utilization of template. The synthesis method is based on an oxidative polymerization of pyrrole monomer which imply the use of an oxidizing agent (e.g., FeCl_3) and stabilizer (e.g., polyvinyl alcohol (PVA)). The oxidizing agent acts as the initiator of PPy polymerization. The concentration of reactants (pyrrole, oxidizing agent and stabilizer) has a critical effect on the final structural and morphological properties of PPy NPs.

PPy NRs were synthesized using electrochemical polymerization approach and structures were grown on the top of Au NRs in the AAO template. The polymerization of PPy is based on oxidation of pyrrole via an oxidizing agent (e.g. tetraethylammonium tetrafluoroborate) and reaction is carried out in

an electrochemical cell under a potentiostatic (constant potential) mode. The synthesis factors such as type and concentration of reactants, applied voltage and temperature play the key role in the definition of final PPy properties.

Au NPs, **Ag NPs** and **CdTe QDs** were synthesized by wet chemical synthesis. The modified PPy NPs were prepared by mixing of PPy NPs solution with the corresponding aqueous solutions of Au NPs, Ag NPs or CdTe QDs.

3.2 Material characterization

The functional properties of material (e.g., physical, chemical, mechanical, electrical, thermal, magnetic and optical) are determined by its composition (type of structural elements) and structure (arrangement of electrons, atoms and molecules within component). The properties of materials are strongly depended on the synthesis and processing conditions and some of them can be changed by the tailoring of materials to nanoscale dimensions. Thus, the investigation of composition, structure and dimensions of materials is essential for the understanding of their feature which are the key function for the performances and final application of the materials [193].

In the following sub-chapters, the principles and utilization of *Microscopy Techniques*, *Spectroscopy Techniques* and *Mass Spectrometry* are described. These methods were used to investigate the structural and morphological characteristics of PPy based gas sensing materials described in Section 3.1. The specific experiment conditions for each used method are included in the corresponding articles in Chapter 4, Chapter 5 and Chapter 6.

3.2.1 Microscopy Techniques

Microscopic techniques such as **optical**, **electron microscopy** (e.g., Scanning Electron Microscopy (SEM), Transmission Electron Microscopy (TEM)) and **scanning probe microscopy** (e.g., Atomic Force Microscopy (AFM)) are commonly used for the morphological (shape and size), topography (texture, smoothness or roughness) and structural characterization of materials.

SEM is an important imaging technique used for the examinations of surface features of the specimen. The surface of specimen is bombarded with a focused primary electron beam and the various reflected signals which originate from different volumes of interaction (see Figure 3.2) are collected and then displayed into SEM image. **Secondary electrons (SE)** have a very low energy and they originate very close to a sample surface, thus the strong topographic contrast images (with high resolution geometry of an object or a surface) are obtained by SE detection. **Backscattered electrons (BSE)** are also used to provide the topographic images with the stronger contrast due to chemical composition (demonstration of multiphase composition in the samples). However, BSE images cannot provide the identification of different elements in the sample. The distribution of chemical elements in sample is reachable by collecting of emitted **Auger electrons** and **X-rays photons** from specimen which can be detected by using an electron analyzer detector and energy dispersive X-ray (EDX) spectrometer, respectively [194, 195].

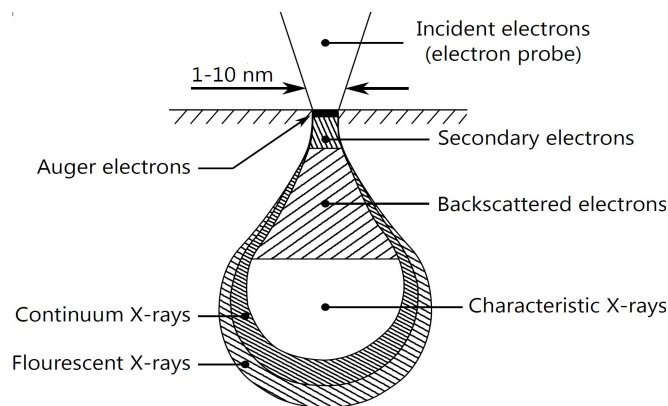


Figure 3.2: Schematic overview of the pear-shaped volume with the different reflected signals when a primary electron beam is incident on a solid surface. The signals originate from: secondary electrons, backscattered electrons, Auger electrons and X-Ray photons; Auger electrons originate from a depth of 5–20 Å, whereas the X-ray information depth is 0.1–10 μm. The image is adopted from [196].

TEM is a powerful tool used to examine the details about inner features of the materials (e.g. crystallization). In comparison with SEM which detects the scattered electrons emitted from the surface of the sample, TEM detects the transmitted electrons from the sample, it operates at a higher voltage range and ensures much higher resolution images. The imaging principle of TEM can be described as follows: the focused electron beam is used to hit the specimen; the electrons which pass through the specimen are collected and used to obtain the real image of the specimen [197].

The examples of the typical SEM and TEM images are shown in Figure 3.3.

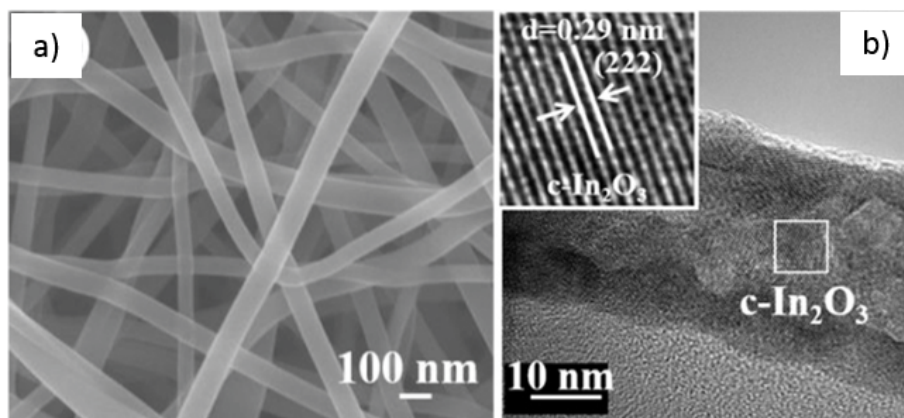


Figure 3.3: The images of In_2O_3 nanowires: (a) SEM image reveals information on the morphology of the surface while (b) TEM image offers the information about the inner structure of the sample with an atomic resolution. The images are adopted from [198].

AFM is a sophisticated non-destructive analytical technique used for high resolution topographic images of a surface. It can be used to provide 3D information of the probed surface from submicron to nanometer length scale. Apart from the topographic information (e.g., surface roughness), AFM images can also include the information about mapping of mechanical (stiffness, adhesion, elasticity, friction), chemical and electrical properties of the sample. The working principle of AFM is based on the sensing of force (van der Waals) between an oscillating cantilever (a sharp tip) and the surface of the sample. The developed force deflects the cantilever toward or away from the sample surface and this displacement is measured by a photo-detector. The measured signal gives a map of the surface topography [199]. The schematic illustration of the AFM working principle is shown in Figure 3.4.

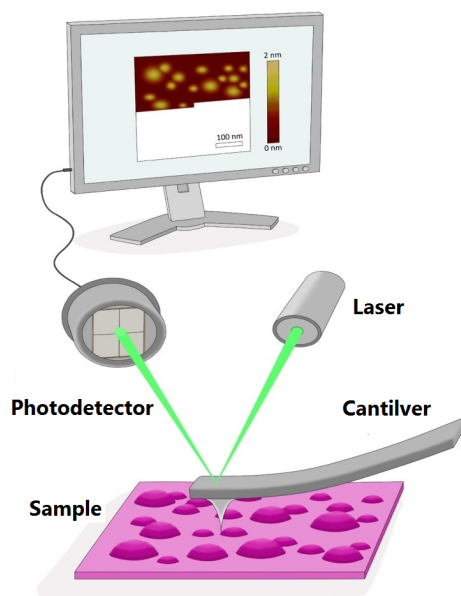


Figure 3.4: Schematic illustration of the AFM setup. The image is adopted from [200].

3.2.2 Spectroscopy Techniques

The spectroscopy is an instrumentally assisted study which analyzes the interaction between a matter and an electromagnetic radiation. Typically, a spectroscopy instrument consists of three parts: a radiation source (electromagnetic spectrum is shown in Figure 3.5), material under study (sample) and a detection system which measures the outcome of interaction between the radiation and the matter. The outcome signals of various spectroscopy techniques have been intensively used to provide the information about atomic and molecular structures of materials.

Spectroscopy techniques (e.g., XPS, Raman, Fourier transform infrared spectrometry (FTIR), Ultraviolet–visible (UV-Vis)) were used for the investigation of chemical composition and structural identification of bare and modified PPy sensing materials which were studied in this thesis. Additionally, the changes in PPy structural properties upon exposure to different environmental conditions (e.g., specific gas analyte) were also monitored with the spectroscopy techniques (XPS, Raman, FTIR). The working principles of those techniques are described below.

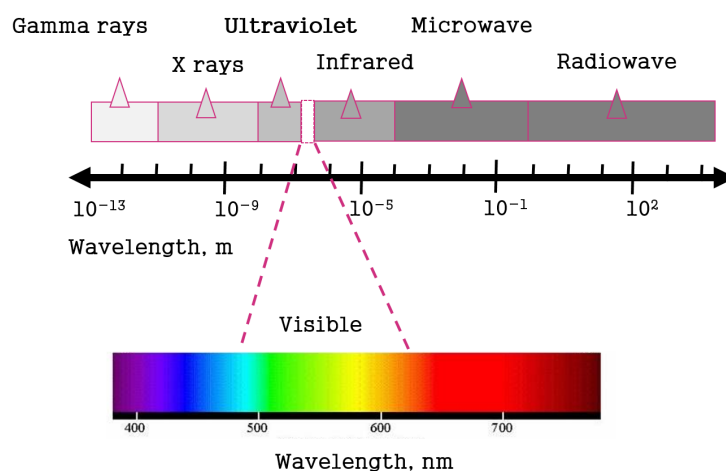


Figure 3.5: Electromagnetic spectrum; X-rays and infrared light are used as the exciting source for XPS and FTIR spectroscopy, respectively; visible light is used for Raman and UV-vis spectroscopy.

XPS is a surface semi-quantitative analytical technique used to obtain the information about the elemental composition (which atoms are presented) and speciation (how the atoms are bound) of the outer 10 nm or less of any solid surface with the detectable range above 0.05 atomic % [201, 202]. X-rays are used as the exciting source of photons which transfer the energy to electron. If this transfer energy is sufficient, the emission of the electron from the atom core level occurs by a photoelectric effect. The kinetic energy that remains on the emitted electron is quantitatively measured and it forms XPS spectrum. The binding energy of an emitted electron from particular core level (1s, 2s, 2p, 3s, 3p, etc.) is unique for each element presented in the material surface and it can be calculated as the difference between X-ray photon energy and measured kinetic energy. The binding energy gives the information about electronic structure and spatial distribution of all bonded electrons within a respective atom, ion or molecule. The schematic illustration of photo-electron emission is presented in Figure 3.6.

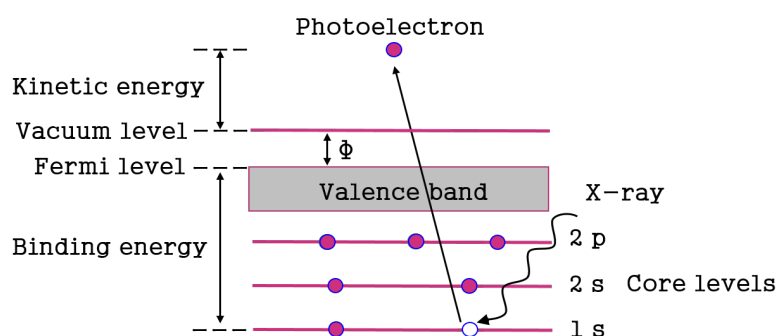


Figure 3.6: The illustration of photo-electron emission.

Raman Spectroscopy is a non-destructive technique used to measure the vibrational modes of a molecule and in such way to determine and identify the molecular structure of the sample. Briefly, the principle of method is based on the radiation of sample with a monochromatic source of light (visible) which causes the molecular vibrations in sample and an inelastic scattering of light [203, 204]. The shift in frequency of the scattered radiation with respect to that of the incident light represents the Raman shift which is measured in the Raman spectrum. Raman scattering occurs only when the molecular motion causes a change in the polarizability of the molecule. There are two type of Raman scattering: Stokes and anti-Stokes. For Stokes Raman bands is characteristic that a final vibrational state of the molecule has a higher energy compared to the original and that the scattered photon has a lower frequency than the incident radiation (energy lost due to the molecular vibration). The opposite effect is typical for anti-Stokes Raman bands, see Figure 3.7. Stokes lines has the higher intensity in Raman spectra and there are most commonly used for characterization.

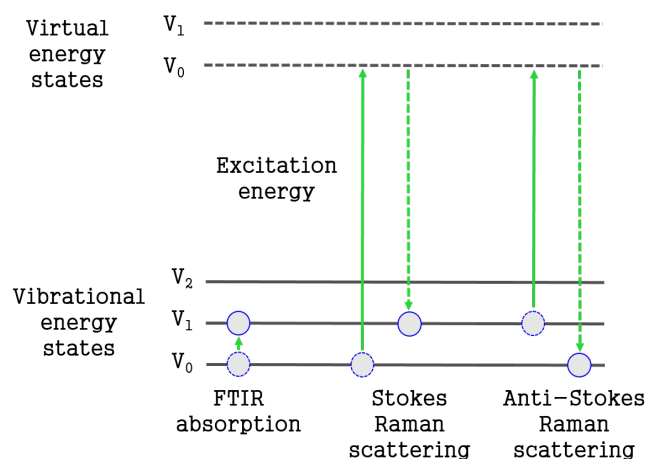


Figure 3.7: The energy states involved in FTIR absorption, Stokes and anti-Stokes Raman scattering.

FTIR is another powerful method which provides the information about chemical composition of materials based on the measured molecular vibrations. FTIR is complementary technique with Raman spectroscopy, but in contrast to Raman, an infrared light is used for the excitation of the molecules and the vibration of molecule to higher energetic states is due to the effect of the absorbed light by molecule (see Figure 3.7). The molecular dipole moment is changed during the vibrations of molecules which are IR active and the energy of absorbed radiation is measured in FTIR spectrum [203, 204].

FTIR and Raman spectra provide a “fingerprint” of the particular molecules as each chemical bond presented in the molecules has a specific vibrational energy. There are several types of bond vibrations which can be recorded in Raman and FTIR spectrum: stretching vibrations (symmetrical and asymmetrical), in plain bending vibrations (scissoring and rocking) and out-of-plane bending vibrations (twisting and wagging). The illustration of those bond vibrations is shown in Figure 3.8.

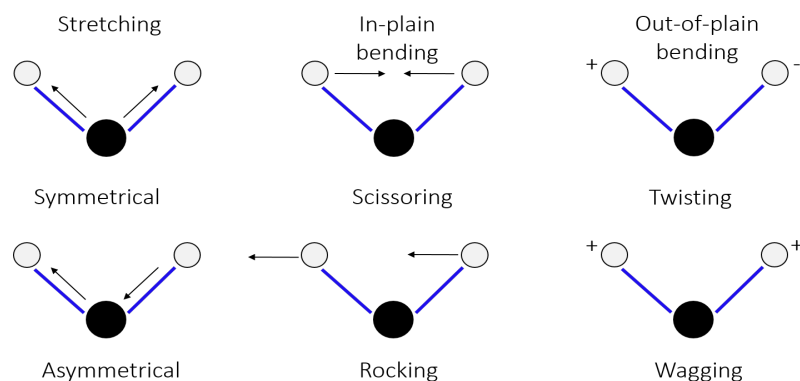


Figure 3.8: Illustration of fundamental bond vibrations; + and - denote movement above and behind the plane of the paper.

UV–Vis spectroscopy is one of the important characterization techniques used to study the optical properties of materials. It can be used for identification of the molecules by defining of their band gap. The sample is excited with near-ultraviolet (180–390 nm) or visible (390–780 nm) radiation and the quantity of absorbed light by sample is measured. When a photon hits a molecule and is absorbed, the molecule is promoted into a more excited energetic state. UV-visible light has enough energy to promote electrons to a higher electronic state, from the HOMO to the LUMO. The energy difference between the HOMO and the LUMO is called the band gap. Typically, these orbitals are called bonding and anti-bonding. The energy of the photon must exactly match the band gap for the photon to be absorbed. Thus, molecules with different chemical structures have different energy band gaps and different absorption spectra.

3.2.3 Mass Spectrometry

Mass spectrometry is an analytical technique that uses a mass spectrometer to separate ions by their mass to charge ratio. It has the ability to identify unknown compounds in the specimen of interest by determination of its chemical composition (isotopic, elemental, and/or molecular).

Time-of-Flight Secondary Ion Mass Spectrometry (ToF-SIMS) is a semi-quantitative destructive analytical technique with a very high sensitivity (ppm to ppb) compared to some other elemental analysis techniques (e.g. LOD of XPS and SEM/EDX is 0.1–1 and 1 %, respectively) [205]. Thus, ToF-SIMS can be used for the identification of traces amount of elements (all elements in the periodic table) and chemical species from less than one monolayer at the surface and/or from the depth of 2–30 nm of a sample by using the depth profiling applications (sputtering with ion beam). The principle of this technique is based on the analysis of detected secondary ions resulting from bombardment of a surface by primary ions (e.g., Ar^+ , O_2^+ , Cs^+ , Bi^+). The positive and negative secondary ions (fraction of sputtered atoms and/or molecules that are ionized from the surface of interest) are accelerated into a flight path on their way towards a detector. The mass of secondary ions is determined by measuring the exact time at which they reach the detector (time-of-flight). The schematic illustration of ToF-SIMS method is shown in Figure 3.9.

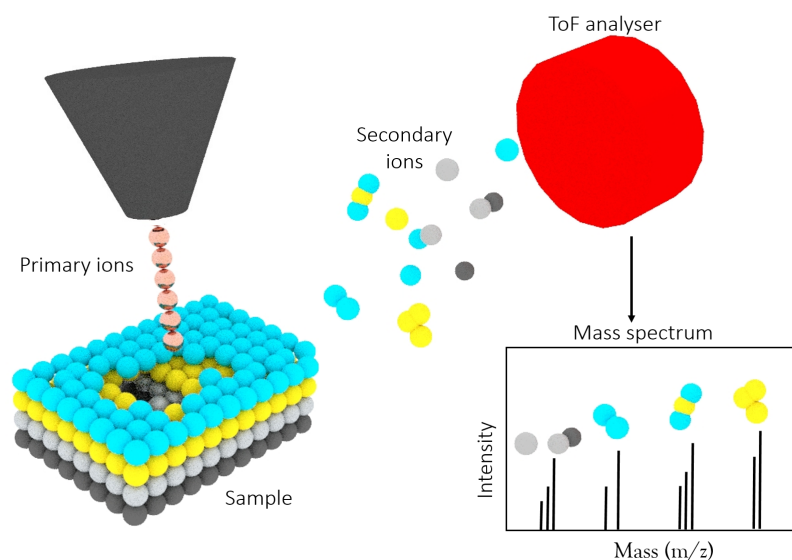


Figure 3.9: Schematic illustration of ToF-SIMS analysis principle; the high-energy primary ions from pulsed ion beam are used to bombard the sample surface; the emitted secondary ions are detected by ToF analyser and shown in a mass spectrum.

3.3 Gas sensors fabrication and characterization

This sub-chapter includes the descriptions of methods used for the fabrication, electrical and gas characterization of PPy based L-SAW sensors.

3.3.1 L-SAW sensors fabrication

L-SAW sensors consist of a piezoelectric substrate with integrated IDTs, first guiding layer and second guiding/sensitive layer. The L-SAW platforms (see Figure 3.10) made of the piezoelectric substrate and first guiding layer are fabricated using various microfabrication processes such as metallization, lithography and plasma enhanced chemical vapor deposition. The L-SAW platforms were fabricated at IMB-CNM, CSIC, Barcelona, Spain. Thus, the design and development of L-SAW platforms will not be discussed here, the detail description can be found elsewhere [206], and the specific geometrical features (width, periodicity, number of finger pairs, acoustic aperture of IDTs) are reported in the journal papers published during the thesis (see Section 5.4.1).

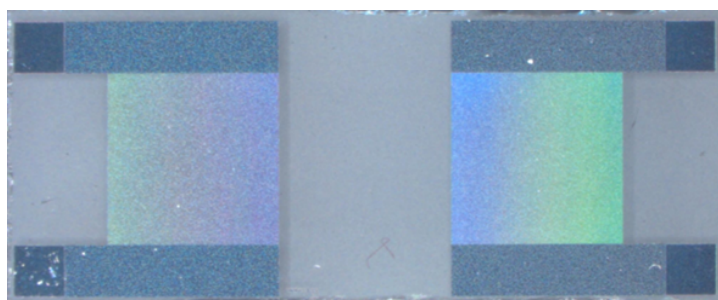


Figure 3.10: The photograph of L-SAW platform.

The second guiding/sensitive layer formed of bare PPy NPs and/or PPy NPs modified with Au NPs, Ag NPs and/or CdTe QDs was deposited on the L-SAW platforms using spin coating technique.

Spin coating is a method used for the fabrication of thin, uniform films on a flat substrate by using centrifugal force. The solution of desired material is dropped on the surface of substrate which is then spun off at the high velocity. The properties of deposited film (e.g., thickness) depend on the applied velocity and acceleration of spinner, deposition time, viscosity of material, surface tension of substrate, and etc. The image of the spin coater (Laurell WS-650-23 B) used for deposition of PPy based layers is shown in Figure 3.11.



Figure 3.11: Image of the spin coater (Laurell WS-650-23 B). The image is adopted from [207].

3.3.2 Electrical characterization of L-SAW sensors

The L-SAW sensors were characterized electrically by measuring of the transmission scattering parameter (S_{21}). The transmission coefficient S_{21} refers to how much power of the incident SAW is transmitted from input to output IDTs at the given frequency. S_{21} parameter of the L-SAW devices was measured by using of a network analyser (Agilent 4395A) which works in the frequency range of 10 Hz–500 MHz. The measured data is displayed as the magnitude of S_{21} (insertion loss) versus resonant frequency of SAW sensor. The network analyser used for the characterization of PPy based L-SAW sensors is shown in Figure 3.12.



Figure 3.12: The photograph of network analyser (Agilent 4395A).

3.3.3 Gas characterization of L-SAW sensors

Gas sensing tests of the PPy based L-SAW sensors were carried out simultaneously in a continuous flow system equipped with mass flow controllers and calibrated cylinders of gases (acetone (Praxair, 100 ppm), ammonia (Praxair, 100 ppm), ethanol (Praxair, 100 ppm), ethylene (Praxair, 100 ppm) and toluene (Praxair, 200 ppm)). The sensor response was measured using an electronic measurement system equipped with an amplifier, directional coupler and frequency counter. First generation of the developed L-SAW sensors (PPy and Au/PPy) in this work were measured using this system. However, later this system (based on the same components) was modified into a portable electronic nose system. The electronic nose system is composed from sensor array, signal conditioning, data acquisition and transmission, and application software. The sensor array is designed to measure four different L-SAW sensors in the same time. It also includes the place for a reference sensor which is used for the mixing of signals. The signal conditioning module introduces each sensor device of the array into a feedback loop composed of two amplification states and a directional coupler. The output signals (mixed signals from L-SAW and reference devices) are amplified, filtered, and finally acquired by a frequency counter in the acquisition and transmission module. This data is transmitted to a PC by wireless communication. The photograph of the portable electronic nose system used for gas characterization of L-SAW sensors is shown in Figure 3.13, while the schematic illustration of the experiment set up is presented in Figure 3.14.

The non-portable and portable systems used for the gas characterization of PPy based L-SAW sensors was designed and fabricated at Instituto de Ciencias Aplicadas y Tecnología (ICAT), UNAM, Mexico City, Mexico. The detail description of the system can be found elsewhere [208, 209].

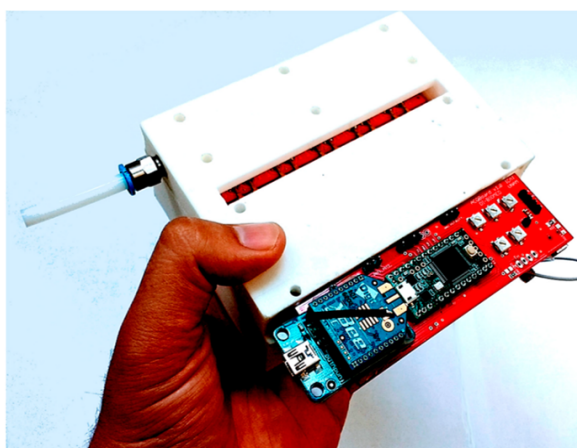


Figure 3.13: Photograph of the electronic nose system. Photograph is adopted from [208].

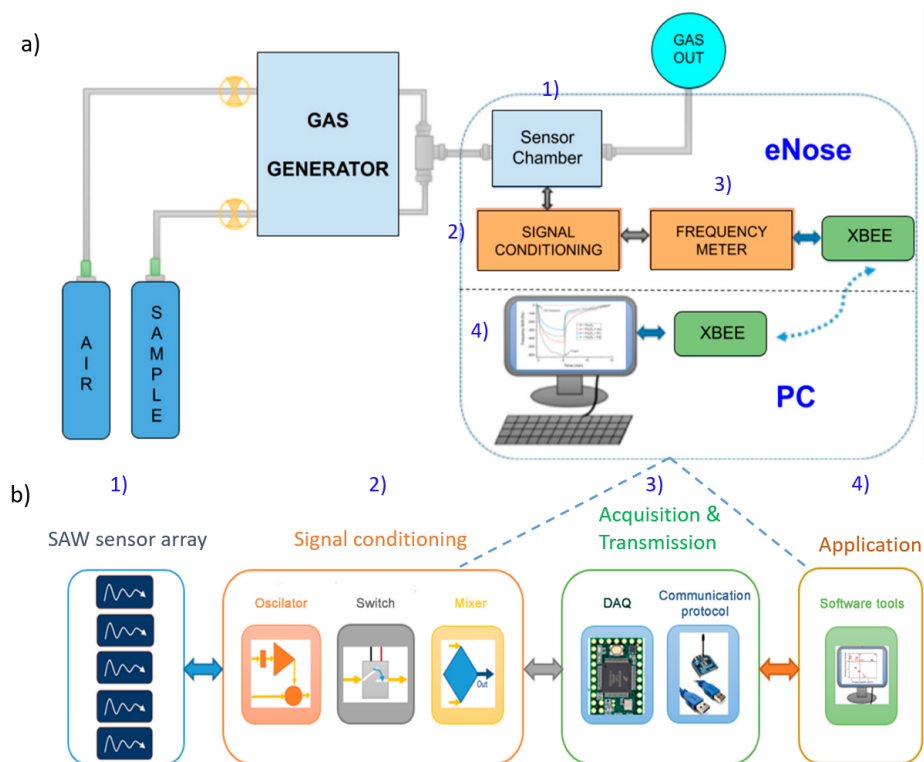


Figure 3.14: Schematic illustration of: experimental setup for the gas characterization of L-SAW sensors (a); electronic nose system composite of L-SAW sensor array, signal conditioning, acquisition and transmission and application software (b). Image is adopted from [208].

Chapter 4

Polypyrrole in gas sensing

4.1 Motivation

PPy nanostructures have been very often used as the gas sensitive layer and implemented in sensors with various types of transducing principles. Different synthesis approaches are used for the development of the PPy active layers, where their final morphology and physico-chemical parameters strongly depend on the applied synthesis conditions. The understanding of correlation between the physico-chemical properties of the layer (e.g., morphology), and its gas sensing capability is essential for fabrication of the gas sensor with sufficient performances. Thus, in this chapter, the synthesis and sensing activity of various PPy nanostructures were over viewed. PPy NRs and PPy NPs were developed by electrochemical and wet chemical methods, their properties including morphology and chemical composition were investigated, and their gas sensing potential was verified using spectroscopy techniques such as Raman and XPS. The implementation of PPy NRs into chemo-resistive sensors was also studied.

4.2 Outputs

The first scientific contribution includes a review on *Nanostructured polypyrrole-based ammonia and volatile organic compound sensors* [210] (Section 4.4.1). This work describes the synthesis of PPy based materials used for fabrication of ammonia and VOCs sensors in detail and compared their sensing effectivity with other CPs, as well as with other well-known gas sensing materials such as MOX. According to this literature survey, nanoscaled PPy with different shapes such as NRs, nanowires, nanotubes, etc., was developed using both, electrochemical and chemical synthesis approaches. PPy sensing layer with different morphological and structural properties responded to tested gases. Generally, the PPy structures with smaller size provided higher sensitivity due to their higher active surface area. The literature review showed that PPy gas sensors working on a chemo-resistive transducing principle have received much more attention among the scientists than the other once (e.g., optical, SAW). The most frequently these sensors were tested for the detection of ammonia and some VOCs (e.g. alcohols-ethanol, methanol). Overall, the sensing performances have been dependent on the morphology of sensitive layer, and additionally, they have been improved by functionalization of the host material (PPy) with various nanosized materials (e.g., noble metals, MOXs, etc.).

The second scientific contribution includes the study of PPy by Raman and XPS during gas sorption. These results are presented in a journal article, *Raman and XPS studies of ammonia sensitive polypyrrole nanorods and nanoparticles* [211] (Section 4.4.2), in which PPy structures in the form of NRs and NPs were investigated. PPy NRs (diameters of 50 nm and lengths of 300 nm) and PPy NPs (diameters between 30 and 50 nm) were prepared in this thesis using an electrochemical and chemical approaches, and characterized by determination of their morphology, chemical composition and sensing capability to ammonia. Raman and XPS analysis confirmed the existence of PPy in the form of neutral PPy species as the major component, and minor presence of charge carrier species (polarons and bipolarons) in both PPy samples. Planar conformation of PPy NPs and planar with a degree of non-planar configuration in PPy NRs were observed. The potential of both samples for ammonia sensing was proven by the shifts of PPy bands in Raman and XPS spectra after ammonia exposure. The tested samples showed different sensing mechanisms between PPy and ammonia, namely, NRs involve proton and electron transfer mechanisms, as opposed to the NPs, which show a mechanism dominated by

electron transfer. The results indicate that the selected synthesis approach and conditions contributed to different morphology, surface area and orientation of PPy structures in those samples, which further led to different detection mechanisms between PPy NRs and PPy NPs with ammonia.

The third scientific contribution summarizes the development of PPy NRs based chemo-resistive sensors, and the results are presented in a conference article, *Gold/polypyrrole nanorods for gas sensing application* [212] (Section 4.4.3). The gas sensing test of chemo-resistive sensors based on PPy NRs grown over Au NRs ('sandwich structure') was carried out towards different concentrations (25, 50 and 100 ppm) of nitrogen dioxide and ammonia at RT. The results showed the negligible response of those sensors to both gases. The negligible responses obtained to ammonia are inconsistent with the literature and previous Raman and XPS observations. This may be caused by the architecture of the chemo-resistive gas sensor with the bottom and top electrodes along the 'sandwich structure', which impede the diffusion of the target gases and the acquisition of the electrical signal.

4.3 Conclusions

In summary, literature reports based on various PPy nanostructures (mostly implemented into chemo-resistive sensors) demonstrated the capability of those materials for sensing of gases (e.g., ammonia), where sensing performances are strongly affected by morphology, size and physical/chemical properties of material as well as by whole design of sensing device. *In-situ* gas sensing test performed using Raman and XPS analysis suggested the potential of electrochemically synthesised PPy NRs and chemically synthesised PPy NPs to sense ammonia. Different sensing properties of those materials, for instance, the reaction mechanism between ammonia and PPy NRs (electron and proton transfer) and/or PPy NPs (electron transfer) appear to be connected to the particular morphological and chemical composition of each film. Electrochemically developed PPy NRs showed inadequacies for their application in gas sensor devices based on chemo-resistive transducing mode due to a complicated architecture caused by synthesis and post-synthesis integration processes, which results in negligible responses of sensor. Therefore, the obtained results moved the direction of this research to the use of PPy NPs as the sensing layer in the L-SAW gas sensors.

4.4 Articles

4.4.1 Journal Article 1

Šetka, M., Drbohlavová, J., Hubálek, J., *Nanostructured polypyrrole-based ammonia and volatile organic compound sensors*, *Sensors*, 17, 2017, doi: 10.3390/s17030562.

4.4.2 Journal Article 2

Šetka M., Calavia, R., Vojtkvka, L., Llobet, E., Drbohlavova, J., Vallejos, S., *Raman and XPS studies of ammonia sensitive polypyrrole nanorods and nanoparticles*, *Scientific Reports*, 9, 2019, doi: 10.1038/s41598-019-44900-1.

4.4.3 Conference article 1

Šetka, M., Drbohlavová, J., Vallejos, S., Márik, M., Llobet, E., Hubálek, J., *Gold/polypyrrole nanorods for gas sensing application*, *Proceedings of SPIE (Smart Sensors, Actuators, and MEMS VIII)*, 2017, doi: 10.1117/12.2265565.

Review

Nanostructured Polypyrrole-Based Ammonia and Volatile Organic Compound Sensors

Milena Šetka ¹, Jana Drbohlavová ^{1,2,*} and Jaromír Hubálek ^{1,2}

¹ Central European Institute of Technology, Brno University of Technology, Purkyňova 123, 612 00 Brno, Czech Republic; milena.setka@ceitec.vutbr.cz (M.Š.); hubalek@feec.vutbr.cz (J.H.)

² Faculty of Electrical Engineering and Communication, Brno University of Technology, Technická 10, 616 00 Brno, Czech Republic

* Correspondence: drbohla@feec.vutbr.cz; Tel.: +420-541-146-196

Academic Editors: Eduard Llobet and Stella Vallejos

Received: 31 December 2016; Accepted: 6 March 2017; Published: 10 March 2017

Abstract: The aim of this review is to summarize the recent progress in the fabrication of efficient nanostructured polymer-based sensors with special focus on polypyrrole. The correlation between physico-chemical parameters, mainly morphology of various polypyrrole nanostructures, and their sensitivity towards selected gas and volatile organic compounds (VOC) is provided. The different approaches of polypyrrole modification with other functional materials are also discussed. With respect to possible sensors application in medicine, namely in the diagnosis of diseases via the detection of volatile biomarkers from human breath, the sensor interaction with humidity is described as well. The major attention is paid to analytes such as ammonia and various alcohols.

Keywords: gas sensor; VOC sensor; nanostructures; conductive polymers; polypyrrole; polyaniline; ammonia; ethanol

1. Introduction

Recently, the gas sensors have found a new potential in medical applications such as detection of various volatile organic compounds (VOCs), which can be considered as biomarkers related to different diseases—especially pulmonary ones [1,2]. Their biggest advantage comes from the non-invasiveness of patient screening via VOC breath-prints produced mainly through changes in specific biochemical pathways in the body [3]. This attractive research direction with huge social impact motivated many researchers to develop novel sensing material which will be suitable for such application, i.e., the detection of extremely low gas concentrations and VOCs in exhaled human breath.

The sensitivity and mainly selectivity of any sensing layer strongly depend on the overall sensor construction and type of a specific material which is used for their fabrication. Nanomaterials have undoubtedly gained the most attention among scientists since they offer high surface to volume ratios resulting in higher sensitivity, versatility of their surface modification towards detection of chosen VOC analytes, and last but not least, relatively easy fabrication methods [4,5]. Among different materials, metal [6] and metal oxides [7] represents the most popular approaches for fabrication of sensing layers in these systems. On the contrary, conducting polymers (CPs) either individually or in a hybrid form, i.e., in the combination with other materials such as various noble metals as silver [8,9], gold [10], palladium [11], metal oxides e.g., ZnO [12], SnO₂ [13], carbon-based materials such as carbon nanotubes [14,15] or various form of graphene [16,17], are still rarely studied. The functionalization of polymers with the abovementioned materials was found to have a significant effect on enhanced sensor performance, especially via improved adsorption of organic compounds and via detection of low concentration VOCs. Therefore, CPs represent an important class of functional organic materials

for next-generation electronic and optical sensors [18,19]. However, the polymers are unstable at the nanometer scale due to the nature of covalent bonds which makes their nanostructures unstable as well. Because of this, so far progress in the synthesis of polymer nanomaterials has been relatively slow, and only limited research has been conducted on the fascinating properties polymer nanomaterials possess, in contrast to inorganic nanomaterials.

Comparing the number of scientific works devoted to ammonia and VOC sensors, there is a significant lack of information about the sensor concept based on polymer sensing materials which needs to be covered. Therefore, we provide this concise and didactic review on the recent development of different polymer-based sensors with a main focus on polypyrrole (PPy). Following a general introduction, we summarize the latest attempts of researchers focusing on the fabrication of such sensors according to the polymer used for the sensing layer in the first section and then according to target analytes in the second section. We also show an example of sensor interaction with ammonia and VOC analytes via an appropriate “sensing” model and we describe their interference with humidity as well, which represents one of the major challenges in the practical application in detection of VOCs in breath. To conclude, we provide a discussion about sensor limitations as well as biggest achievements so far and showed the promising future perspectives.

2. Basic Characteristics of CP

From the material point of view, CPs such as PPy [20,21], polyaniline (PANI) [22,23], polydiacetylene (PDA) [24,25] and various derivatives of polythiophene like poly(3,4-ethylenedioxythiophene) (PEDOT) [26,27] are the most promising materials for gas sensing applications. The structures of PPy, PANI and PEDOT are illustrated in Figure 1. It can be seen that all of them have a heteroatom in their monomer units, namely sulphur in the case of PEDOT and nitrogen in the case of PPy and PANI. The list of suitable polymers also includes some less common compounds, for example poly(vinylidene fluoride-hexafluoropropylene) [15] and polydiallyldimethylammonium chloride [28,29].

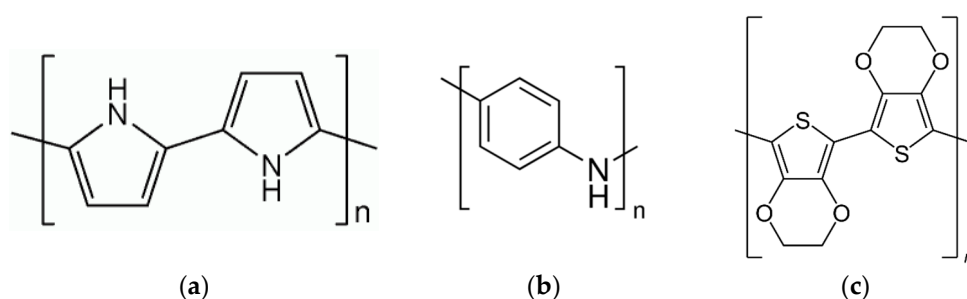


Figure 1. Structures of some conductive polymers: (a) PPy; (b) PANI and (c) PEDOT.

In general, the main advantage of all the abovementioned polymers is their capability of working at room temperature, which make them outstanding compared with other materials, for instance metal and metal-oxides which require very high temperatures (from 200 °C [30–32] up to 400 °C [33,34], or even higher [35]). Moreover, CPs have been in the spotlight of research investigations, especially in the field of chemical sensors, thanks to their high conductivity which results from π -electron conjugation [36,37]. The aromatic ring of CPs consist of chains with single and double bonds, which lead to broad π -electron conjugation. Basically, the sensitive and rapid response to various chemical species is caused by the oxidation level of the CP, which is readily affected by chemical or electrochemical doping/de-doping (oxidation/reduction) mechanisms between the CP and the exposed analytes [38]. Other benefits which make CP significant in the range of sensing materials are:

- the fast charge-discharge mechanism which is related directly with polymer structure, i.e., the presence of conjugated bonds, and applied voltage,

- high charge density causing high conductivity,
- solid stability in ambient conditions,
- the physico-chemical properties of the systems which are not easily changed by an external stimulus,
- and last but not least easy a low cost way of preparation [39].

CPs with nanometric features have demonstrated improved properties, similarly to other nanoscaled materials like metal or metal oxides [40]. For instance nanoscaled CPs are more conductive and sensitive compared with bulk materials owing to their higher surface area and conductive pathways, what is reflected in a rapid adsorption and absorption/desorption kinetics for analytes [41–43]. Due to this high electrical conductivity and fast electron transport, CPs have also received great attention in the field of electrochemical high power energy storage devices such as supercapacitors [44]. Here, CPs are often combined with other materials, namely metal [45], metal oxides [46–48], and carbon materials such as carbon nanotubes and graphene [49–51].

According to the literature survey, the most common characterization of CP structures is performed using Fourier Transformed Infrared (FT-IR) spectroscopic analysis [21,52,53]. Since the review is focused on PPy, we summarize the observed FT-IR peaks for PPy characteristic vibrations from different published works in the Table 1. The corresponding peaks for PPy appear in the range of 700–3000 cm^{-1} .

Table 1. FT-IR spectroscopic analysis of PPy.

| Vibration of the PPy Structure | Wavenumber (cm^{-1}) of PPy Prominent Peaks |
|------------------------------------|--|
| C–H stretching | 2854–2931 [54] |
| C–H in plane deformation vibration | 1039–1220 [54,55] |
| C–H out-of-plane vibration | 804–931 [55,56] |
| C–H wagging vibration | 782 [54] |
| C=C stretching of pyrrole ring | 1538–1553 [17,57] |
| C–N | 1192 [57] 1484 [54] |
| N–H stretching | 3432–3443 [17] |

3. Preparation of PPy Sensing Layers

PPy is a p-type organic conductive polymer created by oxidation of pyrrole monomer, further denoted as Py (Figure 1). The synthesis of PPy is relatively easy due to the oxidation of Py, its water solubility, great adherence to different types of substrates, and commercial availability. Nanostructured PPy materials have been synthesized in the form of nanoparticles [58,59], nanowires [21,60], nanorods [10], nanosheets [61], nanotubes [53] and nanoribbons [62]. In general, the methods for nanostructured polymer preparation can be classified according to type of reaction: electrochemical (see Section 3.1) or chemical (see Section 3.2). Few examples of these methods are listed in the Table 2.

In both types of synthetic approaches the polymer nanostructures can be prepared using template and template-free methods. The researchers usually distinguish among three different template methods, namely hard-template synthesis, soft-template synthesis [53,63,64], and reactive template synthesis [65]. One of the most used hard templates is nanoporous anodic alumina oxide (AAO) which provided uniform dimension of pores, high density, high aspect ratio and controllable diameter of nanostructures. AAO template can be used either for chemical [60] or electrochemical synthesis [39] of PPy nanostructures (such as nanowires, nanorods or nanotubes). In addition, it can be also used for the synthesis of organic–inorganic hybrid materials, where the PPy nanostructures are combined with an inorganic materials, such as Au-PPy nanorods [10] or CdS-PPy nanowires [66,67].

Table 2. Overview of preparation methods of PPy nanostructured sensing layer.

| Nanostructures Morphology | Type of Substrate | Fabrication Process | Oxidation Agent | Ref. |
|--|-------------------------------------|---|---|----------|
| Nanowires diameter: 50 nm | Silicon | AAO template assisted electrochemical polymerisation in potentiostatic mode at 1 V | Lithium perchlorate LiClO ₄ | [21] |
| Nanobelts, nanosheets and nanobricks with diameter of 400 nm | Stainless steel foil | Electrochemical polymerisation in potentiodynamic mode cycling from 0 to +1.2 V | Potassium nitrate KNO ₃ | [61] |
| Nanoribbons length of 1 cm and diameter of | Silicon | Ni nanobands assisted electrochemical polymerisation in potentiostatic mode at 0.7 V | Lithium perchlorate LiClO ₄ | [62] |
| Nanorods of Au/PPy diameter: 200 nm | Glass | AAO template assisted electrochemical polymerisation in potentiostatic mode at 0.95 V | Tetraethyl-ammonium tetrafluoroborate (C ₂ H ₅) ₄ N(BF ₄) | [10] |
| Nanotube diameter: 50 nm | Glass | Soft template assisted chemical polymerization | Ferric chloride FeCl ₃ | [53] |
| Nanowires diameter: 300 nm | Silicon with SiO ₂ layer | AAO template assisted chemical polymerisation | Ferric chloride FeCl ₃ | [60] |
| Nanoparticles diameter: 20, 60, 100 nm | Glass | Chemical polymerization | Ferric chloride FeCl ₃ | [58, 59] |
| Globular structures with diameter of about 590 nm | Printed circuit board | Chemical polymerization | Ammonium peroxydisulfate (NH ₄) ₂ S ₂ O ₈ or ferric chloride FeCl ₃ | [68, 69] |
| Nanolayers with thickness of 37, 43, 62, and 71 nm | Various polymeric substrates | Vapour-phase polymerization | Ferric chloride FeCl ₃ | [70] |
| Compact layers (thickness N/A) | Cellulosic paper | “Pen-writing” vapour-phase polymerization | Ferric chloride FeCl ₃ | [71] |

Nowadays, the research trends in the field of sensors, including gas and VOC sensors, are focused on immobilization of sensing layers on various flexible substrates like papers or plastics. Beside traditional cellulose paper, the researchers also tested vellum paper, filter paper and various photopapers as potential substrates for flexible gas sensors. These attractive flexible sensors represent a new alternative technology for fabricating simple, low-cost, portable and disposable analytical devices [72,73]. However, the number of works about CPs deposited on these types of substrate and their application in the gas-phase sensing is still limited. Most flexible gas sensors are based on PANI [74–76]. Less attention is paid to PPy [71], eventually poly(*m*-aminobenzenesulfonic acid) [77], poly-diallyldimethylammonium chloride (PDDAC) [28,29] or polydiacetylene (PDA) [24].

An interesting example of flexible gas sensor with PPy was developed by Jia et al. [71]. They used a simple and low-cost “pen-writing” method for immobilization of PPy on cellulosic paper (Figure 2). The pen-written paper chip with excellent mechanical and electrical properties was then used for in situ detections for ammonia with limit of detection (LOD) as low as 1.2 ppm.

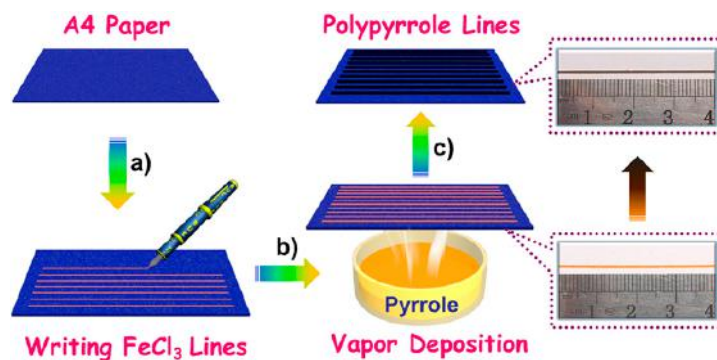


Figure 2. Schematic illustration of pen-writing PPy on A4 paper: (a) pen-writing FeCl_3 solution on the paper; (b) Exposing the FeCl_3 lines to Py vapor; (c) Interfacial polymerization of Py along the FeCl_3 lines. Insets are photographs of A4 paper written with FeCl_3 and PPy after fumigation. Reprinted with permission from [71]. Copyright (2017) American Chemical Society.

3.1. Electrochemical Synthesis

In this method, the synthesis of PPy is based on the polymerization of the Py on electrodes by electrochemical oxidation. From the group of electrochemical synthesis of PPy, one of the well-known synthesis is the electropolymerization, which can be performed using different modes such as galvanostatic (under constant current), potentiostatic (constant potential) [21], potential sweeping techniques such as cyclic voltammetry or other potentiodynamic methods [78].

The final properties of the structures synthesized via electropolymerization of Py are strongly dependent on the Py concentration [79], type of solvent [80,81], applied voltage and current density [82], pH of electrolyte [83] and its temperature [84,85]. The thickness of the deposited material depends on the integrated charges used for electrochemical synthesis [39]. The deposition of PPy is achieved on the conductive surfaces that serve as working electrodes, for this purpose, thin conductive metallic layer such as gold, which can be sputtered or vapour deposited on one side of the membrane, are typically used [86]. The electrochemical cell consists of three electrodes: a conductive metal layer acts as a working one, a platinum sheet as counter electrode, and reference electrode is usually made of Ag/AgCl . The reaction is carried out in an electrolyte solution, which is a mixture of Py monomer, dissolved in an appropriate solvent containing the desired anionic doping salt [87]. After applying a certain voltage in potentiostatic mode or constant current, the polymerization of Py is started. The set values of both magnitudes depend undoubtedly on the size of treated sample, distance between electrodes and their area.

According to Sadki et al., PPy can react by different mechanisms during its electro-polymerization, namely the Diaz, Kim, Pletcher, and Reynolds ones [88]. The Diaz mechanism, which is based on the creation of PPy via coupling of two resonant forms with unpaired electrons, is the most frequently used in the literature [89] and therefore we will describe it in more details. The readers may find detailed information about the other mechanisms in the above mentioned review [88].

During the first step of Diaz mechanism the oxidation of monomer and its transformation into the cation radical $\text{R}^{+\bullet}$ proceed at the applied voltage, see Figure 3a. The radical appeared in the several resonance forms. The reaction between two radicals with unpaired electrons results in formation of bonds between them and creation of the dihydromer. The loss of two protons of dihydromer results in creation of the aromatic dimer, the reaction is illustrated in Figure 3b. The next step is the oxidation of dimer and creation of the dimer radical. This oxidation is happening faster than oxidation of the monomer, because the unpaired electron is now delocalized over the two rings, and needs lower oxidation potential for creation of radicals. The appropriate resonance form of dimer reacts with suitable resonance form of monomer and they are giving the structure, which after the loss of two protons, makes the neutral trimer, the reaction is presented in Figure 4. The described steps are repeating in the same order (creation of radical, coupling, and deprotonation) until the final polymer

structure is obtained. The final PPy structure is oxidized conducting form with a positive charge after every three to four Py units. This charge is then counter-balanced by an electrolyte anion. The Diaz mechanism confirmed the main fact about PPy, existence of a p-type radical [88].

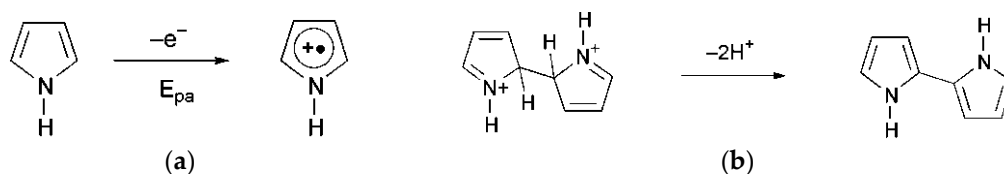


Figure 3. The schematic illustration of Py dimer's synthesis: (a) formation of the cation radical $R^{+\bullet}$ and (b) formation of the aromatic dimer. Reproduced from [88] with permission of The Royal Society of Chemistry.

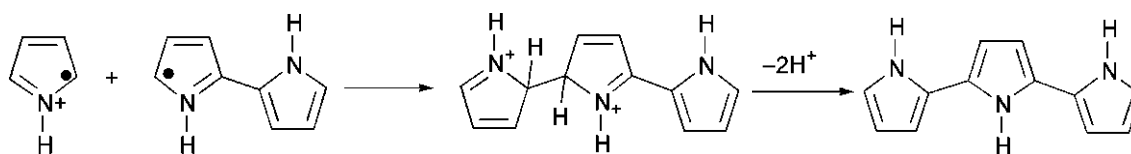


Figure 4. The schematic illustration of Py trimers's synthesis. Reproduced from [88] with permission of The Royal Society of Chemistry.

Concerning template-assisted electrochemical synthesis, Zhang et al. obtained PPy nanowires with diameters about 50 nm using the AAO template via electrochemical polymerization of Py (Figure 5) [21]. The three electrode system was used for the synthesis of the PPy nanowires. The electropolymerization process of Py was carried out in the solution of Py with lithium perchlorate ($LiClO_4$), which served as the oxidizing agent.

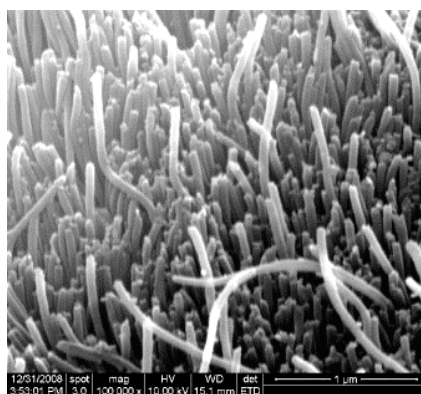


Figure 5. SEM image of the PPy nanowires grown in the AAO template. Reproduced from [21]. Copyright (2017), with permission from Elsevier.

The applied voltage during the electropolymerization was 1 V. The reaction time was 650 s. The final structure consisted of the PPy nanowires with the thin PPy layer formed on the top of the nanowires. The authors explained the changes in the current at the constant potential during the growing of the PPy nanostructures passed through three different stages: (1) creation of the PPy nucleus; (2) PPy nanowires; and (3) thin PPy film. The beginning of the electropolymerization is followed by the decreasing of the current (see Figure 6, from point a to b) which corresponds to formation of PPy nucleates. After the first step is finished, the current decreased to certain point and stayed constant (from b to c) till the all AAO pores are filled with the PPy, more precisely till the moment when the nanowires are created. In the last stage the current started to increase again

(from point c to d), manifesting the growth of the PPy out of the AAO pores and finally the creation of the thin PPy film on the top. Subsequently, the created structures were sputter-deposited with gold layer from both sides, which had the function of the electrodes and the created chemiresistive sensor was used for the detection of ammonia.

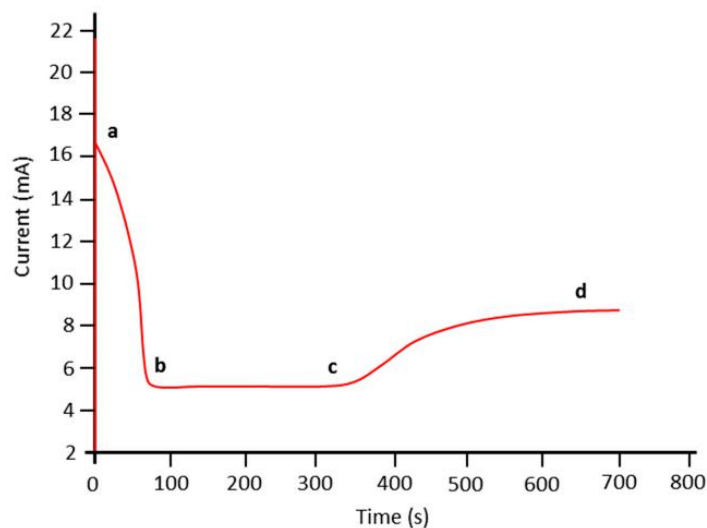


Figure 6. Current-time curve during PPy synthesis. Reproduced from [21]. Copyright (2017), with permission from Elsevier.

Lee et al. obtained the metal-organic framework, which is based on gold-polypyrrole (Au-PPy) nanorods with a diameter of about 200 nm [10]. In the first step, they synthesised gold nanorods via electrodeposition into AAO nanoporous template and in the second step, they deposited the PPy nanorods via electropolymerization of the Py. The electropolymerization reaction was carried out in Py solution dissolved in acetonitrile, where tetraethylammonium tetrafluoroborate was used as the oxidizing agent. The applied voltage was 0.95 V. The Au-PPy nanorods (see Figure 7) served as the sensor for the detection of the VOC (namely of acetic acid, benzene, and toluene).



Figure 7. Schematic illustration of Au-PPy nanorods.

3.2. Chemical Synthesis

Compared with the electrochemical synthesis of the PPy, the chemical method is simpler because it does not require any special instruments [36,90,91]. The type of surfactant, e.g., sodium dodecylbenzene sulfonate [92], and the oxidizing agent are the most responsible for the polymerization of Py and the final conductivity of PPy. The researchers made attempts to increase the electrical conductivity of PPy by using various dopants, namely lithium perchlorate (LiClO_4), *p*-toluene sulfonate and naphthalene sulfonic acid [69].

Common oxidants used for Py polymerisation include ferric chloride, ferric perchlorate and ammonium peroxydisulphate. According to the literature, ferric chloride (FeCl_3) is the most used oxidizing agent [93–95]. The reaction path is simple: after the addition of the Py in the aqueous solution of FeCl_3 , the anions from the solution come into contact with the neutral polymer matrix changing it into Py^+ cations spontaneously. These Py cations are then participating in the polymerization and formation of black PPy [96].

Kwon et al. synthesized the PPy nanoparticles with different diameter size (20, 60, and 100 nm) by the polymerisation of the Py via its chemical oxidation [58,59]. The synthesis is based on the reaction between water-soluble polymers (polyvinyl alcohol dissolved in the water) and metal cations (FeCl_3) in aqueous solution. These compounds form the complex, which has the main role in the oxidizing process of the Py monomer. In particular, FeCl_3 behaves as the oxidizing agent which initiate the chemical oxidation of Py, while polyvinyl alcohol (PVA) acts as a self-assembled precursor. PVA is responsible for a steric stability during the growth of polymer nanoparticles. The size of nanoparticles is related with appropriate concentration of these two reactants which are mixed and dissolved in water. After addition of the Py to this mixture and its contact with FeCl_3 , the oxidation of Py and its polymerization reaction begin. This is represented by the creation of black solution which corresponds to created PPy nanoparticles (Figure 8). Therefore, the advantage of this synthesis of PPy compared with others methods which will be described in next section, lies in no extra requirements for special surfactants or specific templates.

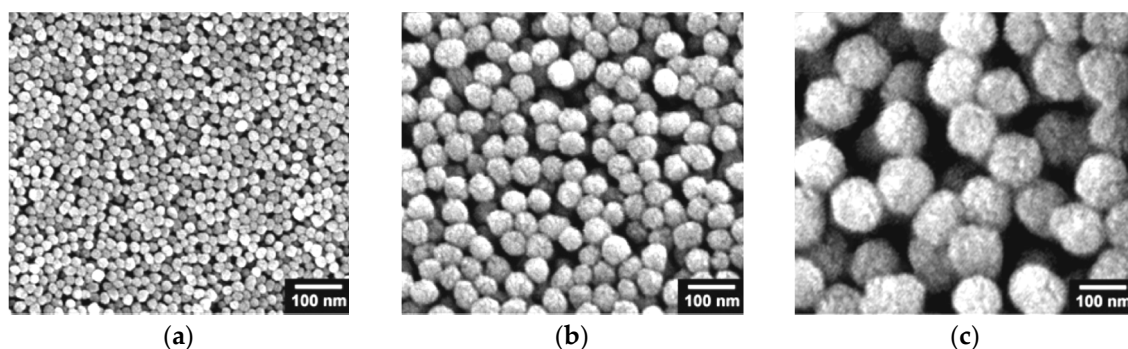


Figure 8. SEM images of PPy nanoparticles with diameter of (a) 20 nm; (b) 60 nm; and (c) 100 nm. Reprinted with permission from [58]. Copyright (2017) American Chemical Society.

Less common chemical synthesis approach of PPy is based on vapour phase polymerisation [70]. The method involves application of the oxidant to the surface using a solvent coating process and subsequently exposure of the coated surface to the vapour of the monomer. This vapour phase polymerization was initially described by Mohammadi et al. where the authors used FeCl_3 or H_2O_2 as oxidants in order to form PPy films [97].

Hernandez et al. used an AAO template for chemical polymerization of PPy nanowires [60]. The authors used a previously prepared AAO template, which they immersed in the cold Py solution and they added FeCl_3 as the oxidizing agent for chemical polymerization of Py. The nanowires were observed after the dissolution of AAO in hydrofluoric acid. The dried PPy nanowires were later dissolved in ethanol and dispersed across the microfabricated gold electrodes on SiO_2/Si substrate. The authors concluded that the nanowires synthesized via chemical polymerization are more ordered compared to electrochemically synthesized ones.

Similar work employing combination of chemical synthesis and template was used by Hassanzadeh et al. for the creation of a PPy nanostructured hydrogen sensor [98]. This gas sensor based on PPy nanowire arrays was fabricated through chemical polymerization in an AAO membrane (Figure 9). The authors used commercial Whatman anodiscs with pore diameter of 200 nm and thickness of 60 μm . They optimized the polymerization time up to 3 h and molar ratio of oxidant

(0.2 M FeCl_3) to Py monomer (0.2 M aqueous solution). This molar ratio provided the highest specific surface area of about $173 \text{ m}^2/\text{g}$. After dissolving the AAO template 10% HF, the obtained PPy nanostructured arrays supported with PPy layers were rinsed and copper wire electrodes connecting the sensing layer with measuring circuit were attached to the opposite ends of PPy sensing array with silver paste.

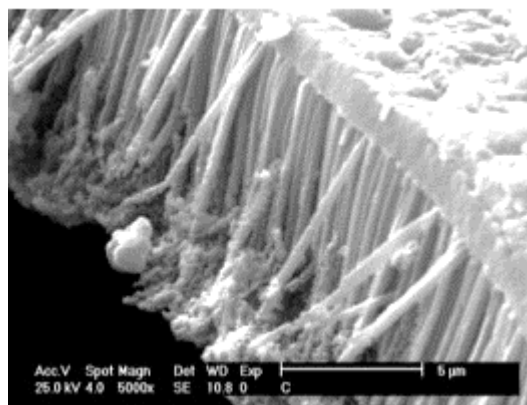


Figure 9. SEM image of PPy nanostructured array prepared by chemical synthesis in AAO template after its dissolving. Reprinted from [98]. Copyright (2017), with permission from Elsevier.

Yang et al. used the complex of anhydrous FeCl_3 and methyl orange as a soft template for chemical synthesis of PPy nanostructures [63]. In this approach, a certain amount of the Py monomer was added on the already prepared soft template, and it was stirred for 24 h. FeCl_3 was responsible for the oxidation in the polymerization reaction of Py and resulted in formation of PPy nanostructures. After finishing the process, the sample was washed and dried. PPy dispersion in water was then drop-casted onto the glass substrate. The same method was used by Joulazadeh et al., where they observed PPy with nanotubular morphology [13,53] (Figure 10).

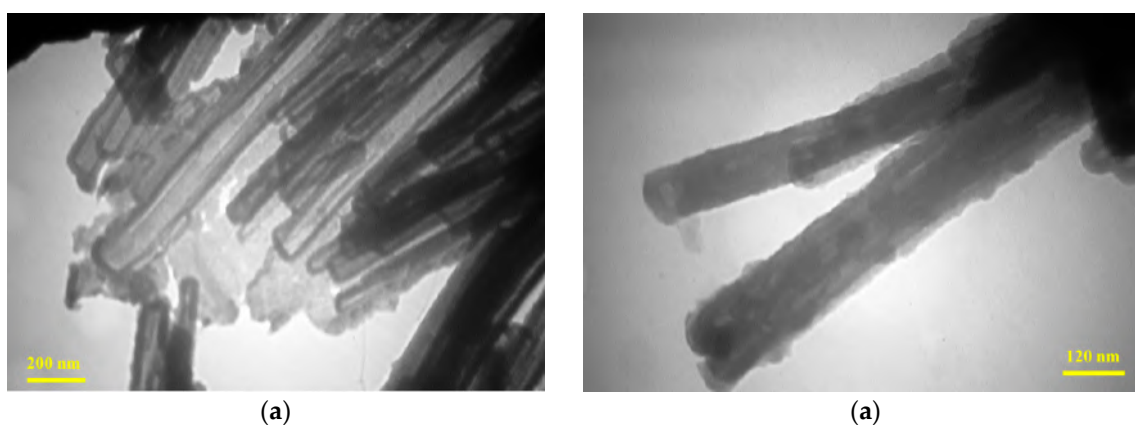


Figure 10. TEM images (a,b) of synthesized PPy nanotubes with two different magnitudes. Reprinted from [13]. Copyright (2017), with permission from Elsevier.

Dubal et al. used MnO_2 reactive template with three different morphologies, namely nanorods, nanowires and urchins, for chemical synthesis of PPy nanotubes, nanofibers and urchins [65] (Figure 11). They dispersed MnO_2 nanostructures in deionized water and then added 1 M HCl $\text{K}_2\text{Cr}_2\text{O}_7$ and Py monomer. The mixture was stirred and then sonicated. Later, the solution was stirred for 5 h and maintained at room temperature for 24 h. Once the PPy nanostructures were obtained, the MnO_2 template was dissolved.

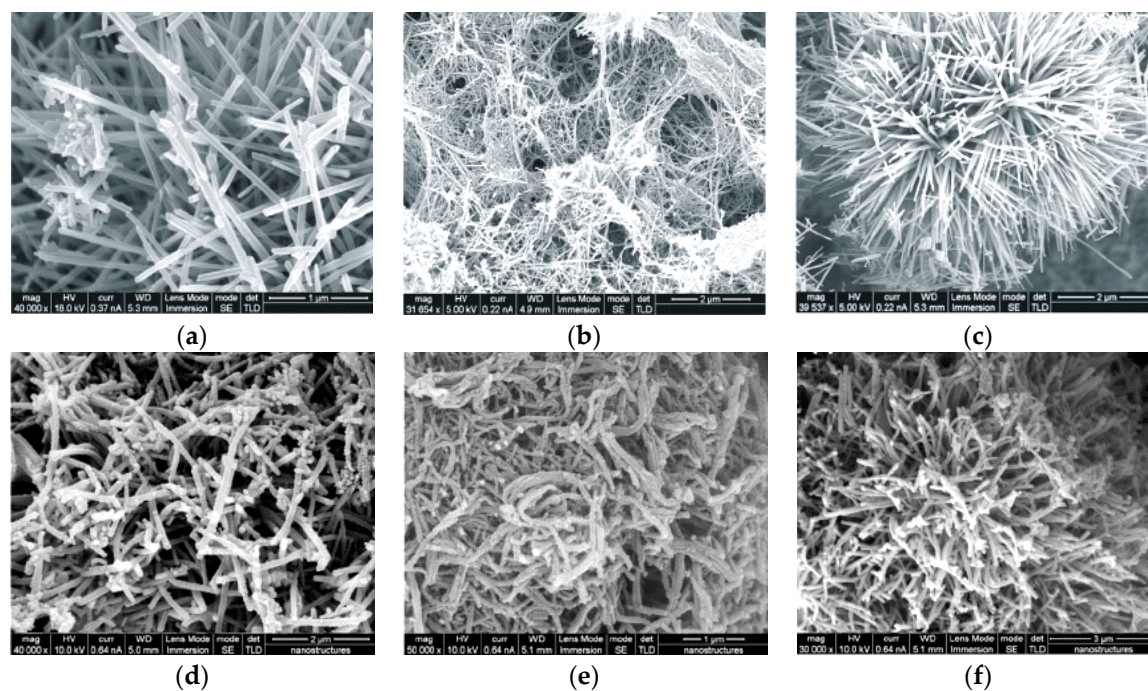


Figure 11. SEM images of three different MnO₂ nanostructures: (a) nanorods; (b) nanowires; and (c) urchins with corresponding morphologies of PPy: (d) nanotubes; (e) nanofibers; and (f) urchins. Reprinted from [65]. Copyright (2017), with permission from Elsevier.

4. Gas and VOC Sensing

When talking about the main functional characteristics of sensors, one has to take into account several parameters such as sensitivity, selectivity, stability, response time and recovery time [99]. Depending on the type of transducing mechanism, these parameters may vary a lot. In general, it is expected that the sensitivity of any type of gas sensors must lay in the range of ppm or even ppb. The response time is defined as the necessary time to reach 90% of the total measured electrical magnitude change, and it is as fast, as in units of seconds. The recovery time, which is defined as the time required for the measured electrical magnitude to return to the original value, upon switching from sensor's exposure of the target gas to 100% carrier gas (syntactic air or some halogen gas) is also expressed in units of seconds. The other important parameter is sensor saturation, which means that dependence of the sensor response on the concentration of analyte is no longer linear [11,53]. In other words, the signal that needs to be measured is larger than the dynamic range of the sensor.

Most of sensors based on CP polymers operate via a chemiresistive transducing mechanism. In comparison with chemiresistive PPy-based sensors, less attention is paid to optical sensors, even though they usually provide excellent sensitivity. Also, some works are related to the PPy sensors which work in an impedance and capacitance mode. Hence, we will briefly describe the working principle of mentioned transducing mechanisms in the following paragraphs:

Chemiresistive sensors belonging to the electrochemical sensors group are based on the measurement of a change in resistance R . It means the sensor response S in % is correlated with the change in the electrical resistance before and after interaction with analyte (gas or VOC) using the following equation:

$$S = \frac{R_{gas} - R_0}{R_0} \cdot 100\%, \quad (1)$$

where R_{gas} is the value of the resistance after exposing to the gas, and R_0 after exposing to the carrier gas, respectively. In general, the resistance of sensor is expected to revert to its original value during all response/recovery cycles, indicating that the sensing process is reversible for the sensor.

Optical sensors usually measure the changes of optical absorption at specific wavelengths [100]. The sensor response (ΔA) can be then calculated as:

$$\Delta A = \frac{A_{gas} - A_{air}}{A_{air}} \cdot 100\%, \quad (2)$$

where A_{gas} is value of the absorbance when the sample is exposed to the target gas, and A_{air} is value of the absorbance when the sample is exposed to air.

Capacitance sensors measure the change in dielectric constant of films between the electrodes as a function of the gas concentration.

Impedance sensors measure the resulting current when a sinusoidal voltage is applied. Impedance as a complex number is then calculated as the ratio of voltage to current in the frequency domain [101]. Impedance sensors read resistive and capacitive part as a dependence on the presence of gas at variable frequency. The technique offers interesting possible benefits in the discrimination of gas and VOC analytes [102,103]. The sensing process of sensors based on CP can be divided into three stages (Figure 12):

1. Recognition of the analytes: the CP nanostructures act as sensitive layer and interact with the analytes with different level of selectivity.
2. Signal transduction: if the sensitive layer recognizes the analytes, it is reflected as a change of electronic charge-transfer properties of the CP. That changes are in the quantitative correlation with the concentration of the analytes [104,105]. The oxidation or reduction reactions proceeding between the sensitive layer and exposed analytes cause a physical swelling of the polymer structure.
3. Electrical readout: finally, the previously described steps are monitored as changes of the electrical resistance or more general of any electrical magnitude.

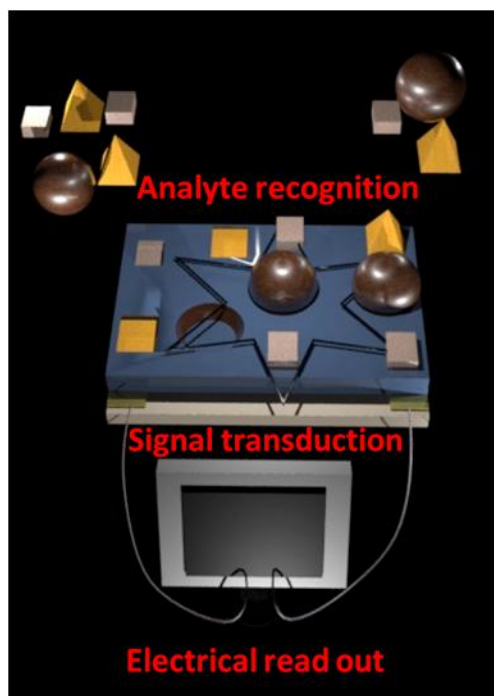


Figure 12. Schematic illustration of an electrochemical sensor consisting of substrate, electrodes, and CP film which is acting as sensing material and transducer. The overall sensing process involves analyte recognition, signal transduction, and electrical readout.

In the following subsections, we will provide more detailed description of most frequently used types of CP-based gas sensors. Our focus will be on the sensing properties of previously mentioned PPy nanostructures, where we will compare the minimum LOD, sensor response, response time and recovery time, and also perceive the sensitivity to target gases and VOC, especially ammonia, various alcohols and water vapor. In addition, comparison between the sensing performances of the PPy gas sensors and the sensors based on other material, namely metal, metal oxide and carbon base materials, for the detection of ammonia and some most frequently detected alcohols, will be summarized in following part. It will provide the better understanding of the advantages and disadvantages of PPy based sensors.

4.1. Detection of Ammonia

PPy behaves like p-type semiconductors via appropriate doping [106] and can affect the change of conductivity through interaction with gas or vapour [107,108]. The sensing mechanism of PPy nanostructures is different for various analytes depending on the presence of their functional groups. According to our rigorous literature survey, we found the highest response of PPy based sensor was recognized for ammonia. Regarding suggested medical application, ammonia can be found in elevated concentrations between 0.8 to 14 ppm in exhaled breath of patients with diagnosis of renal disorders or ulcers, while in normal subjects it is in the range of 0.15–1.8 ppm [62,109].

NH₃ is an electron-donating molecule reducing the holes density in PPy and thus resulting in the increase of the electrical resistance. In opposite, the analytes such as alcohols behave as electron-acceptors because they create new holes in the PPy structure, leading to the decrease in the electrical resistance [41]. In other words, during ammonia sensing the donation of a lone pair of electrons of nitrogen to the initially oxidized PPy results in the decrease in the conductivity and the formation of neutralized PPy [110].

The first possible reversible interaction mechanism between the PPy and ammonia electron donating molecules which decrease the doping level of PPy by compensating the effect of the original dopant (denoted here as A⁻), can be described as follows [21,111,112]:



An alternative mechanism for the compensation reaction (see Figure 13), which involves the proton transfer between the polymer and ammonia which is a strong base and can easily attack protons of PPy, could be written as:

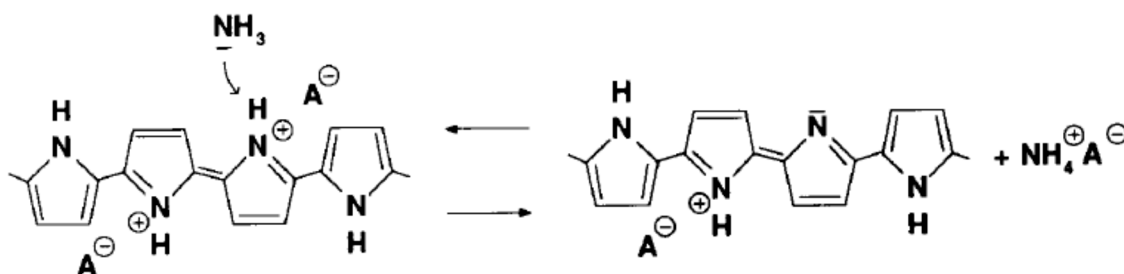


Figure 13. The schematic illustration of PPy interaction with ammonia. Reprinted from [111] with permission from Elsevier. Copyright 2017.

Similarly to PPy, PANI also interacts reversibly with ammonia which is related to their low redox potentials (−0.2 V and 0.2 V versus SSCE, respectively). An overview of PPy-based sensors, including their response time, recovery time and LOD towards ammonia is provided in Table 3.

Table 3. Overview of PPy used as active layers for detection of ammonia at room temperature.

| Polymer Type | LOD | Response Time/Recovery Time | Transducing Mechanism | Ref. |
|---|------------------------|---|-----------------------|-------|
| PPy nanoparticles | 5 ppm | Less than 1 s/2 s | Chemiresistive | [58] |
| Multidimensional PPy nanotubes | 0.01 ppm | Less than 1 s/55–60 s | Chemiresistive | [113] |
| Single PPy nanowire | 40 ppm | 15–10 min (for 40–300 ppm)/ 15 min for 40 ppm | Chemiresistive | [36] |
| PPy nanowires | 1.5 ppm | 60 s for 73 ppm/prolonged with increasing of con. (1.5–73 ppm) | Chemiresistive | [18] |
| Single crystal PPy nanotube | 0.00005 ppm | ~16 s/~16 s for 1 ppm | Chemiresistive | [114] |
| PPy nanoribbons | 0.5 ppm | ~8 min/3 min | Chemiresistive | [62] |
| PPy nanotubes PPy/Ag–AgCl composite Nanotubes | – | >1000 s for 100 ppm/–150 s for 100 ppm/500 s | Chemiresistive | [115] |
| PPy/ZnO nanocomposite PPy/SnO ₂ nanocomposite | 10 ppm | ~100 s for 24 ppm/100 s ~50 s for 24 ppm/250 s for first 3 cycles | Chemiresistive | [13] |
| PPy/graphene nanocomposite decorated with TiO ₂ nanoparticles | 1 ppm | ~36 s/~16 s for 50 ppm | Chemiresistive | [116] |
| Au/PPy nanopeapods | 0.007 ppm _v | ~15 min for 5 ppm _v /did not reach R ₀ value | Chemiresistive | [117] |

The PPy nanoparticles prepared by Kwon et al. [58] were deposited on the gold interdigitated microelectrodes by a spin-coating and a drop-casting method, and used to develop a chemiresistive sensor for the detection of ammonia. The PPy nanoparticles on the top of electrodes were deposited by a spin-coating method which provided a more homogeneous distribution and also higher sensitivity to gases compared to the drop-casting method where nanoparticles were randomly distributed. Significant results were noticed for ammonia, where the sensor showed a LOD close to 5 ppm. The response time of the sensor was less than 1 s. In the case of the recovery time, 30 s was necessary for the sensor to recover after exposure to 5 ppm of NH₃.

The same authors described the work of a chemiresistive sensor with a special nanostructure design based on multidimensional PPy nanotubes decorated with nanowires and nanonodules via vapour deposition polymerization [113]. Compared with the nanoparticles which they already described in the previously mentioned paper [58], those specific nanostructures showed an impressive response to NH₃: the minimum LOD was 10 ppb.

An ammonia sensor based on PPy nanowires with diameters around 50 nm designed by Zhang et al. [21] was able to respond in the percentage range from 10% to 26% for ammonia concentrations from 1.5 ppm to 77 ppm, respectively. 60 s was enough for the sensor to respond to 77 ppm of ammonia. Comparing the response and response time of the single PPy nanowire sensor from [60], where the response was only about 7% for the concentration of 73 ppm of ammonia and the response time was 10 min, we can notice a marked improvement in the sensor characteristics.

Beside a polymer nanostructured array, researchers have also attempted to use a single polymer nanostructure as published by Hernandez et al. [60]. A single PPy nanowire placed on microfabricated gold electrodes on a SiO₂/Si substrate was used for the detection of ammonia. The sensor showed sensitivity to ammonia at concentrations as low as approximately 40 ppm. The authors also monitored

the sensor response to NO₂, but the sensor did not show any sensitivity to this analyte. These results are opposite to those of Chougule et al. who confirmed the sensor response of 14% to 100 ppm of NO₂ using a PPy film with a granular structure [118].

Xue et al. fabricated a single crystal high-oriented PPy nanotube array using an AAO template under low temperature [114]. The growth of the PPy nanotubes on a cold surface allows nice ordered structures. The diameter of the resulting nanowires is about 100–110 nm, where the external diameter of the nanotubes is around 100 nm and the wall thickness about 10 nm. The ammonia sensing properties of this PPy nanotube array have been studied at room temperature. This sensor easily detects ammonia down to 1 ppm, and exhibits very rapid response and recovery times (16 s). The LOD can even reach 0.05 ppb as the highest sensitivity. Therefore, the authors concluded that those ultrahigh performances of PPy nanotubes are the result of not only the hollow structure and high surface area of nanotubes, but also a consequence of the high crystallinity of the structures.

The single PPy nanoribbons with different conductivities and thicknesses synthesized by Chartuprayoon et al. [62], showed successful sensing properties for the detection of ammonia in the concentration range between 0.5 ppm and 50 ppm. The concentration of 0.5 ppm can be considered as the minimum LOD. As the conductivity of the PPy nanostructures is the most important parameter for the sensing performance, the PPy nanoribbons with the conductivity of 0.003 S/cm and 6.5 S/cm showed significant responses to low concentration of ammonia, namely about 8% and 2% for 0.5 ppm and about 15% and 28% for 50 ppm. The response time and recovery time of the sensors were about 8 min and 3 min, respectively, which can be considered very slow times compared to the previously described sensors.

The detection of ammonia was also successful in the case of PPy nanocomposites decorated with various metal oxides (SnO₂ and ZnO) [13]. In this work the authors found the sensor responses were higher than that observed for the pristine PPy. In addition, a ZnO-based PPy nanocomposite was found to result in a more pronounced response, namely 34%, for 30 ppm of ammonia compared to SnO₂, which response was only 25% for the same ammonia concentration. This phenomena can be attributed to Zn²⁺ cations that can act as redox-active species and thus increase the charge density and conductivity of the PPy nanocomposite. Considering the response time and recovery time, the faster response time was observed in the case of SnO₂-based sensor. However, this sensor was not able to recover after three cycles of ammonia exposure, which was opposite to the ZnO-based sensor. The authors explained that reversibility of the ZnO-based sensor is a consequence of its hollow nanotubular morphology, while the SnO₂/PPy nanostructures had non-hollow morphology, therefore the adsorption and desorption processes happen faster.

One more example of PPy nanostructures decorated with metal oxides is described in the work of Xiang et al. [116]. PPy-graphene nanocomposite decorated with TiO₂ nanoparticles with diameters of 10–30 nm was used as the sensitive layer of the ammonia sensor. The sensor response to 50 ppm of ammonia was 102.2%, with a response time and recovery time of 36 and 16 s, respectively. Compared with the ZnO-based PPy nanocomposite [13], where the response to 50 ppm of ammonia was about 50%, the PPy/graphene/TiO₂ nanostructures had much higher sensitivity.

The significant performance of ammonia sensors was recognized in the work of Yan et al. [117]. Compared with the previously described PPy-based sensors, the authors used a special viral-template, based on a genetically modified M13 bacteriophage with a gold-binding peptide. Au nanoparticles were assembled on the template, and these conferred electrical conductivity to the bio-template, what enabled the electropolymerization of the PPy and the formation of Au/PPy nanopeapods. These specific metal-semiconductor, bio-templated nanomaterials had a LOD of 0.007 ppmv, what can be considered as noteworthy sensitivity for nanostructures. The authors claimed that the sensing performances may be influenced by the low thickness of the PPy shell (17.4 nm) along the length of the nanopeapods.

An overview of sensors for the detection of ammonia based on other nanomaterials is provided in the Tables 4 and 5. If we take into account the sensing performances of the literature reports

of sensors shown in these tables, we can see that various gas sensing materials were used for the detection of ammonia, including n-type oxide semiconductors (such as SnO₂ [119]) and p-type oxide semiconductors (such as CuO [120]). In addition, the mentioned sensing materials can work at high operating temperatures, or even at room temperature. It is difficult to note significant differences in the sensing properties of the described sensors. However, the sensors' characteristics depends on the type and morphology of the sensing layers. From the group of the metal oxide-based ammonia sensors, we can identify Co₃O₄ nanosheet structures as the sensitive layer with the best performance, with the lowest LOD (0.2 ppm) and the most improved response time/recovery times (~9 s/~134 s) [121]. Otherwise, if we consider LOD and response time/recovery times as the major parameters for detection of biomarkers related to different diseases (very low concentrations of target analysis are related to diseases [45,108]), we can conclude that single crystal PPy nanotubes showed the most advanced sensing properties for the detection of ammonia, with LOD (0.00005 ppm) and response/recovery times of less than 16 s/16 s [114].

Table 4. Overview of different nanomaterials used as active layers for detection of ammonia at room temperature.

| Polymer Type | LOD | Response Time/Recovery Time | Transducing Mechanism | Ref. |
|---|---------|-----------------------------|-----------------------|-------|
| Nanofibrous PANI films | 5 ppm | ~200 s/~100 s | Chemiresistive | [122] |
| PbS quantum dots/TiO ₂ nanotube | 2 ppm | -/- | Chemiresistive | [121] |
| Co ₃ O ₄ nanosheets | 0.2 ppm | ~9 s/~134 s | Chemiresistive | [121] |
| Carbon nanotubes/SnO ₂ nanocomposite | 10 ppm | ~100 s/~192 s | Chemiresistive | [123] |
| CuO Nanostructures | 50 ppm | ~6 min/~5–6 min | Chemiresistive | [120] |
| Au-decorated tungsten oxide nanoneedles | - | ~4 s/~4 min for 100 ppm | Optical | [124] |

Table 5. Overview of different nanomaterials used as active layers for detection of ammonia at higher temperature.

| Type of Material | LOD | Response Time/Recovery Time | Operative Temperature | Transducing mechanism | Ref. |
|---|----------|-----------------------------|-----------------------|-----------------------|-------|
| V ₂ O ₅ and V ₇ O ₁₆ thin-film structures | 0.2 ppm | ~1 h/~2 h | 350 °C | Chemiresistive | [125] |
| SnO ₂ -Nb-Pt nanocrystalline | 10 ppm | ~150 s/~170 s | 355 °C | Chemiresistive | [126] |
| Nanoporous NiO thin films | 20 ppm | ~89 s/~128 s | 250 °C | Chemiresistive | [127] |
| Pt activated SnO ₂ nanoparticle clusters | 10 ppm | ~75 s/~67 s for 50 ppm | 115 °C | Chemiresistive | [119] |
| Mixed WO ₃ -SnO ₂ nanostructures | 0.52 ppm | ~220 s/~195 s for 400 ppm | 200 °C | Chemiresistive | [128] |

4.2. Detection of Other Gases and VOC

An overview of CP sensors for the detection of VOCs is listed in the Table 6. The chemiresistive sensor based on PPy nanoparticles prepared by Kwon et al. [58] was used for the detection of VOCs such as acetonitrile, acetic acid, and methanol. Significant results were noticed for methanol, where the sensor showed a minimum LOD close to 50 ppm of methanol. The response time of the sensor was less than 1 s. This value can be considered as faster compared with other methanol sensors based on

CPs, where the response time was 8 s for 1 ppm of methanol and 2 s for 2000 ppm of methanol [11]. In the case of the recovery time, 90 s was necessary for sensor to recover after exposure to 50 ppm of methanol. On the other hand, the sensor did not show a LOD for acetonitrile and acetic acid as low as in the case of NH₃ and methanol, namely the minimum LOD was 100 ppm of acetonitrile and acetic acid. The response and recovery times were more or less similar, i.e., less than 1 s and less than 10 s, respectively. Considering the sensing mechanism between the tested VOCs and the PPy sensing layer, it can be presumed that acetonitrile as a weak proton-transfer base (pK_a = 25) behaves like ammonia, causing an increase in the electrical resistance, whereas the acetic acid vapor reacts similarly to alcohols, thus causing a decrease in the electrical resistance. The conclusions from this work are that the sensor's response and the recovery time correlate with the size of the nanoparticles: better response and longer recovery time are observed for sensing layers with smaller nanoparticle diameters. As already explained above, in general the nanostructures with smaller diameter provide a higher surface-to-volume ratio and higher conductivity together with efficient charge carrier transport [129]. The longer recovery time can be explained by a slow desorption of the gas molecules from the PPy nanoparticle backbone.

Table 6. Overview of CPs used as active layers for detection of other gases and VOCs.

| Polymer Type | Target Analytes | LOD | Response Time/Recovery Time | Transducing Mechanism | Ref. |
|---|--|---|---|--|-------|
| PPy nanoparticles | Methanol Acetonitrile Acetic acid | 50 ppm 100 ppm 100 ppm | 1 s/90 s <1 s/<10 s <1 s/<10 s | Chemiresistive | [58] |
| PANI/Pd Nanocomposite | Methanol | 1 ppm | ~8 s/~9 s | Chemiresistive | [11] |
| Multidimensional PPy nanotubes | Ethanol | 1 ppm | < 1 s/4–5 s | Chemiresistive | [113] |
| Nanotubular PPy | Butanol Propanol Methanol Ethanol | 3 ppm for all alcohols | Data for 10 ppm: ~200 s/>5 s ~200 s/>5 s ~150 s/5 s ~110 s/5 s | Chemiresistive | [53] |
| Nanofibrillar PANI | Butanol Propanol Methanol Ethanol | 3 ppm for all alcohols | Data for 10 ppm: ~100 s/not completely recovered ~80 s/not completely recovered ~80 s/~15 s ~80 s/~15 s | Chemiresistive | [53] |
| Au/PPy nanorods | Benzene Toluene Acetic acid | 10 ppm for all analytes | 20 s/40 s | Optical based on localized surface plasmon resonance | [10] |
| PPy coated quartz fibres | Methanol Ethanol Acetone Toluene Chloroform Isopropyl alcohol | 1 ppm for methanol 10–30 ppm for other VOC | Data for 286 ppm of methanol: 200 s/400 s. Data for 6 ppm of methanol: 100 s/200 s. | Optical based on reflectance | [130] |
| Al/PPy/Au/dodecylbenzene sulfonic acid diodes | Methanol | 20 ppm | 10 min/6 h | Capacitive | [131] |
| PPy films on n-silicon | Acetone | 10 ppm | -/- | Capacitive | [132] |
| Single PPy nanowire | Heptanal Acetophenone Isopropyl myristate 2-Propanol | 8.982 ppm 798 ppb 134 ppm 129.5 ppm | -/- | Chemiresistive | [133] |
| PPy film on gold IDE/FR4 | Acetone Ethanol Isopropyl alcohol | - | -/- | Impedance | [102] |
| PPy film on gold | Methanol Acetone Ethyl acetate Ethanol | - | ~100 s/~50 s | Impedance | [103] |

Besides ammonia, multidimensional PPy nanotubes decorated with nanowires and nanonodules [113] were used for the detection of ethanol. The authors observed a sensor response to ethanol with a minimum LOD of 1 ppm. They found the sensor response for 100 ppm of ethanol was about 4%, which is higher than in the case of a sensor based on pure PANI nanostructures where the sensor response was only around 1% for the same ethanol concentration [8]. However when the PANI nanostructures were decorated with nanosized silver nanoparticles, the sensor response increased up to 18%. The response time of sensors based on multidimensional PPy nanotubes [113] was extremely fast in comparison with PANI based sensors described in [8], i.e., 1 s and 52 s, respectively.

Joulazadeh et al. used nanotubular PPy and nanofibrillar PANI (see Figure 10) for the detection of various alcohols (propanol, butanol, methanol, and ethanol) [53]. Nanostructures of this kind showed a very low LOD to the mentioned alcohols up to 3 ppm. From this work can be concluded that the resistance increase is related to the exposure to the gases. The hydrogen bonding interactions between the polar –OH groups of alcohols and the polymer result in dipole–dipole interactions, and delocalization carriers along the PPy chains which is manifested by the increase of the resistance [87]. PPy exhibited an acceptable performance in the presence of all tested alcohol vapors, however the response and the recovery time varied for different exposed alcohols. The sensor showed higher response to propanol and butanol, what is attributed to the longer alkyl chain comparing to ethanol and methanol, and thus to higher electrophilicity [134]. Methanol and ethanol had shorter recovery times, which is coherent with a faster desorption process due to their smaller molecular size compared with propanol and butanol. This effect of analyte size, namely the length of hydrocarbon chain in aliphatic alcohols, on the sensor response and recovery time was also observed for PANI-based sensors [22]. All types of the abovementioned sensors showed reversible behavior. If we compare both polymers tested in reference [53], the authors concluded that both sensors (PPy and PANI) were able to detect the same minimum limit concentration of alcohols in the range of 3 ppm, but the response of the PANI sensor was higher for all tested alcohols. Also, the PANI sensor had the faster response time to all tested alcohols in comparison with PPy sensor. The better observed response of the PANI sensor can be probably related with the higher surface area-to-volume ratio of the nanostructures, which is manifested in the easy adsorption of the target analytes on the sensitive layer [135]. However, the PPy sensor was able to completely recover and showed a reversible behaviour for all mentioned alcohols, what was not the case of the PANI sensor. This phenomenon can be attributed to the analyte molecules, which are trapped within the interconnected structure of the sensing layer [136].

PPy nanocomposites decorated with SnO₂ and ZnO oxides [13], besides the detection of ammonia, were also used for the detection of ethanol and methanol. Unfortunately, the tested sensors did not have good response for ethanol and methanol like for ammonia. The sensitivity to 30 ppm of ammonia was about 34% in the case of a PPy/ZnO sensor and 25% in the case of a PPy/SnO₂ sensor. The best response was shown again the sensor based on PPy decorated with ZnO, namely 3% for 30 ppm of ethanol, and 1.5% for 30 ppm of methanol. The SnO₂ sensor had responses of 2.4% and 1.3% for the 30 ppm of ethanol and methanol, respectively. The ammonia in the contact with PPy can affect the intrachain conductivity in PPy macromolecules, whereas alcohols, such as methanol and ethanol, can only influence the interchain conductivity process [137]. The authors claimed that the contribution of the intrachain conductivity to the total conductivity of a conducting polymer is much higher than that of the interchain conductivity. Therefore the sensors' response is expected to be much greater in the presence of ammonia than that of alcohols.

In the work of Huang and colleagues a sensor was made by a combination of ZnO nanoparticles with mean size of 28 nm and 20 wt% of PANI and tested in the detection of various alcohols and ketones [12]. The sensor showed response times to methanol, ethanol and acetone within 148, 32 and 49 s, respectively, and recovery times within 118, 109 and 160 s, respectively, at an operating temperature of 90 °C. As expected, according to our previous explanation about the influence of the alcohol chain length on the sensitivity, the sensor showed a higher response to ethanol than to methanol. This response to ethanol was also higher than to acetone.

Lee et al. have developed a PPy-based nanostructured sensor combined with gold, which serves as a source for localized surface plasmon resonance (SPR) [10]. Beside the common experimental set-up parts used for chemiresistive gas sensors such as a gas chamber and mass flow controller, their set-up requires in addition a spectrometer and an optical probe which sends the light vertically to the Au-PPy nanorods. The absorbed light was then sent back to the spectrometer through a light detector. The authors tested the detection of three different analytes, namely benzene, toluene and acetic acid. The baseline for the adsorption spectrum was obtained with N₂. This sensor was able to detect 10 ppm of mentioned VOC, The response and recovery time were 20 and 40 s, respectively.

PPy structures behave as semiconductor materials thus they can be used for the creation of electrical devices which do not need to work by a chemiresistive transduction mechanism. The PPy as p-type semiconducting polymers with a metal contact can form Schottky barriers. Campos et al. presented Schottky barrier devices with heterojunctions between p-doped PPy and n-doped silicon [131]. They used electrochemically polymerized PPy films with thicknesses in the range of 86 to 1140 nm, which were grown on n-silicon working electrodes. The structures were used for the measurements of current density-voltage characteristics (J-V), checking of Schottky barrier diode behavior, capacitance-voltage (C-V) and frequency characteristics of the heterojunction. The measurements were observed under the exposure to air and 10 ppm of acetone. The measurement was based on calculation of current density according to the following equation:

$$J = J_0 \cdot \exp\left(\frac{qV}{nkT}\right), \quad (5)$$

where J_0 is saturation current density, n is the ideality factor or quality factor, V is the applied voltage, k is the Boltzmann's constant, q is the electronic charge, and T is the absolute temperature). From the J-V plot, authors observed the changes of the saturation current density from 3.5×10^{-6} A/cm² to 2.9×10^{-6} A/cm², the ideality factor from 2.3 to 2.1, and the rectification ratio from 4205 to 4370, during the exposure to air and acetone, respectively. The capacitance measurements confirmed the decrease of the saturation current density and an increase in the rectification ratio due to acetone vapor exposure. The PPy/silicon p-n heterojunction behaves as a gas sensor for the detection of 10 ppm of acetone, and the changes of the measured parameters depend on the thickness of the PPy layer.

In other work Campos et al., developed an electrical device for the detection of methanol based on Al/PPy/Au diodes functionalized with dodecylbenzene sulfonic acid (DBSA) [130]. The PPy/DBSA films were prepared via chemical oxidation, where gold and aluminum electrodes were vacuum deposited on the opposite sides of the film. The same as in previous work, the experiments were performed via J-V characteristics and C-V measurements under exposure to nitrogen and methanol, respectively. Therefore, from the changes in the Schottky barrier height and in the carrier concentration of the diodes, which were confirmed by C-V measurements explained that Al/PPy/Au structures are sensitive to 20 ppm of methanol after 10 minutes of exposure. The system needed 6 h to recover.

Impedance measurement at various frequencies could be used for making more selective sensors. Musio et al. designed and constructed PPy-based sensor on patterned electrodes to probe this method [103]. They studied impedance responses to 200 ppm of four different vapours: methanol, acetone, ethyl acetate and ethanol. The sensor was split into resistive and capacitive parts. Both parts were processed into patterns at different frequencies. Impedance was mostly linear, therefore the resistance pattern had no evident frequency dependence but capacitive patterns showed selective detection of ethanol and methanol at low frequencies.

Table 7. Overview of different nanomaterials used as active layers for detection of other gases and VOC.

| Type of Material | Target Analytes | LOD | Response Time/Recovery Time | Operative Temperature | Transducing Mechanism | Ref. |
|--|-----------------|--------------|-----------------------------|-----------------------|-----------------------|-------|
| Mixed WO ₃ -SnO ₂ nanostructures | Ethanol | 0.131 ppm | ~225 s/~300 s for 180 ppm | 300 °C | Chemiresistive | [128] |
| Crystalline/amorphous core/shell MoO ₃ nanocomposite | Ethanol | 10 ppm | <40 s/<40 s | 180 °C | Chemiresistive | [138] |
| MoO ₃ /WO ₃ composite nanostructures | Ethanol | 0.5 ppm | ~13 s/~10 s | 320 °C | Chemiresistive | [139] |
| SnO ₂ -Pd-Pt-In ₂ O ₃ composite | Methanol | 0.1 ppm | ~32 s/~47 s for 100 ppm | 160 °C | Chemiresistive | [140] |
| Porous In ₂ O ₃ nanobelts | Methanol | 0.1 ppm | ~10 s/~10 s for 20 ppm | 370 °C | Chemiresistive | [141] |
| SnO ₂ -ZnO composite nanofibers | Methanol | 1 ppm tested | ~20 s/~40 s for 10 ppm | 350 °C | Chemiresistive | [142] |

A better approach on the sensor response was demonstrated by Bhatt and Jampana by measuring the changes in its capacitance, resistance and the dissipation factor upon exposure to organic volatiles such as acetone, ethanol and isopropyl alcohol [102]. An interdigitated structure with gold electrodes 20 µm wide and 10 µm spaced with electrochemically deposited PPy was tested at range of 10 Hz to 2 MHz. They showed that the dissipation factor (DF), which is a ratio of the resistive and absolute value of the reactive component of impedance, presents peaks at several frequencies corresponding to the resonance frequencies of molecules binding to the PPy. The measurement was provided at high concentration from 10.000 ppm but presented a processing method that is promising to discriminate between chemicals. The magnitude of the dissipation factor was found to be linearly dependent on the VOC concentration. An overview of the sensors based on the other nanomaterials used for detection of VOC and gases is listed in the Table 7. According to the literature overview reported in this table, we can notice that metal oxide-based sensors are able to detect lower concentrations of ethanol and methanol than PPy-based sensors. However, the metal oxide sensors require the quite high operating temperature (180–350 °C). In the case of ethanol, multidimensional PPy nanotubes have the lowest LOD (1 ppm) [113] among the CP group, but considering the metal oxide sensors, MoO₃/WO₃ composite nanostructures gave a response to 0.1 ppm of ethanol [139]. On the other hand, the best response time/recovery time is noticed for multidimensional PPy nanotubes (<1 s/4–5 s) [113], so we can conclude this sensor is the fastest one among the sensors described in this work. In the case of methanol, the best results are observed for the sensor based on porous In₂O₃ nanobelts, where the LOD was 0.1 ppm and response time/recovery time were approximately about 10 s/10 s for 20 ppm of methanol [101].

4.3. Detection of Humidity

Beside the detection of the gases and VOCs mentioned above, researchers have found applications of PPy-based sensors for humidity detection [143]. Indeed, the sensitivity to humidity (water vapour) is a very important parameter because it is the most significant interfering vapour. Some works focused on the relative humidity sensing are briefly presented in the following paragraphs. Joulazadeh et al. studied the humidity sensing performances for the previously described PPy nanostructures synthesized via anhydrous FeCl₃ and methyl orange [64]. The tubular morphology of PPy nanostructures showed positive changes of the resistance ($R > R_0$) for a low humidity concentration (25 ppm of water vapour), and negative changes ($R < R_0$) for higher concentrations (56 ppm of water vapour). The authors explained that the increasing and decreasing resistance for different concentrations of humidity for PPy is affected by proton exchanges between the water molecules and the polymer NH₂⁺ groups and by the swelling effect of the polymer chains. The same behaviour is

expected for PANI-based sensors [144,145]. The increase in resistance at lower concentrations can be explained by the greater distances in interchain connectivity of the polymer network [9]. The proton transfer between the water molecules and NH_2^+ is not feasible due to the swelling phenomenon of polymer chains which increases the distance between the chains. In the case of the higher humidity concentration, the resistance increases at the beginning which is related with effect above described, but at one point it started to decrease, as a consequence of water molecules absorbed on the surface of the polymer, enabling the transfer of protons.

Lin et al. used impedance sensors for the measurement of humidity [146]. The analysis was based on measurement of resistance and capacitance by an AC voltage with an amplitude of 1 V. The response time or recovery time are defined as the times required for the impedance of a sensor to change by 90% of the total impedance. The sensitive layer of the sensor was based on different amounts of graphene composited with PPy structures, where polymerization of the PPy layer is done via chemical oxidation. The authors checked the impedance values versus relative humidity (RH), where the samples were exposed to RH in the range from 12% to 90%. The humidity sensitivity is defined as:

$$S = \frac{R_d}{R_h} \quad (6)$$

where R_d and R_h were the impedance at 12% RH and at 90% RH, respectively. PPy sensitivity to RH is poor with an impedance in range $2\text{--}2.5 \times 10^7 \Omega$, where the sensitivity is 60 at 90% RH. The sensor made from 10% graphene/PPy showed the greatest sensitivity to humidity ($S = 138$ at 90% RH). On the other hand, this structure had an efficient response time and recovery time, 15 s as the RH was increased 12%–70%, and 20 s as RH decreased from 70% to 12%, respectively. This response time and recovery time were shorter in comparison with those reported in the works of Joulazadeh et al. [143], where the response time was 41 s when the RH changed from 11% to 95%, and the recovery time was 120 for RH changes from 95% to 11% RH. The authors suggested the potential application of graphene/PPy composite in the fabrication of high-performance humidity sensors.

The work of Yang et al. presented a MEMS helix interdigitated electrode chemically coated by PPy with grain diameters of about 0.3–0.5 μm making the film porous [147]. CMOS electronics integrated within the MEMS structure form a ring oscillator as the sensing circuits. Capacitance changes are transduced to frequency. The work presents a logarithmic dependency of frequency on RH in the range 32 MHz/80%RH to 38.5 MHz/25%RH and sensitivity 99 kHz/%RH at 25 °C. Temperature dependency was also demonstrated, decreasing to 32 kHz/%RH at 75 °C.

5. Conclusions

In this review, we have described the synthesis of PPy-based ammonia and VOC sensors in detail and compared their sensing effectivity with other CP, primarily with PANI, as well as with other well-known gas sensing materials such as metal oxides. We showed all necessary synthesis parameters together with the type of reactants such as a polymer precursor and an oxidant agent for a successful preparation of polymer sensing layer. We explained the uniformity and homogeneity of polymer nanostructures depend strongly on the type of synthesis, eventually application of template, which ensures the ordering of polymer nanostructures. According to our literature survey, the majority of research works were devoted to the electrochemical synthesis approach combined with various templates.

The prepared polymer nanostructures can be of different shapes such as nanoparticles, nanorods, nanowires, nanotubes, nanoplates, nanoribbons, etc. Concerning the nanostructure size, one can conclude the smaller size can provide increased surface to volume ratio, i.e., higher active surface area and thus higher sensitivity. However, the recovery time of a sensor with smaller size of nanostructures was found to be longer than in the case of bigger polymer structures. Beside polymer size and morphology, its functionalization with various nanosized materials like noble metals, metal oxides

and different types of carbon was found to have a crucial effect on the final sensitivity and usually resulted in enhanced sensor performance.

It is obvious that the overall polymer morphology has also a significant influence on the sensitivity performance as we showed in few summarizing tables: the lowest LOD in the ppb level was found for single crystal PPy nanotube sensors for ammonia. This LOD meets the requirement for practical sensor applications in the analysis of human breath and disease diagnostics. Such a low detectable concentration of ammonia was not achieved with metal oxide-based gas sensors, where the best LOD was found to be 0.2 ppm for a Co_3O_4 nanostructured sensor working at room temperature, and V_2O_5 sensors operating at temperature of 350 °C. Beside the sensitivity as a key parameter representing the sensor efficiency, one has also to take into account the sensor response and recovery time. We can conclude that performance of PPy-based sensors in the case of ammonia detection is really enticing since their fastest response and recovery times are found to be less than 1 s and 2 s, respectively, for 5 ppm of ammonia. In the case of alcohol sensing, the lowest LOD was found to be 1 ppm for ethanol using a chemiresistive sensor with PPy nanotubes and 1 ppm for methanol using a PPy-coated quartz fiber optical sensor. These limits of detection were 10× surpassed with metal oxide based sensors, where the lowest concentration of 0.1 ppm was detected for methanol and ethanol using sensing layers fabricated from composites of SnO_2 , WO_3 and In_2O_3 .

The review showed that gas and VOC sensors based on PPy working on a chemiresistive transducing principle have received much more attention than the other ones. PPy sensors were most frequently tested for the detection of ammonia and several type of alcohols. In general, the PPy sensor response was higher to ammonia than to other gases and VOC. This is due to the electron-donating behavior of ammonia and its high affinity to the PPy structure. This observation indicates the future perspectives in the application of this sensor and can further expand the research focus towards detection of other electron-donating molecules which have not been sufficiently studied so far.

Even though CP-based sensors can be tailored for particular properties, easily processed and selected to be inert in the environment containing the analyte, still there are some remaining challenges which have to be addressed. The main drawback of these sensors lies in their irreversibility which is believed to be caused by nucleophilic attack of the analytes on the carbon backbone. The other disadvantage is a short sensor lifetime. The sensing properties of CP-based sensors as well as the other sensors are significantly influenced by the ambient conditions, such as temperature and humidity. In addition, a swelling effect usually occurs in CP layers, which can cause electrical resistance changes in chemiresistive sensors. Therefore, in order to successfully make use of CP-based gas and VOC sensors in medical applications, the development of the sensor market has to aim at emerging technologies employing smart and cheap flexible sensors with long-term stability of the sensing material.

Acknowledgments: Research described in this paper was financed by Czech Ministry of Education in the frame of National Sustainability Program under grant LO1401. For research, infrastructure of the SIX Center was used.

Author Contributions: All authors contributed equally to write this review.

Conflicts of Interest: The authors declare no conflict of interest.

References

1. Haick, H.; Cohen-Kaminsky, S. Detecting Lung infections in breathprints: Empty promise or next generation diagnosis of infections. *Eur. Respir. J.* **2015**, *45*, 21–24. [[CrossRef](#)] [[PubMed](#)]
2. Van de Kant, K.D.G.; van der Sande, L.; Jobsis, Q.; van Schayck, O.C.P.; Dompeling, E. Clinical use of exhaled volatile organic compounds in pulmonary diseases: A systematic review. *Respir. Res.* **2012**, *13*, 1–23. [[CrossRef](#)] [[PubMed](#)]
3. Broza, Y.Y.; Mochalski, P.; Ruzsanyi, V.; Amann, A.; Haick, H. Hybrid Volatolomics and Disease Detection. *Angew. Chem. Int. Ed.* **2015**, *54*, 11036–11048. [[CrossRef](#)] [[PubMed](#)]
4. Broza, Y.Y.; Haick, H. Nanomaterial-based sensors for detection of disease by volatile organic compounds. *Nanomedicine* **2013**, *8*, 785–806. [[CrossRef](#)] [[PubMed](#)]

5. Konvalina, G.; Haick, H. Sensors for Breath Testing: From Nanomaterials to Comprehensive Disease Detection. *Acc. Chem. Res.* **2014**, *47*, 66–76. [[CrossRef](#)] [[PubMed](#)]
6. Peng, G.; Tisch, U.; Adams, O.; Hakim, M.; Shehada, N.; Broza, Y.Y.; Billan, S.; Abdah-Bortnyak, R.; Kuten, A.; Haick, H. Diagnosing lung cancer in exhaled breath using gold nanoparticles. *Nat. Nanotechnol.* **2009**, *4*, 669–673. [[CrossRef](#)] [[PubMed](#)]
7. Vallejos, S.; Gràcia, I.; Bravo, J.; Figueras, E.; Hubálek, J.; Cané, C. Detection of volatile organic compounds using flexible gas sensing devices based on tungsten oxide nanostructures functionalized with Au and Pt nanoparticles. *Talanta* **2015**, *139*, 27–34. [[CrossRef](#)] [[PubMed](#)]
8. Choudhury, A. Polyaniline/silver nanocomposites: Dielectric properties and ethanol vapour sensitivity. *Sens. Actuators B Chem.* **2009**, *138*, 318–325. [[CrossRef](#)]
9. Kabir, L.; Mandal, A.R.; Mandal, S.K. Humidity-sensing properties of conducting polypyrrole-silver nanocomposites. *J. Exp. Nanosci.* **2008**, *3*, 297–305. [[CrossRef](#)]
10. Lee, J.-S.; Yoon, N.-R.; Kang, B.-H.; Lee, S.-W.; Gopalan, S.-A.; Kim, S.-W.; Lee, S.-H.; Kwon, D.-H.; Kang, S.-W. Au-Polypyrrole Framework Nanostructures for Improved Localized Surface Plasmon Resonance Volatile Organic Compounds Gas Sensing. *J. Nanosci. Nanotechnol.* **2015**, *15*, 7738–7742. [[CrossRef](#)] [[PubMed](#)]
11. Athawale, A.A.; Bhagwat, S.V.; Katre, P.P. Nanocomposite of Pd-polyaniline as a selective methanol sensor. *Sens. Actuators B Chem.* **2006**, *114*, 263–267. [[CrossRef](#)]
12. Huang, J.; Yang, T.L.; Kang, Y.F.; Wang, Y.; Wang, S.R. Gas sensing performance of polyaniline/ZnO organic-inorganic hybrids for detecting VOCs at low temperature. *J. Nat. Gas Chem.* **2011**, *20*, 515–519. [[CrossRef](#)]
13. Joulazadeh, M.; Navarchian, A.H. Ammonia detection of one-dimensional nano-structured polypyrrole/metal oxide nanocomposites sensors. *Synth. Met.* **2015**, *210*, 404–411. [[CrossRef](#)]
14. Bachhav, S.G.; Patil, D.R. Study of Polypyrrole-Coated MWCNT Nanocomposites for Ammonia Sensing at Room Temperature. *J. Mater. Sci. Chem. Eng.* **2015**, *3*, 30–44. [[CrossRef](#)]
15. Daneshkhah, A.; Shrestha, S.; Agarwal, M.; Varahramyan, K. Poly(vinylidene fluoride-hexafluoropropylene) composite sensors for volatile organic compounds detection in breath. *Sens. Actuators B Chem.* **2015**, *221*, 635–643. [[CrossRef](#)]
16. Tung, T.T.; Castro, M.; Pillin, I.; Kim, T.Y.; Suh, K.S.; Feller, J.F. Graphene-Fe₃O₄/PIL-PEDOT for the design of sensitive and stable quantum chemo-resistive VOC sensors. *Carbon* **2014**, *74*, 104–112. [[CrossRef](#)]
17. Feng, X.M.; Yan, Z.Z.; Li, R.M.; Liu, X.F.; Hou, W.H. The synthesis of shape-controlled polypyrrole/graphene and the study of its capacitance properties. *Polym. Bull.* **2013**, *70*, 2291–2304. [[CrossRef](#)]
18. Yoon, H. Current Trends in Sensors Based on Conducting Polymer Nanomaterials. *Nanomaterials* **2013**, *3*, 524–549. [[CrossRef](#)]
19. Janata, J.; Josowicz, M. Conducting polymers in electronic chemical sensors. *Nat. Mater.* **2003**, *2*, 19–24. [[CrossRef](#)] [[PubMed](#)]
20. Guernion, N.; Ewen, R.J.; Pihlainen, K.; Ratcliffe, N.M.; Teare, G.C. The fabrication and characterisation of a highly sensitive polypyrrole sensor and its electrical responses to amines of differing basicity at high humidities. *Synth. Metals* **2002**, *126*, 301–310. [[CrossRef](#)]
21. Zhang, L.; Meng, F.; Chen, Y.; Liu, J.; Sun, Y.; Luo, T.; Li, M.; Liu, J. A novel ammonia sensor based on high density, small diameter polypyrrole nanowire arrays. *Sens. Actuators B Chem.* **2009**, *142*, 204–209. [[CrossRef](#)]
22. Athawale, A.A.; Kulkarni, M.V. Polyaniline and its substituted derivatives as sensor for aliphatic alcohols. *Sens. Actuators B Chem.* **2000**, *67*, 173–177. [[CrossRef](#)]
23. Kim, J.-S.; Sohn, S.-O.; Huh, J.-S. Fabrication and sensing behavior of PVF2 coated-polyaniline sensor for volatile organic compounds. *Sens. Actuators B Chem.* **2005**, *108*, 409–413. [[CrossRef](#)]
24. Eaidkong, T.; Mungkarndee, R.; Phollookin, C.; Tumcharern, G.; Sukwattanasinitt, M.; Wacharasindhu, S. Polydiacetylene paper-based colorimetric sensor array for vapor phase detection and identification of volatile organic compounds. *J. Mater. Chem.* **2012**, *22*, 5970–5977. [[CrossRef](#)]
25. Yoon, J.; Chae, S.K.; Kim, J.M. Colorimetric sensors for volatile organic compounds (VOCs) based on conjugated polymer-embedded electrospun fibers. *J. Am. Chem. Soc.* **2007**, *129*, 3038–3039. [[CrossRef](#)] [[PubMed](#)]
26. Kim, T.; Kwak, D. Flexible VOC Sensors Using Conductive Polymers and Porous Membranes for Application to Textiles. *Fibers Polym.* **2012**, *13*, 471–474. [[CrossRef](#)]

27. Park, E.; Kwon, O.S.; Park, S.J.; Lee, J.S.; You, S.; Jang, J. One-pot synthesis of silver nanoparticles decorated poly(3,4-ethylenedioxythiophene) nanotubes for chemical sensor application. *J. Mater. Chem.* **2012**, *22*, 1521–1526. [[CrossRef](#)]
28. Arena, A.; Donato, N.; Saitta, G.; Bonavita, A.; Rizzo, G.; Neri, G. Flexible ethanol sensors on glossy paper substrates operating at room temperature. *Sens. Actuators B Chem.* **2010**, *145*, 488–494. [[CrossRef](#)]
29. Sarfraz, J.; Ihalainen, P.; Maattanen, A.; Peltonen, J.; Linden, M. Printed hydrogen sulfide gas sensor on paper substrate based on polyaniline composite. *Thin Solid Films* **2013**, *534*, 621–628. [[CrossRef](#)]
30. Lee, C.T.; Lee, H.Y.; Chiu, Y.S. Performance Improvement of Nitrogen Oxide Gas Sensors Using Au Catalytic Metal on SnO₂/WO₃ Complex Nanoparticle Sensing Layer. *IEEE Sens. J.* **2016**, *16*, 7581–7585. [[CrossRef](#)]
31. Karmaoui, M.; Leonardi, S.G.; Latino, M.; Tobaldi, D.M.; Donato, N.; Pullar, R.C.; Seabra, M.P.; Labrincha, J.A.; Neri, G. Pt-decorated In₂O₃ nanoparticles and their ability as a highly sensitive (<10 ppb) acetone sensor for biomedical applications. *Sens. Actuators B Chem.* **2016**, *230*, 697–705.
32. Bamsaoud, S.F.; Rane, S.B.; Karekar, R.N.; Aiyer, R.C. Nano particulate SnO₂ based resistive films as a hydrogen and acetone vapour sensor. *Sens. Actuators B Chem.* **2011**, *153*, 382–391. [[CrossRef](#)]
33. Tharsika, T.; Haseeb, A.; Akbar, S.A.; Sabri, M.F.M.; Hoong, W.Y. Enhanced Ethanol Gas Sensing Properties of SnO₂-Core/ZnO-Shell Nanostructures. *Sensors* **2014**, *14*, 14586–14600. [[CrossRef](#)] [[PubMed](#)]
34. Righettoni, M.; Tricoli, A.; Pratsinis, S.E. Si:WO₃ Sensors for Highly Selective Detection of Acetone for Easy Diagnosis of Diabetes by Breath Analysis. *Anal. Chem.* **2010**, *82*, 3581–3587. [[CrossRef](#)] [[PubMed](#)]
35. Singh, S.; Kaur, H.; Singh, V.N.; Jain, K.; Senguttuvan, T.D. Highly sensitive and pulse-like response toward ethanol of Nb doped TiO₂ nanorods based gas sensors. *Sens. Actuators B Chem.* **2012**, *171–172*, 899–906. [[CrossRef](#)]
36. Geng, L.; Wu, S. Preparation, characterization and gas sensitivity of polypyrrole/ γ -Fe₂O₃ hybrid materials. *Mater. Res. Bull.* **2013**, *48*, 4339–4343. [[CrossRef](#)]
37. Hamilton, S.; Hopher, M.J.; Sommerville, J. Polypyrrole materials for detection and discrimination of volatile organic compounds. *Sens. Actuators B Chem.* **2005**, *107*, 424–432. [[CrossRef](#)]
38. Bhat, N.V.; Gadre, A.P.; Bambole, V.A. Structural, mechanical, and electrical properties of electropolymerized polypyrrole composite films. *J. Appl. Polym. Sci.* **2001**, *80*, 2511–2517. [[CrossRef](#)]
39. Lee, S.; Cho, M.S.; Nam, J.D.; Lee, Y. Fabrication of Polypyrrole Nanorod Arrays for Supercapacitor: Effect of Length of Nanorods on Capacitance. *J. Nanosci. Nanotechnol.* **2008**, *8*, 5036–5041. [[CrossRef](#)] [[PubMed](#)]
40. Sun, Y.F.; Liu, S.B.; Meng, F.L.; Liu, J.Y.; Jin, Z.; Kong, L.T.; Liu, J.H. Metal Oxide Nanostructures and Their Gas Sensing Properties: A Review. *Sensors* **2012**, *12*, 2610–2631. [[CrossRef](#)] [[PubMed](#)]
41. Yoon, H.; Jang, J. Conducting-Polymer Nanomaterials for High-Performance Sensor Applications: Issues and Challenges. *Adv. Funct. Mater.* **2009**, *19*, 1567–1576. [[CrossRef](#)]
42. Hatchett, D.W.; Josowicz, M. Composites of intrinsically conducting polymers as sensing nanomaterials. *Chem. Rev.* **2008**, *108*, 746–769. [[CrossRef](#)] [[PubMed](#)]
43. Liu, X.; Cheng, S.; Liu, H.; Hu, S.; Zhang, D.; Ning, H. A Survey on Gas Sensing Technology. *Sensors* **2012**, *12*, 9635–9665. [[CrossRef](#)] [[PubMed](#)]
44. Song, H.K.; Palmore, G.T.R. Redox-active polypyrrole: Toward polymer-based batteries. *Adv. Mater.* **2006**, *18*, 1764–1768. [[CrossRef](#)]
45. Ehsani, A.; Jaleh, B.; Nasrollahzadeh, M. Electrochemical properties and electrocatalytic activity of conducting polymer/copper nanoparticles supported on reduced graphene oxide composite. *J. Power Sources* **2014**, *257*, 300–307. [[CrossRef](#)]
46. Wei, W.F.; Cui, X.W.; Chen, W.X.; Ivey, D.G. Manganese oxide-based materials as electrochemical supercapacitor electrodes. *Chem. Soc. Rev.* **2011**, *40*, 1697–1721. [[CrossRef](#)] [[PubMed](#)]
47. Wang, N.; Zhao, P.; Liang, K.; Yao, M.; Yang, Y.; Hu, W. CVD-grown polypyrrole nanofilms on highly mesoporous structure MnO₂ for high performance asymmetric supercapacitors. *Chem. Eng. J.* **2017**, *307*, 105–112. [[CrossRef](#)]
48. Wu, X.; Wang, Q.; Zhang, W.; Wang, Y.; Chen, W. Nanorod structure of Polypyrrole-covered MoO₃ for supercapacitors with excellent cycling stability. *Mater. Lett.* **2016**, *182*, 121–124. [[CrossRef](#)]
49. Liu, C.; Cai, Z.; Zhao, Y.; Zhao, H.; Ge, F. Potentiostatically synthesized flexible polypyrrole/multi-wall carbon nanotube/cotton fabric electrodes for supercapacitors. *Cellulose* **2016**, *23*, 637–648. [[CrossRef](#)]

50. Liu, Y.; Zhou, J.; Tang, J.; Tang, W.H. Three-Dimensional, Chemically Bonded Polypyrrole/Bacterial Cellulose/Graphene Composites for High-Performance Supercapacitors. *Chem. Mater.* **2015**, *27*, 7034–7041. [[CrossRef](#)]
51. Wang, Z.B.; Zhang, C.L.; Xu, C.Q.; Zhu, Z.H.; Chen, C.N. Hollow polypyrrole nanosphere embedded in nitrogen-doped graphene layers to obtain a three-dimensional nanostructure as electrode material for electrochemical supercapacitor. *Ionics* **2017**, *23*, 147–156. [[CrossRef](#)]
52. Rao, V.; Praveen, P.; Latha, D. A novel method for synthesis of polypyrrole grafted chitin. *J. Polym. Res.* **2016**, *23*, 6. [[CrossRef](#)]
53. Joulazadeh, M.; Navarchian, A.H. Alcohol Sensibility of One-Dimensional Polyaniline and Polypyrrole Nanostructures. *IEEE Sens. J.* **2015**, *15*, 1697–1704. [[CrossRef](#)]
54. Jang, J.; Bae, J. Carbon nanofiber/polypyrrole nanocable as toxic gas sensor. *Sens. Actuator B Chem.* **2007**, *122*, 7–13. [[CrossRef](#)]
55. Basavaraja, C.; Kim, W.J.; Kim, D.G.; Huh, D.S. Synthesis and characterization of soluble polypyrrole-poly(epsilon-caprolactone) polymer blends with improved electrical conductivities. *Mater. Chem. Phys.* **2011**, *129*, 787–793. [[CrossRef](#)]
56. Tu, J.C.; Li, N.; Yuan, Q.; Wang, R.; Geng, W.C.; Li, Y.J.; Zhang, T.; Li, X.T. Humidity-sensitive property of Fe²⁺ doped polypyrrole. *Synth. Metals* **2009**, *159*, 2469–2473. [[CrossRef](#)]
57. Kang, H.C.; Geckeler, K.E. Enhanced electrical conductivity of polypyrrole prepared by chemical oxidative polymerization: Effect of the preparation technique and polymer additive. *Polymer* **2000**, *41*, 6931–6934. [[CrossRef](#)]
58. Kwon, O.S.; Hong, J.Y.; Park, S.J.; Jang, Y.; Jang, J. Resistive Gas Sensors Based on Precisely Size-Controlled Polypyrrole Nanoparticles: Effects of Particle Size and Deposition Method. *J. Phys. Chem. C* **2010**, *114*, 18874–18879. [[CrossRef](#)]
59. Hong, J.Y.; Yoon, H.; Jang, J. Kinetic Study of the Formation of Polypyrrole Nanoparticles in Water-Soluble Polymer/Metal Cation Systems: A Light-Scattering Analysis. *Small* **2010**, *6*, 679–686. [[CrossRef](#)] [[PubMed](#)]
60. Hernandez, S.C.; Chaudhuri, D.; Chen, W.; Myung, N.V.; Mulchandani, A. Single polypyrrole nanowire ammonia gas sensor. *Electroanalysis* **2007**, *19*, 2125–2130. [[CrossRef](#)]
61. Dubal, D.P.; Lee, S.H.; Kim, J.G.; Kim, W.B.; Lokhande, C.D. Porous polypyrrole clusters prepared by electropolymerization for a high performance supercapacitor. *J. Mater. Chem.* **2012**, *22*, 3044–3052. [[CrossRef](#)]
62. Chartuprayoon, N.; Hangarter, C.M.; Rheem, Y.; Jung, H.; Myung, N.V. Wafer-Scale Fabrication of Single Polypyrrole Nanoribbon-Based Ammonia Sensor. *J. Phys. Chem. C* **2010**, *114*, 11103–11108. [[CrossRef](#)]
63. Yang, X.M.; Zhu, Z.X.; Dai, T.Y.; Lu, Y. Facile fabrication of functional polypyrrole nanotubes via a reactive self-degraded template. *Macromol. Rapid Commun.* **2005**, *26*, 1736–1740. [[CrossRef](#)]
64. Joulazadeh, M.; Navarchian, A.H.; Niroomand, M. A Comparative Study on Humidity Sensing Performances of Polyaniline and Polypyrrole Nanostructures. *Adv. Polym. Technol.* **2014**, *33*. [[CrossRef](#)]
65. Dubal, D.P.; Caban-Huertas, Z.; Holze, R.; Gomez-Romero, P. Growth of polypyrrole nanostructures through reactive templates for energy storage applications. *Electrochim. Acta* **2016**, *191*, 346–354. [[CrossRef](#)]
66. Guo, Y.B.; Tang, Q.X.; Liu, H.B.; Zhang, Y.J.; Li, Y.L.; Hu, W.P.; Wang, S.; Zhu, D.B. Light-controlled organic/inorganic P-N junction nanowires. *J. Am. Chem. Soc.* **2008**, *130*, 9198. [[CrossRef](#)] [[PubMed](#)]
67. Sankir, N.D.; Dogan, B. Investigation of structural and optical properties of the CdS and CdS/PPy nanowires. *J. Mater. Sci.* **2010**, *45*, 6424–6432. [[CrossRef](#)]
68. Chitte, H.K.; Bhat, N.V.; Gore, A.V.; Shinde, G.N. Synthesis of Polypyrrole Using Ammonium Peroxy Disulfate (APS) as Oxidant Together with Some Dopants for Use in Gas Sensors. *Mater. Sci. Appl.* **2011**, *2*, 1491–1498. [[CrossRef](#)]
69. Chitte, H.K.; Bhat, N.V.; Walunj, V.E.; Shinde, G.N. Synthesis of Polypyrrole Using Ferric Chloride (FeCl₃) as Oxidant Together with Some Dopants for Use in Gas Sensors. *J. Sens. Technol.* **2011**, *1*, 47–56. [[CrossRef](#)]
70. Kim, J.; Sohn, D.; Sung, Y.; Kim, E.-R. Fabrication and characterization of conductive polypyrrole thin film prepared by in situ vapor-phase polymerization. *Synth. Met.* **2003**, *132*, 309–313. [[CrossRef](#)]
71. Jia, H.; Wang, J.; Zhang, X.; Wang, Y. Pen-Writing Polypyrrole Arrays on Paper for Versatile Cheap Sensors. *ACS Macro Lett.* **2014**, *3*, 86–90. [[CrossRef](#)]
72. Liana, D.D.; Raguse, B.; Gooding, J.J.; Chow, E. Recent Advances in Paper-Based Sensors. *Sensors* **2012**, *12*, 11505–11526. [[CrossRef](#)] [[PubMed](#)]

73. Cunningham, J.C.; DeGregory, P.R.; Crooks, R.M. New Functionalities for Paper-Based Sensors Lead to Simplified User Operation, Lower Limits of Detection, and New Applications. In *Annual Review of Analytical Chemistry*; Bohn, P.W., Pemberton, J.E., Eds.; Annual Reviews: Palo Alto, CA, USA, 2016; Volume 9, pp. 183–202.
74. Steffens, C.; Manzoli, A.; Francheschi, E.; Corazza, M.L.; Corazza, F.C.; Oliveira, J.V.; Herrmann, P.S.P. Low-cost sensors developed on paper by line patterning with graphite and polyaniline coating with supercritical CO₂. *Synth. Metals* **2009**, *159*, 2329–2332. [[CrossRef](#)]
75. Sarfraz, J.; Tobjork, D.; Osterbacka, R.; Linden, M. Low-Cost Hydrogen Sulfide Gas Sensor on Paper Substrates: Fabrication and Demonstration. *IEEE Sens. J.* **2012**, *12*, 1973–1978. [[CrossRef](#)]
76. Mousavi, S.; Kang, K.; Park, J.; Park, I. Polyaniline-polystyrene nanofibers directly written on cheap flexible substrates by electrospinning, a low-cost and sensitive hydrogen sulfide gas sensor. In Proceedings of the 2016 IEEE 29th International Conference on Micro Electro Mechanical Systems (MEMS), Shanghai, China, 24–28 January 2016; pp. 917–919.
77. Huang, L.H.; Jiang, P.; Wang, D.; Luo, Y.F.; Li, M.F.; Lee, H.; Gerhardt, R.A. A novel paper-based flexible ammonia gas sensor via silver and SWNT-PABS inkjet printing. *Sens. Actuators B Chem.* **2014**, *197*, 308–313. [[CrossRef](#)]
78. Bai, H.; Shi, G.Q. Gas sensors based on conducting polymers. *Sensors* **2007**, *7*, 267–307. [[CrossRef](#)]
79. Patois, T.; Lakard, B.; Monney, S.; Roizard, X.; Fievet, P. Characterization of the surface properties of polypyrrole films: Influence of electrodeposition parameters. *Synth. Met.* **2011**, *161*, 2498–2505. [[CrossRef](#)]
80. Otero, T.F.; Rodríguez, J. Role of protons on the electrochemical polymerization of pyrrole from acetonitrile solutions. *J. Electroanal. Chem.* **1994**, *379*, 513–516. [[CrossRef](#)]
81. Kupila, E.L.; Kankare, J. Electropolymerization of pyrrole in aqueous solvent mixtures studied by in situ conductimetry. *Synth. Met.* **1996**, *82*, 89–95. [[CrossRef](#)]
82. Patois, T.; Lakard, B.; Martin, N.; Fievet, P. Effect of various parameters on the conductivity of free standing electrosynthesized polypyrrole films. *Synth. Met.* **2010**, *160*, 2180–2185. [[CrossRef](#)]
83. Paramo-Garcia, U.; Batina, N.; Ibanez, J.G. The Effect of pH on the Morphology of Electrochemically-grown Polypyrrole Films: An AFM Study. *Int. J. Electrochem. Sci.* **2012**, *7*, 12316–12325.
84. Nakata, M.; Taga, M.; Kise, H. Synthesis of Electrical Conductive Polypyrrole Films By Interphase Oxidative Polymerization—Effects of Polymerization Temperature and Oxidizing-Agents. *Polym. J.* **1992**, *24*, 437–441. [[CrossRef](#)]
85. Karami, H.; Nezhad, A.R. Investigation of Pulse-Electropolymerization of Conductive Polypyrrole Nanostructures. *Int. J. Electrochem. Sci.* **2013**, *8*, 8905–8921.
86. Li, C.; Bai, H.; Shi, G.Q. Conducting polymer nanomaterials: Electrosynthesis and applications. *Chem. Soc. Rev.* **2009**, *38*, 2397–2409. [[CrossRef](#)] [[PubMed](#)]
87. Babaei, M.; Alizadeh, N. Methanol selective gas sensor based on nano-structured conducting polypyrrole prepared by electrochemically on interdigital electrodes for biodiesel analysis. *Sens. Actuators B Chem.* **2013**, *183*, 617–626. [[CrossRef](#)]
88. Sadki, S.; Schottland, P.; Brodie, N.; Sabouraud, G. The mechanisms of pyrrole electropolymerization. *Chem. Soc. Rev.* **2000**, *29*, 283–293.
89. Genies, E.M.; Bidan, G.; Diaz, A.F. Spectroelectrochemical study of polypyrrole films. *J. Electroanal. Chem. Interfacial Electrochem.* **1983**, *149*, 101–113. [[CrossRef](#)]
90. Yang, C.; Liu, P.; Guo, J.; Wang, Y. Polypyrrole/vermiculite nanocomposites via self-assembling and in situ chemical oxidative polymerization. *Synth. Met.* **2010**, *160*, 592–598. [[CrossRef](#)]
91. Joshi, A.; Gangal, S.A.; Gupta, S.K. Ammonia sensing properties of polypyrrole thin films at room temperature. *Sens. Actuators B Chem.* **2011**, *156*, 938–942. [[CrossRef](#)]
92. Bahraeian, S.; Abron, K.; Pourjafarian, F.; Majid, R.A. Study on Synthesis of Polypyrrole via Chemical Polymerization Method. In Proceedings of the 2nd International Conference on Sustainable Materials, Penang, Malaysia, 26–27 March 2013; pp. 707–710.
93. Yeole, B.; Sen, T.; Hansora, D.P.; Mishra, S. Effect of electrical properties on gas sensitivity of polypyrrole/cds nanocomposites. *J. Appl. Polym. Sci.* **2015**, *132*. [[CrossRef](#)]
94. Sanches, E.A.; Alves, S.F.; Soares, J.C.; da Silva, A.M.; da Silva, C.G.; de Souza, S.M.; da Frota, H.O. Nanostructured Polypyrrole Powder: A Structural and Morphological Characterization. *J. Nanomater.* **2015**, *16*, 301. [[CrossRef](#)]

95. Rawal, I.; Kaur, A. Synthesis of mesoporous polypyrrole nanowires/nanoparticles for ammonia gas sensing application. *Sens. Actuators A Phys.* **2013**, *203*, 92–102. [[CrossRef](#)]
96. Macdiarmid, A.G.; Epstein, A.J. The Polyanilines—Potential Technology Based On New Chemistry and New Properties. In *Science and Applications of Conducting Polymers*; Salaneck, W.R., Clark, D.T., Samuelsen, E.J., Eds.; Adam Hilger Ltd.: Bristol, UK, 1991; pp. 117–127.
97. Mohammadi, A.; Hasan, M.A.; Liedberg, B.; Lundstrom, I.; Salaneck, W.R. Chemical vapor-deposition (cvd) of conducting polymers—Polypyrrole. *Synth. Met.* **1986**, *14*, 189–197. [[CrossRef](#)]
98. Hassanzadeh, N.; Omidvar, H.; Tabaian, S.H. Chemical synthesis of high density and long polypyrrole nanowire arrays using alumina membrane and their hydrogen sensing properties. *Superlattices Microstruct.* **2012**, *51*, 314–323. [[CrossRef](#)]
99. Egging, B.R. *Chemical Sensors and Biosensors*; Wiley: West Sussex, UK, 2008.
100. Hodgkinson, J.; Tatam, R.P. Optical gas sensing: A review. *Meas. Sci. Technol.* **2013**, *24*, 59. [[CrossRef](#)]
101. Rheume, J.M.; Pisano, A.P. A review of recent progress in sensing of gas concentration by impedance change. *Ionics* **2011**, *17*, 99–108. [[CrossRef](#)]
102. Bhatt, C.M.; Jampana, N. Multi frequency interrogation of polypyrrole based gas sensors for organic vapors. *Microsyst. Technol. Micro Nanosyst. Inf. Storage Process. Syst.* **2011**, *17*, 417–423. [[CrossRef](#)]
103. Musio, F.; Ferrara, M.C. Low frequency A.C. response of polypyrrole gas sensors. *Sens. Actuators B Chem.* **1997**, *41*, 97–103. [[CrossRef](#)]
104. Trojanowicz, M. Application of conducting polymers in chemical analysis. *Microchim. Acta* **2003**, *143*, 75–91. [[CrossRef](#)]
105. Brahim, S.; Wilson, A.M.; Narinesingh, D.; Iwuoha, E.; Guiseppi-Elie, A. Chemical and Biological Sensors Based on Electrochemical Detection Using Conducting Electroactive Polymers. *Microchim. Acta* **2003**, *143*, 123–137. [[CrossRef](#)]
106. Bazzaoui, M.; Martins, J.I.; Machnikova, E.; Bazzaoui, E.A.; Martins, L. Polypyrrole films electrosynthesized on stainless steel grid from saccharinate aqueous solution and its behaviour toward acetone vapor. *Eur. Polym. J.* **2007**, *43*, 1347–1358. [[CrossRef](#)]
107. Bhat, N.V.; Gadre, A.P.; Bambole, V.A. Investigation of electropolymerized polypyrrole composite film: Characterization and application to gas sensors. *J. Appl. Polym. Sci.* **2003**, *88*, 22–29. [[CrossRef](#)]
108. Lin, C.W.; Liu, Y.L.; Thangamuthu, R. Investigation of the relationship between surface thermodynamics of the chemically synthesized polypyrrole films and their gas-sensing responses to BTEX compounds. *Sens. Actuators B Chem.* **2003**, *94*, 36–45. [[CrossRef](#)]
109. Kumar, G.; Mishra, S.; Jain, A. Development of breath ammonia analysis system for disease diagnosis. *Asian J. Biochem. Pharm. Res.* **2013**, *3*, 36–43.
110. Jang, W.-K.; Yun, J.; Kim, H.-I.; Lee, Y.-S. Improvement of ammonia sensing properties of polypyrrole by nanocomposite with graphitic materials. *Colloid Polym. Sci.* **2013**, *291*, 1095–1103. [[CrossRef](#)]
111. Gustafsson, G.; Lundström, I.; Liedberg, B.; Wu, C.R.; Inganäs, O.; Wennerström, O. The interaction between ammonia and poly(pyrrole). *Synth. Met.* **1989**, *31*, 163–179. [[CrossRef](#)]
112. Carquigny, S.; Sanchez, J.-B.; Berger, F.; Lakard, B.; Lallemand, F. Ammonia gas sensor based on electrosynthesized polypyrrole films. *Talanta* **2009**, *78*, 199–206. [[CrossRef](#)] [[PubMed](#)]
113. Kwon, O.S.; Park, S.J.; Yoon, H.; Jang, J. Highly sensitive and selective chemiresistive sensors based on multidimensional polypyrrole nanotubes. *Chem. Commun.* **2012**, *48*, 10526–10528. [[CrossRef](#)] [[PubMed](#)]
114. Xue, M.Q.; Li, F.W.; Chen, D.; Yang, Z.H.; Wang, X.W.; Ji, J.H. High-Oriented Polypyrrole Nanotubes for Next-Generation Gas Sensor. *Adv. Mater.* **2016**, *28*, 8265–8270. [[CrossRef](#)] [[PubMed](#)]
115. Yang, X.; Li, L.; Zhao, Y. Ag/AgCl-decorated polypyrrole nanotubes and their sensory properties. *Synth. Met.* **2010**, *160*, 1822–1825. [[CrossRef](#)]
116. Xiang, C.L.; Jiang, D.D.; Zou, Y.J.; Chu, H.L.; Qiu, S.J.; Zhang, H.Z.; Xu, F.; Sun, L.X.; Zheng, L.J. Ammonia sensor based on polypyrrole-graphene nanocomposite decorated with titania nanoparticles. *Ceram. Int.* **2015**, *41*, 6432–6438. [[CrossRef](#)]
117. Yan, Y.R.; Zhang, M.L.; Moon, C.H.; Su, H.C.; Myung, N.V.; Haberer, E.D. Viral-templated gold/polypyrrole nanopeapods for an ammonia gas sensor. *Nanotechnology* **2016**, *27*, 325502. [[CrossRef](#)] [[PubMed](#)]
118. Chougule, M.A.; Sen, S.; Patil, V.B. Development of Nanostructured Polypyrrole (PPy) Thin Film Sensor for NO₂ Detection. *Sens. Transducers* **2012**, *139*, 122–132.

119. Liu, X.; Chen, N.; Han, B.Q.; Xiao, X.C.; Chen, G.; Djerdj, I.; Wang, Y.D. Nanoparticle cluster gas sensor: Pt activated SnO₂ nanoparticles for NH₃ detection with ultrahigh sensitivity. *Nanoscale* **2015**, *7*, 14872–14880. [[CrossRef](#)] [[PubMed](#)]
120. Bhuvaneshwari, S.; Gopalakrishnan, N. Hydrothermally synthesized Copper Oxide (CuO) superstructures for ammonia sensing. *J. Colloid Interface Sci.* **2016**, *480*, 76–84. [[CrossRef](#)] [[PubMed](#)]
121. Liu, Y.; Wang, L.; Wang, H.; Xiong, M.; Yang, T.; Zakharova, G.S. Highly sensitive and selective ammonia gas sensors based on PbS quantum dots/TiO₂ nanotube arrays at room temperature. *Sens. Actuators B Chem.* **2016**, *236*, 529–536. [[CrossRef](#)]
122. Kumar, L.; Rawal, I.; Kaur, A.; Annapoorni, S. Flexible room temperature ammonia sensor based on polyaniline. *Sens. Actuators B Chem.* **2017**, *240*, 408–416. [[CrossRef](#)]
123. Hoa, N.D.; Van Quy, N.; Cho, Y.S.; Kim, D. Nanocomposite of SWNTs and SnO₂ fabricated by soldering process for ammonia gas sensor application. *Phys. Status Solidi A* **2007**, *204*, 1820–1824.
124. Qadri, M.U.; Annanouch, F.E.; Aguilo, M.; Diaz, F.; Borull, J.F.; Pujol, M.C.; Llobet, E. Metal Decorated WO₃ Nanoneedles Fabricated by Aerosol Assisted Chemical Vapor Deposition for Optical Gas Sensing. *J. Nanosci. Nanotechnol.* **2016**, *16*, 10125–10132. [[CrossRef](#)]
125. Huotari, J.; Lappalainen, J.; Eriksson, J.; Bjorklund, R.; Heinonen, E.; Miinalainen, I.; Puustinen, J.; Lloyd Spetz, A. Synthesis of nanostructured solid-state phases of V₇O₁₆ and V₂O₅ compounds for ppb-level detection of ammonia. *J. Alloys Compd.* **2016**, *675*, 433–440. [[CrossRef](#)]
126. Krivetskiy, V.; Malkov, I.; Garshev, A.; Mordvinova, N.; Lebedev, O.I.; Dolenko, S.; Efitorov, A.; Grigoriev, T.; Rummyantseva, M.; Gaskov, A. Chemically modified nanocrystalline SnO₂-based materials for nitrogen-containing gases detection using gas sensor array. *J. Alloys Compd.* **2017**, *691*, 514–523. [[CrossRef](#)]
127. Dalavi, D.S.; Harale, N.S.; Mulla, I.S.; Rao, V.K.; Patil, V.B.; Kim, I.Y.; Kim, J.H.; Patil, P.S. Nanoporous network of nickel oxide for ammonia gas detection. *Mater. Lett.* **2015**, *146*, 103–107. [[CrossRef](#)]
128. Nayak, A.K.; Ghosh, R.; Santra, S.; Guha, P.K.; Pradhan, D. Hierarchical nanostructured WO₃-SnO₂ for selective sensing of volatile organic compounds. *Nanoscale* **2015**, *7*, 12460–12473. [[CrossRef](#)] [[PubMed](#)]
129. Park, Y.H.; Song, H.-K.; Lee, C.-S.; Jee, J.-G. Fabrication and its characteristics of metal-loaded TiO₂/SnO₂ thick-film gas sensor for detecting dichloromethane. *J. Ind. Eng. Chem.* **2008**, *14*, 818–823. [[CrossRef](#)]
130. Qin, H.Y.; Kukarni, A.; Zhang, H.; Kim, H.; Jiang, D.; Kim, T. Polypyrrole thin film fiber optic chemical sensor for detection of VOCs. *Sens. Actuators B Chem.* **2011**, *158*, 223–228. [[CrossRef](#)]
131. Campos, M.; Simoes, F.R.; Pereira, E.C. Influence of methane in the electrical properties of polypyrrole films doped with dodecylbenzene sulfonic acid. *Sens. Actuators B Chem.* **2007**, *125*, 158–166. [[CrossRef](#)]
132. Campos, M. Gas sensing properties based on a doped conducting polymer/inorganic semiconductor. In Proceedings of the 2nd IEEE International Conference on Sensors, Toronto, ON, Canada, 22–24 October 2003; pp. 1126–1129.
133. Xu, Y.W.; Lee, H.; Hu, Y.S.; Huang, J.Y.; Kim, S.; Yun, M. Detection and Identification of Breast Cancer Volatile Organic Compounds Biomarkers Using Highly-Sensitive Single Nanowire Array on a Chip. *J. Biomed. Nanotechnol.* **2013**, *9*, 1164–1172. [[CrossRef](#)] [[PubMed](#)]
134. Hwang, H.R.; Roh, J.G.; Lee, D.D.; Lim, J.O.; Huh, J.S. Sensing behavior of the polypyrrole and polyaniline sensor for several volatile organic compounds. *Met. Mater. Int.* **2003**, *9*, 287–291. [[CrossRef](#)]
135. Low, K.; Chartuprayoon, N.; Echeverria, C.; Li, C.L.; Bosze, W.; Myung, N.V.; Nam, J. Polyaniline/poly(epsilon-caprolactone) composite electrospun nanofiber-based gas sensors: Optimization of sensing properties by dopants and doping concentration. *Nanotechnology* **2014**, *25*, 115501. [[CrossRef](#)] [[PubMed](#)]
136. Kebiche, H.; Debarnot, D.; Merzouki, A.; Poncin-Epaillard, F.; Haddaoui, N. Relationship between ammonia sensing properties of polyaniline nanostructures and their deposition and synthesis methods. *Anal. Chim. Acta* **2012**, *737*, 64–71. [[CrossRef](#)] [[PubMed](#)]
137. Brédas, J.L.; Silbey, R. *Conjugated Polymers: The Novel Science and Technology of Highly Conducting and Nonlinear Optically Active Materials*; Springer: Dordrecht, The Netherlands, 2012.
138. Wang, L.Q.; Gao, P.; Bao, D.; Wang, Y.; Chen, Y.J.; Chang, C.; Li, G.B.; Yang, P.P. Synthesis of Crystalline/Amorphous Core/Shell MoO₃ Composites through a Controlled Dehydration Route and Their Enhanced Ethanol Sensing Properties. *Cryst. Growth Des.* **2014**, *14*, 569–575. [[CrossRef](#)]
139. Sun, Y.J.; Chen, L.; Wang, Y.; Zhao, Z.T.; Li, P.W.; Zhang, W.D.; Leprince-Wang, Y.; Hu, J. Synthesis of MoO₃/WO₃ composite nanostructures for highly sensitive ethanol and acetone detection. *J. Mater. Sci.* **2017**, *52*, 1561–1572. [[CrossRef](#)]

140. Li, Y.; Deng, D.; Xing, X.; Chen, N.; Liu, X.; Xiao, X.; Wang, Y. A high performance methanol gas sensor based on palladium-platinum-In₂O₃ composited nanocrystalline SnO₂. *Sens. Actuators B Chem.* **2016**, *237*, 133–141. [[CrossRef](#)]
141. Li, Y.S.; Xu, J.; Chao, J.F.; Chen, D.; Ouyang, S.X.; Ye, J.H.; Shen, G.Z. High-aspect-ratio single-crystalline porous In₂O₃ nanobelts with enhanced gas sensing properties. *J. Mater. Chem.* **2011**, *21*, 12852–12857. [[CrossRef](#)]
142. Tang, W.; Wang, J.; Yao, P.J.; Li, X.G. Hollow hierarchical SnO₂-ZnO composite nanofibers with heterostructure based on electrospinning method for detecting methanol. *Sens. Actuators B Chem.* **2014**, *192*, 543–549. [[CrossRef](#)]
143. Sun, A.H.; Li, Z.X.; Wei, T.F.; Li, Y.; Cui, P. Highly sensitive humidity sensor at low humidity based on the quaternized polypyrrole composite film. *Sens. Actuators B Chem.* **2009**, *142*, 197–203. [[CrossRef](#)]
144. Zeng, F.-W.; Liu, X.-X.; Diamond, D.; Lau, K.T. Humidity sensors based on polyaniline nanofibres. *Sens. Actuators B Chem.* **2010**, *143*, 530–534. [[CrossRef](#)]
145. Chani, M.T.S.; Karimov, K.S.; Khalid, F.A.; Moiz, S.A. Polyaniline based impedance humidity sensors. *Solid State Sci.* **2013**, *18*, 78–82. [[CrossRef](#)]
146. Lin, W.D.; Chang, H.M.; Wu, R.J. Applied novel sensing material graphene/polypyrrole for humidity sensor. *Sens. Actuators B Chem.* **2013**, *181*, 326–331. [[CrossRef](#)]
147. Yang, M.Z.; Dai, C.L.; Lu, D.H. Polypyrrole Porous Micro Humidity Sensor Integrated with a Ring Oscillator Circuit on Chip. *Sensors* **2010**, *10*, 10095–10104. [[CrossRef](#)] [[PubMed](#)]



© 2017 by the authors. Licensee MDPI, Basel, Switzerland. This article is an open access article distributed under the terms and conditions of the Creative Commons Attribution (CC BY) license (<http://creativecommons.org/licenses/by/4.0/>).

SCIENTIFIC REPORTS

OPEN

Raman and XPS studies of ammonia sensitive polypyrrole nanorods and nanoparticles

Milena Šetka¹, Raúl Calavia², Lukáš Vojkůvka³, Eduard Llobet², Jana Drbohlavová^{1,4} & Stella Vallejos^{1,5}

Received: 4 January 2019

Accepted: 28 May 2019

Published online: 11 June 2019

Polypyrrole (PPy) nanorods (NRs) and nanoparticles (NPs) are synthesized via electrochemical and chemical methods, respectively, and tested upon ammonia exposure using Raman and X-ray photoelectron spectroscopy (XPS). Characterization of both nanomaterials via Raman spectroscopy demonstrates the formation of PPy, displaying vibration bands consistent with the literature. Additionally, XPS reveals the presence of neutral PPy species as major components in PPy NRs and PPy NPs, and other species including polarons and bipolarons. Raman and XPS analysis after ammonia exposure show changes in the physical/chemical properties of PPy, confirming the potential of both samples for ammonia sensing. Results demonstrate that the electrochemically synthesized NRs involve both proton and electron transfer mechanisms during ammonia exposure, as opposed to the chemically synthesized NPs, which show a mechanism dominated by electron transfer. Thus, the different detection mechanisms in PPy NRs and PPy NPs appear to be connected to the particular morphological and chemical composition of each film. These results contribute to elucidate the mechanisms involved in ammonia detection and the influence of the synthesis routes and the physical/chemical characteristics of PPy.

Nanomaterials belong to one of the most active research areas of science and technology due to their size dependent properties, which are beneficial in different applications including medicine, environment, energy and various industries. Specifically, gas sensitive nanomaterials have proven possessing enhanced functionalities with better sensitivity and stability. These materials have also shown versatility for their surface modification, improving the selective detection of different vapours and gases¹. Inorganic materials based on metals² and/or semiconducting metal oxides³ are the most commonly used and studied gas sensitive materials. However, functional conductive polymers (CPs) including polyaniline (PANI)^{4,5}, polydiacetylene (PDA)^{6,7}, poly(3,4-ethylenedioxythiophene) (PEDOT)⁸ and polypyrrole (PPy)⁹ have shown potential for a next generation of flexible and wearable gas sensors¹⁰. The main advantage of CPs lies in their capability to operate at room temperature, as opposed to semiconducting metal oxides, which need high temperatures to operate (typically between 200 °C and 500 °C¹¹).

In particular, PPy has been synthesized in the form of nanoparticles^{12,13}, nanowires^{14,15}, nanorods¹⁶, nanotubes¹⁷ and nanoribbons¹⁸ generally by electrochemical (electro-polymerization) or chemical methods, with both referring to the oxidative polymerization of the monomer pyrrole (Py). While electro-polymerized PPy is achieved using an appropriate electrolyte solution (Py and an oxidizing agent) under constant applied voltage or current in an electrochemical cell, chemically polymerized PPy is achieved via wet chemical synthesis by the oxidation of Py with an oxidizing agent such as FeCl₃. The final properties of PPy in both synthesis methods are strongly dependent on factors such as the Py concentration, type of oxidizing substance and solvent^{19–21}. Apart from those factors, the electro-polymerization of PPy also depends on the applied voltage and current density²¹. The electrochemical synthesis enables a wide choice of oxidizing agents, and localized control over

¹Central European Institute of Technology, Brno University of Technology, Purkyňova 123, 612 00, Brno, Czech Republic. ²Minos-Emas, Universitat Rovira i Virgili, Av. Països Catalans 26, 43007, Tarragona, Spain. ³Scientific-Technical Resources Service, Universitat Rovira i Virgili, Av. Països Catalans 26, 43007, Tarragona, Spain. ⁴Department of Microelectronics, SIX Research Centre, Faculty of Electrical Engineering and Communication, Brno University of Technology, Technická 3058/10, 61600, Brno, Czech Republic. ⁵Instituto de Microelectrónica de Barcelona (IMB-CNM, CSIC), Campus UAB, Carrer dels Til·lers, 08193, Cerdanyola del Vallès, Barcelona, Spain. Correspondence and requests for materials should be addressed to S.V. (email: stella.vallejos@imb-cnm.csic.es)

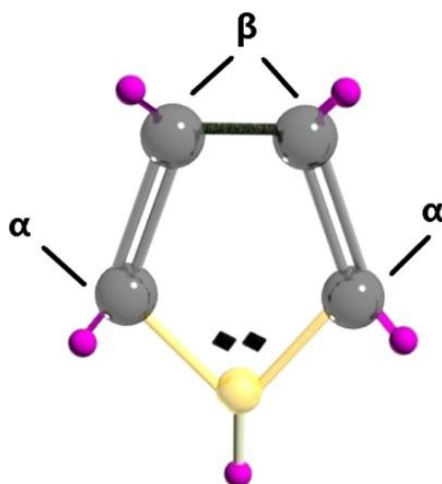


Figure 1. Molecular illustration of pyrrole monomer with the C atoms represented in grey, N atom in yellow and H atoms in purple colour.

material thickness and geometry, whereas the chemical synthesis provides the ability to generate nanostructures in a continuous, rather than batch mode. The latter implies higher throughputs and simpler instrumentation^{22,23}.

Most of the chemical, electrical, and mechanical properties of PPy originate from its hetero-atomic and conjugated backbone structure (σ and π bonds)¹¹, which contains polarons and/or bipolarons. These are oxidized states of PPy, associated with intermediate energy levels arose within the electronic band gap region of the polymer due to oxidation²⁴. Polarons form upon oxidation, when a π -electron is removed from the neutral PPy chain, whereas bipolarons appear upon further oxidation, when a second electron is removed from the PPy chain²⁵. This electron transfer occurring between PPy and the dopant anion (i.e., anion from the oxidizing agent) causes electron delocalization and in turn the structural lattice distortion of the PPy ring²⁶. Additionally, the chemical, electrical, and mechanical properties of PPy can also be linked to its morphology (i.e., the physical organisation of the macromolecules on a microscopic scale), which is determined by the conformation and arrangement of the Py chain segments in space (Fig. 1). The resulting PPy configuration is dependent on the synthetic route and variables such as the type of the dopant anions employed. Usually, Py rings tend to connect through α -positions leading to a planar configuration of PPy. However, Py rings can also connect through β -positions, or both α - and β -positions in the same ring leading to a nonplanar configuration, due to the steric crowding of the substituent hydrogen atoms, and the presence of defects in the structure^{27,28}. Consequently, the sensing properties of PPy are influenced in part by its morphology as well as its oxidation level, which is readily affected by chemical or electrochemical doping/de-doping (oxidation/reduction) mechanisms during the exposure of PPy to the gas analyte. Spectroscopy techniques such as Raman and X-ray photoelectron spectroscopy (XPS) allow for the characterization of these chemical or electrochemical properties. Raman facilitates the analysis of the intermolecular interactions and XPS provides a semi-quantitative analysis of surface chemical composition.

PPy with different morphologies has been reported previously as being sensitive to diverse gases and vapours, particularly to ammonia¹¹. Generally, the literature attributes these sensing properties to the transfer of protons or electrons between PPy and the gaseous analytes. However, often the correlation of these mechanisms with the morphology and synthesis method of PPy have been explored less^{29,30}. Hence, here we get an insight using spectroscopy techniques such as Raman and XPS into the dominant gas detection mechanisms of PPy NRs and PPy NPs synthesized electrochemically and chemically, respectively, towards ammonia as a model gas molecule.

Results and Discussion

Physical and chemical characteristics of the PPy NRs and PPy NPs. Figure 2 displays the morphology of the PPy NRs and PPy NPs observed via SEM and TEM, respectively. SEM of the PPy NRs (Fig. 2a) revealed quasi-aligned structures with a diameter of ~ 50 nm and a length of ~ 340 nm (grown on the top of 340 nm long Au NRs employed as template). TEM of the PPy NPs (Fig. 2b) proved the formation of homogeneously distributed compact spherical NPs with different sizes between 30 and 50 nm.

Raman analysis of PPy NRs and PPy NPs at room temperature (Fig. 3) displayed various Raman bands between 620 and 1609 cm^{-1} , consistent with those reported previously in the literature^{31–42}. Table 1 shows a summary of the Raman peaks observed in Fig. 3 with the assigned predominant band vibrations. Both samples displayed similar Raman bands with slight shifts of less than 20 cm^{-1} , most likely caused by the different laser wavelengths used for excitation of each sample (see experimental section).

XPS analysis of the films showed characteristic C 1s, and N 1s core level peaks both for the PPy NRs and PPy NPs (Fig. 4). Further examination of the C 1s core level peaks and their deconvolution into Gaussian components revealed different characteristics for the PPy NRs and PPy NPs. Thus, the C 1s spectrum for the PPy NRs films

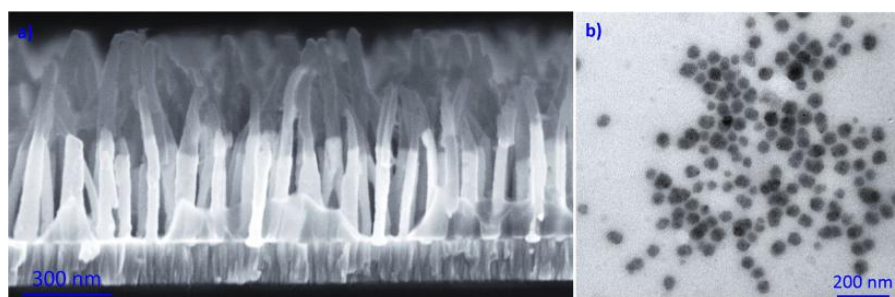


Figure 2. SEM and TEM images of the PPy NRs (a) and PPy NPs (b), respectively.

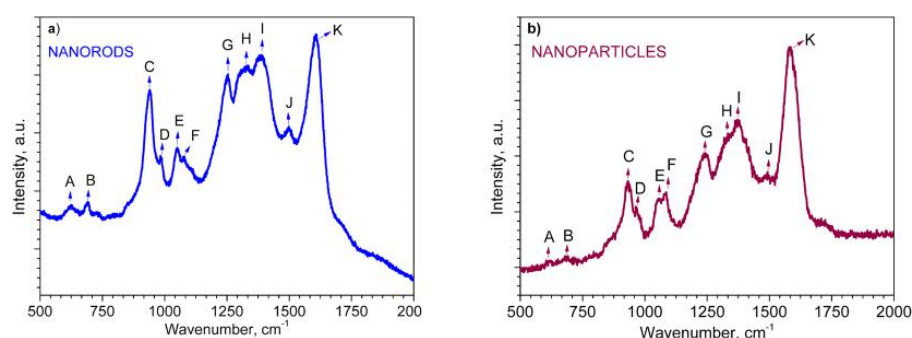


Figure 3. Raman spectra of the PPy NRs (a) and PPy NPs (b). The assignment of each peak is presented in Table 1.

| Band | Wavenumbers, cm^{-1} | Assignment |
|------|-------------------------------|--|
| A | 620–626 | C–C ring torsional |
| B | 687–690 | C–H wagging |
| C | 933–939 | C–C ring deformation (bipolarons) |
| D | 963–985 | C–C ring deformation (polarons) |
| E | 1050–1056 | C–H in-plane deformation (polarons) |
| F | 1079–1084 | C–H in-plane deformation (bipolarons) |
| G | 1241–1253 | Antisymmetric C–H in-plane bending, ring stretching |
| H | 1330–1333 | C–C in-ring, antisymmetric C–N stretching |
| I | 1372–1389 | C–C in-ring, antisymmetric C–N stretching, C–H bending, N–H bending stretching |
| J | 1492–1498 | C–C, C=N stretching |
| K | 1583–1609 | C=C in-ring, C–C inter-ring stretching |

Table 1. Assignment of Raman peaks for PPy NRs and PPy NPs in Fig. 3.

consist of four components (Fig. 4a) with the most intense peak at 284.7 eV. This peak corresponds to α carbon atoms in the Py ring (carbon atom bonded to a functional group, Fig. 1), which are presented as C–C, C–H or C=C^{43,44}. In contrast, the component at 284.2 eV is linked to β carbon atoms (carbon atoms that are not bonded to the functional group, Fig. 1)⁹. The component centred at 286.3 eV is related to the bonds between carbon and nitrogen in PPy structures, specifically attributed to the =C–N⁺ bond of PPy polarons⁴⁵. Finally, the fourth component with the smallest area, appearing at the highest binding energy (288.6 eV), is assigned to C=O species⁴⁶. Similarly, the C 1s core level peak recorded on the PPy NPs showed four components (Fig. 4b). Three of these components correspond to α carbon atoms, the =C–N⁺ bond of PPy polarons, and the C=O species identified in the PPy NRs, whereas the fourth component at 287.7 eV corresponds to the –C=N⁺ bond of bipolaron charge carrier species⁴⁵.

The deconvolution of N 1s XPS core level peaks recorded on the PPy NRs and PPy NPs displayed different characteristics. For instance, the N 1s peak for PPy NRs showed four components (Fig. 4c), while the weak intensity N 1s peak recorded on the PPy NPs showed the presence of only three components (Fig. 4d). In line with the

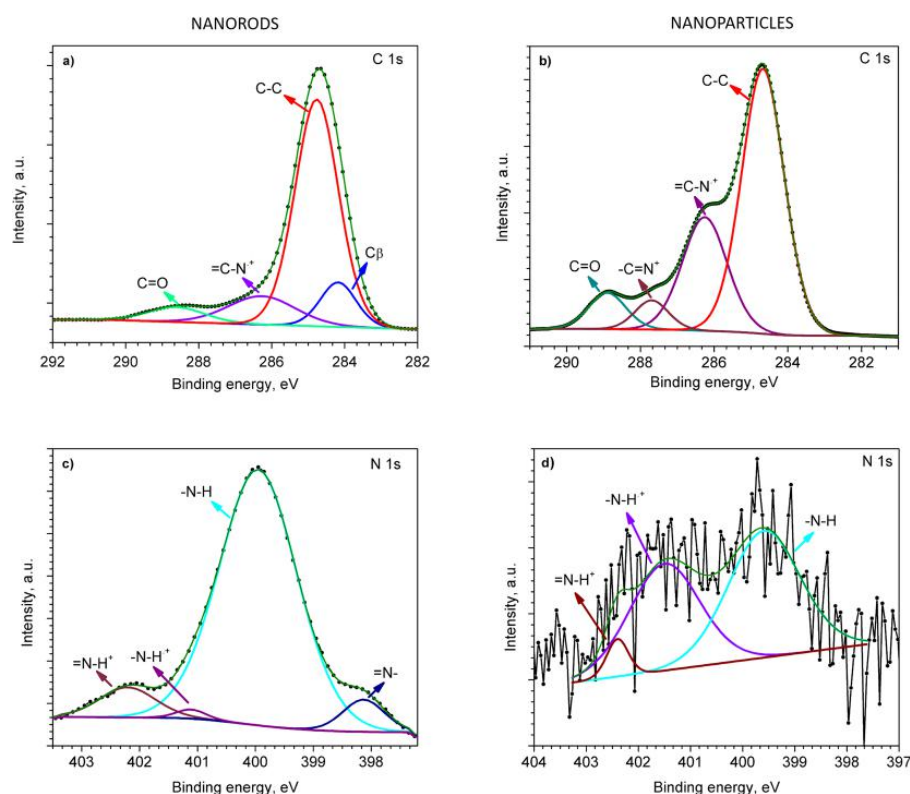


Figure 4. C 1s (a,b) and N 1s (c,d) XPS core level peaks recorded on the PPy NRs (left) and PPy NPs (right).

literature, the components at ~ 400 eV are assigned to neutral nitrogen in the Py ring ($-N-H$ structures), whereas the components shifted to the higher binding energies are most likely related to the positively charged nitrogen of polaron ($-N-H^+$) and bipolaron ($=N-H^+$) species. The component with the lowest binding energy, at 398 eV, corresponds to imine ($=N-$) structure^{43,44,47,48}.

Both samples (PPy NRs and PPy NPs) indicated a major presence of α carbon atoms in the PPy ring matching with the planar conformation of PPy (i.e., Py rings linked by α -positions). However, the presence of β carbon atoms and deprotonated nitrogen atoms ($=N-$) in the PPy NRs (Fig. 4a,c) suggest a degree of disorder in this sample. This signifies a nonplanar PPy configuration deviated from the ideal arrangement of PPy, in which Py rings are linked only via the α -positions. This could be attributed in part to the use of a higher number of reactants in the electrochemical synthesis as compared to the chemical synthesis, which in turn results in the incorporation of a higher number of impurities^{49,50}. Also, it could be attributed to the use of 'spherical' dopant anions such as BF_4^- (tetraethylammonium tetrafluoroborate) for PPy NRs, which cause particular defects in PPy, leading to non-planar configuration and different orientation at the surface⁵¹. The XPS survey spectra for both types of PPy films and the estimation of the concentration of these elements at the surface is shown in Fig. S1 (found for PPy NRs: Au, B, P, Cr and F, found for PPy NPs: Cl, Si and Fe).

The O 1s core level spectrum was also recorded for both samples. O 1s core levels are present due to the PPy degradation by OH^{\cdot} radicals. This oxygen is in the form of C-O-C and C=O moieties in the NRs and C=O and C-O in the NPs. The NPs also indicate the presence of iron oxide traces^{46,52,53} (Fig. S2).

Gas sensing properties. To get an insight into the sensing properties of the PPy NRs and PPy NPs, sensing tests with *in-situ* Raman spectroscopy were performed towards various gas analytes, including ammonia, ethanol, acetone, and toluene. Generally, results revealed repeatable and marked changes in the PPy bands of both samples (i.e. PPy NRs and PPy NPs) after ammonia exposure, contrary to the tests upon ethanol, acetone, and toluene, which showed negligible changes in the characteristic Raman bands of both samples. Thus, further gas sensing tests were focused on ammonia (0.3%) as a model analyte. Other ammonia concentrations were also analysed without noticing significant changes in PPy bands.

Previous reports in the literature suggest that the detection mechanism of PPy towards ammonia occurs either via proton transfer (deprotonation) and/or electron transfer (electron injection)⁵⁴. In the proton transfer reaction, the protonated form of PPy ($-N^+-H-$ site) loses protons, whereas the nitrogen atoms of NH_3 establish

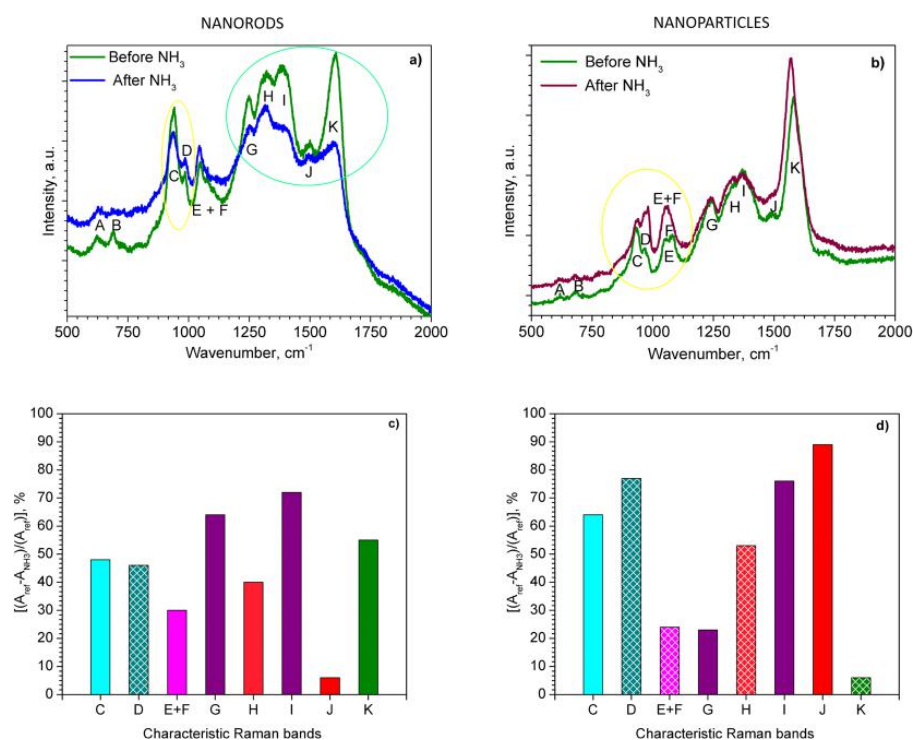
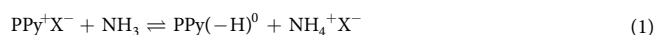


Figure 5. Raman spectra of the PPy NRs (a) and PPy NPs (b) before (green line) and after the exposure to ammonia (blue and brown line); Relative changes of each Raman band area $[(A_{ref} - A_{NH_3})/(A_{ref})]$ for the PPy NRs (c) and PPy NPs (d) after ammonia exposure. The area of the corresponding band (i.e., C, D, E, etc.) before and after ammonia exposure is expressed by A_{ref} and A_{NH_3} , respectively. The patterned columns represent an increase in peak area after ammonia exposure, whereas the full color columns represent a decrease.

coordination bonds with free atomic orbital of dopant X^- (e.g., BF_4^- for the NRs and Cl^- for the NPs), which leads to the deprotonation of PPy and creation of ammonium salt. This reaction can be described as follows⁵⁴:



Alternatively, the electron transfer can occur via reversible transformation of the positively charged PPy backbone (PPy^+) into the neutral form (PPy^0). Thus, when PPy is exposed to ammonia, a lone pair of electrons on the nitrogen atom of ammonia causes the reduction of PPy backbone (see Supplementary Information, Fig. S3)³⁸. This electron transfer reaction could be written as follows⁵⁴:



Figure 5a,b compare the Raman bands recorded before (reference spectra) and after exposing the PPy NRs and PPy NPs to ammonia (the characteristic Raman bands are labelled according to Table 1). Overall, the spectra after ammonia exposure revealed a slight shift (less than 10 cm^{-1}) to lower wavenumbers. This shift, however, was fully recovered after removing ammonia from the sample environment, which indicated a good reversibility of the system. The Raman bands (highlighted in green and yellow circles) in Fig. 5a,b show significant changes in the intensity and the full width at half maximum (FWHM) with respect to the reference.

The column chart for the PPy NRs in Fig. 5c compares the relative change of area for each Raman band after ammonia exposure. The changes are particularly marked for the C, G, H, I and K vibration bands which display approximately 48, 64, 40, 72 and 55% decrease in peak area after ammonia exposure, respectively. On the contrary, the D band is the only vibration band showing an increase in peak area and indicates a change of approximately 46% after ammonia exposure. The diminution and broadening of the I band, which is modulated in part by the intensity of various modes (see Table 1) has been demonstrated previously to be indicative of the deprotonation of PPy³⁸. Consequently, this shows the presence of a mechanism in which protons from $-N^+-H-$ site of PPy NRs are transferred to ammonia⁵⁵. In contrast, the changes observed in the bands C and D which correspond to polaron and bipolaron species, suggest the presence of an electron transfer mechanism in PPy NRs during ammonia exposure. This is consistent with the decrease of C peak (bipolaron) and increase of D peak (polaron) which indicates the conversion of bipolarons into polarons via the donation of electrons from ammonia. The

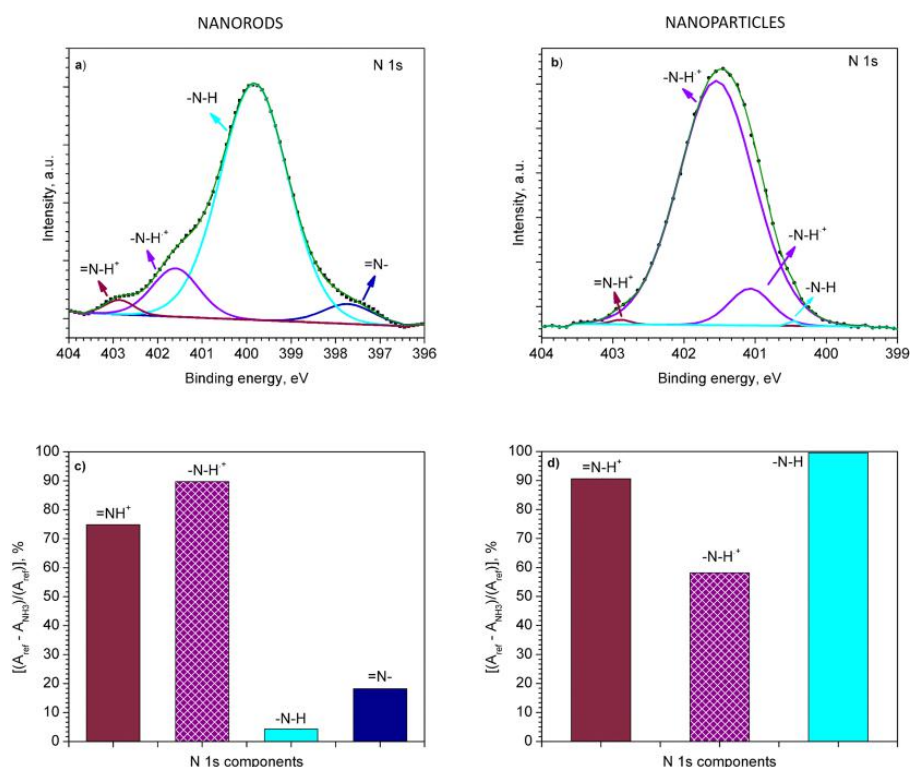


Figure 6. N 1s core level XPS spectra for the NRs (a) and NPs (b) after the exposure to ammonia. Relative change in area $[(A_{ref} - A_{NH_3}) / (A_{ref})]$ of each PPy component after ammonia exposure (NRs (c) and NPs (d)). The area of the corresponding components (i.e., -N-H, -N-H⁺, etc.) before and after ammonia exposure is expressed by A_{ref} and A_{NH_3} , respectively. Patterned and full color columns represent an increase or decrease in peak area after ammonia exposure, respectively.

presence of both mechanisms (i.e. proton and electron transfer) causes a new resonance structure in the ring³⁸ and in turn, the changes in the G, H, I and K bands as noticed in Fig. 5a,c. Thus, the new rearranged PPy structure may be characterized by different angles among the atoms and length of the bonds compared to the original PPy structure (i.e., before ammonia exposure).

Further XPS analysis of the PPy NRs after ammonia exposure also confirmed the presence of an electron transfer mechanism. After ammonia exposure, the XPS results revealed an increase of polarons and simultaneous decrease of bipolarons species in the N 1s core level peak (Fig. 6a). For instance, after ammonia exposure, the ratio of the components related to polarons and bipolarons was 6 times higher than the ratio recorded before ammonia exposure (Fig. 4c). The relative changes in area of the characteristic component after ammonia exposure are displayed in Fig. 6c. Similarly, the C 1s core level XPS spectrum (Fig. 7a) after ammonia exposure also indicates an increase of =C-N⁺ (polaron) species (Fig. 7c), with a slight change in the relation of β carbon atoms, C-C and C=O components (Fig. 7c) as compared to the components obtained before ammonia exposure (Fig. 4a). The presence of a proton transfer mechanism, as noticed via Raman for the PPy NRs after ammonia exposure, was not evidenced in the XPS analysis, probably due to the different principles of XPS and Raman. XPS allows observing the chemical and/or electronic states of the elements at the material surface (up to 10 nm in depth) and Raman analyzes vibrational, rotational, and other low-frequency modes within the bulk of the material.

As far as the PPy NPs results concern, the changes on the Raman spectra of PPy NPs after ammonia exposure are also manifested by relative changes of area in each band (Fig. 5b). The most noticeable changes after ammonia exposure are observed for the bands C, I and J with a decrease in peak area of 64, 76 and 89%, respectively. In contrast, the D and H bands showed an increase in peak area of 77 and 53%, respectively (Fig. 5d). The changes in the C and D Raman bands for PPy NPs after ammonia exposure indicate a decrease in the amount of bipolarons (C band) with simultaneous increase of polarons (D band). This fact is also supported by the disappearance of the bipolarons band (F) and the sharpness of the polarons band (E) after ammonia exposure. Previous works attributed the loss of the F band after reduction of oxidized PPy⁴¹. This statement is also consistent with the shift of the K band to the lower wavenumbers which also indicates a reduced (less oxidized) PPy structure³⁵. Consequently, the conversion of bipolarons into polarons leads to a distortion of the bonds and angles along the PPy chain (Fig. S3). This is in agreement with the new resonance recorded for the H, I, and J bands after ammonia exposure

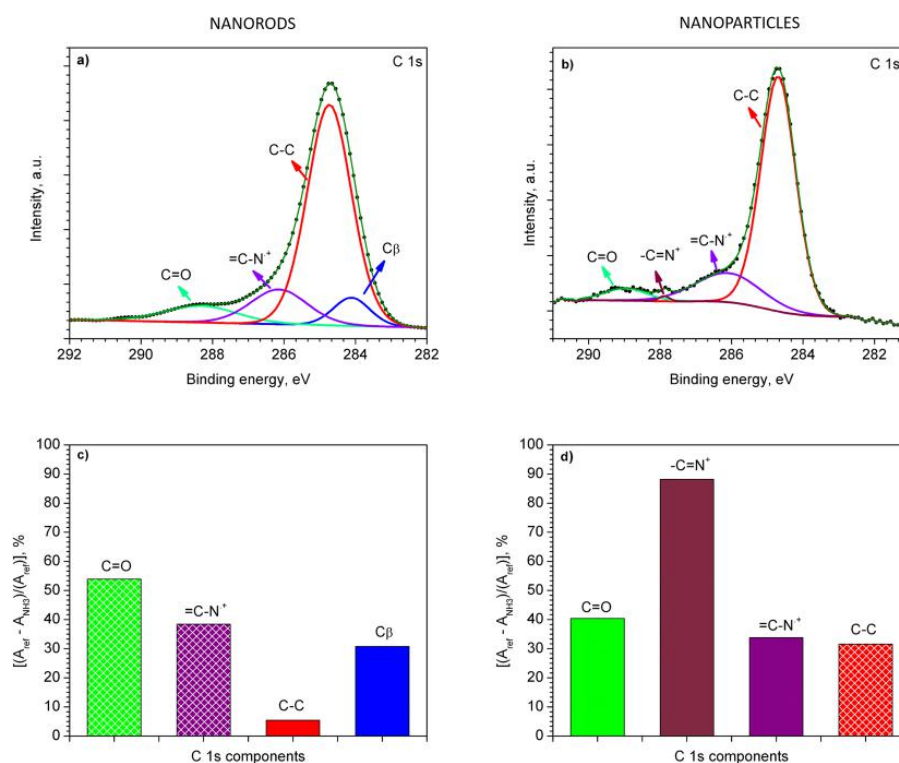


Figure 7. C 1s core level XPS spectra for the NRs (a) and NPs (b) after the exposure to ammonia. Relative change in area $[(A_{ref} - A_{NH_3}) / (A_{ref})]$ of each PPy component after ammonia exposure (NRs (c) and NPs (d)). The area of the corresponding components (i.e., C_β, C-C, etc.) before and after ammonia exposure is expressed by A_{ref} and A_{NH_3} , respectively. Patterned and full color columns represent an increase or decrease in peak area after ammonia exposure, respectively.

(Fig. 5b). This new resonance is manifested by the loss of J band and the large changes in the peak area of H and I bands (Fig. 5d) which indicate the break of C=N double bond of bipolarons and the conversion to C-N single bonds of polarons.

The N 1s core level spectrum also demonstrates the presence of positively charged nitrogen ($-N-H^+$) of polaron species (Fig. 6b), with a strong decrease in the bipolaron ($=N-H^+$) species and neutral nitrogen ($-N-H$) (Fig. 6d) after ammonia exposure. These results indicate a nine-fold increase of the polarons to bipolarons ratio as compared to the ratio registered before ammonia exposure. The C 1s XPS core level spectra of the PPy NPs after ammonia exposure (Fig. 7b) also points out to the conversion of bipolarons into polarons. XPS spectra (Figs 4b and 7b) show a lower polaron to bipolaron before (i.e., 7) than after (i.e., 35) ammonia exposure, indicating a five-fold increase in this ratio. These results are consistent with the Raman analysis described above, indicating that the PPy NPs exposed to ammonia follow a detection mechanism dominated by electron transfer, with no evidence of a proton transfer mechanism as noticed for the PPy NRs.

In summary, these results indicate that the ammonia detection mechanisms in PPy are prone to be adjusted by the synthesis route, namely by tuning reactants, concentrations, and/or applied charge density in the case of electrodeposition. These synthesis conditions at the first stage define the morphology, surface area and orientation of PPy. However, in a more advanced stage this influences the detection mechanisms of ammonia. Considering the specific synthesis conditions and gas analyte studied in this work, Raman and XPS tests evidenced electron transfer mechanisms in both, the electrochemically synthesized PPy NRs and the chemically synthesized PPy NPs, whereas the presence of detection mechanism in which protons are transferred was only evidenced in the case of PPy NRs. The possibility to tailor these mechanisms as a function of the synthesis route would be beneficial for specific sensing principles. For instance, a sensing based on mass-sensitive principle, in which the presence of proton-based mechanism could be more favourable considering that the relative mass of protons is higher (~2000 times more) than that of electrons.

Conclusions

An electrochemical and chemical synthesis of polypyrrole to form rods (PPy NRs) and particles (PPy NPs) at nanoscale was developed. SEM and TEM analysis revealed PPy NRs with diameters of 50 nm and lengths of 300 nm, approximately, and PPy NPs with diameters between 30 and 50 nm. The mechanisms involved during the exposure to ammonia of these materials were addressed *in-situ*, using Raman and XPS analysis. Results

demonstrated a detection mechanism dominated by both electron and proton transfer in the case of PPy NRs, as opposed to PPy NPs which showed a mechanism based on electron transfer. The results are affected in part by different morphological/structural properties of the films and by the incorporation of different impurities derived from the particular steps of each synthesis process. This proves a significant impact of the entire technological process on the detection behavior of the same material.

Materials and Methods

Electrochemical synthesis. PPy NRs were synthesized on the top of preformed gold nanorods (Au NRs)⁵⁶ via template-based electropolymerization enabled by a two-electrode system under potentiostatic (constant potential) mode. Silicon wafers with thermally oxidized silicon dioxide layer (1.5 × 1.5 mm) covered, from bottom to top, by sputter-deposited titanium (Ti, 20 nm thick), tungsten (W, 150 nm thick) and aluminium (Al, 500 nm thick) were used as a substrate. The deposition of above mentioned layers was performed using RFICP Kaufman ion-beam source, KRI®.

In the first step, the electrochemical anodization of Al and W was performed under 40 V in 0.3 M oxalic acid at 10 °C. These conditions led to the formation of nanoporous anodized alumina oxide (AAO) template with tungsten trioxide (WO₃) nanodots at the bottom which were subsequently etched in a phosphate buffer solution (pH = 7, T = 25 °C). This step allowed the formation of W nanodimpled surface as a base for the growth of the Au NRs. The pulsed galvanic deposition of gold (Au) was carried out in potassium dicyanoaurate solution under following conditions: 35 pulses, pulse length of 400 ms, a period of 2 s between pulses, a current of 1 mA, and a potential of 5 V.

Then PPy was deposited under a voltage of 2 V for 120 s during the electropolymerization. The PPy was formed in a mixture of Py monomer and anionic doping salt, tetraethylammonium tetrafluoroborate, with the molar ratio of 2:1, dissolved in acetonitrile solvent. To clean the surface and eliminate any over deposition of the PPy, the polymer layer was etched using oxygen plasma with applied power of 100 W at 50 mTorr and a gas flow of 50 sccm of O₂ for 15 min. Finally, the AAO template was selectively dissolved in the aqueous solution of chromium trioxide and phosphoric acid at 60 °C for 600 s.

Chemical synthesis. PPy NPs were obtained via oxidative chemical polymerization of Py monomer based on the formation of complex between water-soluble polymer poly vinyl alcohol (PVA) and iron cations (III) of FeCl₃ in aqueous solution, as described previously¹³. Briefly, 7.5 wt% PVA was diluted in distilled water and stirred till all PVA was completely dissolved. Subsequently, 3.73 g of FeCl₃ was added to the solution; after this step, a change of color from transparent to yellow was observed. The stirring was continued for 5 min until an equilibrium was established, then 0.69 cm⁻³ of Py monomer was dropped in the reaction mixture. As soon as the Py mixed with the oxidant (FeCl₃), a rapid polymerization reaction occurred. This turned the solution into a characteristic black color that indicates the formation of PPy. The stirring process was kept constant for 5 h, subsequently the PPy NPs were separated from the solution via centrifugation (6000 RPM for 60 min) and diluted in ethanol. Finally, PPy NPs were drop coated on silicon tiles (1.5 × 1.5 mm) and dried at 80 °C for 30 min.

Material analysis and gas tests. Raman analysis was carried out using a Renishaw InVia Raman microscope employing 785 nm and 633 nm laser beam for PPy NRs and PPy NPs, respectively. The spectra were recorded using a power lower than 1 mW (i.e., power density was 0.1627 mW/μm² for PPy NRs and 0.0085 mW/μm² for PPy NPs), and a 20× objective. Raman spectra were recorded at 60 °C. During the measurements, the samples were placed in a chamber equipped with a continuous gas flow system. Nitrogen was used as reference and simultaneously as a carrier gas for the saturated ammonia vapour which was produced by bubbling ammonia (Panreac, 30% w/v) at room temperature. The resulting ammonia concentration was contrasted using a commercial photoionization detector (MiniRAE30000 with an operating range of 0–1.5%). Thus, PPy NRs and PPy NPs samples were exposed either to nitrogen or 0.3% of ammonia for 5 min. Afterwards, the Raman spectra were recorded. After ammonia exposure, the samples were cleaned in N₂ flow for 15 min. The Raman spectra before and after ammonia exposure presented in this work were recorded on the same sample and site. Moreover, the same procedure was repeated in various sites of the sample to confirm the tendency of the spectra.

In order to further study the mechanisms of ammonia detection, the PPy NRs and PPy NPs were exposed to ammonia flow for 20 min at 60 °C and subsequently, the XPS spectra were recorded. These analyses were performed on the same samples used for Raman. The XPS spectra before and after ammonia were measured in various nearby sites. XPS was carried out using Kratos AXIS Supra spectrometer with monochromatic Kα X-ray radiation, emission current of 15 mA, hybrid lens mode and charge compensation on. High-resolution spectra were collected with analyser pass energy of 20 eV and with 0.1 eV energy resolution. The deconvolution of all XPS data was elaborated using Casa XPS v.2.3.18 software (the spectra were calibrated with respect to the C 1s peak at 284.7 eV).

References

1. Andre, R. S. *et al.* Hybrid nanomaterials designed for volatile organic compounds sensors: A review. *Materials & Design* **156**, 154–166, <https://doi.org/10.1016/j.matdes.2018.06.041> (2018).
2. Peng, G. *et al.* Diagnosing lung cancer in exhaled breath using gold nanoparticles. *Nature Nanotechnology* **4**, 669–673, <https://doi.org/10.1038/nnano.2009.235> (2009).
3. Sun, Y. F. *et al.* Metal Oxide Nanostructures and Their Gas Sensing Properties: A Review. *Sensors* **12**, 2610–2631, <https://doi.org/10.3390/s120302610> (2012).
4. Athawale, A. A. & Kulkarni, M. V. Polyaniline and its substituted derivatives as sensor for aliphatic alcohols. *Sensors and Actuators B-Chemical* **67**, 173–177, [https://doi.org/10.1016/s0925-4005\(00\)00394-4](https://doi.org/10.1016/s0925-4005(00)00394-4) (2000).
5. Kim, J.-S., Sohn, S.-O. & Huh, J.-S. Fabrication and sensing behavior of PVF₂ coated-polyaniline sensor for volatile organic compounds. *Sensors and Actuators B: Chemical* **108**, 409–413, <https://doi.org/10.1016/j.snb.2004.11.072> (2005).

6. Eaidkong, T. *et al.* Polydiacetylene paper-based colorimetric sensor array for vapor phase detection and identification of volatile organic compounds. *Journal of Materials Chemistry* **22**, 5970–5977, <https://doi.org/10.1039/C2JM16273C> (2012).
7. Yoon, J., Chae, S. K. & Kim, J. M. Colorimetric sensors for volatile organic compounds (VOCs) based on conjugated polymer-embedded electrospun fibers. *Journal of the American Chemical Society* **129**, 3038–3039, <https://doi.org/10.1021/ja067856+> (2007).
8. Park, E. *et al.* One-pot synthesis of silver nanoparticles decorated poly(3,4-ethylenedioxythiophene) nanotubes for chemical sensor application. *Journal of Materials Chemistry* **22**, 1521–1526, <https://doi.org/10.1039/C1JM13237G> (2012).
9. Guernion, N. *et al.* The fabrication and characterisation of a highly sensitive polypyrrole sensor and its electrical responses to amines of differing basicity at high humidities. *Synthetic Metals* **126**, 301–310, [https://doi.org/10.1016/S0379-6779\(01\)00572-0](https://doi.org/10.1016/S0379-6779(01)00572-0) (2002).
10. McQuade, D. T., Pullen, A. E. & Swager, T. M. Conjugated Polymer-Based Chemical Sensors. *Chemical Reviews* **100**, 2537–2574, <https://doi.org/10.1021/cr9801014> (2000).
11. Šetka, M., Drbohlavová, J. & Hubálek, J. Nanostructured Polypyrrole-Based Ammonia and Volatile Organic Compound Sensors. *Sensors* **17**, <https://doi.org/10.3390/s17030562> (2017).
12. Kwon, O. S. *et al.* Resistive Gas Sensors Based on Precisely Size-Controlled Polypyrrole Nanoparticles: Effects of Particle Size and Deposition Method. *Journal of Physical Chemistry C* **114**, 18874–18879, <https://doi.org/10.1021/jp1083086> (2010).
13. Hong, J. Y., Yoon, H. & Jang, J. Kinetic Study of the Formation of Polypyrrole Nanoparticles in Water-Soluble Polymer/Metal Cation Systems: A Light-Scattering Analysis. *Small* **6**, 679–686, <https://doi.org/10.1002/sml.200902231> (2010).
14. Hernandez, S. C. *et al.* Single polypyrrole nanowire ammonia gas sensor. *Electroanalysis* **19**, 2125–2130, <https://doi.org/10.1002/elan.200703933> (2007).
15. Zhang, L. *et al.* A novel ammonia sensor based on high density, small diameter polypyrrole nanowire arrays. *Sensors and Actuators B: Chemical* **142**, 204–209, <https://doi.org/10.1016/j.snb.2009.07.042> (2009).
16. Lee, J.-S. *et al.* Au-Polypyrrole Framework Nanostructures for Improved Localized Surface Plasmon Resonance Volatile Organic Compounds Gas Sensing. *Journal of Nanoscience and Nanotechnology* **15**, 7738–7742, <https://doi.org/10.1166/jnn.2015.11194> (2015).
17. Joulazadeh, M. & Navarchian, A. H. Alcohol Sensibility of One-Dimensional Polyaniline and Polypyrrole Nanostructures. *Ieee Sensors Journal* **15**, 1697–1704, <https://doi.org/10.1109/jsen.2014.2360915> (2015).
18. Chartuprayoon, N. *et al.* Wafer-Scale Fabrication of Single Polypyrrole Nanoribbon-Based Ammonia Sensor. *Journal of Physical Chemistry C* **114**, 11103–11108, <https://doi.org/10.1021/jp102858w> (2010).
19. Kausaitė-Minkstimiene, A., Mazeiko, V., Ramanavičienė, A. & Ramanavičius, A. Evaluation of chemical synthesis of polypyrrole particles. *Colloids and Surfaces A: Physicochemical and Engineering Aspects* **483**, 224–231, <https://doi.org/10.1016/j.colsurfa.2015.05.008> (2015).
20. Patois, T. *et al.* Characterization of the surface properties of polypyrrole films: Influence of electrodeposition parameters. *Synthetic Metals* **161**, 2498–2505, <https://doi.org/10.1016/j.synthmet.2011.10.003> (2011).
21. Patois, T., Lakard, B., Martin, N. & Fievet, P. Effect of various parameters on the conductivity of free standing electro synthesized polypyrrole films. *Synthetic Metals* **160**, 2180–2185, <https://doi.org/10.1016/j.synthmet.2010.08.005> (2010).
22. Inzelt, G., Pineri, M., Schultze, J. W. & Vorotyntsev, M. A. Electron and proton conducting polymers: recent developments and prospects. *Electrochimica Acta* **45**, 2403–2421, [https://doi.org/10.1016/S0013-4686\(00\)00329-7](https://doi.org/10.1016/S0013-4686(00)00329-7) (2000).
23. Joshi, A., Gangal, S. A. & Gupta, S. K. Ammonia sensing properties of polypyrrole thin films at room temperature. *Sensors and Actuators B: Chemical* **156**, 938–942, <https://doi.org/10.1016/j.snb.2011.03.009> (2011).
24. Santos, M. J. L., Brolo, A. G. & Girotto, E. M. Study of polaron and bipolaron states in polypyrrole by *in situ* Raman spectroelectrochemistry. *Electrochimica Acta* **52**, 6141–6145, <https://doi.org/10.1016/j.electacta.2007.03.070> (2007).
25. Le, T. H., Kim, Y. & Yoon, H. Electrical and Electrochemical Properties of Conducting Polymers. *Polymers* **9**, 32, <https://doi.org/10.3390/polym9040150> (2017).
26. Balint, R., Cassidy, N. J. & Cartmell, S. H. Conductive polymers: Towards a smart biomaterial for tissue engineering. *Acta Biomaterialia* **10**, 2341–2353, <https://doi.org/10.1016/j.actbio.2014.02.015> (2014).
27. Yurtsever, M. & Yurtsever, E. Structural studies of polypyrroles: I. An ab-initio evaluation of bonding through α and β carbons. *Synthetic Metals* **98**, 221–227, [https://doi.org/10.1016/S0379-6779\(98\)00195-7](https://doi.org/10.1016/S0379-6779(98)00195-7) (1999).
28. Meerholz, K. & Heinze, J. Influence of chain length and defects on the electrical conductivity of conducting polymers. *Synthetic Metals* **57**, 5040–5045, [https://doi.org/10.1016/0379-6779\(93\)90859-U](https://doi.org/10.1016/0379-6779(93)90859-U) (1993).
29. Deogaonkar, S. C. & Bhat, N. V. Polymer based fabrics as transducers in ammonia & ethanol gas sensing. *Fiber. Polym.* **16**, 1803–1811, <https://doi.org/10.1007/s12221-015-5172-6> (2015).
30. Kharat, H. J. *et al.* Synthesis of polypyrrole films for the development of ammonia sensor. *Polymers for Advanced Technologies* **18**, 397–402, <https://doi.org/10.1002/pat.903> (2007).
31. Liu, Y.-C. Characteristics of vibration modes of polypyrrole on surface-enhanced Raman scattering spectra. *Journal of Electroanalytical Chemistry* **571**, 255–264, <https://doi.org/10.1016/j.jelechem.2004.05.015> (2004).
32. Le, H. N. T., Bernard, M. C., Garcia-Renaud, B. & Deslouis, C. Raman spectroscopy analysis of polypyrrole films as protective coatings on iron. *Synthetic Metals* **140**, 287–293, [https://doi.org/10.1016/S0379-6779\(03\)00376-x](https://doi.org/10.1016/S0379-6779(03)00376-x) (2004).
33. Gupta, S. Hydrogen bubble-assisted syntheses of polypyrrole micro/nanostructures using electrochemistry: structural and physical property characterization. *Journal of Raman Spectroscopy* **39**, 1343–1355, <https://doi.org/10.1002/jrs.2002> (2008).
34. Liu, Y.-C., Hwang, B.-J., Jian, W.-J. & Santhanam, R. *In situ* cyclic voltammetry-surface-enhanced Raman spectroscopy: studies on the doping–undoping of polypyrrole film. *Thin Solid Films* **374**, 85–91, [https://doi.org/10.1016/S0040-6090\(00\)01061-0](https://doi.org/10.1016/S0040-6090(00)01061-0) (2000).
35. Crowley, K. & Cassidy, J. *In situ* resonance Raman spectroelectrochemistry of polypyrrole doped with dodecylbenzenesulfonate. *Journal of Electroanalytical Chemistry* **547**, 75–82, [https://doi.org/10.1016/S0022-0728\(03\)00191-8](https://doi.org/10.1016/S0022-0728(03)00191-8) (2003).
36. Xie, Y. B. & Du, H. X. Electrochemical capacitance of a carbon quantum dots-polypyrrole/titania nanotube hybrid. *Rsc Advances* **5**, 89689–89697, <https://doi.org/10.1039/c5ra16538e> (2015).
37. Kopecka, J. *et al.* Polypyrrole Nanotubes and Their Carbonized Analogs: Synthesis, Characterization, Gas Sensing Properties. *Sensors* **16**, 13, <https://doi.org/10.3390/s16111917> (2016).
38. Stejskal, J. *et al.* Polypyrrole salts and bases: superior conductivity of nanotubes and their stability towards the loss of conductivity by deprotonation. *RSC Advances* **6**, 88382–88391, <https://doi.org/10.1039/c6ra19461c> (2016).
39. Li, M., Wei, Z. X. & Jiang, L. Polypyrrole nanofiber arrays synthesized by a biphasic electrochemical strategy. *Journal of Materials Chemistry* **18**, 2276–2280, <https://doi.org/10.1039/b800289d> (2008).
40. Kostic, R. *et al.* Vibrational spectroscopy of polypyrrole, theoretical-study. *Journal of Chemical Physics* **102**, 3104–3109, <https://doi.org/10.1063/1.468620> (1995).
41. Liu, Y.-C. & Hwang, B.-J. Identification of oxidized polypyrrole on Raman spectrum. *Synthetic Metals* **113**, 203–207, [https://doi.org/10.1016/S0379-6779\(00\)00188-0](https://doi.org/10.1016/S0379-6779(00)00188-0) (2000).
42. Ishpal, R. & Kaur, A. Spectroscopic and electrical sensing mechanism in oxidant-mediated polypyrrole nanofibers/nanoparticles for ammonia gas. *Journal of Nanoparticle Research* **15**, 1637, <https://doi.org/10.1007/s11051-013-1637-y> (2013).
43. Wang, H. *et al.* Microstructure, distribution and properties of conductive polypyrrole/cellulose fiber composites. *Cellulose* **20**, 1587–1601, <https://doi.org/10.1007/s10570-013-9945-z> (2013).
44. El Jaouhari, A. *et al.* Corrosion resistance and antibacterial activity of electro synthesized polypyrrole. *Synthetic Metals* **226**, 15–24, <https://doi.org/10.1016/j.synthmet.2017.01.008> (2017).

45. Jain, S. *et al.* Ammonia detection of 1-D ZnO/polypyrrole nanocomposite: Effect of CSA doping and their structural, chemical, thermal and gas sensing behavior. *Applied Surface Science* **396**, 1317–1325, <https://doi.org/10.1016/j.apsusc.2016.11.154> (2017).
46. Idla, K. *et al.* An XPS and AFM study of polypyrrole coating on mild steel. *Surface and Interface Analysis* **25**, 837–854, 10.1002/(sici)1096-9918(199710)25:11<837::aid-sia307>3.0.co;2-2 (1997).
47. Schweiger, B., Kim, J., Kim, Y. J. & Ulbricht, M. Electropolymerized Molecularly Imprinted Polypyrrole Film for Sensing of Clofibrilic Acid. *Sensors* **15**, 4870–4889, <https://doi.org/10.3390/s150304870> (2015).
48. Ruangchuay, L., Schwank, J. & Sirivat, A. Surface degradation of α -naphthalene sulfonate-doped polypyrrole during XPS characterization. *Applied Surface Science* **199**, 128–137, [https://doi.org/10.1016/S0169-4332\(02\)00564-0](https://doi.org/10.1016/S0169-4332(02)00564-0) (2002).
49. Wehrle, B., Limbach, H.-H., Mortensen, J. & Heinze, J. Solid-state 15N CP/MAS NMR study of the structure of polypyrrole. *Synthetic Metals* **38**, 293–298, [https://doi.org/10.1016/0379-6779\(90\)90082-V](https://doi.org/10.1016/0379-6779(90)90082-V) (1990).
50. Ribó, J. M., Dicko, A., Tura, J. M. & Bloor, D. Chemical structure of polypyrrole: X-ray photoelectron spectroscopy of polypyrrole with 5-yliden-3-pyrrolin-2-one end groups. *Polymer* **32**, 728–732, [https://doi.org/10.1016/0032-3861\(91\)90487-4](https://doi.org/10.1016/0032-3861(91)90487-4) (1991).
51. Kiani, M. S. & Mitchell, G. R. The role of the counter-ion in the preparation of polypyrrole films with enhanced properties using a pulsed electrochemical potential. *Synthetic Metals* **48**, 203–218, [https://doi.org/10.1016/0379-6779\(92\)90062-N](https://doi.org/10.1016/0379-6779(92)90062-N) (1992).
52. Rajagopalan, R. & Iroh, J. O. Characterization of polyaniline–polypyrrole composite coatings on low carbon steel: a XPS and infrared spectroscopy study. *Applied Surface Science* **218**, 58–69, [https://doi.org/10.1016/S0169-4332\(03\)00579-8](https://doi.org/10.1016/S0169-4332(03)00579-8) (2003).
53. Buitrago-Sierra, R., Garcia-Fernandez, M. J., Pastor-Blas, M. M. & Sepulveda-Escribano, A. Environmentally friendly reduction of a platinum catalyst precursor supported on polypyrrole. *Green Chemistry* **15**, 1981–1990, <https://doi.org/10.1039/c3gc40346g> (2013).
54. Qin, Y., Zhang, T. & Cui, Z. Core-shell structure of polypyrrole grown on $W_{18}O_{49}$ nanorods for high performance gas sensor operating at room temperature. *Organic Electronics* **48**, 254–261, <https://doi.org/10.1016/j.orgel.2017.06.014> (2017).
55. Rawal, I., Sehrawat, K. & Kaur, A. Vibrational spectroscopic investigations of ammonia gas sensing mechanism in polypyrrole nanostructures. *Vibrational Spectroscopy* **74**, 64–74, <https://doi.org/10.1016/j.vibspec.2014.07.012> (2014).
56. Drbohlavova, J. *et al.* Gold Nanostructured Surface for Electrochemical Sensing and Biosensing: Does Shape Matter? *Analytical Letters* **49**, 135–151, <https://doi.org/10.1080/00032719.2015.1043662> (2016).

Acknowledgements

This work has been supported by the Czech Science Foundation (GAČR) via Grant no. 17-16531S, CEITEC Nano Research Infrastructure (IDL2015041, MEYS CR, 2016–2019) and the Ramón y Cajal programme from MINECO are also acknowledged. R.C. and E.L. are supported by MINECO and FEDER under grant no. TEC2015-71663-R.

Author Contributions

M.S. and S.V. wrote the main manuscript text. All authors were involved in the experimental work and/or results analysis, and reviewed the manuscript.

Additional Information

Supplementary information accompanies this paper at <https://doi.org/10.1038/s41598-019-44900-1>.

Competing Interests: The authors declare no competing interests.

Publisher's note: Springer Nature remains neutral with regard to jurisdictional claims in published maps and institutional affiliations.



Open Access This article is licensed under a Creative Commons Attribution 4.0 International License, which permits use, sharing, adaptation, distribution and reproduction in any medium or format, as long as you give appropriate credit to the original author(s) and the source, provide a link to the Creative Commons license, and indicate if changes were made. The images or other third party material in this article are included in the article's Creative Commons license, unless indicated otherwise in a credit line to the material. If material is not included in the article's Creative Commons license and your intended use is not permitted by statutory regulation or exceeds the permitted use, you will need to obtain permission directly from the copyright holder. To view a copy of this license, visit <http://creativecommons.org/licenses/by/4.0/>.

© The Author(s) 2019

Gold/polypyrrole nanorods for gas sensing application

Milena Šetka^{*1}, Jana Drbohlavová^{1,2}, Stella Vallejos¹, Marian Márik¹, Eduard Llobet³, Jaromír Hubálek^{1,2}

¹Central European Institute of Technology, Brno University of Technology, Purkyňova 123, 612 00 Brno, Czech Republic

²Department of Microelectronics, Faculty of Electrical Engineering and Communication, Brno University of Technology, Technická 3058/10, 616 00 Brno, Czech Republic

³Minos-Emas, Universitat Rovira i Virgili, Av. Pasios Catalans 26, 43007 Tarragona, Spain

ABSTRACT

This work describes the preparation of gold/polypyrrole nanorods (AuPPy NRs) using anodized alumina oxide (AAO) template and both pulsed galvanic deposition and electropolymerization for the deposition of Au and polypyrrole (PPy) nanorods (NRs), respectively. Characterization of the whole structure after AAO etching revealed the formation of a high density of NRs along the substrate with uniform diameters of approximately 50 nm and total lengths of 700 nm, the last corresponding to 1/3 and 2/3 of the length of the Au and PPy NRs, respectively. These structures are provided of bottom/top electrodes and a heating element coupled to the backside of the substrate, and their gas sensing properties towards various concentrations of NO₂ in resistive configuration are presented.

Keywords: gas sensor, gold/polypyrrole nanorods, anodic oxidation, nanoporous alumina, pulsed galvanic deposition, electropolymerization, NO₂

1. INTRODUCTION

Gold nanostructures have attracted a great attention due to their potential application in chemical and biochemical sensing, having been used for the detection of volatile organic compounds (VOCs), medical diagnostics, and biological imaging because of their unique optical and electrical properties, high chemical stability, facile synthesis, surface functionalization and biocompatibility [1-4]. Gas sensors based on gold nanostructures have high sensitivity and selectivity, good reproducibility and long-term stability [1]. Among various shapes gold nanoparticles [4, 5] and nanorods [6, 7] have received most attention.

In order to enhance the sensing properties of gold in terms of sensitivity and selectivity, the material can be functionalized with other compounds such as biomolecules [8], conductive polymers [9-11], etc. Conductive polymers display a unique blend of material properties and the literature shows that they can also be combined with other materials, including noble metals as silver [12], gold [11], palladium [13], metal oxides e.g., ZnO [14], SnO₂ [15], carbon-based materials such as carbon nanotubes [14,15] or various form of graphene [16, 17]. The reported hybrid forms between organic and inorganic materials have a significant effect on enhanced gas sensor performance.

PPy is one of the most studied and promising conductive polymer for gas sensing [18, 19]. This material has a p-type conductive behaviour and it is attractive due to its unique features such as fast charge-discharge mechanism, high energy density and good thermal stability, and last but not least easy and low cost way of the preparation [19, 20]. PPy have been also attracted a significant attention especially in the field of chemiresistive sensors, thanks to its high conductivity which results from π -electron conjugation. The π -electron conjugation belongs to single and double bonds of chains in the aromatic ring of PPy. PPy nanostructures such as single crystal PPy nanotube [21], Au/PPy nanopeapods [10] were able to detect very low concentrations of ammonia, 0.05 ppb and 7 ppb, respectively. Also, the gas sensors based on nanostructured PPy were sensitive to different volatile organic components (VOCs) [19], e.g., sensor based on multidimensional PPy nanotubes detected ethanol in concentration as low as 1 ppm [22]. Generally, PPy can be synthesised either electrochemically [23] or chemically [24] via oxidation of pyrrole (Py) monomer.

Moreover, the gas sensing characteristics of PPy have shown to be improved by tuning its properties at the nanoscale. Nanomaterials have undoubtedly attracted the most attention among scientists as they offer high surface-to-volume ratios

• milena.setka@ceitec.vutbr.cz; phone +420 739 762 532

that allow for higher sensor sensitivity and selectivity [25, 26]. Therefore, in this work we focus on the fabrication of nanostructured inorganic/organic frameworks of AuPPy NRs for gas sensing. We use anodized alumina oxide (AAO) template for the deposition of the AuPPy NRs. This nanoporous template enables the deposition of two different materials into the pores, one inorganic (Au) and the other organic (PPy). We combined scanning electron microscopy (SEM), Energy-dispersive X-ray spectroscopy (EDX) and Raman analysis to study the morphology of nanostructures, homogeneity of surface coverage, elementary analysis and the nanostructure size.

2. EXPERIMENTAL PART

2.1. Materials

Titanium (Ti) (99.99%), tungsten (W) (99.999%), purchased from Porex, Czech Republic, and aluminium (Al) (99.999%), purchased from Goodfellow, United Kingdom, were used for the deposition of metallic layers. For the fabrication of AuPPy NRs the following chemicals were used: oxalic acid, boric acid, chromium trioxide, phosphoric acid (98%), sodium dihydrogen phosphate dihydrate (99%), obtained from Penta, Czech Republic, potassium dicyanoaurate (gold 68.3%, purity 99.9%), obtained from Safina, Czech Republic, disodium hydrogen phosphate dihydrate (98%), obtained from Fluka, Czech Republic, Py, acetonitrile and tetraethylammonium tetrafluoroborate (TEABF₄) (99%) obtained from Sigma Aldrich, USA. Deionized water (18.2 M Ω) was bought from Millipore RG system MilliQ (Millipore Corp., USA).

2.2. Preparation of AuPPy NRs

AuPPy NRs were synthesized via combination of three techniques: electrochemical anodization, pulsed galvanic deposition and electropolymerization. The schematic illustration of each step of fabrication process of AuPPy NRs is shown in *Figure 1*.

In order to isolate the nanostructures from n-doped silicon (Si) and thus minimize junction effects at the interface between Si and other metal layers, 4 inch Si wafer covered with 1 μ m layer of SiO₂ was used as starting substrates. Subsequently, Ti layer (20 nm thick), W layer (150 nm thick) and Al layer (500 nm thick) were sputter-deposited by ion beam sputtering method on the wafer, using a RFICP Kaufman ion-beam source (KRI®) (*Figure 1 a*). Au layer (50 nm thick) was sputter-deposited under the W layer to provide better visibility of the not anodized (pristine) W just for the later cross-section analysis in scanning electron microscope (SEM).

The wafer was cut it into pieces (1.5x1.5 mm) and each piece was electrochemically anodized in a two electrode system with potentiostatic (constant potential) mode. Al layer was used as working electrode and an inox (stainless steel) tube as counter electrode. The electrochemical anodization of Al and W was carried out in 0.3 M oxalic acid at 40 V with the electrolyte temperature at 10 °C. These conditions led to the transformation of Al layer into the nanoporous AAO template (*Figure 1 b*). After anodizing Al, the process was prolonged for 100 s to oxidize the bottom tungsten layer and create tungsten trioxide (WO₃) nanodots (*Figure 1 c*), which were selectively etched in a phosphate buffer solution (pH= 7, T=25 °C). This etching process created W nano-dimpled structure on the surface, which were used as a base for the Au NRs to improve their stability. (*Figure 1 d*)

After the etching process of WO₃ nanodots, washing and drying of the samples the pulsed galvanic deposition of Au was carried out in the two electrode cell (the same as electrochemical anodization), with galvanostatic (under constant current) mode using a potassium dicyanoaurate solution. This deposition process was performed applying 35 pulses with current of 1 mA, pulse length of 400 ms, period between pulses of 2 s and voltage amplitude of 5 V (*Figure 1 e*). A different number of applied pulses in the range between 30 and 65 pulses were performed during the deposition process of Au, finding optimum conditions when using 35 pulses. Thus 35 pulses were employed for further studies. When 1/3 of AAO pores was filled with Au, the electrochemical deposition of PPy was performed. Thus, PPy was deposited in potentiostatic (constant potential) mode at room working temperature, using a two electrode cell and applying a voltage of 2 V for 120 s during the electropolymerization. The PPy reaction was carried out in a solution, containing a mixture of Py monomer and anionic doping salt, TEABF₄, dissolved in acetonitrile solvent. The molar ratio between Py monomer and TEATFB was 2:1. (*Figure 1 f*). Finally the AAO template was selectively etched to free the AuPPy NRs by immersing the samples in the aqueous solution of chromium trioxide and phosphoric acid at 60 °C for 600 s. (*Figure 1 g*)

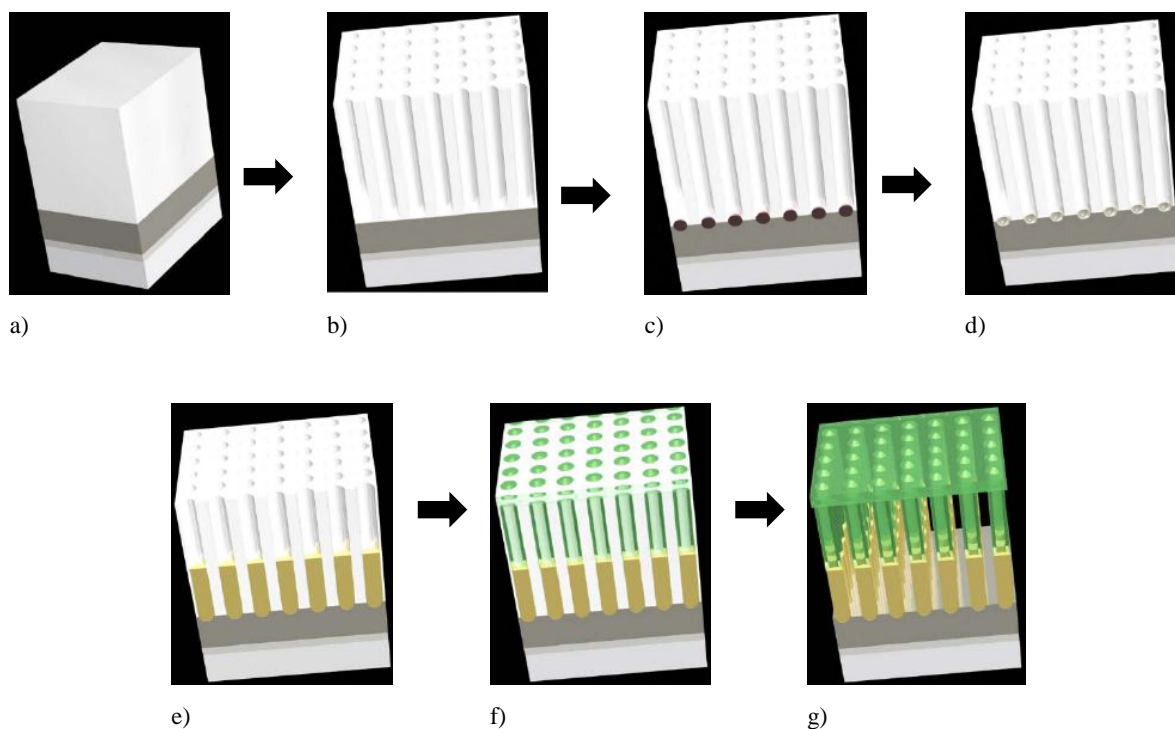


Figure 1. Schematic illustration of the fabrication process of AuPPy NRs; a) From bottom to top Si wafer covered with: 1 μm SiO_2 , 20 nm Ti, 150 nm W, and 500 nm Al; b) AAO template after the electrochemical anodization of the Al in 0.3 M oxalic acid; c) AAO template after the oxidation of W, and creation of WO_3 nanodots; d) AAO template after the etching of WO_3 nanodots in phosphate buffer forming the nanodimpled surface; e) Au deposition using potassium dicyanoaurate solution; f) PPy deposition using solution of Py monomer and TEABF₄ in acetonitrile; g) AuPPy NRs after the selective etching of AAO template;

2.3. Fabrication and sensor characterization

In order to observe the gas sensing measurements of the AuPPy NRs, the structures were connected with top and bottom Ag electrodes (electrode gap: 8 mm) employing a commercial ink (Heraeus, AD1688-06). The top electrode was connected to the active layer (PPy part) and the bottom electrode to the aluminium substrate. (Figure 2 a) Substrates were glued to a hotplate in order to measure the gas response at different operating temperatures, if required (Figure 2 b). The delivery and mixing of gases were performed employing a mass flow system consisting computer-controlled mass-flow controllers (Bronkhorst hi-tech 7.03.241), as described previously [27].

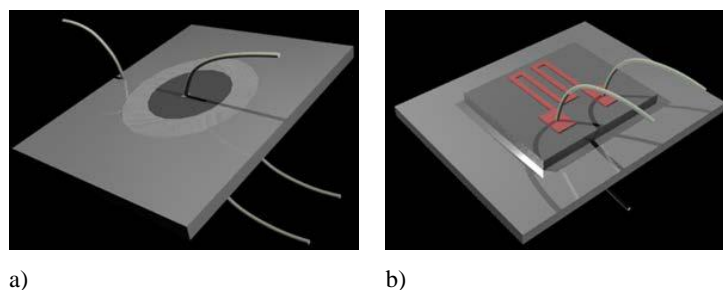


Figure 2. Schematic representation of the sensors a) deposition of the bottom-top Au electrodes; b) gluing of the hotplate at the backside of the substrate.

2.4. Characterization of AuPPy NR

Morphology analysis were examined by TESCAN MIRA II field emission SEM equipped with EDX analysis. Raman analysis was carried out using a Renishaw InVia Raman microscope employing 633 nm laser beam, and the spectra were recorded at a power lower than 1 mW, and using 20× objective.

3. RESULTS AND DISCUSSION

3.1. Morphology analysis

SEM images of the WO_3 nanodots before (left, schematically illustrated in Figure 1c) and after (right, schematically illustrated in Figure 1d) the AAO template etching are presented in Figure 3a. The choice of optimal fabrication conditions (i.e. 0.3 M oxalic acid and applied voltage of 40 V) provided homogeneous surface coverage and uniform nanopore size with the diameter of about 50 nm. The SEM analysis also shows homogeneous AAO templates suitable for electrochemical deposition of Au NRs with diameter pores of 50 nm. The electrochemical deposition of Au into nanoporous alumina template was successfully achieved and the homogeneous surface of gold nanorods is displayed in Figure 3b (this correspond to step Figure 1e of the fabrication process). The diameter of the Au NRs was approximately 50 nm and the length was about 250 nm. We noticed that the length of the Au NRs was dependent on the number of applied pulses during the pulsed galvanic deposition, and we found optimal conditions when applying 35 pulses. Figure 3c presents a SEM image of the AuPPy NRs (Figure 1g – fabrication part). It can be seen that AuPPy NRs appeared in the ‘sandwich structure’, connected from the bottom part with the metallic layer of W (100 nm thick) and from the top part covered with the over deposited layer of PPy (100 nm thick). The top layer of PPy served as electrical contact for the fabrication of gas sensor and the thickness of the layer was influenced by the electropolymerization time. AuPPy NRs arrays were grown perpendicularly to the W layer, and they are well packed and have uniform diameters of 50 nm, similarly to the Au NRs without PPy. The total length of the AuPPy NRs is 700 nm, where the Au and PPy parts take 1/3 and 2/3 of the total length. SEM analysis confirmed that almost each pore of the template is filled with AuPPy NRs, which indicates a good efficiency and high density of nanorods arrays along the substrate.

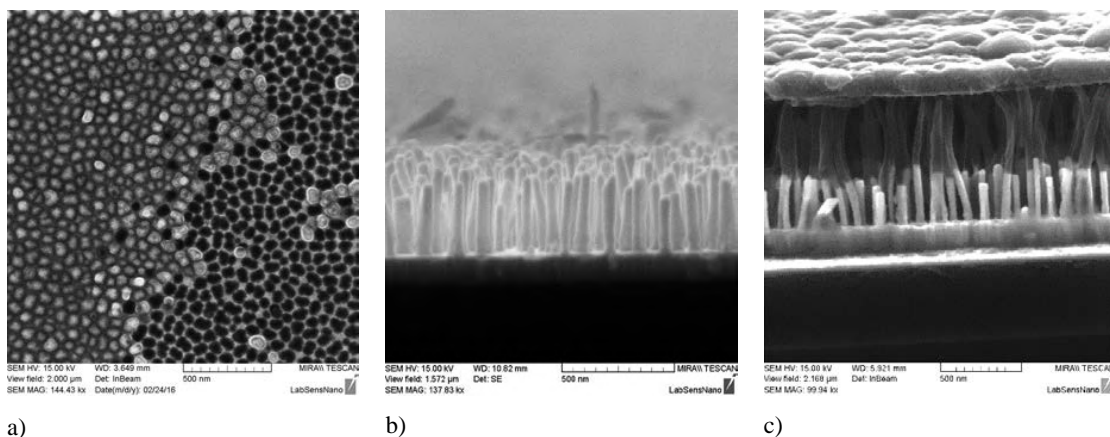


Figure 3. a) SEM image of AAO template with WO_3 nanodots (left half of the image), and after etching of WO_3 nanodots (right half of the image); electrochemical anodization of W/Al bilayer in 0.3 M oxalic acid at 40 V; b) SEM image of Au NRs after the etching of Al_2O_3 , the number of applied pulses: 35; c) SEM image of the AuPPy NRs after the etching of Al_2O_3 , electropolymerization time of 120 s.

3.2. Chemical analysis (EDX and RAMAN)

The relative amount of the different elements presented in the AuPPy NRs were determined using an EDX point analysis and the corresponding results are shown in Figure 4 and Table 1. The presence of W and Au is associated with

spectrum 1, which corresponds to Au NRs. The relative amount of oxygen (O), nitrogen (N) and carbon (C) belong to spectrum 2, which is related with PPy part as expected.

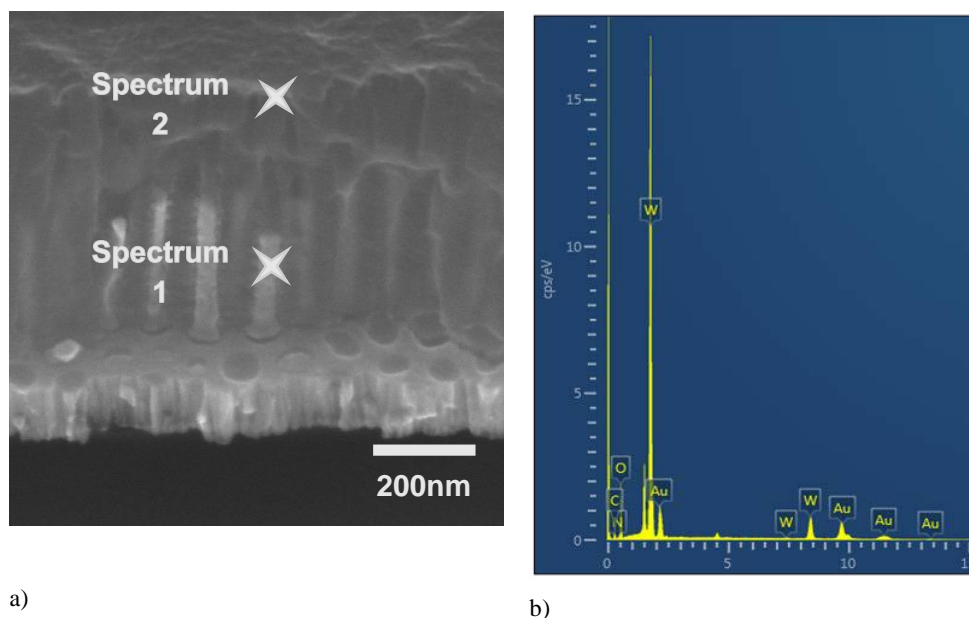


Figure 4. EDX analysis of AuPy NRs; a) SEM image; b) EDX spectra

Table 1. EDX analysis of AuPPy NRs

| Element | Line Type | Spectrum 1 (Wt%) | Spectrum 2 (Wt%) |
|---------------|-----------|------------------|------------------|
| N | K series | 1.02 | 1.17 |
| O | K series | 41.10 | 48.23 |
| W | L series | 38.14 | 36.89 |
| Au | L series | 19.74 | 13.71 |
| Total: | | 100.00 | 100.00 |

Raman spectroscopy was performed to characterize the structure of the synthesized nanostructures. Figure 5 shows the Raman spectrum of AuPPy NRs at room temperature. The characteristic Raman peaks positions of the AuPPy NRs and their comparison with the literature reports for other PPy structures and Au/PPy composites are shown in Table 2.

Table 2. Characteristic Raman peaks and representing bond stretching of PPy structures and Au/PPy composites

| | | Peaks assignments | | | | |
|------------|---|-------------------------|----------------------|-----------------|-----------------------------|---|
| Morphology | Raman peaks position (cm ⁻¹) | C=C backbone stretching | C-N stretching | Ring stretching | C-H plane bending vibration | Ring deformation vibrations associated with the polarons/bipolarons |
| | AuPPy NRs | 1586 | 1406 and 1320 | 1258 | 1045 | 983/926 |
| | PPy nanofibers [28] | 1607 | 1394 and 1323 | 1257 | 1076 and 1046 | 982/929 |
| | PPy films decorated with Au nanoparticles [29] | 1592 | 1372 | - | 1081 and 1050 | 971/934 |
| | PPy films [30] | 1599 | 1375 | 1250 | 1082 and 1052 | 930 |
| | PPy nanoparticles [31] | 1596 | 1355 | 1237 | 1086 and 1055 | 986/934 |
| | PPy/nanoporous Au composite [32] | 1581 | - | - | 1070 and 1053 | 987/941 |

The Raman peaks obtained for AuPPy NRs come from PPy part of the NRs. The peaks which appeared at the wavenumber in the range between 1580–1620 cm⁻¹ are related to the C=C backbone stretching [33, 34]. Therefore, if we look at the wavenumber arrange of the C=C backbone stretching bonds, we can see that the structures based on pure PPy has this peak shifted o higher wavenumber (closer to 1600 cm⁻¹). However, the mixtures of PPy with the noble metals such as gold had shifted peak to smaller wavenumber (closer to 1800 cm⁻¹). This peak for our AuPPy NRs was presented at 1586 cm⁻¹. The peaks at 1406 and 1320 cm⁻¹ are attributed to the antisymmetric C–N stretching of PPy [28] and the peak at 1258 cm⁻¹ is assigned to the ring stretching of the PPy [28], whereas the peak located at 1045 cm⁻¹ is related to the symmetrical C–H in-plane bending [35]. The peaks at 984 and 927 cm⁻¹ are associated with the polaron and bipolaron structure, and they are assigned to ring deformation vibrations [28]. These results demonstrate that AuPPy NRs Raman spectra is consistent with previously reported PPy based materials.

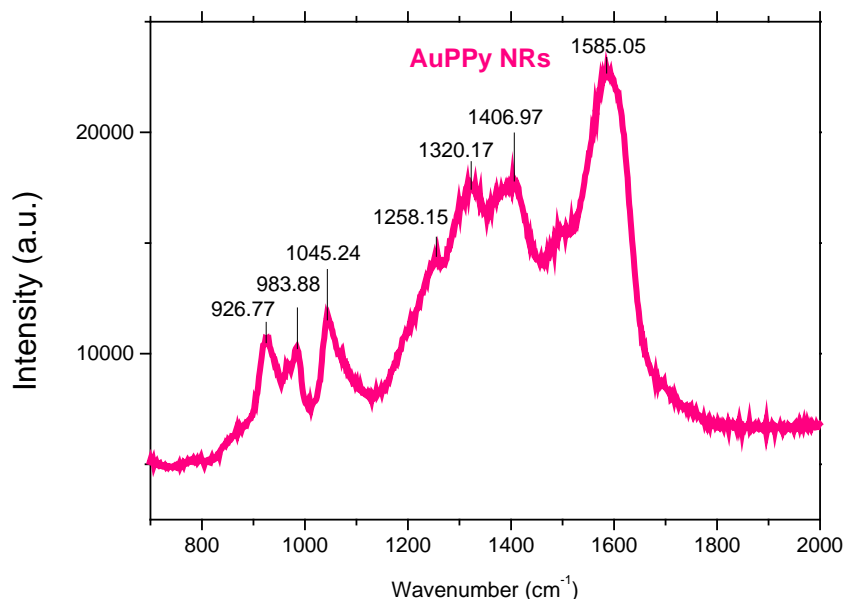


Figure 5. Raman spectrum of AuPPy NRs

3.3. Gas sensing

AuPPy NRs were tested towards different concentrations (25, 50 and 100, ppm) of NO_2 in dry air by means of DC resistance measurements at room temperature. PPy is a p-type material and when it interacts with oxidizing gases such as NO_2 , there is an increase in charge carrier concentration, as NO_2 behaves as an electro-acceptor. This results in creation of new charge carriers (holes), and in turn in the increment of conductivity (decrement of the electrical resistance) [36]. However, our tests showed negligible resistance changes to this gas, (even when increasing the temperature above room temperature), showing a constant electrical resistance of 42 k Ω at room temperature that changed to 39.5 k Ω after exposure to NO_2 without finding a steady state. Previous works in the literature also stated the low sensitivity of chemoresistive PPy based gas sensors to NO_2 , for instance Hernandez et al. demonstrated insensitive PPy structures to NO_2 [37], similarly Tai et al.[38] reported unchanged electrical resistance when TiO_2 /PPy nanocomposite sensors were exposed to NO_2 . The literature also state that the sense of ammonia and other type of analytes that behave as electron-donors have a higher affinity to the PPy structure [19]. Thus, further work on the tests of other gaseous molecules, including ammonia, for validation of our system is in progress.

4. CONCLUSIONS

In summary, the synthesis of inorganic/organic framework AuPPy NRs has been demonstrated using nanoporous AAO template prepared via electrochemical anodization of Al, and successfully deposition of Au and PPy into the AAO template via pulsed galvanic deposition and electropolymerization, working with the two electrode system. Optimal synthesis conditions, including the number of applied pulses and electropolymerization time, resulted in the creation of the 'sandwich structure' morphologies of AuPPy NRs with pore diameters of 50 nm and lengths of 700 nm, approximately. The gas sensing test of these systems towards NO_2 showed negligible response, however in light of the literature reports for PPy other gaseous species, such as ammonia, have been considered for the validation of these system in the future.

Acknowledgments:

This work has been supported by the Czech Science Foundation (GAČR) via Grant no. 17-16531S and via Nanotechnologies and Novel Materials II, Grant no. STI-S-17-4755.

References

- [1] L. M. Zanolì, R. D'Agata, and G. Spoto, "Functionalized gold nanoparticles for ultrasensitive DNA detection," *Analytical and Bioanalytical Chemistry*, 402(5), 1759-1771 (2012).
- [2] J. Drbohlavová, H. Kynčlová, R. Hrdý *et al.*, "Gold Nanostructured Surface for Electrochemical Sensing and Biosensing: Does Shape Matter?," *Analytical Letters*, 49(1), 135-151 (2016).
- [3] H. Li, and Y.-W. Yang, "Gold nanoparticles functionalized with supramolecular macrocycles," *Chinese Chemical Letters*, 24(7), 545-552 (2013).
- [4] G. Peng, U. Tisch, O. Adams *et al.*, "Diagnosing lung cancer in exhaled breath using gold nanoparticles," *Nature Nanotechnology*, 4(10), 669-673 (2009).
- [5] S. Zhang, P. Song, J. Zhang *et al.*, "Highly sensitive detection of acetone using mesoporous In₂O₃ nanospheres decorated with Au nanoparticles," *Sensors and Actuators B: Chemical*, 242, 983-993 (2017).
- [6] M. E. Nasir, W. Dickson, G. A. Wurtz *et al.*, "Hydrogen Detected by the Naked Eye: Optical Hydrogen Gas Sensors Based on Core/Shell Plasmonic Nanorod Metamaterials," *Advanced Materials*, 26(21), 3532-3537 (2014).
- [7] L. T. Lanh, T. T. Hoa, N. D. Cuong *et al.*, "Shape and size controlled synthesis of Au nanorods: H₂S gas-sensing characterizations and antibacterial application," *Journal of Alloys and Compounds*, 635, 265-271 (2015).
- [8] D. Compagnone, G. C. Fusella, M. Del Carlo *et al.*, "Gold nanoparticles-peptide based gas sensor arrays for the detection of food aromas," *Biosensors & Bioelectronics*, 42, 618-625 (2013).
- [9] R. Khalil, S. Homaeigohar, D. Haussler *et al.*, "A shape tailored gold-conductive polymer nanocomposite as a transparent electrode with extraordinary insensitivity to volatile organic compounds (VOCs)," *Scientific Reports*, 6, 10 (2016).
- [10] Y. R. Yan, M. L. Zhang, C. H. Moon *et al.*, "Viral-templated gold/polypyrrole nanopeapods for an ammonia gas sensor," *Nanotechnology*, 27(32), 9 (2016).
- [11] J.-S. Lee, N.-R. Yoon, B.-H. Kang *et al.*, "Au-Polypyrrole Framework Nanostructures for Improved Localized Surface Plasmon Resonance Volatile Organic Compounds Gas Sensing," *Journal of Nanoscience and Nanotechnology*, 15(10), 7738-7742 (2015).
- [12] A. Choudhury, "Polyaniline/silver nanocomposites: Dielectric properties and ethanol vapour sensitivity," *Sensors and Actuators B: Chemical*, 138(1), 318-325 (2009).
- [13] A. A. Athawale, S. V. Bhagwat, and P. P. Katre, "Nanocomposite of Pd-polyaniline as a selective methanol sensor," *Sensors and Actuators B: Chemical*, 114(1), 263-267 (2006).
- [14] J. Huang, T. L. Yang, Y. F. Kang *et al.*, "Gas sensing performance of polyaniline/ZnO organic-inorganic hybrids for detecting VOCs at low temperature," *Journal of Natural Gas Chemistry*, 20(5), 515-519 (2011).
- [15] M. Joulazadeh, and A. H. Navarchian, "Ammonia detection of one-dimensional nano-structured polypyrrole/metal oxide nanocomposites sensors," *Synthetic Metals*, 210, 404-411 (2015).
- [16] S. G. Bachhav, and D. R. Patil, "Study of Polypyrrole-Coated MWCNT Nanocomposites for Ammonia Sensing at Room Temperature," *Journal of Materials Science and Chemical Engineering*, 3, 30-44 (2015).
- [17] A. Daneshkhan, S. Shrestha, M. Agarwal *et al.*, "Poly(vinylidene fluoride-hexafluoropropylene) composite sensors for volatile organic compounds detection in breath," *Sensors and Actuators B: Chemical*, 221, 635-643 (2015).
- [18] J. J. Miasik, A. Hooper, and B. C. Tofield, "Conducting polymer gas sensors," *Journal of the Chemical Society-Faraday Transactions I*, 82, 1117-& (1986).
- [19] M. Šetka, J. Drbohlavová, and J. Hubálek, "Nanostructured Polypyrrole-Based Ammonia and Volatile Organic Compound Sensors," *Sensors*, 17, (2017).
- [20] S. Lee, M. S. Cho, J. D. Nam *et al.*, "Fabrication of Polypyrrole Nanorod Arrays for Supercapacitor: Effect of Length of Nanorods on Capacitance," *Journal of Nanoscience and Nanotechnology*, 8(10), 5036-5041 (2008).
- [21] M. Q. Xue, F. W. Li, D. Chen *et al.*, "High-Oriented Polypyrrole Nanotubes for Next-Generation Gas Sensor," *Advanced Materials*, 28(37), 8265-8270 (2016).
- [22] O. S. Kwon, S. J. Park, H. Yoon *et al.*, "Highly sensitive and selective chemiresistive sensors based on multidimensional polypyrrole nanotubes," *Chemical Communications*, 48(85), 10526-10528 (2012).

- [23] L. Zhang, F. Meng, Y. Chen *et al.*, "A novel ammonia sensor based on high density, small diameter polypyrrole nanowire arrays," *Sensors and Actuators B: Chemical*, 142(1), 204-209 (2009).
- [24] O. S. Kwon, J. Y. Hong, S. J. Park *et al.*, "Resistive Gas Sensors Based on Precisely Size-Controlled Polypyrrole Nanoparticles: Effects of Particle Size and Deposition Method," *Journal of Physical Chemistry C*, 114(44), 18874-18879 (2010).
- [25] Y. Y. Broza, and H. Haick, "Nanomaterial-based sensors for detection of disease by volatile organic compounds," *Nanomedicine*, 8(5), 785-806 (2013).
- [26] G. Konvalina, and H. Haick, "Sensors for Breath Testing: From Nanomaterials to Comprehensive Disease Detection," *Accounts of Chemical Research*, 47(1), 66-76 (2014).
- [27] S. Vallejos, V. Khatko, J. Calderer *et al.*, "Micro-machined WO₃-based sensors selective to oxidizing gases," *Sensors and Actuators B-Chemical*, 132(1), 209-215 (2008).
- [28] M. Li, Z. X. Wei, and L. Jiang, "Polypyrrole nanofiber arrays synthesized by a biphasic electrochemical strategy," *Journal of Materials Chemistry*, 18(19), 2276-2280 (2008).
- [29] E. G. Pineda, F. Alcaide, M. J. R. Presa *et al.*, "Electrochemical Preparation and Characterization of Polypyrrole/Stainless Steel Electrodes Decorated with Gold Nanoparticles," *Acs Applied Materials & Interfaces*, 7(4), 2677-2687 (2015).
- [30] Y.-C. Liu, "Characteristics of vibration modes of polypyrrole on surface-enhanced Raman scattering spectra," *Journal of Electroanalytical Chemistry*, 571(2), 255-264 (2004).
- [31] T. M. Wu, and S. H. Lin, "Characterization and electrical properties of polypyrrole/multiwalled carbon nanotube composites synthesized by in situ chemical oxidative polymerization," *Journal of Polymer Science Part B-Polymer Physics*, 44(10), 1413-1418 (2006).
- [32] Y. Hou, L. Zhang, L. Y. Chen *et al.*, "Raman characterization of pseudocapacitive behavior of polypyrrole on nanoporous gold," *Physical Chemistry Chemical Physics*, 16(8), 3523-3528 (2014).
- [33] H. N. T. Le, M. C. Bernard, B. Garcia-Renaud *et al.*, "Raman spectroscopy analysis of polypyrrole films as protective coatings on iron," *Synthetic Metals*, 140(2-3), 287-293 (2004).
- [34] Y. C. Liu, "Characteristics of vibration modes of polypyrrole on surface-enhanced Raman scattering spectra," *Journal of Electroanalytical Chemistry*, 571(2), 255-264 (2004).
- [35] Y.-C. Liu, and B.-J. Hwang, "Identification of oxidized polypyrrole on Raman spectrum," *Synthetic Metals*, 113(1-2), 203-207 (2000).
- [36] H. Yoon, and J. Jang, "Conducting-Polymer Nanomaterials for High-Performance Sensor Applications: Issues and Challenges," *Advanced Functional Materials*, 19(10), 1567-1576 (2009).
- [37] S. C. Hernandez, D. Chaudhuri, W. Chen *et al.*, "Single polypyrrole nanowire ammonia gas sensor," *Electroanalysis*, 19(19-20), 2125-2130 (2007).
- [38] H. L. Tai, Y. D. Jiang, G. Z. Xie *et al.*, "Self-assembly of TiO₂/polypyrrole nanocomposite ultrathin films and application for an NH₃ gas sensor," *International Journal of Environmental Analytical Chemistry*, 87(8), 539-551 (2007).

Chapter 5

Love wave sensors based on polypyrrole modified with catalytic metal nanoparticles

5.1 Motivation

Due to the complexity to fabricate functional sensing devices based on PPy NRs and the poor sensitivity observed in the preliminary studies discussed in previous chapter, the fabrication and tests of PPy were directed to the use of PPy NPs due to their simple synthesis and easy implementation with the electronic system using different coating techniques (e.g., spin coating, drop coating). In Section 2.1 it was found that the use of hybrid sensing materials ensures the development of gas sensors with enhanced sensing performances. As there is a lack of literature reports related to SAW sensors (especially those with L-SAW principle) based either on bare PPy or PPy modified with other materials (e.g., metallic particles), their development was investigated in this thesis. This chapter describes the fabrication of L-SAW sensors based on non-modified PPy NPs and PPy NPs modified with Au and Ag NPs, and their gas sensing tests toward the target gases.

5.2 Outputs

The scientific contribution related to the study of metal modified PPy were disseminated in a journal article, *Love wave sensors based on gold nanoparticle-modified polypyrrole and their properties to ammonia and ethylene* [213] (Section 5.4.1). This work discuss the use of non-modified and Au modified PPy layers for sensing of ammonia and ethylene. Non-modified and modified PPy layers with two different Au loadings (1:10 and 1:2) were implemented into multi-guiding L-SAW transducing platforms using spin coating technique. Microscopic (SEM, TEM, AFM) and spectrometry (TOF-SIMS) characterization methods confirmed the presence of both components (PPy and Au NPs) in the prepared sensors. All of three types of developed L-SAW sensors (bare PPy, Au/PPy (1:10) and Au/PPy (1:2)) responded to ammonia and ethylene in the concentration range of 2 to 10 ppm at RT. The sensors based on Au/PPy demonstrated enhanced sensing performances over bare PPy sensors. The estimated detection of ammonia up to 67 ppb and ethylene up to 87 ppb in dry conditions may be feasible using Au/PPy (1:10) and Au/PPy (1:2) L-SAW sensors, respectively. These results are presented in *Journal article 3*–

As the Au modified PPy L-SAW sensors showed improved sensing properties (e.g., higher response) over non-modified PPy sensors, the functionalization of PPy with other catalytic metals was investigated in this thesis. Therefore, the second scientific contribution from this section includes the study of Ag/PPy L-SAW towards VOCs (acetone, ethanol and toluene) in dry and wet environment at RT. These results was summarized in a journal article, *Love Wave Sensors with Silver Modified Polypyrrole Nanoparticles for VOCs Monitoring* [214] (Section 5.4.2). Ag/PPy L-SAW were proven functional with high response, namely the sensitivity of 910 Hz/ppm for acetone, 742 Hz/ppm for ethanol and 340 Hz/ppm for toluene, and response time bellow 2.5 min. Ag/PPy sensors showed enhanced performances compared to bare PPy sensors but also to other state of the art SAW sensors. The LOD of the Ag/PPy

L-SAW sensors was estimated to be 3, 5 and 20 ppb for acetone, ethanol and toluene, respectively. The achieved sensitivity of these sensors to all tested VOCs makes them suitable candidates for real application, as the concentration ranges of those VOCs found in the human breath, food and environment analysis are above LOD obtained for Ag/PPy sensors. Moderate response of Ag/PPy L SAW sensors was observed in wet air (with 10 and 30 % RH) compared to dry environment.

Moreover, for comparison purposes, PPy NPs, Au/PPy and Ag/PPy layers were integrated with chemo-resistive transducing platforms using the same preparation procedure as for the deposition of those sensitive layers in L-SAW sensors, i.e. spin coating. The sensors were tested to 80 ppm of ethanol. The sensors showed extremely high resistance in $G\Omega$ range with the difficulty to be measured with the standard equipment. Only Au/PPy sensors showed response to ethanol which was measurable. These results are included in Appendix A.

5.3 Conclusions

In summary, the selection of PPy NPs as a primary gas sensing material of investigation together with the simple and repeatable fabrication of micro sensing elements based on L-SAW principle turned out to be the right decision. The obtained results showed the positive response of the fabricated sensors to all target gases. High response of PPy based L-SAW sensors to low concentration (in ppb levels for acetone, ethanol and toluene) at RT met the expectations which were set up in the beginning of this thesis. Generally, the sensors based on organic-inorganic hybrid materials showed the enhanced sensing performances over non-modified (bare PPy). Therefore, the further direction of this thesis was established on exploring new PPy nanocomposites and their implementation in L-SAW sensors, as the last proved better sensing properties over chemo-resistive sensors.

5.4 Articles

5.4.1 Journal article 3

Šetka, M., Bahos, F.A., Matatagui, D., Potoček, M., Kral, Z., Drbohlavová, J., Gràcia, I., Vallejos, S., *Love wave sensors based on gold nanoparticle-modified polypyrrole and their properties to ammonia and ethylene. Sensors and Actuators B: Chemical*, 304, 2019, doi:10.1016/j.snb.2019.127337.

5.4.2 Journal article 4

Šetka, M., Bahos, F.A., Matatagui, D., Gràcia, I., Figueras, E., Drbohlavová, J., Vallejos, S., *Love wave sensors with silver modified polypyrrole nanoparticles for VOCs monitoring, Sensors*, 20, 2020, doi:10.3390/s20051432.



Love wave sensors based on gold nanoparticle-modified polypyrrole and their properties to ammonia and ethylene

M. Šetka^a, F.A. Bahos^b, D. Matatagui^b, M. Potoček^a, Z. Kral^d, J. Drbohlavová^a, I. Gràcia^c, S. Vallejos^{a,c,*}

^a CEITEC - Central European Institute of Technology, Brno University of Technology, 61200, Brno, Czech Republic

^b Instituto de Ciencias Aplicadas y Tecnología (ICAT), Universidad Nacional Autónoma de México, Ciudad Universitaria, Ciudad de México, 04510, Mexico

^c Instituto de Microelectrónica de Barcelona (IMB-CNM, CSIC), Campus UAB, 08193, Bellaterra, Spain

^d Thermo Fisher Scientific, Analytical Instruments - Materials and Structural Analysis, Hillsboro, OR 97123, USA



ARTICLE INFO

Keywords:
Gas sensors
SAW sensors
Polypyrrole

ABSTRACT

This work presents the fabrication and gas sensing properties of Love wave sensors based on non-modified and gold nanoparticle-modified polypyrrole. Results demonstrate the integration of uniform polypyrrole layers with smooth granular surface and the incorporation of dispersed crystalline gold nanoparticles within the modified layers. Gas sensing tests of the sensors in dry conditions show enhanced sensing performance to ethylene and ammonia for the modified systems as compared to those without modification and those reported in the literature. The effect of humidity proves significant in both systems with the results showing a decrease of sensitivity in humid conditions. Despite this weakness, the relatively facile and scalable fabrication of these sensors, as well as their sensing response at room temperature may be attractive in gas detection systems, in which high humidity levels can be restricted by the use of filter or preconditioning elements.

1. Introduction

Over the last decades, piezoelectric acoustic devices have gained enormous interest for sensor applications, including gas sensors, because of their operation at room temperature (RT), high sensitivity, low limits of detection (LOD), relatively easy fabrication and low cost. Against a host of competing technologies for piezoelectric acoustic sensors, surface acoustic wave (SAW) based gas sensors have gained more interest than their bulk acoustic wave (BAW) counterparts, generally due to their higher operating frequency and in turn higher sensitivity [1].

In SAW sensors, the propagation of acoustic wave (either Rayleigh, Shear Horizontal SAW, Love, Leaky, Stoneley, or Lamb waves) is limited to the surface and tuned in part by the cut of the piezoelectric crystal [[2]]. In particular, Love SAW (L-SAW) based sensors allow effective guidance of the wave close to the sensing surface by confining the wave energy in a thin guiding layer. This slows the velocity of the wave with respect to the piezoelectric substrate and make the surface highly sensitive to small perturbation [3]. To this end, elastic layers such as SiO₂ are commonly used on the top of piezoelectric substrates as guiding layers (particularly due to their low acoustic loss), but they cannot achieve a very high sensitivity due to shear stiffness. However,

other materials, such as polymers, with slower transverse wave velocity and lower density than SiO₂ (due to their viscoelastic properties) can also serve as guiding layers, providing further advantages in terms of sensitivity, although with greater propagation loss than SiO₂. In this context, a multiguiding layer concept, in which elastic and viscoelastic properties of SiO₂ and polymer are balanced is generally more advantageous [4]. The Love wave propagation and the attenuation are strongly dependent on the properties of the guiding layer, including the thickness and stiffness, thus with the optimal thickness of the multiguiding layers is possible to achieved the high sensitive L-SAW sensors with appropriate attenuation of the wave [3,5]. Additionally, the specific use of gas sensitive polymers in the multiguiding layer, which interact physically/chemically with the analytes, can also provide further enhancement in terms of sensitivity and selectivity via polymer modification or functionalization [1b,2b].

Polypyrrole (PPy) is a conductive polymer that has proved sensitivity to various gases and organic vapours, including ammonia, ethanol, and acetone [6]. In general, PPy was integrated in chemiresistive sensors, and so far, only few examples of the use of PPy in SAW sensors were reported in the literature. These examples include SAW sensors based on Rayleigh waves to detect ammonia [[7]], acetone[7c], NO₂ [8] and H₂S [8], or shear horizontal SAW (e.g., Leaky) to detect

* Corresponding author at: CEITEC - Central European Institute of Technology, Brno University of Technology, 61200, Brno, Czech Republic.
E-mail addresses: stella.vallejos@imb-cnm.csic.es, vargas@feec.vutbr.cz (S. Vallejos).

<https://doi.org/10.1016/j.snb.2019.127337>

Received 9 July 2019; Received in revised form 19 October 2019; Accepted 23 October 2019

Available online 30 October 2019

0925-4005/© 2019 The Author(s). Published by Elsevier B.V. This is an open access article under the CC BY-NC-ND license (<http://creativecommons.org/licenses/by-nc-nd/4.0/>).

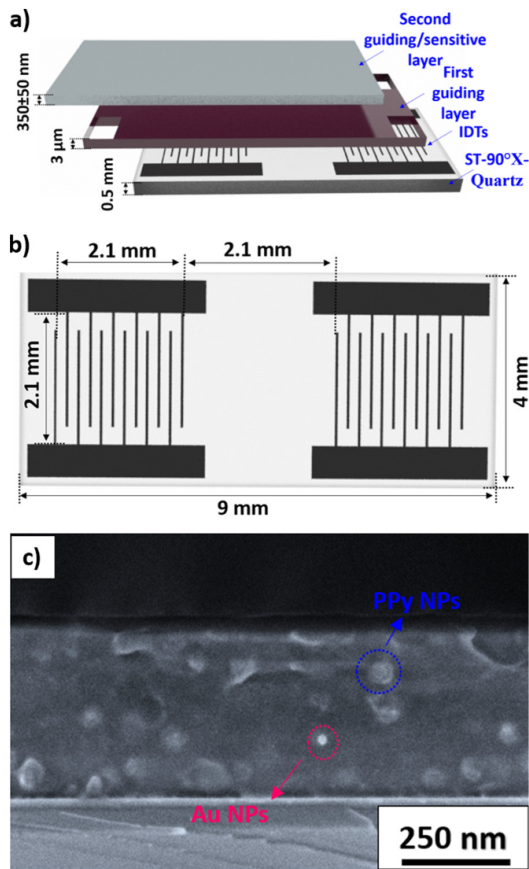


Fig. 1. (a) (b) Schematic view of the L-SAW sensing element. SEM-image of the PPY guiding/sensitive layer modified with Au NPs after spin coating; notice the difference in brightness/contrast of the PPY grains and the Au NPs.

hydrogen [9]. According to published research, we found that the utilization of PPY in L-SAW sensors is less common. However, our recent preliminary results [10] showed the potential of PPY-based L-SAW sensors to detect low concentrations of ammonia.

Certainly, the synthesis route of PPY defines its gas sensing properties, and although there are various available electrochemical or chemical routes for the synthesis of nanoscaled PPY, the integration of PPY with SAW platforms using chemical routes is yet more scalable and relatively easier. Furthermore, chemical routes also facilitate the functionalization of PPY with diverse nanosized materials, including noble metals, carbon-based materials or metal oxides.

The potential application of L-SAW sensors in early disease diagnosis may be promising due to their high sensitivity and low LOD [1b], which are in the ppb range as those of specific gas biomarkers contained in human breath [11]. For instance, ethylene and ammonia have found to be relevant biomarkers of oxidative stress (OS), a condition that damages the cells in human body and can lead eventually to chronic diseases such as atherosclerosis, cancer, diabetes, cardiovascular, neurodegenerative and other degenerative diseases in humans [12]. This condition is generally caused by the presence of reactive oxygen species (ROS) in the body [13], which cause oxidative degradation (lipid peroxidation) of polyunsaturated fatty acids and thus release of ethylene in human breath [14]. The increment of ROS, moreover, has recently found to be also connected to the accumulation of uremic toxins caused by kidney dysfunctions and in turn to the release of ammonia gas in exhaled breath [15].

In this context, the present study reports the fabrication of

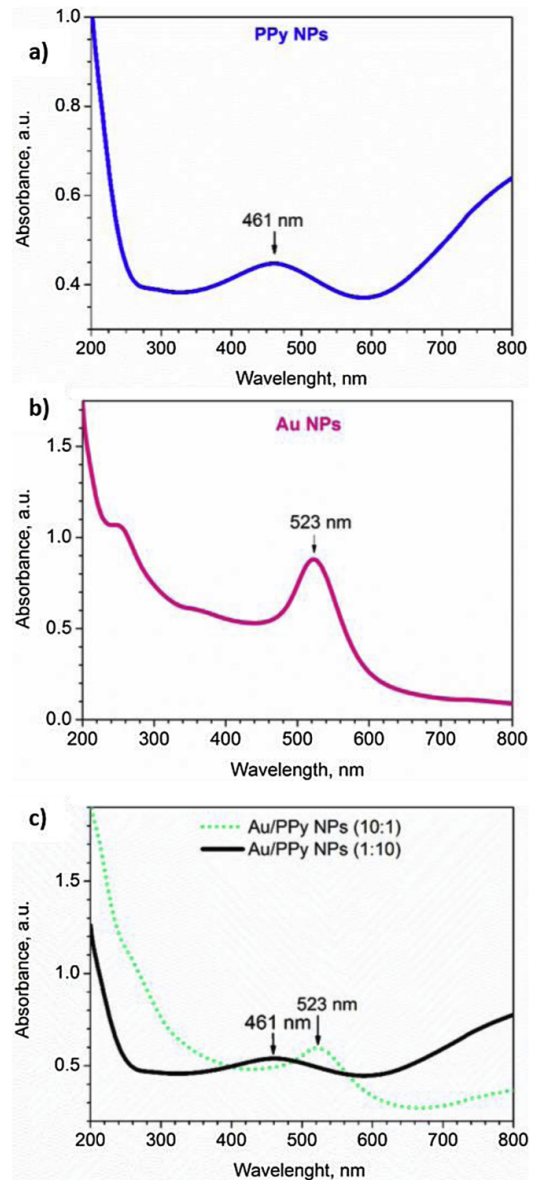


Fig. 2. UV-vis analysis of (a) PPY NPs, (b) Au NPs, (c) Au/PPy NPs (1:10, black color) and Au/PPy NPs (10:1, green color). (For interpretation of the references to colour in this figure legend, the reader is referred to the web version of this article).

multiguiding L-SAW sensors based on SiO₂ and gas sensitive PPY nanoparticles (NPs) functionalized with gold NPs. The work deepens into the properties of the second guiding layer and the influence of two different gold loadings on the sensing functionality towards low concentrations of ammonia and ethylene as potential gaseous biomarkers.

2. Experimental

2.1. Synthesis of PPY and Au/PPy NPs

PPy NPs were obtained via oxidative chemical polymerization of pyrrole monomer, as described previously [16]. In the first step, polyvinyl alcohol (PVA, 7.5 g) was dissolved in 92.5 ml of deionized water,

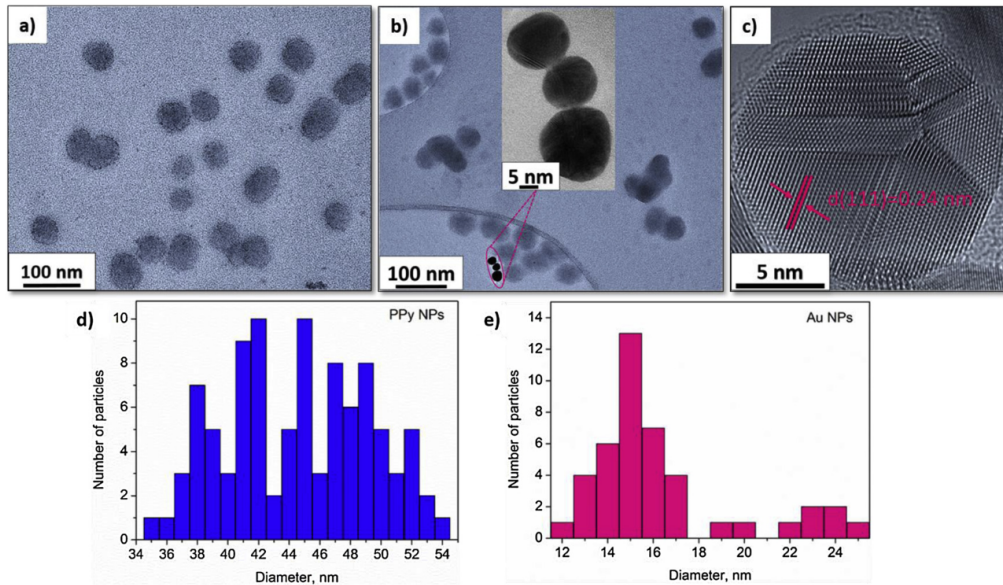


Fig. 3. HR-TEM images of the (a) PPY NPs and (b) Au/PPy NPs with (c) close view on the Au NPs. Size distribution of the (d) PPY NPs and (e) Au NPs estimated for a population of 100 and 45 particles, respectively.

whereupon 3.73 g of iron cations (III) of FeCl_3 were added in the solution and stirred for 10 min. In second step, pyrrole (0.01 mol) was added to this aqueous solution and stirred for 5 h at RT. As soon as pyrrole was mixed with the oxidant (FeCl_3), a rapid polymerization reaction occurred, which turned the solution into a characteristic black color indicating the formation of PPY.

Colloid Au NPs were synthesized according to Turkevich method [17], i.e., in a wet chemical synthesis, via the reduction of gold salt by sodium citrate. Briefly, 20 mL of 0.001 M of gold (III) chloride trihydrate ($\text{HAuCl}_4 \cdot 3\text{H}_2\text{O}$) was added to a flask and placed on a stirring hotplate at 150 °C. As soon as the solution reach its boiling point, 2 mL of 1% sodium citrate dihydrate ($\text{Na}_3\text{C}_6\text{H}_5\text{O}_7 \cdot 2\text{H}_2\text{O}$) was added and temperature was decreased to 100 °C. The reaction was run until the solution became reddish. Afterwards the solution was removed from the hotplate and cool down.

Au/PPy NPs were prepared by mixing Au and PPY NPs solutions with two different ratios, 1:10 and 1:2. The Au/PPy NPs solution was sonicated in ultrasonic bath for 10 min and used immediately, either for its characterization or for spin coating on the L-SAW substrates for sensing test.

2.2. Material characterization

The absorption spectra of PPY, Au and Au/PPy NPs were measured at room temperature using UV-vis-NIR spectrophotometer (Cary 5000) in the range of 200–800 nm. The NPs solutions were measured in 1 cm optical path quartz cuvette. The morphology and size distribution of the PPY, Au and Au/PPy NPs were examined using High Resolution Transmission Electron Microscope (HR-TEM, FEI TITAN Themis 60–300 kV with Cs image corrector) at accelerating voltages of 60 kV for PPY and Au/PPy NPs and 300 kV for Au NPs. The samples for HR-TEM analysis were prepared by placing a drop of the corresponding NPs solution onto TEM holey carbon holey grids.

2.3. Love-wave sensors fabrication

L-SAW delay line platforms consisting of a piezoelectric substrate (ST-90°X quartz, 9 mm × 4 mm × 0.5 mm) with two (input/output) aluminium interdigitated transducing (IDTs, 200 nm thick) ports, see

Fig. 1. The double finger pair IDTs have four strips per period ($\lambda = 28 \mu\text{m}$) and this structure is repeated 75 times for each port. The IDTs aperture and distance between IDTs ports (delay line) are 2.1 mm. The first guiding SiO_2 layer (3 μm thick) was deposited on the top of substrate. Additionally, SiO_2 layer served as an isolating layer between IDTs and second guiding layer. The whole fabrication process consisted of various microfabrication steps, including metallization, oxide deposition and lithography; further details of the fabrication process were reported previously [18].

The second guiding/sensitive layer (350 ± 50 nm thick) was spin-coated over the first (SiO_2) guiding layer at a speed of 4000 rpm and acceleration of 4000 rpm/s for 1 min. To control the reproducibility of the spin coating, the L-SAW substrates were placed into a customized holder built to keep the substrates in a fix position and alignment during the coating. Moreover, shadow masks were used to cover the electrode contacts placed in the outside corners. Subsequently, the delay line and IDTs ports area was covered with 60 μl of the corresponding solution (i.e., PPY, Au/PPy (1:10) or (1:2)) and spin coated. The edge effect (study by profilometry) near to the electrode contact and their possible wave reflection was controlled by applying a thin film of silicon (dried at 60 °C for 1 h) at the outside corners.

To fabricate the L-SAW device with appropriate wave attenuation and prevent high noise in the oscillator system, the thickness of first and second guiding/sensitive layer were tuned experimentally. Results for various systems, including SiO_2 layers with 1.6, 2.5, 3, and 3.8 μm and PPY or Au/PPy spin coated at various rpm (from 2000 to 4000), showed a good compromise in terms of losses (~20 dB) for the L-SAW sensors comprising a 3 μm SiO_2 layer. Therefore, these systems were employed for further material and gas sensing tests.

2.4. Love-wave sensors characterization

The morphology of the second guiding layer (PPY, Au/PPy (1:10) and (1:2)) after their integration with the L-SAW substrates were characterized using FIB/SEM Microscope (Helios G4 NanoLab DualBeam™) and Scanning Probe Microscope (Bruker Dimension Icon, working in ScanAsyst-Air Type mode). The L-SAW sensors were electrically characterized before and after the integration of PPY or Au/PPy NPs using RF transmission parameter S_{21} (360B Automatic Network

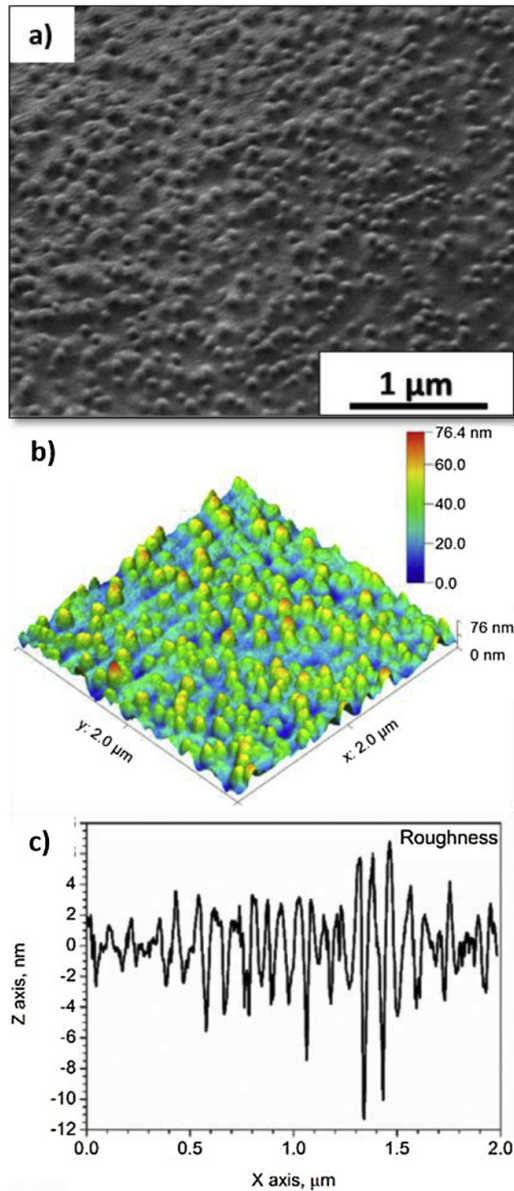


Fig. 4. (a) Top view SEM image and (b) 3D AFM image of the second guiding/sensitive layer based on Au/PPy NPs after spin coating. (c) Roughness profile of the layer analysed from the AFM images.

Analyzer, Wiltron) to analyse the insertion loss of each sample. All tested L-SAW sensors were analysed by Time-of-Flight Secondary Ion Mass Spectrometry (ToF-SIMS) using TOF.SIMS5 (Ion-ToF). ToF-SIMS combined with sputter depth profiling is used to provide the information of the surface chemical composition, where layer-by-layer sputtering allows reconstructing elemental and molecular distribution by sample depth [19]. A crater with area of $300 \times 300 \mu\text{m}^2$ was sputtered by Cs^+ beam (1 keV). Electron flood gun was used to reduce charging of the sample. The pulsed Bi^+ with acceleration voltage of 30 keV was used as the primary ion in order to collect the secondary ion mass spectra. The secondary ions emitted from the surface of the crater bottom were detected in negative ion mode by the TOF mass spectrometer. The analyses were obtained from areas of $100 \times 100 \mu\text{m}^2$. The instrument was tuned for a mass resolution greater than 4000 at $m/z =$

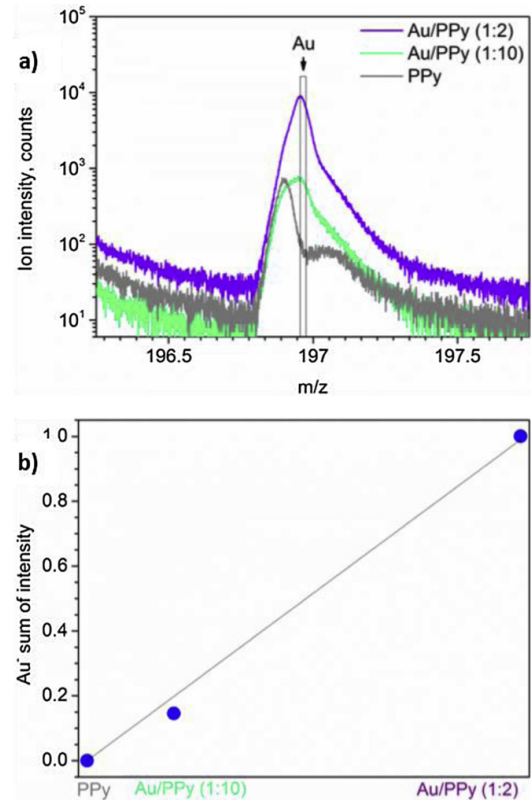


Fig. 5. (a) Negative SIMS spectrum of Au^- ion in the depth profile of PPy and Au/PPy (1:10 and 1:2) guiding/sensitive layers. (b) Correlation of Au NP loadings and intensity of secondary Au^- ions in PPy and Au/PPy (1:10 and 1:2) guiding/sensitive layers.

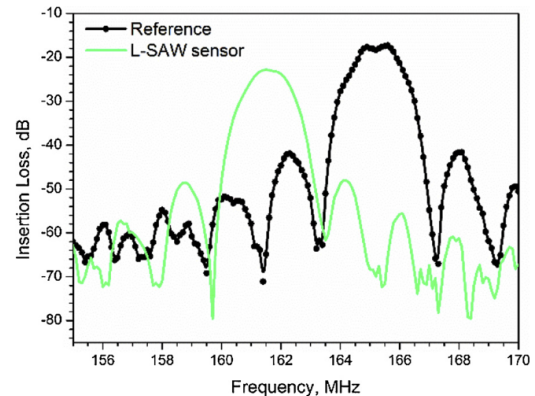


Fig. 6. Electrical response registered for the reference sample (uncoated, with only SiO_2 guiding layer) and the L-SAW sensors containing the second guiding/sensitive PPy layer.

^{29}Si .

2.5. Ethylene and ammonia tests

The gas sensing properties of the L-SAW sensors were tested at RT (24°C) in a continuous gas flow test chamber. The tests consisted in monitoring the frequency changes of the sensors toward various ethylene (Praxair) and ammonia (Praxair) concentrations (2, 5 and 10 ppm)

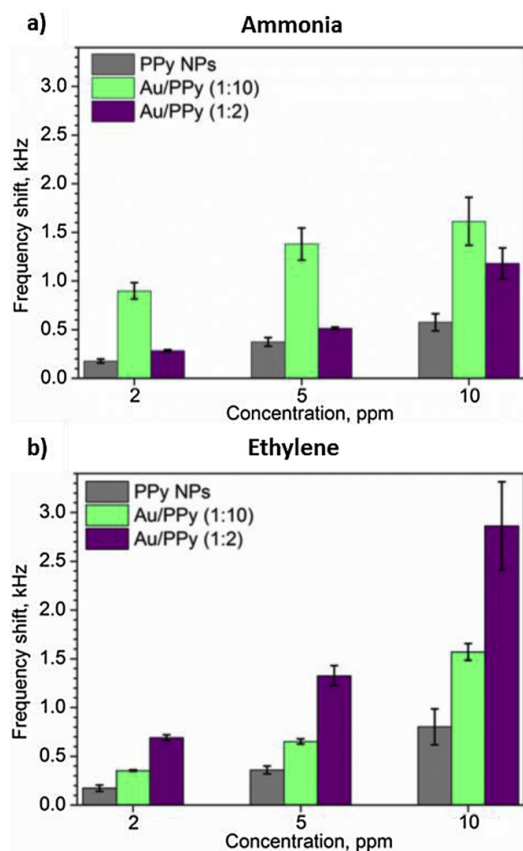


Fig. 7. Frequency shifts recorded on the non-modified PPy and modified PPy L-SAW sensors with low (1:10) and high (1:2) gold loadings at 2, 5 and 10 ppm of (a) ammonia and (b) ethylene.

using synthetic dry air as diluting and carrier gas. Further tests of the sensors in humid ambient were performed at 10 and 30 % RH as these are the humidity levels reached in 'actual' breath samples after pre-conditioning and filtering moisture [20]. Both, temperature and humidity were monitored inside the test chamber using a humidity/temperature sensor (SHT71, operating ranges from 0 to 100 % relative humidity (RH), accuracy of ± 3 % RH).

Each L-SAW sensor works in an oscillator circuit, which includes an amplifier and a directional coupler. Therefore, the oscillating frequency of the sensor is shifted for any perturbation. In addition, the amplification stage of the oscillator is controlled by a rheostat device, which optimizes the gain of the oscillator for each sensor, to prevent that the insertion losses exceed the amplifier gain during the gas experiment. The measurements of the frequency for a period of two minutes generally displayed good stability with the noise not exceeding 10 Hz. A heterodyne configuration was used for signal acquisition, mixing the signal of the oscillator coupled to a reference L-SAW sensor (with only SiO₂ guiding layer) and the signal of the oscillator coupled to the PPy based L-SAW sensor. The frequencies obtained from the mixer were acquired by a frequency counter. The sensors were placed in a continuous flow test chamber (100 mL/min) equipped with mass-flow controllers. The exposure time of the sensors to each analyte concentration was set to 2 min, with a subsequent purging using synthetic dry air for 30 min. The reference L-SAW sensor was used in the gas sensing array, to compensate thermal and other environmental dependent drifts on the piezoelectric substrates. During the gas test, the reference element was not exposed to target gas analytes, and the final

output signal of the L-SAW sensors was subtracted from the reference sample. Therefore, the sensor response was defined as the frequency shift, which is the divergence of sensors frequency read off during the exposure to synthetic air and gas.

3. Results and discussion

3.1. Characterization of the PPy and Au/PPy NPs

Fig. 2 displays the UV-vis spectra of the synthesized PPy, Au, and Au/PPy NPs; the spectrum of Au/PPy (10:1) mixture, i.e., with 10 times higher volumetric amount of Au NPs than PPy NPs, is also included in Fig. 2c for comparative purpose. The UV-vis spectrum of PPy NPs (Fig. 2a) shows a broad absorption peak at 461 nm assigned to π - π^* electron transition from valence band to the conduction band due to the presence of polarons [21]. The UV-vis spectrum of the Au NPs (Fig. 2b) is consistent with the literature showing the maximum of surface plasmon resonance absorption at 523 nm and indicating the formation of NPs with diameters between 15 and 20 nm [22]. The analysis of the Au/PPy NPs with different Au loadings (i.e., 1:10 and 1:2) showed similar spectra to that recorded on the non-modified PPy NPs (Fig. 2a). However, the comparison of the spectra for Au/PPy NPs (1:10, Fig. 2c - black line) and Au/PPy NPs (10:1, Fig. 2c - green dot line) demonstrates that the shape and position of the absorption maximum depends on the dominant volumetric quantity. Therefore, the apparent absence of the Au plasmon peak at 523 nm in the Au/PPy NPs (1:10 and 1:2) solutions is connected with the low amount of Au NPs in these mixtures.

HR-TEM analysis of the PPy NPs (Fig. 3a) showed amorphous spherical particles with sizes between 35 and 55 nm (Fig. 3d). Similarly, HR-TEM analysis of the Au/PPy NPs (Fig. 3b) displayed the presence of segregated PPy and Au spherical particles; notice the brightness/contrast differences, which indicate the presence of both, Au (higher contrast) and PPy (low contrast) NPs. The number of PPy NPs were remarkably larger in comparison to the Au NPs in the tested sample, confirming the relatively low amount of Au NPs in the Au/PPy mixture. The average particle size analysis indicates that the mean diameter of Au NPs is approximately 15 nm for a size distribution ranging between 12 and 25 nm (Fig. 3e). HR-TEM of the Au NPs emphasized their high crystallinity showing lattice fringe spacing of 0.24 nm (Fig. 3c). This is consistent with the (111) plane of the face centred cubic (fcc) gold ($d = 2.35500 \text{ \AA}$, ICCD card no. 04-0784).

In summary, the analysis of the solutions prepared for spin coating of the second guiding/sensitive layers demonstrate the synthesis of both PPy and Au NPs. UV-vis and HR-TEM pointed out to weak chemical interactions between the Au and the PPy NPs in the mixed solutions.

3.2. Characterization of PPy and Au/PPy NPs integrated with Love-wave platforms

SEM (Fig. 4a) and AFM (Fig. 4b) analysis of the second guiding/sensitive layers, after spin coating of the L-SAW transducing platforms, displayed uniform films with granular morphology. The films proved good adhesion to the substrate and the thickness of the films observed by cross-sectional SEM images (see Fig. 1b) was found to be $350 \pm 50 \text{ nm}$. For this thickness of the guiding layer (PPy, Au/PPy), L-SAW sensors showed the appropriate attenuation (low insertion loss). The PPy and Au/PPy guiding/sensitive layers analyzed by scanning probe microscope (Fig. 4c) in an area of $2 \mu\text{m} \times 2 \mu\text{m}$ showed relatively low RMS (root mean square) roughness of approximately $2.5 \pm 0.4 \text{ nm}$. The uniform and optimal thickness, low surface roughness, and strong adhesion of the film to the substrates are significant factors that favor the attenuation of the acoustic wave propagation and in turn the sensor sensitivity [2b].

In order to confirm the incorporation of the Au NPs into the spin coated guiding/sensitive layers, the samples (PPy, Au/PPy (1:10) and (1:2)) were investigated by TOF-SIMS technique. SIMS is a semi-

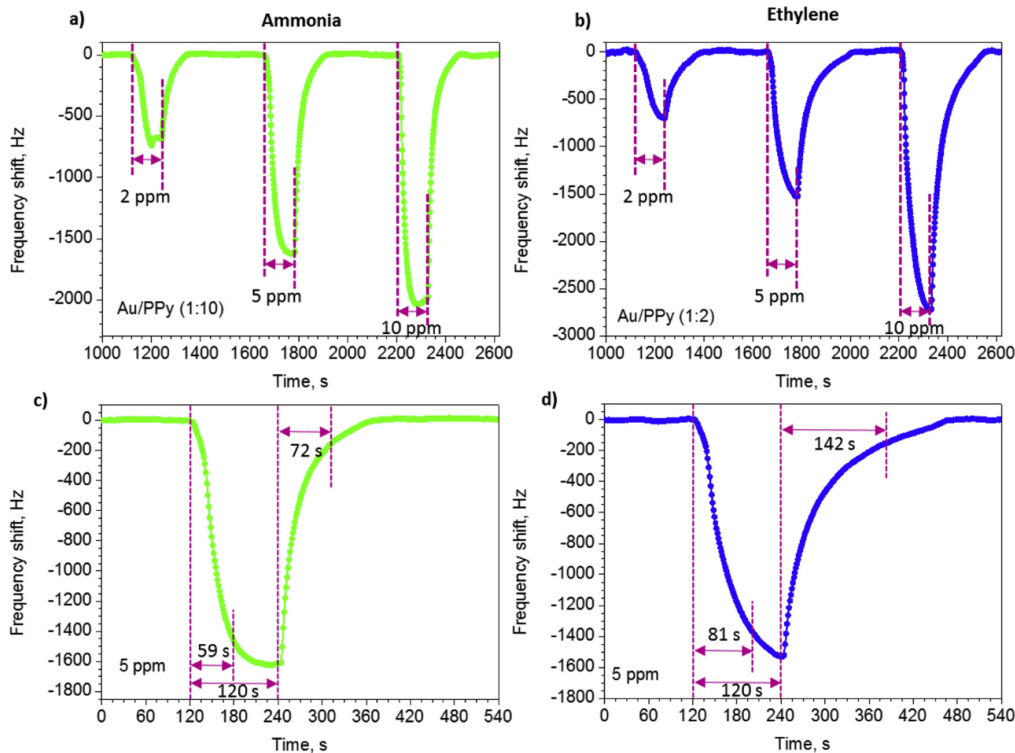


Fig. 8. (a) Response of the Au/PPy (1:10) based L-SAW sensor to 2, 5 and 10 ppm of ammonia. (b) Response of the Au/PPy (1:2) based L-SAW sensor to 2, 5 and 10 ppm of ethylene. Time-dependent response curve of (c) Au/PPy (1:10) sensor to 5 ppm of ammonia and (d) Au/PPy (1:2) sensor to 5 ppm of ethylene.

quantitative method, which allows to obtain information of solids by sputtering the solid surface and collecting ejected secondary ions from the topmost surface. Fig. 5a shows the comparative SIMS spectra of Au^- molecular ion within the samples. These results demonstrate the presence of characteristic fragmented ions of Au^- at 196.97 m/z (marked area) in the Au/PPy samples, in contrast to the bare PPy samples. Moreover, the intensity of the counts of Au^- ions is consistent with the amount of Au NPs used for each sample; notice the sharper and more intense Au^- peak for Au/PPy (1:2) compared to Au/PPy (1:10). The correlation of the Au^- ion intensity (collected in the depth profile of 200 nm) and Au NPs loadings in the samples (Fig. 5b) confirmed the proportional increase of Au^- signal with respect to the Au NPs amounts introduced to the samples. Additionally, the presence of characteristic fragments for PPy (e.g., $\text{C}_x\text{H}_y\text{N}$), PVA (e.g., $\text{C}_x\text{H}_y\text{O}_2$) and FeCl_3 (e.g., FeClN , FeCN) were confirmed in the depth profile of samples by SIMS analysis.

Fig. 6 shows the characteristic signals obtained by measuring the transmission scattering parameter (S_{21}) of the L-SAW sensors before (only SiO_2 guiding layer) and after integration of second guiding/sensitive layer (PPy). Very similar electrical response has been observed for all tested sensors (PPy, Au/PPy (1:10) and (1:2)), with the frequency and the insertion loss of $161.6 \pm 0.4 \text{ MHz}$ and $22.4 \pm 0.5 \text{ dB}$, respectively. The decrease in the frequencies for the PPy or Au/PPy L-SAW sensors with respect to the reference (165.2 Hz and -18.2 dB) is consistent with the increase of weight on the piezoelectric substrate (mass loading effect). Additionally, viscoelastic properties of PPy also can contribute to frequency changes and lead to changes in device attenuation.

In summary, the incorporation of the second guiding/sensitive layers with the piezoelectric substrates demonstrates similar morphological and electrical properties for the non-modified and gold modified PPy layers, despite the two different gold loadings incorporated in the

modified layers.

3.3. L-SAW gas sensing tests

The ammonia and ethylene gas sensing tests of the L-SAW sensors based on PPy and Au-modified PPy NPs (1:10 and 1:2) at room temperature are presented in Fig. 7. In general, all sensors registered positive responses upon exposure to different concentrations of target analytes. The sensors based on Au/PPy NPs demonstrated enhanced sensing properties towards both tested gases compared to the sensors based on non-modified PPy NPs. We observed further that the sensors based on low Au loadings (i.e., 1:10) provided better responses to ammonia (Fig. 7a) compared to those based on high Au loadings (i.e., 1:2). Namely, Au/PPy (1:10) sensors showed higher frequency shifts and an increase of the response by approximately 5, 4 and 3 times to 2, 5 and 10 ppm of ammonia, respectively, as compared to PPy sensors. In contrast, the results obtained for ethylene (Fig. 7b) registered improved responses for Au/PPy (1:2) sensor (higher Au loading) compared to Au/PPy (1:10) sensor, as opposite to that observed for the ammonia tests. The frequency shifts of Au/PPy (1:2) sensors with regard to non-modified PPy sensors is increased approximately by 4 times for 2, 5 and 10 ppm of ethylene. The enhanced response of the Au/PPy (1:2) sensors to ethylene could be related to the higher loading of Au NPs in this sample and the proved catalytic activity of gold, which encourages the oxidation of ethylene at room temperature [23].

Fig. 8a and b show the response of Au/PPy (1:10) and Au/PPy (1:2) L-SAW sensors to various concentrations of ammonia and ethylene, respectively, with the frequency changes of the sensors showing proportional increment to gas concentration. The decrease of frequency (negative frequency shift) obtained during the exposure of the L-SAW sensors to ammonia and ethylene are most likely connected to the dominance of mass loading effects, rather than the electrical effects,

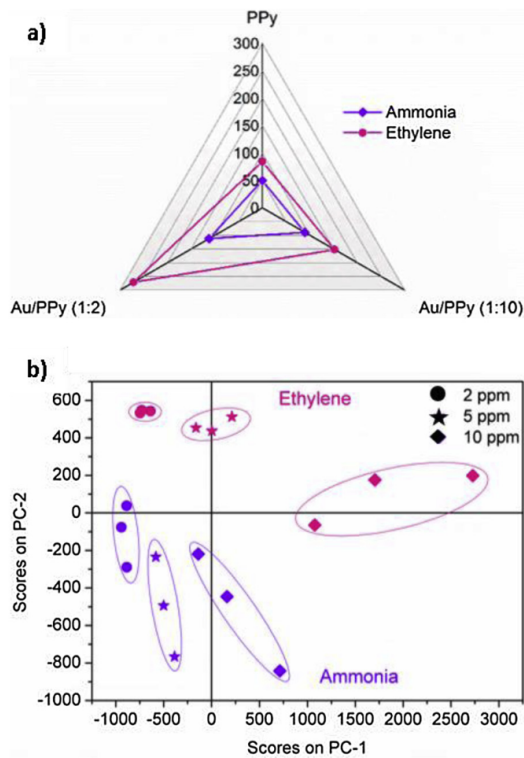


Fig. 9. (a) Sensitivity (Hz/ppm) of the L-SAW sensor based on PPy NPs and Au-modified PPy films (Au/PPy 1:10 and Au/PPy 1:2) to ammonia and ethylene (calculated for concentrations between 2 ppm and 10 ppm). (b) Scores or projections of measurements in an orthogonal base of principal components analysed for the PPy, Au/PPy (1:10) and (1:2) L-SAW sensors.

which are expected to cause positive frequency shift during the interaction of PPy and these reducing analytes [24]. This fact is connected with the low conductivity (electrical resistance between 500 M Ω –1 G Ω) of the second guiding/sensitive layer and the insignificant resistance changes recorded during its exposure to gases such as ammonia and ethylene (this was proved by testing the PPy and Au/PPy layers deposited directly on the top of the electrodes to both target analytes). Similarly, the elastic effects in the response of the L-SAW sensors can also be disregarded, as generally the elastic changes in the sensitive material are associated with a frequency increase (a positive frequency shift) [24b]. Therefore, the negative frequency shifts recorded on the L-SAW sensors are associated to the changes in the propagation path of the surface waves induced by the mass loading of the analytes at the sensitive layer; where the mass loading refers to physical/chemical

sorption of target gas molecules at/in the sensitive layer.

Fig. 8c and d show a detailed view of the response and the time required to reach 90 % of the response and recovery. In general, the non-modified and gold-modified L-SAW sensors showed similar response and recovery times for the same analyte and concentration. The response and recovery times toward ethylene were longer than for ammonia. For instance, results show that the response and recovery times were 59 s and 72 s for Au/PPy (1:10) sensors to 5 ppm of ammonia, respectively, and 81 s and 142 s for Au/PPy (1:2) sensors to 5 ppm of ethylene. This may be related to the difference in molecular size of these gases (kinetic diameter for ethylene molecule of 0.42 nm [25] and ammonia molecule 0.36 nm [26]), which slows down the diffusion of ethylene molecules within the sensitive layer respect to ammonia [26], making the response and recovery time longer for ethylene.

Fig. 9a shows the sensitivity of PPy, Au/PPy (1:10) and Au/PPy (1:2) L-SAW sensors to ammonia and ethylene for concentration between 2 ppm and 10 ppm. The sensitivity is defined as the ratio between the change in sensors response (Δ frequency shift) and a fixed analyte concentration change (ΔC). The sensitivity of the Au/PPy (1:10) sensors to ammonia and ethylene was found to be ~ 1.8 times higher than that of non-modified PPy sensors. The sensitivity of the Au/PPy (1:2) sensors with respect to the PPy sensors was improved ~ 2.2 and ~ 3.2 times to ammonia and ethylene, respectively. The score plot obtained by principal component analysis (PCA) of the non-modified and Au-modified PPy sensors (Fig. 9b) shows an appraisal of the selectivity and the possibility to discriminate ammonia and ethylene by concentrations using and array of the non-modified and gold-modified L-SAW sensors.

Table 1 compares the key characteristics and results of our L-SAW sensors with other piezoelectric sensors reported in the literature. The results show that the sensors described in this work possess higher frequency shifts (i.e., response) for the lowest tested analyte concentration (2 ppm) than other piezoelectric devices such as Rayleigh and Shear Horizontal SAW or BAW (e.g., quartz crystal microbalance) sensors. The enhanced sensitivity of our L-SAW sensors, compared to other type of SAW sensors, is attributed in part to the multiguiding layer structure of these sensors, which combines the properties of the SiO₂ and the gas sensitive PPy layers to trap the wave energy near the surface. This structure slows down the wave propagation velocity and makes the L-SAW sensors sensitive towards any changes occurring on the surface [2a,27]. Additionally, the improved ammonia and ethylene sensing performances of Au/PPy sensors, with respect to the non-modified PPy, can be attributed to the catalytic effect of the Au NPs and the subsequent enrichment of PPy surface by spill-over of reactive species through catalysis [28]. The influences of the PPy modification by different Au NPs loadings on the L-SAW sensor responses to ammonia and ethylene are slightly different. The higher density of Au NPs on PPy L-SAW sensors (Au/PPy (1:2)) favors the sensitivity to ethylene. Previously was described that the oxidation of ethylene is increased by the increase of Au loadings at room temperature [23] in contrast to

Table 1

The comparison of sensing characteristics of ammonia and ethylene gas sensors based on different piezoelectric transducing platforms.

| Type of sensor | Structure | Sensitive layer | Gas | RH (%) | Temp. (°C) | Response (Hz) | LTC (ppm) | LOD (ppm) | Ref. |
|----------------|----------------------------|---|----------|--------|------------|---------------|-----------|-----------|-----------|
| L-SAW | ST-Quartz/SiO ₂ | Au/PPy | Ammonia | 0 | 24 | 898 | 2 | 0.067 | This work |
| L-SAW | ST-Quartz/SiO ₂ | Fe ₂ O ₃ /WO ₃ | Ammonia | NR | NR | 627 | 25 | 1 | [30] |
| R-SAW | ST-Quartz | PPy | Ammonia | NR | NR | 20 | 10 | NR | [7b] |
| SH-SAW | ST-Quartz | ZnO | Ammonia | 25 | 25 | 110 | 10 | NR | [31] |
| QCM | AT-Quartz crystal | PDA/HMSSs | Ammonia | 50 | 25 | 250 | 10 | NR | [32] |
| L-SAW | ST-Quartz/SiO ₂ | Au/PPy | Ethylene | 0 | 24 | 690 | 2 | 0.087 | This work |
| R-SAW | XY LiNbO ₃ | ZnO | Ethylene | NR | NR | 200 | 100 | NR | [33] |
| QCM | AT-PC | AgBF ₄ /PVP | Ethylene | NR | NR | 115 | 1 | 0.42 | [34] |

RH: Relative humidity, Temp.: Temperature, LTC: Lowest tested concentration, LOD: Limit of detection, Response: Frequency shift, L-SAW: Love wave SAW; R-SAW: Rayleigh SAW; SH-SAW: shear horizontal SAW; ST, XY, AT: refer to crystal cut; QCM: quartz crystal microbalance; PC: piezoelectric crystal; PDA/HMSSs: polydopamine/hollow mesoporous silica spheres; AgBF₄/PVP: AgBF₄/polyvinylpyrrolidone, NR: Non-reported.

ammonia, which required a temperature activation [29].

The high responses of our L-SAW sensors also contribute to lower LODs than those of other devices. For instance, the LOD for ammonia was 67 ppb using Au/PPy (1:10) and for ethylene 87 ppb using Au/PPy (1:2) sensors, considering that the minimum signal intensity is 3 times higher than noise. These LODs are within the limits required in the early diagnosis of OS dependant diseases (e.g. schizophrenia, diabetes). According to the literature, the concentrations of gaseous biomarkers found in healthy controls and patients with OS dependent diseases oscillate from 8 to 246 ppb for ethylene and from 290 to 2020 ppb for ammonia [14b,35]. Further tests of the sensors to ethylene and ammonia in humid ambient registered a loss of the response of approximately 2 times at 10 % RH and 5 times at 30 % RH. Additionally, the humidity introduced instability to the signal, making the responses less reproducible and reliable, particularly at the low tested concentration (2 ppm). Thus, the sensitivity of the sensors was also affected. For instance, at 30% RH the sensitivity of the Au/PPy (1:10) sensors to ammonia decreased from 92 in dry air to 40. Similarly, the sensitivity of the Au/PPy (1:2) sensors to ethylene decreased from 270 in dry air to 72. These significant changes in the response of the sensors in humid ambient may be connected with the swelling of the polymeric guiding/sensitive layer by water vapor. In humid ambient, water molecules fill the free volume in the polymeric layer, making it unavailable for the gas sorption and, thus, less responsive to the target analyte [36]. A comparison of these results and those of the literature is rather complex as most of the reports (e.g., those listed in Table 1) do not make reference to the humidity levels during the tests and/or the degree of humidity interference in sensor response. However, based on the reports in Table 1 (row 4 and 5) for 25% and 50% RH one can notice that the lowest measured concentrations of ammonia in dry and humid conditions are yet lower for our sensors. Humidity interference is an undesired and recurrent effect at RT operation that needs the implementation of additional strategies to be compensated. These strategies may include further tuning of the polymer properties using other additives (hydrophobic inorganic materials or organic molecules) [37] or coupling filters or preconditioning elements to the sensors as forecasted for next generation of portable breath analyser [20].

In summary, the Au-modified PPy L-SAW sensors demonstrate enhanced sensing responses compared to the non-modified PPy sensors in dry conditions, with better sensitivity and lower LOD to ethylene and ammonia than those reported earlier in the literature for other SAW-based gas sensing elements at RT. The tests in humid ambient affect the sensor performance modifying the LOD to higher concentration levels than those obtained in dry ambient, thus, indicating the need for further strategies to compensate the interference of humidity on the sensor response.

4. Conclusion

Love wave gas sensors based on a multiguiding layer structure consisting of SiO₂ and either non-modified or gold modified polypyrrole were developed in this work. Results demonstrated the incorporation of dispersed crystalline gold nanoparticles into the modified polypyrrole based sensors and the enhanced performance of these sensors, compared to the non-modified polypyrrole based sensors, to ethylene and ammonia. Gas sensing tests in dry conditions showed that the detection limit of the gold modified sensors reaches lower ppb level for both tested gases (67 ppb for ammonia and 87 ppb for ethylene) as compared to other similar systems in the literature. These improvements are attributed in part to the multiguiding structure and to the incorporation of gold nanoparticles into the gas sensitive polypyrrole layer, which potentially promotes the sorption of reactive species through catalysis. The incorporation of humidity to the tests changed significantly the response magnitudes of the gold modified and non-modified sensors and in turn the sensitivity, which decreased approximately 2 times for the Au/PPy (1:10) sensors to ammonia and 4 times for the Au/PPy (1:2)

to ethylene. Generally, these results suggest the need for further improvements at the material and/or filtering level to restrict the humidity effect in the sensor response. Despite these weaknesses, the relatively easy and scalable fabrication of these sensors, as well as their sensing performance towards low ethylene and ammonia concentrations make the modified structures attractive for future studies and applications where gases and/or VOCs are involved.

Declaration of Competing Interest

The authors declare that they have no known competing financial interests or personal relationships that could have appeared to influence the work reported in this paper.

The authors declare the following financial interests/personal relationships which may be considered as potential competing interests.

Acknowledgments

This work has been supported in part by the Czech Science Foundation (GAČR) via Grant no. 17-16531S, the Spanish Ministry of Economy and Competitiveness via projects TEC2015-74329-JIN-(AEI/FEDER,EU), and TEC2016-79898-C6-1-R (AEI/FEDER, EU) and by Universidad Nacional Autónoma de México via Grant DGAPA-UNAM-PAPIIT TA100118. The support of the Internal Grant Agency (IGA) student junior project no. STI-J-18-5559 and the Ramón y Cajal are also acknowledged. This research has made use of the infrastructures the Spanish ICTS Network MICRONANOFABS, partially supported by MINECO, and CEITEC Nano Research Infrastructure, supported by MEYS (2016-2019). We also acknowledge the support received from Ondřej Chmela for Scanning Probe Microscope analysis and from Selena Islas in the UV-vis Spectrophotometer.

References

- [1] a) A. Bryant, D.L. Lee, J.F. Vetelino, A surface acoustic wave gas detector, *IEEE Trans. Sonics Ultrason.* 29 (1982) 167-167;
b) A. Afzal, N. Iqbal, A. Mujahid, R. Schirhagl, Advanced vapor recognition materials for selective and fast responsive surface acoustic wave sensors: a review, *Anal. Chim. Acta* 787 (2013) 36-49.
- [2] a) S.J. Ippolito, A. Trinchì, D.A. Powell, W. Włodarski, Acoustic wave gas and vapor sensors, in: E. Comini, G. Faglia, G. Sberveglieri (Eds.), *Solid State Gas Sensing*, Springer US, Boston, MA, 2009, pp. 1-44;
b) J. Devkota, P.R. Ohodnicki, D.W. Greve, SAW sensors for chemical vapors and gases, *Sensors*, (2017), p. 28.
- [3] J.R. Frago-Mora, D. Matatagui, F.A. Bahos, J. Fontecha, M.J. Fernandez, J.P. Santos, I. Sayago, I. Gràcia, M.C. Horrillo, Gas sensors based on elasticity changes of nanoparticle layers, *Sens. Actuators B Chem.* 268 (2018) 93-99.
- [4] A.L. Zou, L.Z. Hu, Y. Qiu, G.Y. Cao, J.J. Yu, L.N. Wang, H.Q. Zhang, B. Yin, L.L. Xu, High performance of 1-D ZnO microwire with curve-side hexagon as ethanol gas sensor, *J. Mater. Sci.: Mater. Electron.* 26 (2015) 4908-4912.
- [5] J.S. Liu, L.J. Wang, Y.Y. Lu, S.T. He, Properties of Love waves in a piezoelectric layered structure with a viscoelastic guiding layer, *Smart Mater. Struct.* 22 (2013) 8.
- [6] M. Šetka, J. Drbohlavová, J. Hubálek, Nanostructured polypyrrole-based ammonia and volatile organic compound sensors, *Sensors* 17 (2017) 28.
- [7] a) M. Penza, E. Milella, V.I. Anisimkin, Monitoring of NH₃ gas by LB polypyrrole-based SAW sensor, *Sens. Actuators B Chem.* 47 (1998) 218-224;
b) X. Chen, D.M. Li, S.F. Liang, S. Zhan, M. Liu, Gas sensing properties of surface acoustic wave NH₃ gas sensor based on Pt doped polypyrrole sensitive film, *Sens. Actuators B Chem.* 177 (2013) 364-369;
c) F. Li, H. Li, H. Jiang, K. Zhang, K. Chang, S. Jia, W. Jiang, Y. Shang, W. Lu, S. Deng, M. Chen, Polypyrrole nanoparticles fabricated via Triton X-100 micelles template approach and their acetone gas sensing property, *Appl. Surf. Sci.* 280 (2013) 212-218.
- [8] X.F. Yan, D.M. Li, C.C. Hou, X. Wang, W. Zhou, M. Liu, T.C. Ye, Comparison of response towards NO₂ and H₂S of PPy and PPy/TiO₂ as SAW sensitive films, *Sens. Actuators B Chem.* 161 (2012) 329-333.
- [9] L. Al-Masbat, H.D. Tran, W. Włodarski, R.B. Kaner, K. Kalantar-zadeh, Polypyrrole nanofiber surface acoustic wave gas sensors, *Sens. Actuators B Chem.* 134 (2008) 826-831.
- [10] M. Šetka, F.A. Bahos, D. Matatagui, Z. Kral, I. Gràcia, J. Drbohlavová, S. Vallejos, Polypyrrole based love-wave gas sensor devices with enhanced properties to ammonia, *Proceedings 2* (2018) 786.
- [11] S.J. Kim, S.J. Choi, J.S. Jang, H.J. Cho, I.D. Kima, Innovative nanosensor for disease diagnosis, *Acc. Chem. Res.* 50 (2017) 1587-1596.

- [12] a) B. Uttara, A.V. Singh, P. Zamboni, R.T. Mahajan, Oxidative stress and neurodegenerative diseases: a review of upstream and downstream antioxidant therapeutic options, *Curr. Neuropharmacol.* 7 (2009) 65–74;
b) E. Ozbek, Induction of oxidative stress in kidney, *Int. J. Nephrol.* 2012 (2012) 465897–465897.
- [13] a) K. Kolanjiappan, S. Manoharan, M. Kayalvizhi, Measurement of erythrocyte lipids, lipid peroxidation, antioxidants and osmotic fragility in cervical cancer patients, *Clin. Chim. Acta* 326 (2002) 143–149;
b) Z. Ni, G. Angelidou, G. Coliva, M. Lange, M. Fedorova, Analytical strategies to uncover the diversity of lipid peroxidation products and their biological effects, *Free Radic. Biol. Med.* 124 (2018) 560–561.
- [14] a) L.M. Paardekooper, G. van den Bogaart, M. Kox, I. Dingjan, A.H. Neerincx, M.B. Bendix, M. ter Beest, F.J.M. Harren, T. Risby, P. Pickkers, N. Marczin, S.M. Cristescu, Ethylene, an early marker of systemic inflammation in humans, *Sci. Rep.* 7 (2017) 10;
b) M. Petrus, A.-M. Bratu, C. Popa, Spectroscopic analysis of breath ethylene and oxidative stress relation with glycaemic status in type 2 diabetes, *Opt. Quantum Electron.* 49 (2016) 2;
c) S.M. Cristescu, R. Kiss, S.T. Hekker, M. Dalby, F.J.M. Harren, T.H. Risby, N. Marczin, B.S.I. Harefield, Real-time monitoring of endogenous lipid peroxidation by exhaled ethylene in patients undergoing cardiac surgery, *Am. J. Physiol.-Lung Cell. Mol. Physiol.* 307 (2014) 509–515.
- [15] a) F. Nuhu, S. Bhandari, Oxidative stress and cardiovascular complications in chronic kidney disease, the impact of anaemia, *Pharmaceuticals* 11 (2018) 15;
b) S. Pastor, L. Rodríguez-Ribera, Z. Corredor, M.L. da Silva Filho, K. Hemminki, E. Coll, A. Förstl, R. Marcos, Levels of DNA damage (Micronuclei) in patients suffering from chronic kidney disease. Role of GST polymorphisms, *Mutat. Res./Genet. Toxicol. Environ. Mutagen.* 836 (2018) 41–46;
c) C. Popa, D.C.A. Dutu, R. Cernat, C. Matei, A.M. Bratu, S. Banita, D.C. Dumitras, Ethylene and ammonia traces measurements from the patients' breath with renal failure via LPAS method, *Appl. Phys. B-Lasers Opt.* 105 (2011) 669–674;
d) J. Obermeier, P. Trefz, J. Happ, J.K. Schubert, H. Staude, D.C. Fischer, W. Miekisch, Exhaled volatile substances mirror clinical conditions in pediatric chronic kidney disease, *PLoS One* 12 (2017) 18.
- [16] O.S. Kwon, J.Y. Hong, S.J. Park, Y. Jang, J. Jang, Resistive gas sensors based on precisely size-controlled polypyrrole nanoparticles: effects of particle size and deposition method, *J. Phys. Chem. C* 114 (2010) 18874–18879.
- [17] J. Turkevich, P.C. Stevenson, J. Hillier, A study of the nucleation and growth processes in the synthesis of colloidal gold, *Discuss. Faraday Soc.* 11 (1951) 55–75.
- [18] D. Matatagui, O. Kolokoltssev, J.M. Saniger, I. Gracia, M.J. Fernandez, J.L. Fontecha, M.D. Horrillo, Acoustic sensors based on amino-functionalized nanoparticles to detect volatile organic solvents, *Sensors* 17 (2017) 9.
- [19] B. Hagenhoff, High resolution surface analysis by TOF-SIMS, *Microchim. Acta* 132 (2000) 259–271.
- [20] A. Prabhakar, R.A. Iglesias, X.N. Shan, X.J. Xian, L.H. Zhang, F. Tsow, E.S. Forzani, N.J. Tao, Online sample conditioning for portable breath analyzers, *Anal. Chem.* 84 (2012) 7172–7178.
- [21] a) Y. Li, P. Bober, D.H. Apaydin, T. Syrový, N.S. Sariciftci, J. Hromádková, I. Sapurina, M. Trchová, J. Stejskal, Colloids of polypyrrole nanotubes/nanorods: a promising conducting ink, *Synth. Met.* 221 (2016) 67–74;
b) M. Rahaman, A. Aldalbahi, M. Almoqbil, S. Alzahly, Chemical and electrochemical synthesis of polypyrrole using carrageenan as a dopant: polypyrrole/multi-walled carbon nanotube nanocomposites, *Polymers* 10 (2018) 20.
- [22] X.H.N. Xu, S. Huang, W. Brownlow, K. Salaita, R.B. Jeffers, Size and temperature dependence of surface plasmon absorption of gold nanoparticles induced by tris (2,2'-bipyridine)ruthenium(II), *J. Phys. Chem. B* 108 (2004) 15543–15551.
- [23] J.J. Li, C.Y. Ma, X.Y. Xu, J.J. Yu, Z.P. Hao, S.Z. Qiao, Efficient elimination of trace ethylene over nano-gold catalyst under ambient conditions, *Environ. Sci. Technol.* 42 (2008) 8947–8951.
- [24] a) X.L. Qi, J.S. Liu, Y. Liang, J.H. Li, S.T. He, The response mechanism of surface acoustic wave gas sensors in real time, *J. Appl. Phys.* 58 (2019) 7;
b) V.B. Raj, H. Singh, A.T. Nimal, M.U. Sharma, M. Tomar, V. Gupta, Distinct detection of liquor ammonia by ZnO/SAW sensor: study of complete sensing mechanism, *Sens. Actuators B: Chem.* 238 (2017) 83–90;
c) Q.B. Tang, Y.J. Guo, Y.L. Tang, G.D. Long, J.L. Wang, D.J. Li, X.T. Zu, J.Y. Ma, L. Wang, H. Torun, Y.Q. Fu, Highly sensitive and selective Love mode surface acoustic wave ammonia sensor based on graphene oxides operated at room temperature, *J. Mater. Sci.* 54 (2019) 11925–11935.
- [25] R.B. Lin, L.B. Li, H.L. Zhou, H. Wu, C.H. He, S. Li, R. Krishna, J.P. Li, W. Zhou, B.L. Chen, Molecular sieving of ethylene from ethane using a rigid metal-organic framework, *Nat. Mater.* 17 (2018) 1128–1133.
- [26] R. Sankar ganes, M. Navaneethan, G.K. Mani, S. Ponnusamy, K. Tsuchiya, C. Muthanizhchelvan, S. Kawasaki, Y. Hayakawa, Influence of Al doping on the structural, morphological, optical, and gas sensing properties of ZnO nanorods, *J. Alloys Compd.* 698 (2017) 555–564.
- [27] F. Herrmann, M. Weilmacht, S. Buttgenbach, Properties of sensors based on shear-horizontal surface acoustic waves in LiTaO₃/SiO₂ and quartz/SiO₂ structures, *IEEE Trans. Ultrason. Ferroelectr. Freq. Control* 48 (2001) 268–273.
- [28] H.G. Moon, Y. Jung, S.D. Han, Y.S. Shim, B. Shin, T. Lee, J.S. Kim, S. Lee, S.C. Jun, H.H. Park, C. Kim, C.Y. Kang, Chemiresistive electronic nose toward detection of biomarkers in exhaled breath, *ACS Appl. Mater. Interfaces* 8 (2016) 20969–20976.
- [29] M.J. Lippits, A.C. Gluhoi, B.E. Nieuwenhuys, A comparative study of the selective oxidation of NH₃ to N₂ over gold, silver and copper catalysts and the effect of addition of Li₂O and CeO_x, *Catal. Today* 137 (2008) 446–452.
- [30] F.A. Bahos, S. Vallejos, I. Gràcia, C. Cané, M.J. Fernández, M.C. Horrillo, D. Matatagui, High-performance ammonia sensor at room temperature based on a love-wave device with Fe₂O₃@WO₃ - x nanoneedles, *Proceedings 1* (2017) 484.
- [31] W. Li, Y.J. Guo, Y.L. Tang, X.T. Zu, J.Y. Ma, L. Wang, Y.Q. Fu, Room-temperature ammonia sensor based on ZnO nanorods deposited on ST-Cut quartz surface acoustic wave devices, *Sensors* 17 (2017) 10.
- [32] J. Zong, Y.S. Zhang, Y. Zhu, Y. Zhao, W. Zhang, Y. Zhu, Rapid and highly selective detection of formaldehyde in food using quartz crystal microbalance sensors based on biomimetic poly-dopamine functionalized hollow mesoporous silica spheres, *Sens. Actuators B Chem.* 271 (2018) 311–320.
- [33] N.H. Hasanuddin, M.H.A. Wahid, M.M. Shahimin, N. Hambali, N.R. Yusof, N.S. Nazir, N.Z. Khairuddin, M.A.M. Azidin, Ieee, Metal oxide based surface acoustic wave sensors for fruits maturity detection, 3rd International Conference on Electronic Design, ed. New York: Ieee, 2016, pp. 52–55.
- [34] M.A.K.P. Tolentino, D.R.B. Albano, F.B. Sevilla, Piezoelectric sensor for ethylene based on silver(I)/polymer composite, *Sens. Actuators B Chem.* 254 (2018) 299–306.
- [35] C. Popa, M. Petrus, A.M. Bratu, Ammonia and ethylene biomarkers in the respiration of the people with schizophrenia using photoacoustic spectroscopy, *J. Biomed. Opt.* 20 (2015) 8.
- [36] J.D. Moon, M. Galizia, H. Borjigin, R. Liu, J.S. Riffle, B.D. Freeman, D.R. Paul, Water vapor sorption, diffusion, and dilation in polybenzimidazoles, *Macromolecules* 51 (2018) 7197–7208.
- [37] J. Zhang, X.H. Liu, G. Neri, N. Pinna, Nanostructured materials for room-temperature gas sensors, *Adv. Mater.* 28 (2016) 795–831.

M. Šetka received the B.Sc. and M.Sc. degree in chemical engineering from the University of Belgrade, Serbia, in 2013 and 2015, respectively. She is currently PhD student at the Central European Institute of Technology (CEITEC) in Brno, Czech Republic. Her research interests include synthesis and characterization of the gas sensitive polymers and development of gas sensors devices.

F. Bahos received the B.Sc degree in Engineering Physics in 2011 from the Cauca University. He received his MEng. degree in Electrical Engineering in 2018 and worked on gas sensors and RF signal conditioning at Instituto de Ciencias Aplicadas y Tecnología de la Universidad Nacional Autónoma de México (ICAT – UNAM). Now, he is working at Sistema de Investigación, Desarrollo Tecnológico e Innovación (Sennova – SENA) on electrical sensors and internet of things.

D. Matatagui is graduated in physics in 2007, received his M.Sc. in Advanced Materials and Nanotechnology in 2008 and his Ph.D. degree in physics in 2012 from the Universidad Autónoma de Madrid. From 2008 to 2013 he was working in the GRIDSEN group at the CSIC (Spain) on I + D + i of bio-chemical microsensors and electronic noses for environmental protection. He was a Research Professor at the National Autonomous University of Mexico (UNAM), in the Biomedical Devices Group at the CCADET on the development of chemical sensors and biosensors. Currently, he is working at the Instituto de Tecnologías Físicas y de la Información (CSIC) developing new sensor technologies.

M. Potoček received his PhD in Physics in 2010. He is currently working as researcher at the Central European Institute of Technology CEITEC and as assistant professor at the Institute of Physical Engineering, Faculty of Mechanical Engineering, Brno University of Technology, Brno, Czech Republic. His research is focused on surface analysis of ultrathin layers surface using Time-of-flight Secondary Ion Mass Spectrometry (TOF-SIMS) and Thermal desorption spectroscopy (TDS).

Z. Kral received his PhD degree in Electronic Engineering from the University Rovira i Virgili, Spain, working on characterization of novel optoelectronic structures like photonic crystals. Shortly after academic career he started in a private technology company focused on development and fabrication of scanning electron microscopes. Currently, he is working for Thermo Fisher Scientific as a senior applications scientist experienced in analytical instruments and failure analysis techniques.



J. Drbohlavova received her PhD degree in physical chemistry in 2008. She works as senior researcher and associate professor at Brno University of Technology in the field of synthesis and characterization of nanomaterials for sensing in medical and environmental applications. From 2017 she also works as Seconded National Expert in the European Commission for nanomaterials standardization, regulation and governance.

I. Gracia received her PhD degree in physics in 1993 from the Autonomous University 18 of Barcelona, Spain, working on chemical sensors. She joined the National Microelectronics Center (CNM) working on photolithography, currently she is full time 20 senior researcher in the Micro-Nano Systems department of the CNM and her work is focused on gas sensing technologies and MEMS reliability.

S. Vallejos received her PhD degree in Electronic Engineering from the Universitat Rovira i Virgili, Spain. Currently, she holds a Ramón y Cajal fellowship and her research is focused on gas sensing technologies and nanomaterials. She is interested in exploring scalable synthesis methods to tailor and engineer the sensing properties of nanomaterials, as well as in the development of gas sensing microsystems for applications in safety, medicine, and environment.

Article

Love Wave Sensors with Silver Modified Polypyrrole Nanoparticles for VOCs Monitoring

Milena Šetka ¹, Fabio A. Bahos ², Daniel Matatagui ^{2,3}, Isabel Gràcia ⁴ , Eduard Figueras ⁴ , Jana Drbohlavová ¹ and Stella Vallejos ^{1,4,*}

¹ CEITEC—Central European Institute of Technology, Brno University of Technology, 61200 Brno, Czech Republic; milena.setka@ceitec.vutbr.cz (M.Š.); jana.drbohlavova@ceitec.vutbr.cz (J.D.)

² Instituto de Ciencias Aplicadas y Tecnología (ICAT), Universidad Nacional Autónoma de México, Ciudad Universitaria, Ciudad de México 04510, Mexico; fbahos@unicauca.edu.co (F.A.B.); daniel.matatagui@icat.unam.mx (D.M.)

³ SENSAVAN, Instituto de Tecnologías Físicas y de la Información (ITEFI, CSIC), Serrano 144, 28006 Madrid, Spain; d.m@csic.es

⁴ Instituto de Microelectrónica de Barcelona (IMB-CNM, CSIC), Campus UAB, 08193 Bellaterra, Spain; isabel.gracia@imb-cnm.csic.es (I.G.); eduard.figueras@imb-cnm.csic.es (E.F.)

* Correspondence: stella.vallejos@imb-cnm.csic.es or vargas@feec.vutbr.cz; Tel.: +34-93-594-7700

Received: 30 January 2020; Accepted: 3 March 2020; Published: 6 March 2020



Abstract: Love wave sensors with silver-modified polypyrrole nanoparticles are developed in this work. These systems prove functional at room temperature with enhanced response, sensitivity and response time, as compared to other state-of-the-art surface acoustic wave (SAW) sensors, towards volatile organic compounds (VOCs). Results demonstrate the monitoring of hundreds of ppb of compounds such as acetone, ethanol and toluene with low estimated limits of detection (~3 ppb for acetone). These results are attributed to the use of silver-modified polypyrrole as a second guiding/sensitive layer in the Love wave sensor structure, which provides further chemically active sites for the gas-solid interactions. The sensing of low VOCs concentrations by micro sensing elements as those presented here could be beneficial in future systems for air quality control, food quality control or disease diagnosis via exhaled breath as the limits of detection obtained are within those required in these applications.

Keywords: polypyrrole; gas sensors; love wave sensors; volatile organic compounds

1. Introduction

Volatile organic compounds (VOCs) are low-molecular-weight organic compounds and most of them are categorized as harmful substances which may have a short term and/or long term negative impact on the environment (e.g., creation of tropospheric ozone) and on health (e.g., allergic reactions, asthma, damage of central nervous system, cancer, etc.) [1]. Hence, currently, there is an increased need of VOCs monitoring for outdoor and indoor air quality control (e.g., VOCs emission from industrial processes, traffic activity, waste treatment and disposal, tobacco smoking, etc.), food quality analysis (e.g., VOCs linked to food spoilage) and health diagnosis (e.g., VOCs associated to disease biomarkers) [1–5]. Therefore, the sensitive and selective detection of low VOCs concentrations using simple and low-cost sensors may have a significant effect on quality of life.

Surface acoustic wave (SAW) sensors have attracted great attention thanks to their sensitivity, low limits of detection (LOD), room temperature operation, low power consumption, relatively simple architecture, small dimensions and ability to work in wireless mode [6]. Moreover, previous literature on SAW sensors states the feasibility to sense gases and vapors by using sensitive materials such

as semiconducting metal oxides [7], polymers [8], graphene oxide [9] and carbon nanotubes [10]. Apart from the competing advantages of those sensing materials, polymers-based SAW structures demonstrated improved performance in gas sensing, owing to their low density and shear velocity. Additionally, polymers also have high sensitivity at room temperature (as opposed to semiconducting metal oxides) and report good cost-effectiveness (compared to carbon based materials) [6,11]. Among various types of SAW structures (e.g., Rayleigh, shear horizontal SAW, Love, leaky), those based on Love waves (L-SAW) have been identified to have high mass sensitivity, generally, due to the surface confinement of energy in the thin guiding layer, which makes the surface extremely sensitive to any perturbations [12].

Polypyrrole (PPy) and its sensing properties to VOCs have been investigated in the past typically by implementing this conductive polymer into chemo-resistive structures [13]. In contrast, the use of PPy in the field of SAW sensors and especially in L-SAW sensors has been rarely described in the literature, in which is found a significantly low amount of reports for L-SAW based PPy structures. Our recent studies, however, indicate that L-SAW sensors with multi-guiding layers containing gold modified PPy as a guiding and gas sensitive material can enhance to a higher degree the sensing performance at room temperature of this sensor as compared to other SAW or chemo-resistive structures with similar PPy modification [14].

In this context, this work explores further the use of L-SAW structures with second guiding/sensitive layers based on silver-modified polypyrrole (Ag/PPy). The work also evaluates the performance of these structures to various VOCs (including ethanol, acetone and toluene), as these vapors are of interest in multiple applications, such as human breath analyzers, food quality analyzers and/or environment monitoring equipment.

2. Materials and Methods

2.1. L-SAW Sensor

The fabrication process of the L-SAW platforms was adopted from our previous works [14,15]. Briefly, the two interdigital transducers (IDTs) ports (input and output) were patterned on the surface of a piezoelectric substrate (ST-90°X quartz). Each port of the IDTs consisted of 75 pairs of double-electrode type aluminium electrodes with a periodicity of 28 μm . The delay line and IDTs aperture were set to 2.1 mm. In this work, a multi-guiding layer structure, in which the first guiding layer consisted of SiO₂ (3 μm thick) and the second guiding layer of a gas sensitive conductive polymer, was employed. The second guiding and gas sensitive layer was formed from either PPy or Ag/PPy nanoparticles (NPs). To integrate the gas sensitive material over the L-SAW platform, both PPy and Ag/PPy were spin coated at a velocity of 2500 rpm. To control the reproducibility of the sensing layer, the L-SAW substrates were placed into a customized holder built to keep the substrates in a fixed and aligned position during the coating process.

PPy NPs were synthesized by an oxidative chemical polymerization as described in our previous work [14], whereas Ag NPs were synthesized by a chemical reduction of AgNO₃ with NaBH₄ using the conditions reported previously [16]. The Ag/PPy NPs solution consisted of a mixture of Ag NPs and PPy NPs in a volumetric ratio of 1:10 since we noticed previously that this relation of catalytic metal and polymer is adequate for both the uniform coating and the sensing properties [14]. The morphology and chemical composition of PPy and Ag NPs were investigated using a high-resolution transmission electron microscope (HR-TEM, FEI TITAN Themis 60–300 kV), Scanning Electron Microscope equipped with focus ion beam (FIB/SEM, Helios G4 NanoLab DualBeam™) and X-ray photoelectron spectroscopy (XPS, Kratos Axis Supra). The electrical characterization and measurements of the transmission scattering parameter (S_{21}) were performed using a network analyser (Agilent 4395A). Figure 1 shows a schematic view of an L-SAW sensor and the two gas sensitive materials deposited by spin coating.

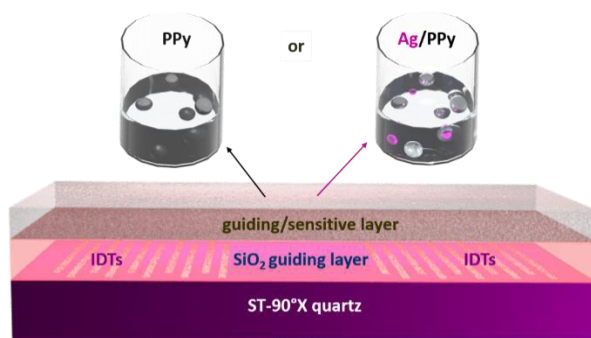


Figure 1. Schematic view of a L-SAW sensor and solutions used for deposition of PPy or Ag/PPy guiding/sensitive layers.

2.2. Gas Sensing Test

Gas sensing tests of the L-SAW sensors (based on PPy and Ag/PPy) were carried out simultaneously in a continuous flow system equipped with mass flow controllers and calibrated gas cylinders of acetone (Praxair, 100 ppm), ethanol (Praxair, 100 ppm) and toluene (Praxair, 200 ppm), as described in our previous work [17]. The sensors were tested towards these gases in a concentration range from 0.5 to 5 ppm, both in dry and humid environments with 10% and 30% relative humidity (RH). The sensors were exposed to each analyte for 2 min and purified with dry or humid synthetic air for 10 min at a constant temperature of 24 °C. The moisture and temperature inside the gas chamber were monitored using a humidity/temperature sensor (SHT71, operating from 0 to 100% RH, accuracy of $\pm 3\%$ RH). The sensing test was performed over a 10 days period with a continuous operation of 10 h per day. The sensor response was measured using an electronic measurement system equipped with an amplifier, directional coupler and frequency counter [18]. The response (frequency shift) was defined as the difference in the resonant frequency produced by the exposure of the sensors to dry/humid air and the target analyte. The response time was defined as the time required to reach 90% of the total frequency shift value, whereas the recovery time was defined as the time required to return to 90% of the baseline frequency after the target gas was purged.

3. Results

3.1. Gas Sensitive Material Properties

The morphology and chemical composition of the gas sensitive materials (i.e., PPy and Ag/PPy) were examined by TEM and XPS. TEM of the PPy NPs (Figure 2a) revealed spherical shaped particles with an average size of 44 ± 10 nm, calculated for a population of 100 particles. XPS displayed characteristic C 1s (Figure 2b) and N 1s (Figure 2c) core level spectra. The components in the C 1s spectrum centred at 284.4, 285.0, 286.3, 288.1 and 288.9 eV are ascribed to the binding energies of the C–C bonds of β atoms, the C–C bonds of α atoms and the C–N, C–O and C=O bonds of PPy, respectively. Similarly, the three components in the N 1s spectrum correspond to the =N– (398.0 eV), –N–H (400.0 eV) and =N–H⁺ (402.3 eV) bonds of PPy. The presence of these components in the C 1s and N 1s core level spectra is consistent with our previous observations [19] and corroborates the synthesis of PPy.

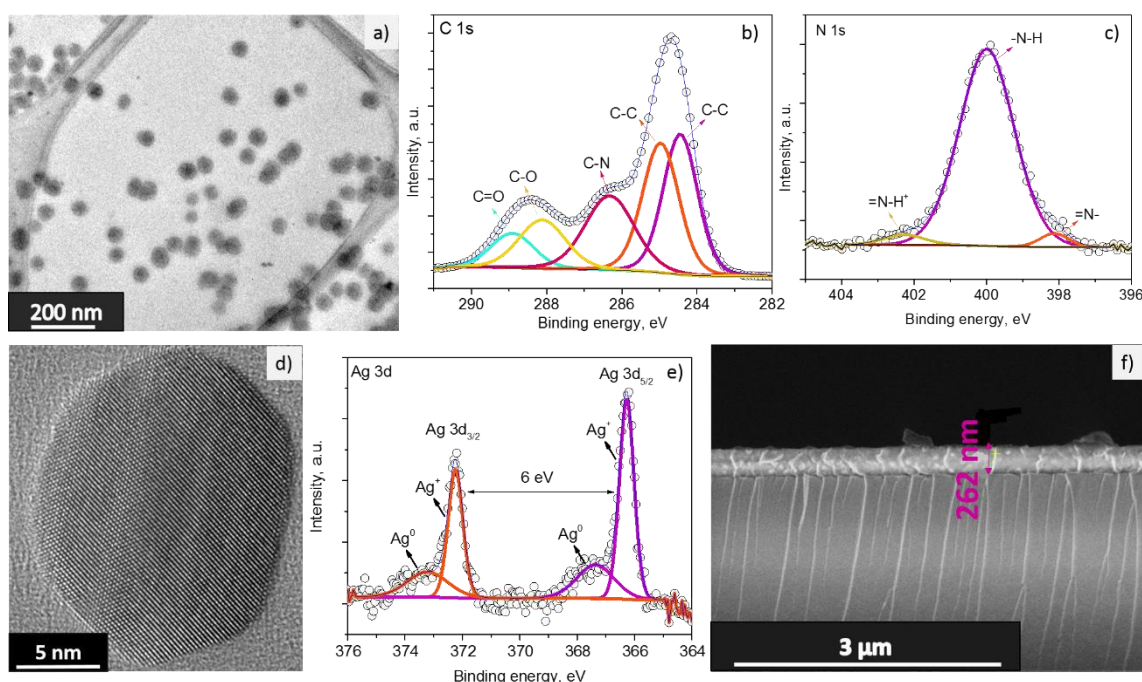


Figure 2. TEM image of PPy NPs (a); high-resolution XPS spectra of the C 1s (b) and N 1s (c) core levels at the PPy NPs; HR-TEM image of the Ag NPs (d); high resolution XPS spectra of the Ag 3d core levels at the Ag NPs (e); typical cross-section SEM image of the L-SAW sensors after spin coating of PPy or Ag/PPy NPs (f).

The synthesis of crystalline Ag NPs was also corroborated by HR-TEM. Figure 2d displays the TEM images of the particles with mean diameter of approximately 17 ± 3 nm (calculated for a population of 30 particles) and lattice fringes with spacing of ~ 0.23 nm, consistent with the (111) planes of Ag face centered cubic phase (JCPDS number 04-0783) [20]. High-resolution XPS analysis of the Ag NPs (Figure 2e) revealed typical Ag 3d doublets separated by 6 eV. The deconvoluted Ag 3d doublet with a pair of components centered at 366.3 and 372.3 eV, and another pair centered at 367.4 and 373.2 eV indicates the presence of Ag^+ and Ag^0 , respectively. This suggests the coexistence of silver oxide (Ag_2O) and metallic silver (Ag), in accordance with previous observations [21].

Further SEM study of the PPy and Ag/PPy NPs guiding/sensitive layers after spin coating showed the integration of uniform sensing layers with a thickness of $\sim 262 \pm 10$ nm on the L-SAW platforms. A typical cross section SEM image of the L-SAW sensors is displayed in Figure 2f.

3.2. Electrical Characterization of the L-SAW Sensors

The PPy and Ag/PPy L-SAW sensors were electrically characterized by measuring the transmission scattering parameter (S_{21}). These results were compared to a reference L-SAW platform with only a SiO_2 guiding layer to determine the frequency shifts after the incorporation of the second guiding/sensitive layer. Figure 3 illustrates the resonant frequency and insertion loss of the reference, PPy and Ag/PPy L-SAW sensors. These results show that the operating frequency and insertion loss of the reference L-SAW sensor are 165.1 MHz and -16 dB, respectively. The figure also shows the shift in the resonance frequency of the PPy and Ag/PPy sensors to lower numbers (161.6 ± 0.1 MHz) with respect to the reference, as well as the increase of the insertion loss (19.7 ± 1 dB). Both these changes are consistent with the use of the PPy and Ag/PPy layers as a second guiding layer. The relatively low insertion losses in the double guiding layer L-SAW structures lead to sensors with low overall noise (lower than 10 Hz) and, in turn, low LOD.

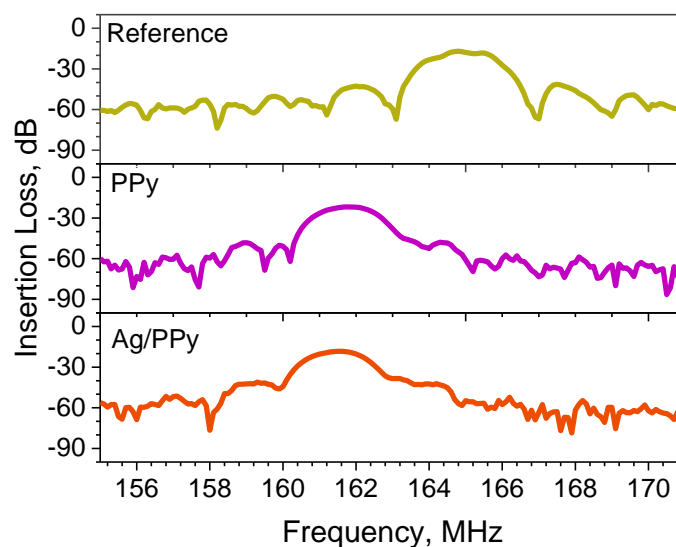


Figure 3. Transmission scattering parameters (S_{21}) of the uncoated (reference) and coated (with PPy or Ag/PPy sensitive layer) L-SAW structures.

3.3. Gas Sensing Properties of the L-SAW Sensors

The sensing capability of the L-SAW sensors (PPy and Ag/PPy) was evaluated by exposing these devices simultaneously to various concentrations (between 0.5 and 5 ppm) of acetone, ethanol and toluene at room temperature. The calibration curves for acetone, ethanol and toluene are shown in Figure 4a,c,e, respectively. These figures show the proportional increase of the sensor response with the increase of concentration for each gas without reaching the saturation point, which indicates the possibility to sense higher concentrations of these analytes. Generally, the results display enhanced responses for the Ag/PPy sensors compared to the PPy sensors for all tested gases, with frequency shifts of approximately 1.4 times more for the Ag/PPy sensors than for the PPy sensors. These results are in line with previous experimental research, which proved the enhancement of gas sensing properties (e.g., sensors response) by the modifications of a host gas sensitive material with metal catalysts (e.g., Ag, Au) due to a “spillover effect” [14,22].

The LOD of the Ag/PPy L-SAW sensors (defined as the concentration providing a signal-to-noise ratio of at least three [23]) was estimated to be 3, 5 and 20 ppb for acetone, ethanol and toluene, respectively. These LOD are below the limits set for acetone, ethanol and toluene in different areas. For instance, the American Conference of Governmental Industrial Hygienists (ACGIH) sets the occupational threshold limit values (TLV) for acetone, ethanol and toluene to 250, 1000 and 20 ppm, respectively, considering 8-h time-weighted averages. Similarly, the concentration of VOCs in the food industry are above (typically by tens or hundreds of ppb) the LOD obtained for our sensors [24]. Additionally, in the breath analysis field, the concentrations of acetone, ethanol and toluene in the exhaled breath (e.g., lung cancer patients register concentrations of 112–2654 ppb of acetone, 13–1520 ppb of ethanol and 9.3–21.3 ppb of toluene) [4] are above the LOD obtained in this work.

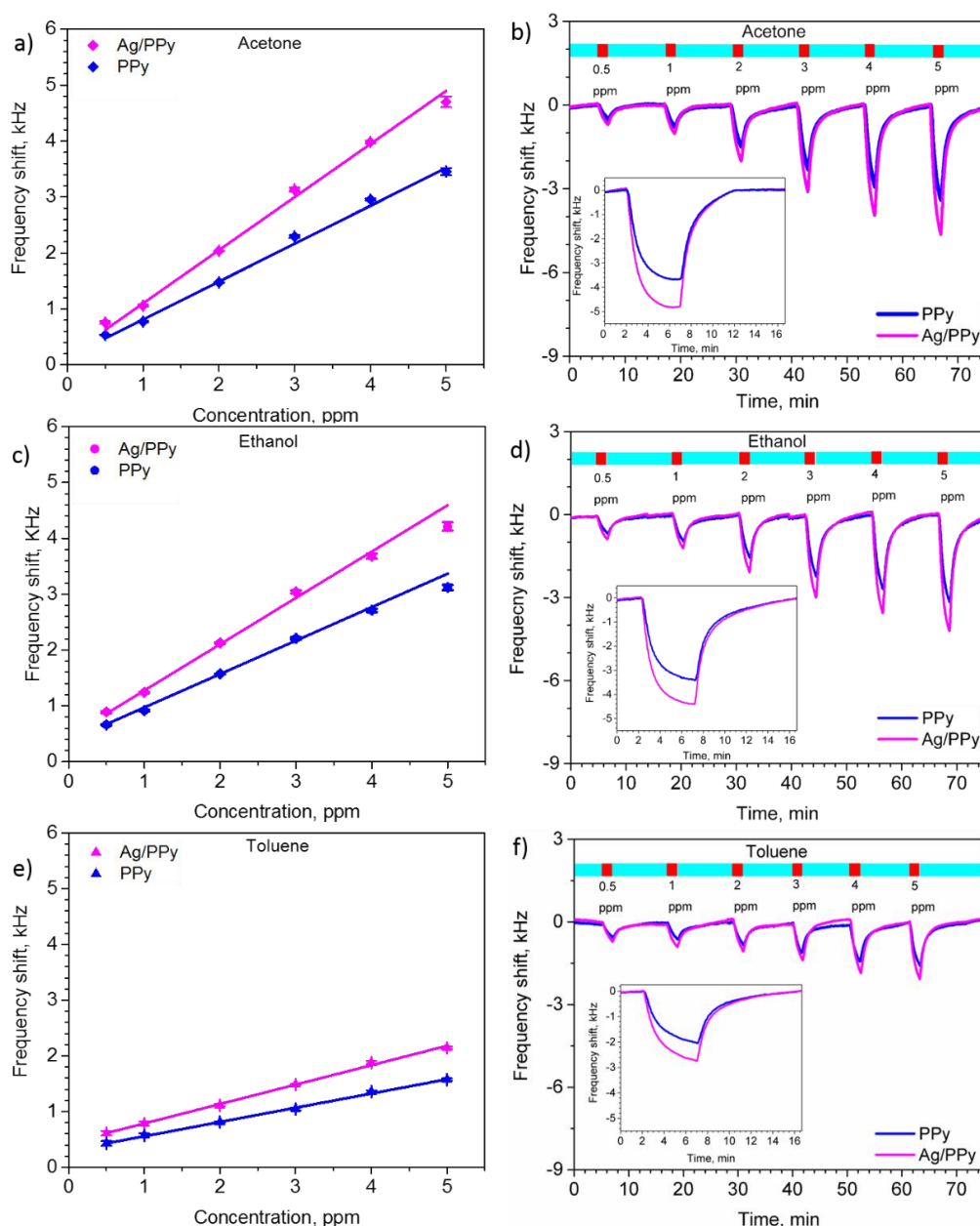


Figure 4. Calibrations curves and dynamic responses of the L-SAW sensors (based on PPy and Ag/PPy) for acetone (a,b), ethanol (c,d), and toluene (e,f). The insets in (b,d,f) display the time dependent response to 5 ppm of each gas.

The dynamic response of the PPy and Ag/PPy L-SAW sensors exposed to various concentrations of acetone, ethanol and toluene are presented in Figure 4b,d,f, respectively. One can notice from these results that the Ag/PPy and PPy sensors displayed stable and reversible responses. In order to reach the steady state of the response and determine the response and recovery time, the sensors were exposed to a gas concentration of 5 ppm for 5 min and then the gas was purged with dry synthetic air for 10 min (see the inset responses in Figure 4b,d,f). Overall, the response and recovery time for the Ag/PPy sensors was approximately 10 s faster than that for the PPy sensors. This could be attributed the catalytic properties of chemically active Ag NPs, which accelerate the gas-solid interactions at the guiding/sensitive film. These results also reveal faster response and recovery time to acetone than to ethanol or toluene for both the PPy and Ag/PPy sensors. The response time for the Ag/PPy sensors to acetone and ethanol, for instance, was below 2.5 min, while the response time to toluene was below

3.5 min. In addition, the Ag/PPy sensors required less than 4 min to recover after acetone exposure and less than 5.5 min after ethanol and toluene exposure.

Results in Figure 4b,d,f also give evidence of the negative frequency shift of the response to acetone, ethanol and toluene. This decrease in the resonant frequency of the L-SAW sensors may indicate that the mass and acoustoelectric loading effects outweigh the elastic effect [25]. The mass loading effect and therefore the decrease of the resonant frequency of the L-SAW sensors may be connected to the change in the mass of the PPy and Ag/PPy guiding/sensitive layer caused by the sorption of gas analytes (i.e., acetone, ethanol and toluene). The acoustoelectric effect, in contrast, may be connected to the adsorption of the gas analytes at the guiding/sensitive layer and the increase of the conductivity of PPy [26], which is also characterized by a decrease in the resonant frequency of the sensor. The contribution of the elastic effect, which is generally observed by an increase in the resonant frequency, is ruled out in this particular case [25].

As the Ag/PPy L-SAW sensors showed improved sensing properties over the PPy sensors, further analysis was performed on these sensors. Figure 5 shows the sensitivity of the Ag/PPy sensors calculated as the ratio between the change in frequency response of the sensor and the change in the gas concentration. These results show the sensitivity to various gases, including acetone (910 Hz/ppm), ethanol (742 Hz/ppm), carbon monoxide (458 Hz/ppm), hydrogen (396 Hz/ppm) and toluene (340 Hz/ppm). Overall, the sensors displayed good stability keeping a constant operating frequency and reproducible responses with standard errors below 5% after testing all gases in dry ambient. One can notice in Figure 5 that the Ag/PPy sensors exhibit a higher sensitivity to acetone than to other analytes such as ethanol and toluene, which register a cross-sensitivity respect to acetone of 81% and 37%, respectively. Similarly, the cross-sensitivity of other gases such as carbon monoxide and hydrogen with respect to acetone is found to be 50% and 43%, respectively. In summary, these results indicate a relatively low interference among the tested analytes.

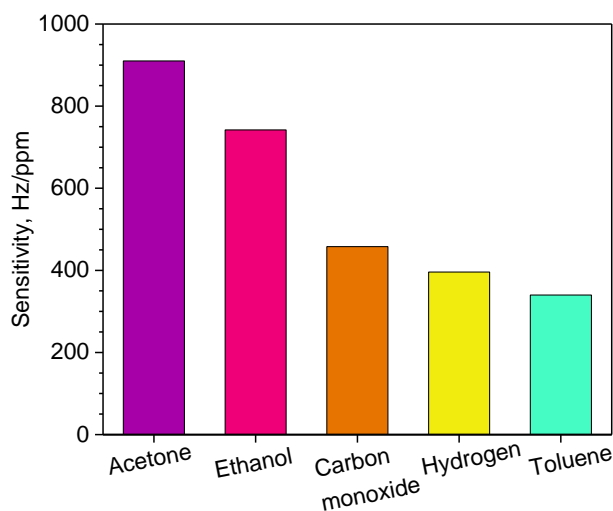


Figure 5. Sensitivity of Ag/PPy L-SAW sensors to acetone, ethanol, carbon monoxide, hydrogen and toluene for concentrations between 0.5 and 5 ppm.

The performance of the Ag/PPy L-SAW gas sensors investigated in this work were summarized and compared with other SAW gas sensors reported in the literature (Table 1). Results indicate that our sensors exhibited significantly higher sensitivity as well as lower LOD to acetone, ethanol and toluene in comparison to other SAW systems. The lowest tested concentrations of those VOCs detected via Ag/PPy L-SAW sensors were crucially lower than the theoretical LOD of state-of-the-art sensors (Table 1). This demonstrates the capability of Ag/PPy based Love wave sensors to detect ppb levels of the target VOCs.

Table 1. Comparative table of state-of-the-art SAW sensors and Ag/PPy L-SAW sensors for acetone, ethanol and toluene.

| Sensitive Material | Gas | LTC (ppm) | HTC (ppm) | Sensitivity (Hz/ppm) | LOD (ppm) | Temperature | Reference |
|--|---------|-----------|-----------|----------------------|-----------|-------------|-----------|
| Ag/PPy | Acetone | 0.5 | 5 | 910 | 0.003 | RT | This work |
| | Ethanol | | | 742 | 0.005 | | |
| | Toluene | | | 340 | 0.020 | | |
| PPy | Acetone | 5.5 | 80 | 116.4 | - | RT | [27] |
| PEI/Fe ₃ O ₄ | Ethanol | 160 | 16,000 | 1.6 | 65 | ND | [28] |
| | Toluene | | | 1.9 | 54 | | |
| MWCNTs-PEI | Ethanol | 200 | 40,000 | 1.2 | 176.5 | ND | [29] |
| | Toluene | | | 1.2 | 170.7 | | |
| PEI/WO ₃ | Acetone | 50 | 800 | 3.4 | 15 | RT | [8] |
| | Ethanol | | | 7.9 | 6 | | |
| | Toluene | | | 4.8 | 11 | | |
| GO | Ethanol | 30 | 750 | 30 | - | ND | [9] |
| | Toluene | | | 24 | - | | |
| ZIF/Au | Acetone | 5 | 25 | 28 | 1.1 | RT | [30] |
| | Ethanol | | | 72 | 0.5 | | |
| SnO ₂ /Co ₃ O ₄ | Toluene | 100 | 900 | 0.6 | 50 | RT | [7] |
| PEUT-MWCNTs | Toluene | 25 | 200 | 12.2 | 0.6 | RT | [10] |

LTC—lowest tested concentration, HTC—highest tested concentration, RT—room temperature, MWCNTs—multi-wall carbon nanotubes, PEI—polyethylenimine, GO—graphene oxide, ZIF—zeolitic imidazolate frameworks, PEUT—polyetherurethane, ND—not defined.

To evaluate the effect of humidity on the sensing response, the Ag/PPy sensors were tested to acetone at RH of 10% and 30%. Figure 6 compares the frequency shift of the sensor to 5 ppm of acetone in dry and humid conditions with 10% and 30% RH. The tests show that the sensor response decreases by a factor of 2 and 7 when the atmosphere changes from dry to 10% and 30% RH, respectively. Humidity tests are generally not reported for state-of-the-art SAW sensors; therefore, these characteristics have not been included in Table 1. The loss of response in the Ag/PPy sensors in a humid atmosphere may be caused by the water vapor sorption into the polymer layer, which fills the free volume fraction in the polymer and reduces the gas permeability [31]. Additionally, after the humidity test, we registered a decrease in the sensor response in dry ambient of about 35% compared to the responses obtained in the initial operation hours (notice that the same sensors were exposed to all target gases in a dry and humid environment accumulating an operation time of 100 h). The irreversible loss of response in the material may be caused by the humidity rather than the testing time, as during the tests in dry ambient the response registered low dispersion as described above. This is a common issue in polymer based gas sensors that needs further technological solutions such as the use of humidity filters or dehydration elements [32] in order to exploit these sensors in future consumer devices.

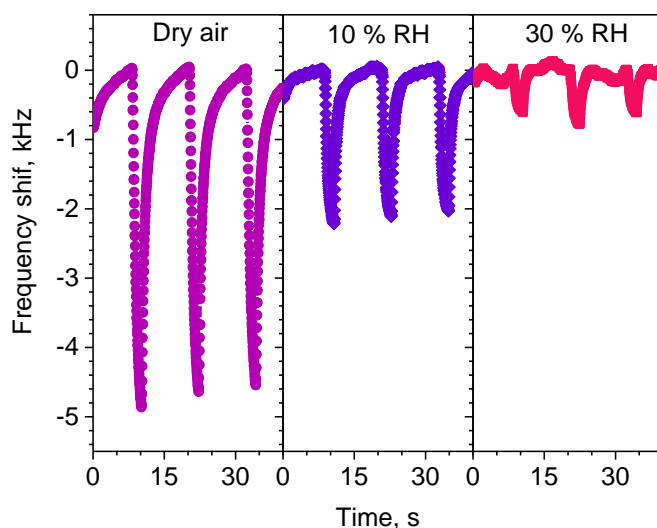


Figure 6. Frequency response of Ag/PPy L-SAW sensor to acetone concentration of 5 ppm under dry air, 10% and 30% relative humidity (RH).

4. Conclusions

This work reports the properties of non-modified and silver-modified PPy L-SAW sensors at room temperature for detection of ppb-levels of VOCs, including acetone, ethanol and toluene. The above results suggest that PPy functionalization using Ag NPs enhances the response, sensitivity and speed of L-SAW sensors to organic vapors, particularly to acetone (910 Hz/ppm). A moderate response to acetone was also registered by running the tests in humid conditions (10% and 30% RH) with the sensors detecting concentrations down to 1 ppm. Overall, these results demonstrated enhanced properties compared to other state-of-the-art SAW sensors, providing a technological solution for monitoring low concentrations of VOCs at room temperature.

Author Contributions: The authors also contributed to the conceptualization (M.Š., D.M. and S.V.); methodology (M.Š., F.A.B., D.M. and I.G.); validation (M.Š., F.A.B. and E.F.); formal analysis, (M.Š. and S.V.); writing—original draft preparation (M.Š.) writing—review and editing (D.M., J.D. and S.V.); and funding acquisition (D.M., E.F. and S.V.). All authors have read and agreed to the published version of the manuscript.

Funding: This research was funded by the Czech Science Foundation (GAČR) via Grant No. 20-20123S, the Spanish Ministry of Economy and Competitiveness via projects TEC2015-74329-JIN-(AEI/FEDER, EU), and TEC2016-79898-C6-1-R (AEI/FEDER, EU) and by Universidad Nacional Autónoma de México via Grant DGAPA-UNAM-PAPIIT TA100118. The support of the “Ramón y Cajal” programme is also acknowledged. This research has made use of the infrastructures the Spanish ICTS Network MICRONANOFABS, partially supported by MINECO, and Czech CEITEC Nano Research Infrastructure, supported by MEYS (2016-2019).

Acknowledgments: This work has been supported in part by the Czech Science Foundation (GAČR) via Grant No. 20-20123S, the Spanish Ministry of Economy and Competitiveness via projects TEC2015-74329-JIN-(AEI/FEDER, EU), and TEC2016-79898-C6-1-R (AEI/FEDER, EU) and by Universidad Nacional Autónoma de México via Grant DGAPA-UNAM-PAPIIT TA100118. The support of the “Ramón y Cajal” programme is also acknowledged. This research has made use of the infrastructures the Spanish ICTS Network MICRONANOFABS, partially supported by MINECO, and Czech CEITEC Nano Research Infrastructure, supported by MEYS (2016-2019).

Conflicts of Interest: The authors declare no conflict of interest.

References

1. Ramírez, N.; Cuadras, A.; Rovira, E.; Borrull, F.; Marcé, R.M. Chronic risk assessment of exposure to volatile organic compounds in the atmosphere near the largest Mediterranean industrial site. *Environ. Int.* **2012**, *39*, 200–209. [[CrossRef](#)] [[PubMed](#)]

2. Bai, J.; Baker, S.M.; Goodrich-Schneider, R.M.; Montazeri, N.; Sarnoski, P.J. Aroma Profile Characterization of Mahi-Mahi and Tuna for Determining Spoilage Using Purge and Trap Gas Chromatography-Mass Spectrometry. *J. Food Sci.* **2019**, *84*, 481–489. [[CrossRef](#)] [[PubMed](#)]
3. Font, X.; Artola, A.; Sanchez, A. Detection, Composition and Treatment of Volatile Organic Compounds from Waste Treatment Plants. *Sensors* **2011**, *11*, 4043–4059. [[CrossRef](#)] [[PubMed](#)]
4. Ulanowska, A.; Kowalkowski, T.; Trawinska, E.; Buszewski, B. The application of statistical methods using VOCs to identify patients with lung cancer. *J. Breath Res.* **2011**, *5*, 11. [[CrossRef](#)]
5. Goodman, N.B.; Wheeler, A.J.; Paevere, P.J.; Selleck, P.W.; Cheng, M.; Steinemann, A. Indoor volatile organic compounds at an Australian university. *Build. Environ.* **2018**, *135*, 344–351. [[CrossRef](#)]
6. Devkota, J.; Ohodnicki, P.R.; Greve, D.W. SAW Sensors for Chemical Vapors and Gases. *Sensors* **2017**, *17*, 28. [[CrossRef](#)]
7. Constantinoiu, I.; Miu, D.N.; Viespe, C. Surface Acoustic Wave Sensors for Ammonia Detection at Room Temperature Based on SnO₂/Co₃O₄ Bilayers. *J. Sens.* **2019**. [[CrossRef](#)]
8. Constantinoiu, I.; Viespe, C. Detection of Volatile Organic Compounds Using Surface Acoustic Wave Sensor Based on Nanoparticles Incorporated in Polymer. *Coatings* **2019**, *9*, 9. [[CrossRef](#)]
9. Nikolaou, I.; Hallil, H.; Conedera, V.; Deligeorgis, G.; Dejous, C.; Rebiere, D. Inkjet-Printed Graphene Oxide Thin Layers on Love Wave Devices for Humidity and Vapor Detection. *IEEE Sens. J.* **2016**, *16*, 7620–7627. [[CrossRef](#)]
10. Sayago, I.; Fernández, M.J.; Fontecha, J.L.; Horrillo, M.C.; Vera, C.; Obieta, I.; Bustero, I. New sensitive layers for surface acoustic wave gas sensors based on polymer and carbon nanotube composites. *Sens. Actuators B Chem.* **2012**, *175*, 67–72. [[CrossRef](#)]
11. Feng, S.B.; Farha, F.; Li, Q.J.; Wan, Y.L.; Xu, Y.; Zhang, T.; Ning, H.S. Review on Smart Gas Sensing Technology. *Sensors* **2019**, *19*, 22. [[CrossRef](#)]
12. Xu, Z.; Yuan, Y.J. Implementation of guiding layers of surface acoustic wave devices: A review. *Biosens. Bioelectron.* **2018**, *99*, 500–512. [[CrossRef](#)]
13. Šetka, M.; Drbohlavová, J.; Hubálek, J. Nanostructured polypyrrole-based ammonia and volatile organic compound sensors. *Sensors* **2017**, *17*, 28. [[CrossRef](#)]
14. Šetka, M.; Bahos, F.A.; Matatagui, D.; Potoček, M.; Kral, Z.; Drbohlavová, J.; Gràcia, I.; Vallejos, S. Love wave sensors based on gold nanoparticle-modified polypyrrole and their properties to ammonia and ethylene. *Sens. Actuators B Chem.* **2019**, *304*, 127337. [[CrossRef](#)]
15. Fragoso-Mora, J.R.; Matatagui, D.; Bahos, F.A.; Fontecha, J.; Fernandez, M.J.; Santos, J.P.; Sayago, I.; Gràcia, I.; Horrillo, M.C. Gas sensors based on elasticity changes of nanoparticle layers. *Sens. Actuators B Chem.* **2018**, *268*, 93–99. [[CrossRef](#)]
16. Mulfinger, L.; Solomon, S.D.; Bahadory, M.; Jeyarajasingam, A.V.; Rutkowsky, S.A.; Boritz, C. Synthesis and Study of Silver Nanoparticles. *J. Chem. Educ.* **2007**, *84*, 322. [[CrossRef](#)]
17. Vallejos, S.; Gràcia, I.; Chmela, O.; Figueras, E.; Hubálek, J.; Cané, C. Chemoresistive micromachined gas sensors based on functionalized metal oxide nanowires: Performance and reliability. *Sens. Actuators B Chem.* **2016**, *235*, 525–534. [[CrossRef](#)]
18. Matatagui, D.; Bahos, F.A.; Gràcia, I.; Horrillo, M.D.C. Portable Low-Cost Electronic Nose Based on Surface Acoustic Wave Sensors for the Detection of BTX Vapors in Air. *Sensors* **2019**, *19*, 5406. [[CrossRef](#)] [[PubMed](#)]
19. Šetka, M.; Calavia, R.; Vojkuvka, L.; Llobet, E.; Drbohlavova, J.; Vallejos, S. Raman and XPS studies of ammonia sensitive polypyrrole nanorods and nanoparticles. *Sci. Rep.* **2019**, *9*, 10. [[CrossRef](#)]
20. Zhang, Q.; Chen, C.; Wan, G.; Lei, M.; Chi, M.; Wang, S.; Min, D. Solar light induced synthesis of silver nanoparticles by using lignin as a reductant, and their application to ultrasensitive spectrophotometric determination of mercury(II). *Microchim. Acta* **2019**, *186*, 727. [[CrossRef](#)]
21. Yu, J.J.; Sun, D.P.; Wang, T.H.; Li, F. Fabrication of Ag@AgCl/ZnO submicron wire film catalyst on glass substrate with excellent visible light photocatalytic activity and reusability. *Chem. Eng. J.* **2018**, *334*, 225–236. [[CrossRef](#)]
22. Wei, L.; Sun, J.; Xu, L.; Zhu, S.D.; Zhou, X.Y.; Yang, S.; Dong, B.; Bai, X.; Lu, G.Y.; Song, H.W. Understanding the noble metal modifying effect on In₂O₃ nanowires: Highly sensitive and selective gas sensors for potential early screening of multiple diseases. *Nanoscale Horiz.* **2019**, *4*, 1361–1371. [[CrossRef](#)]

23. Li, M.; Kan, H.; Che, S.T.; Feng, X.Y.; Li, H.; Li, C.; Fu, C.; Quan, A.J.; Sun, H.B.; Luo, J.T.; et al. Colloidal quantum dot-based surface acoustic wave sensors for NO₂-sensing behavior. *Sens. Actuators B Chem.* **2019**, *287*, 241–249. [[CrossRef](#)]
24. Edirisinghe, R.K.B.; Graham, A.J.; Taylor, S.J. Characterisation of the volatiles of yellowfin tuna (*Thunnus albacares*) during storage by solid phase microextraction and GC-MS and their relationship to fish quality parameters. *Int. J. Food Sci. Technol.* **2007**, *42*, 1139–1147. [[CrossRef](#)]
25. Bhasker Raj, V.; Nimal, A.T.; Parmar, Y.; Sharma, M.U.; Gupta, V. Investigations on the origin of mass and elastic loading in the time varying distinct response of ZnO SAW ammonia sensor. *Sens. Actuators B Chem.* **2012**, *166–167*, 576–585. [[CrossRef](#)]
26. Li, Y.; Ban, H.; Yang, M. Highly sensitive NH₃ gas sensors based on novel polypyrrole-coated SnO₂ nanosheet nanocomposites. *Sens. Actuators B Chem.* **2016**, *224*, 449–457. [[CrossRef](#)]
27. Li, F.; Li, H.; Jiang, H.; Zhang, K.; Chang, K.; Jia, S.; Jiang, W.; Shang, Y.; Lu, W.; Deng, S.; et al. Polypyrrole nanoparticles fabricated via Triton X-100 micelles template approach and their acetone gas sensing property. *Appl. Surf. Sci.* **2013**, *280*, 212–218. [[CrossRef](#)]
28. Viespe, C.; Miu, D. Characteristics of Surface Acoustic Wave Sensors with Nanoparticles Embedded in Polymer Sensitive Layers for VOC Detection. *Sensors* **2018**, *18*, 9. [[CrossRef](#)]
29. Viespe, C.; Grigoriu, C. Surface acoustic wave sensors with carbon nanotubes and SiO₂/Si nanoparticles based nanocomposites for VOC detection. *Sens. Actuators B Chem.* **2010**, *147*, 43–47. [[CrossRef](#)]
30. Bahos, F.A.; Sainz-Vidal, A.; Sanchez-Perez, C.; Saniger, J.M.; Gracia, I.; Saniger-Alba, M.M.; Matatagui, D. ZIF Nanocrystal-Based Surface Acoustic Wave (SAW) Electronic Nose to Detect Diabetes in Human Breath. *Biosensors* **2018**, *9*, 13. [[CrossRef](#)]
31. Moon, J.D.; Galizia, M.; Borjigin, H.; Liu, R.; Riffle, J.S.; Freeman, B.D.; Paul, D.R. Water Vapor Sorption, Diffusion, and Dilation in Polybenzimidazoles. *Macromolecules* **2018**, *51*, 7197–7208. [[CrossRef](#)]
32. Ahmadi, M.T.; Ismail, R.; Anwar, S. *Handbook of Research on Nanoelectronic Sensor Modeling and Applications*; IGI Global: Hershey, PA, USA, 2016.



© 2020 by the authors. Licensee MDPI, Basel, Switzerland. This article is an open access article distributed under the terms and conditions of the Creative Commons Attribution (CC BY) license (<http://creativecommons.org/licenses/by/4.0/>).

Chapter 6

Love wave sensor based on polypyrrole modified with CdTe quantum dots

6.1 Motivation

Nanocomposite (inorganic-organic) materials have attracted a widespread attention in the field of gas sensing by many researches, as an alternative solution to overcome the limitations of single counterparts and to improve the final sensing properties. The various combinations of inorganic-organic materials were reported, for instance, CPs (e.g., PPy) were mixed with noble metals, MOXs, graphene etc. However, the modification of either PPy or others CPs with semiconductor QDs and their implementation into gas sensing platforms gained small attention in previous research, even though QDs showed an outstanding opto-electronic features together with large surface area due to their small size. Therefore, the further objective of my doctoral study was directed to synthesize inorganic-organic nanocomposites based on CdTe/PPy and integrate them with L-SAW. The obtained results are presented and discussed in this chapter.

6.2 Outputs

The scientific contributions of this research study allows for the submission of a journal article (*Cadmium telluride/polypyrrole nanocomposite based Love wave sensors highly sensitive to acetone at room temperature* (Section 6.4.1), in which two types of L-SAW sensors based on CdTe/PPy nanocomposites were developed. CdTe QDs and PPy NPs were mixed in volumetric ratios 1:10 and 1:2. The morphological and chemical characterization techniques (e.g., TEM, FTIR, XPS) identified both main chemical components (PPy and CdTe) in the mixture without indication of chemical reaction between them. The responses of CdTe/PPy based L-SAW sensors were verified to acetone, ethanol and toluene, and compared with responses of bare PPy sensors. The response of PPy sensors to all tested gases were lower than of CdTe/PPy (1:10), but higher than CdTe/PPy (1:2) L-SAW sensors. The decreased response of CdTe/PPy (1:2) sensors compared to others may be influenced by the different properties in the sensing layer (e.g., layer thickness, density or shear stiffness), which further tune the operation frequency of this sensor. In general, all tested sensors showed higher sensitivity to polar molecules (acetone, ethanol) than to nonpolar ones (toluene), with the highest sensitivity noticed to acetone. Considering the sensing performances of tested sensors, CdTe/PPy (1:10) L-SAW was selected as the best option to detect acetone, with the LOD of 5 ppb and sensitivity of 771 Hz/ppm. In addition, these sensors showed only minor cross-sensitivity of 468 Hz/ppm to ethanol and 225 Hz/ppm to toluene. The response time and recovery time of this sensors to 5 ppm of acetone were 155 s and 292 s, respectively. Those parameters are related to operation of this sensor in dry air, while the moderate performances are noticed in humid environment.

6.3 Conclusions

In summary, the development of inorganic-organic nanocomposites based on mixture of PPy NPs with CdTe QDs was achieved. The results confirmed the important role of the doping materials and their

loadings in the overall sensing properties of L-SAW sensors. Thus, when the host material (PPy) was doped with the relatively low amounts of QDs (CdTe/PPy (1:10)), the decrease in the velocity of the acoustic wave was achieved and therefore, the enhancement in the functional properties of this L-SAW sensor was noticed. However, the use of high amounts of QDs (CdTe/PPy (1:2)) contributed to the formation of larger clusters within the second guiding/sensitive layer, which resulted in the creation of systems with higher operation frequency and insertion loss. Those type of properties influenced negatively the gas sensing performance of the L-SAW sensors.

6.4 Articles

6.4.1 Journal Article 5

Šetka, M., Bahos, A.F., Chmela, O., Matatagui, D., Gràcia, I., Drbohlavová, J., Vallejos, S., *Cadmium telluride/polypyrrole nanocomposite based Love wave sensors highly sensitive to acetone at room temperature*. This article is under review since 08.05.2020 in the *Sensors and Actuators B: Chemical*.

Cadmium telluride/polypyrrole nanocomposite based Love wave sensors highly sensitive to acetone at room temperature

M. Šetka¹, F. A. Bahos², O. Chmela¹, D. Matatagui^{2,4}, I. Gràcia³, J. Drbohlavová¹, and S. Vallejos^{1,3}*

¹CEITEC - Central European Institute of Technology, Brno University of Technology, 61200 Brno, Czech Republic

² Instituto de Ciencias Aplicadas y Tecnología (ICAT), Universidad Nacional Autónoma de México, Ciudad Universitaria, Ciudad de México 04510, México

³ Instituto de Microelectrónica de Barcelona (IMB-CNM, CSIC), Campus UAB, 08193 Bellaterra, Spain

⁴ SENSAVAN, Instituto de Tecnologías Físicas y de la Información (ITEFI, CSIC), Serrano 144, 28006 Madrid, Spain.

ABSTRACT

Cadmium telluride/polypyrrole (CdTe/PPy) nanocomposites are synthesized and integrated into Love mode surface acoustic wave (L SAW) sensors, achieving high sensitivity to various volatile organic compounds (VOCs) including acetone, ethanol, and toluene. Chemical/physical analysis of the composites and their integration as second/guiding sensitive layer into the L SAW structure show no evidence of strong chemical interaction among the structural components based on CdTe quantum dots (QDs) and PPy nanoparticles (NPs). The gas sensing tests are focus on the performance of L SAW sensors consisting of CdTe/PPy (1:10), CdTe/PPy (1:2), and non-modified PPy layers. Results reveal that the L SAW sensors containing CdTe/PPy (1:10) composite improve the sensing performances to acetone reaching a sensitivity of 771 Hz/ppm, estimated LOD of 5 ppb, and low cross-sensitivities to ethanol and to toluene compared to the sensors with CdTe/PPy (1:2) or without CdTe modification. The high sensitivity of the L SAW sensors to acetone is connected with the adsorption of acetone at PPy via dipole-dipole interaction and the incorporation of CdTe in the guiding/sensitive L SAW layers.

Keywords: polypyrrole composite, polypyrrole, quantum dots, surface acoustic wave, gas sensors

*Corresponding Author: S. Vallejos

e-mail: stella.vallejos@imb-cnm.csic.es or vargas@feec.vutbr.cz

tel: +34 935947700, fax: +34 935800267

1. INTRODUCTION

In gas sensors, the selection of an active sensing material and its coupling with an appropriate transducer plays a key role in the development of high-performance gas sensing devices. Usually, gas sensitive materials including metal oxides (MOXs), conductive polymers (CPs) or carbon-based materials, e.g., carbon nanotubes (CNTs), in their intrinsic form, can suffer from different disadvantages such as high working temperature, poor selectivity, or low response speed. Thus, a way to overcome these functional limitations frequently involves the incorporation of intentional impurities (metal ions, secondary phases) into these materials, which act as host systems [1-5]. Recently, inorganic-organic composites, for instance, based on combinations of CPs with noble metals or semiconducting MOX, have been reported as a suitable combination for enhancing the sensitivity to gases and vapors, which typically are tough to sense with intrinsic materials [6-8]. Specifically, CPs are attractive for gas sensors due to their relatively simple and diversified scalable synthesis, good electrical conductivity and optical properties, and relatively high environmental stability.

Among various CPs, PPy has been used as an active gas-sensitive material coupled to different transducers. The most recurring PPy based sensors are of chemo-resistive type [7], but this material also found application in gravimetric [9] and optical sensors [10]. Accordingly, PPy based composite materials have shown good sensing

performance mostly towards ammonia. For instance, Beniwal *et al.* developed polyurethane/ferric oxide/PPy nanocomposite based chemo-resistive sensors, which showed a moderate response to low ammonia concentrations (100 ppb) at room temperature [11]. Similarly, Tang *et al.* built up chemo-resistive PPy/graphene sensors, which displayed sensitivity and selectivity to ammonia concentrations between 1 and 4 ppm at room temperature [12]. However, PPy has also shown potential for sensing VOCs, which are classified as hazardous components and their detection in very small amounts, in the sub-ppm range, is of great significance for assessment of potential environmental pollution [13], human health risks [14], diseases diagnosis [15] and food spoilage [16]. Consequently, PPy composites were used for monitoring VOCs such as acetone, ethanol, and ethylene. The study of Bagchi *et al.*, for instance, indicates that SnO₂/PPy composites sensors are sensitive to acetone and ethanol. The authors, however, point out that the sensitivity of SnO₂/PPy composites to VOCs is still limited due to low reactivity of this material at room temperature and only a weak physical interaction between the sensing material and gas is presented [17]. In the same line, our recent studies also suggested the tuning of PPy sensitivity to ethylene by its modification with nanoparticles (e.g., gold). These sensors showed higher reactivity at room temperature than most of MOXs [9]. Hence, the use of other highly reactive inorganic materials for the modification of PPy can allow to improving further PPy sensitivity and selectivity towards VOCs.

Low-dimensional semiconductor materials such as QDs, which have nanoparticle radius below the Bohr's exciton radius of the corresponding material, have attracted widespread attention due to their large specific surface area, catalytic activity and outstanding opto-electronic features [18]. Hence, they have been exploited in various domains such as optical devices, medical diagnosis, solar cells and (bio) sensors [19]. In particular, in the area of gas sensors, QDs have been implemented on chemo-resistive sensors, either in hybrid (α -Fe₂O₃/PANI/PbS QDs [20]) or bare form (carbon QDs [21], ZnO QDs [22]), for monitoring methanol, nitrogen dioxide, and acetylene, respectively. These sensors showed good sensing performance to the tested analytes, which were ascribed to the enlargement of the number of active sites on the sensitive layer surface due to QDs presence. However, the utilization of other catalytic QDs, such as those based on cadmium (e.g., CdTe, CdS, CdSe) [23, 24], and especially their implementation into gravimetric sensors based on SAW transduction mechanism have generally occupied short attention in chemical sensors, including gas sensors.

L SAW gas sensors have shown prospective applications for continuous monitoring of gases and VOCs in the sub-ppm regime since they combine high sensitivity, simplicity in handling, reduced cost and wireless control capabilities [25]. The active sensing layer is the essential component of the L SAW sensors, as any changes or perturbations occurring on its surface causes changes in the acoustic wave velocity or amplitude and thus a response in frequency shift. Generally, polymers are attractive as guiding and sensitive layers for L SAW sensors as they provide slow transverse wave velocity and low density due to their viscoelastic properties. They can also be combined with typical guiding layers based on silicon dioxide (SiO₂) in order to form a multi-guiding layer concept structure [9].

This work reports the development and investigation of composite gas-sensitive materials based on inorganic CdTe QDs and organic PPy NPs. As a proof of concept, the composite system (CdTe/PPy) was incorporated into L SAW transducing platforms and used for monitoring low concentrations (ppb-ppm range) of various VOCs, including acetone, ethanol, and toluene. The work focusses on acetone as a case of study due to the enhanced functionality found for this analyte among the tested gases. Acetone, present in various chemical products (e.g., cleaning products, glue, oil paint, nail color removal), is relevant in air-quality control [26]. This analyte is also of interest in breath analysis as a surrogate biomarker of blood glucose [27], and in food-quality control for fish spoilage detection [16]. Hence, the interest of this study case.

2. EXPERIMENTAL

2.1. Synthesis of CdTe/PPy nanocomposites

PPy NPs were prepared via an oxidative chemical polymerization of pyrrole monomer by ferric chloride hexahydrate (FeCl₃·6H₂O) and polyvinyl alcohol (PVA, Mw = 9000–10000, 80 % hydrolysed) as described in previous report [9]. PVA (7.5 g) was dissolved in deionized water (92.5 ml) and mixed with FeCl₃ (3.73 g) to obtain PVA/FeCl₃ complex, in which the hydroxyl groups of PVA co-ordinate with iron cations by ion-dipole interaction. PVA-PPy NPs blend was formed after adding the pyrrole (0.1 M) in the PVA/FeCl₃ solution and stirring the mixture for 5 h at room temperature. FeCl₃ acts as oxidizing agent and causes polymerization of PPy. PVA behaves as

stabilizing agent for PPy NPs and adsorbs at the PPy NPs surface by strong interaction between pyrrole (N–H bond) and PVA (O–H bond) [28].

The synthesis of **CdTe QDs** capped with mercaptopropionic acid (MPA) was realized according to previous procedure [29]. In the first step, Cd-MPA solution was prepared using cadmium chloride (CdCl_2 , 183 mg) and tri-sodium citrate dihydrate ($\text{HOC}(\text{COONa})(\text{CH}_2\text{COONa})_2 \cdot 2\text{H}_2\text{O}$, 400 mg) dissolved in deionized water (100 ml), whereupon MPA ($\text{HSCH}_2\text{CH}_2\text{CO}_2\text{H}$, 104 ml) was added. Sodium hydroxide (NaOH , 1 M) was used to adjust the pH of the Cd-MPA solution to 10, and subsequently, sodium tellurite (Na_2TeO_3 , 44 mg) and sodium borohydride (NaBH_4 , 100 mg) were added. The mixed solution was heated up to 95 °C and the reaction to form CdTe QDs was carried out using a reflux cooling system for 4 h. Afterwards the QDs were purified using isopropyl alcohol and centrifugation process for one cycle. The CdTe QDs were then dried and stored in fridge.

CdTe/PPy nanocomposite was prepared by mixing PPy NPs and CdTe QDs (concentration of 30 mg/ml) aqueous solutions in volumetric ratios of 1:10 and 1:2. This mixture was sonicated in ultrasonic bath for 10 min before spin coating it as the sensitive layer onto the L-SAW platforms.

2.2. L SAW sensor fabrication

The fabrication procedure of multi-guiding PPy and CdTe/PPy L SAW sensors consists of various microfabrication steps, including metallization, oxide deposition, lithography and spin coating of the PPy NPs or CdTe/PPy nanocomposites. Further details of the fabrication process were described early in our work [9]. **Table 1** summarizes the design parameters and characteristics of the three types of L SAW sensors (PPy, CdTe/PPy (1:10) and CdTe/PPy (1:2)) investigated in this work.

Table 1. Summary of the L SAW sensor characteristics.

| Piezoelectric Substrate | |
|--|--|
| Type | ST-90° X-quartz |
| Dimensions | 9 mm × 4 mm × 0.5 mm |
| Interdigital transducers (IDTs) | |
| Material | Aluminium |
| Thickness | 200 nm |
| Number of ports | 2 |
| Structure | Double finger pair 4 fingers/period |
| Period, λ | 28 μm |
| Number of fingers | 75 |
| Aperture | 2.1 mm |
| Delay line | 2.1 mm |
| First guiding layer | |
| Material | SiO_2 |
| Thickness | 3 μm |
| SAW frequency | 165 MHz |
| Second guiding/sensitive layer | |
| Material and film thickness | PPy 250 ± 10 nm |
| | CdTe/PPy (1:10) 250 ± 8 nm |
| | CdTe/PPy (1:2) 100 ± 5 nm |
| Deposition parameters | Spin coating, velocity of 4000 rpm, acceleration of 4000 rpm/s and time of 1 min |
| Area of deposition | Active area (delay line) + 2 ports of IDTs |

2.3. Characterization of sensing materials

The morphological and structural properties of PPy NPs, CdTe QDs and CdTe/PPy nanocomposites were characterized using High-Resolution Transmission Electron Microscope (HR-TEM, FEI TITAN Themis 60–300 kV) equipped with energy dispersive X-ray (EDS) detector. Fourier transform infrared spectroscopy (FTIR,

Vertex70, Bruker) and X-ray photoelectron spectroscopy (XPS, Kratos Axis Supra) were used to investigate the chemical composition of the PPy and CdTe/PPy L SAW sensors. XPS spectra were analyzed using CasaXPS software (version 2.3.19) and all spectra were calibrated with respect to the C 1s peak at 284.7 eV. The electrical properties (transmission parameter S_{21}) of the sensors were analysed using Network Analyzer (Agilent 4395A). The topographic imaging and thickness measurements of the sensitive layers were characterised using Atomic force microscopy (AFM, Dimension Icon, Bruker) and profilometer (Dektak XT, Bruker), respectively.

2.4. Gas sensing test

A portable electronic nose system was used for the gas characterization of the L SAW sensors as described previously [30]. This system allows the integration of discrete L SAW sensors into an array provided of signal conditioning, data acquisition and transmission, and application software. The gas flow system equipped with mass flow controllers was connected to the portable electronic nose and it consisted of calibrated cylinders of synthetic air (3X, Praxair), acetone (100 ppm, Praxair), ethanol (100 ppm, Praxair) and toluene (200 ppm, Praxair) [31]. The PPy, CdTe/PPy (1:10), and CdTe/PPy (1:2) L SAW sensors were exposed to various concentration (between 0.5 and 5 ppm) of above mentioned analytes at a constant temperature (24 °C), in dry (0 % relative humidity (RH)) and wet environment (10 and 30 % RH). The exposure to each analyte and each concentration lasted for 2 min, while purification time was 10 min. The sensor response (frequency shift) was defined as the divergence in the resonant frequency when sensors is exposed to (dry/humid) air and the target gas. To get an insight into the possible reaction mechanisms to acetone, the sensing properties of the L SAW sensors were also investigated using FTIR before and after exposing the sensors to this analyte for 10 min.

3. RESULTS AND DISCUSSION

3.1. Characterization of the sensitive materials

The morphological and structural characteristics of the PPy NPs, CdTe QDs and CdTe/PPy nanocomposites were investigated by TEM, and the distribution of elements in the composite sample was explored using EDS analysis. **Figure 1a** displays the amorphous PPy NPs with well-defined spherical morphology and sizes between 35 to 55 nm. **Figure 1b** demonstrates the crystalline CdTe QDs (marked by green circles) with average sizes of 3.1 ± 0.7 nm and interplanar spacing between lattice fringes of ~ 0.37 nm, consistent with lattice spacing of the (111) plane of cubic CdTe ($d = 0.374$ nm, JCPDS card No. 15-0770) [32]. The TEM and EDS mapping images of the CdTe/PPy nanocomposite are presented in **Figure 1c** and **Figure 1d**. These images demonstrate the random distribution of small QDs clusters (4.4 ± 0.8 nm) with a tendency to adhere to the PPy NP surface. The EDS mapping corroborates the characteristic PPy elements (i.e., C, N) distributed over the PPy NP area (big particle), while the typical elements for the CdTe QDs (i.e., Te, Cd) are detected only at the outer edge of the PPy NPs (small particles); only Te was evident by EDS.

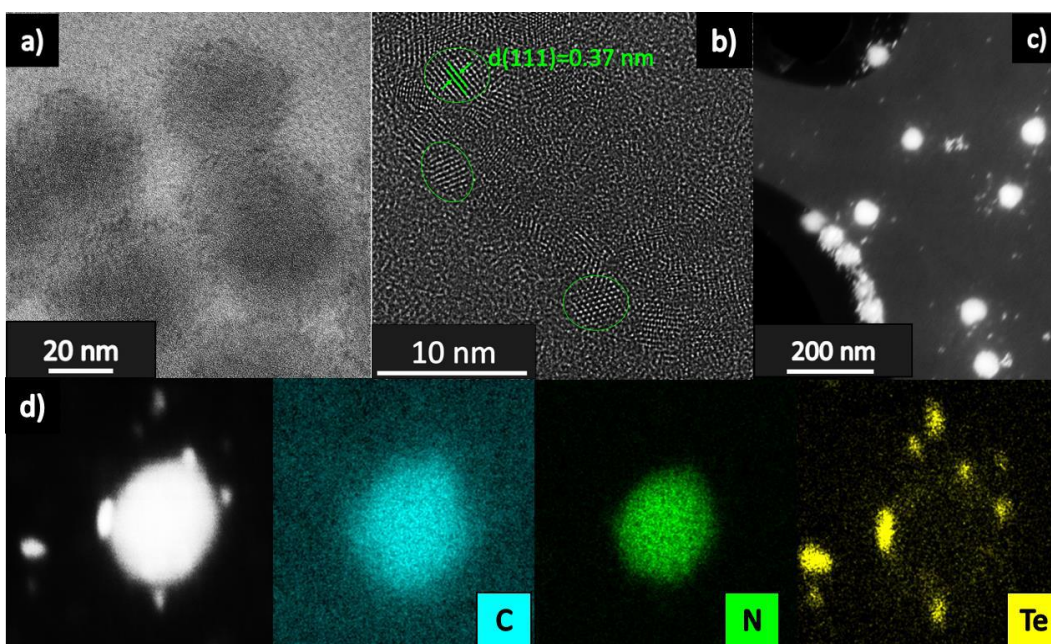


Figure 1. (a) TEM image of the PPy NPs. (b) HR-TEM image of CdTe QDs. (c) TEM image of the CdTe/PPy nanocomposites. (d) TEM and corresponding EDS elemental mapping images of the CdTe/PPy nanocomposites.

FTIR spectroscopy was conducted to examine the molecular structure of PPy NPs and CdTe/PPy composites. The FTIR spectrum of PPy NPs for wavenumbers between 600 and 4000 cm^{-1} is presented in **Figure 2**. The spectrum indicates the presence of vibration peaks assigned to PPy and PVA bonds, which are consistent with previous reports [33-37]. The major PVA peaks (marked with pink color) are related to the vibrations of hydroxyl, acetyl and alkyl groups (all presented in 80 % hydrolyzed PVA) [38], whereas the main PPy peaks (marked with blue color) are assigned to conjugated single and double carbon bonds and the nitrogen bonds in the pyrrole rings. However, it is very likely that the stretching modes of other bands (e.g., C=C and C=N, O-H and N-H) are coupled with each other, since their vibrations exhibit similar stretching frequencies. The wavenumber shifts and peak broadening for certain PVA reflections (e.g., O-H, C-H, C=O and C-O stretching) with respect to typical FTIR spectrum of PVA (**Figure S1, Supplementary information**) may be connected with the adsorption of PVA on PPy and the chemical interactions between those two components in a blend. The FITR spectra of the CdTe/PPy (1:10) and CdTe/PPy (1:2) composites (**Figure S2, Supplementary information**) displayed identical vibration peaks as those for the PPy NPs, indicating that no chemical reaction between this inorganic/organic mixture occurred. The vibration peaks displayed in **Figure 2** and their corresponding assignments are summarized in **Table 2**.

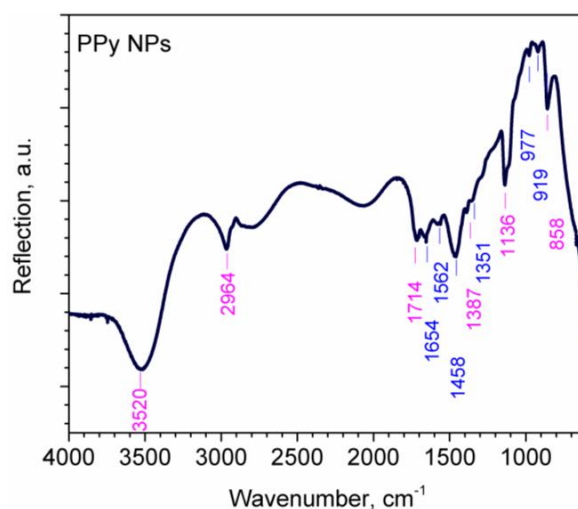


Figure 2. FTIR spectrum of the PPy NPs. Peaks marked with purple and blue color correspond to the vibrations of PVA and PPy bonds, respectively.

Table 2. Band wavenumbers and assignment of FTIR vibration peaks for PVA and PPy.

| Band wavenumbers, cm^{-1} | Assignment | Material |
|------------------------------------|--|----------------|
| 3470 – 3520 | O–H stretching overlapping with N–H stretching | PVA and/or PPy |
| 2950 – 2965 | C–H symmetric stretching | PVA |
| 1710 – 1750 | C=O stretching | PVA |
| 1654, 1562 and 1458 | C=N, C–N, C–N–H or C=C stretching | PPy |
| 1380 – 1390 | –CH ₂ – bending | PVA |
| 1351 | C–H or C–N in-plane deformations | PPy |
| 1130 – 1150 | C–O stretching | PVA |
| 977 | C–H out-of-plane bending | PPy |
| 919 | C–H out-of-plane deformation | PPy |
| 858 | –CH ₂ – rocking | PVA |

3.2. Chemical and electrical characterization of the L SAW sensors

In order to demonstrate the incorporation of the CdTe QDs into the L SAW sensors after spin coating of the CdTe/PPy composites, the sensitive films were examined by XPS. **Figure 3a** shows a comparison of the survey spectra recorded for the PPy, CdTe/PPy (1:10), and CdTe/PPy (1:2) L SAW sensors. Overall, the spectra show the peaks of carbon (C), oxygen (O), nitrogen (N), iron (Fe) and chlorine (Cl) (related to PPy presence) in all samples, with the cadmium (Cd) peak being present only in the CdTe/PPy (1:10) and CdTe/PPy (1:2) sensors (**Figure 3b** and **3c**). This demonstrates the incorporation of both, PPy NPs and CdTe QDs into CdTe/PPy nanocomposite spin coated layers. The atomic percentage of Cd (calculated from survey spectra with respect to all presented elements) is ~0.03 % for the CdTe/PPy (1:10) and ~0.53 % for the CdTe/PPy (1:2) sensors, which is consistent with the volumetric ratios of QDs and NPs introduced in the composite. Tellurite (Te) characteristic peaks are not evident in the survey spectra, however high-resolution XPS scan (**Figure 4**) confirmed the presence of Te at the surface of both CdTe/PPy based layers.

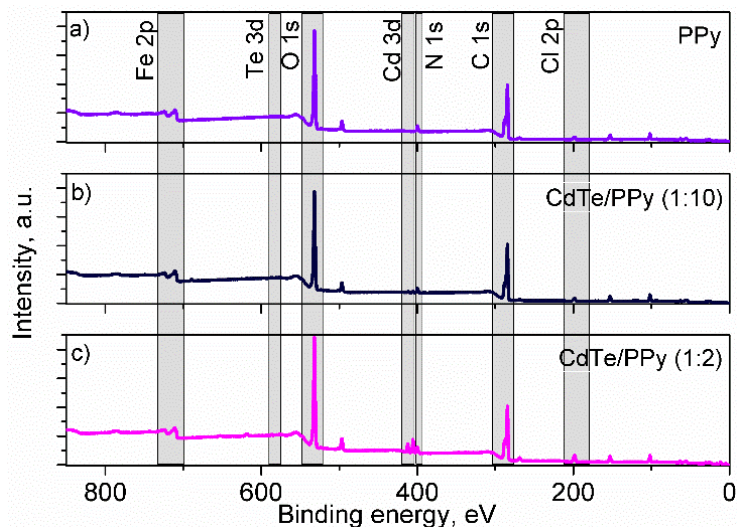


Figure 3. XPS survey spectra of the (a) PPy, (b) CdTe/PPy (1:10), and (c) CdTe/PPy (1:2) L SAW sensors.

The high-resolution core level XPS peaks of examined samples are displayed as follows: C 1s in **Figure 4a**, N 1s in **Figure 4b**, Cd 3d in **Figure 4c** and Te 3d in **Figure 4d**. After deconvolution into Gaussian components, C 1s peak suggests the presence of five singlets. The peaks located at 284.4, 285.0 and 286.3 eV can be attributed to β C atoms, α C atoms, and C–N bonds in PPy, while peaks at 288.1 and 288.9 eV correspond to C–O and C=O bonds, respectively. The C–O and C=O groups are mostly related to the presence of PVA in PPy NPs [39]. The N 1s core level peak shows three components assigned to imine structure ($=N-$ at 398.0 eV), neutral nitrogen in PPy ring ($-N-H$ at 400.0 eV) and bipolaron species of PPy ($=N-H^+$ at 402.3 eV), which is consistent with our previous observations [40]. The Cd 3d spectrum of the CdTe/PPy (1:10) and CdTe/PPy (1:2) sensors shows two characteristic Cd doublets (Cd $3d_{3/2}$ and Cd $3d_{5/2}$) at 405.6 and 412.4 eV, respectively, in agreement with the literature. In addition, the Te 3d core level peak suggests the presence of four components. Two of them (Te $3d_{5/2}$ at 576.3 eV and Te $3d_{3/2}$ at 586.8 eV) assigned to Te–O bonds in TeO_2 or $CdTeO_2$ and the other two (Te $3d_{5/2}$ at 573.1 eV and Te $3d_{3/2}$ at 583.3 eV) related to Te–Cd bonds in CdTe. The Cd 3d and Te 3d spectra are consistent with those reported for CdTe QDs in the literature [41]. A comparison of the C 1s and N 1s spectra for the other samples (i.e., PPy, CdTe/PPy (1:10), and CdTe/PPy (1:2)) displayed no significant changes in the molecular structure of PPy (**Figure S3** and **S4**). These results are in line with the FTIR observations and corroborate the absence of chemical interaction between the PPy NPs and the CdTe QDs.

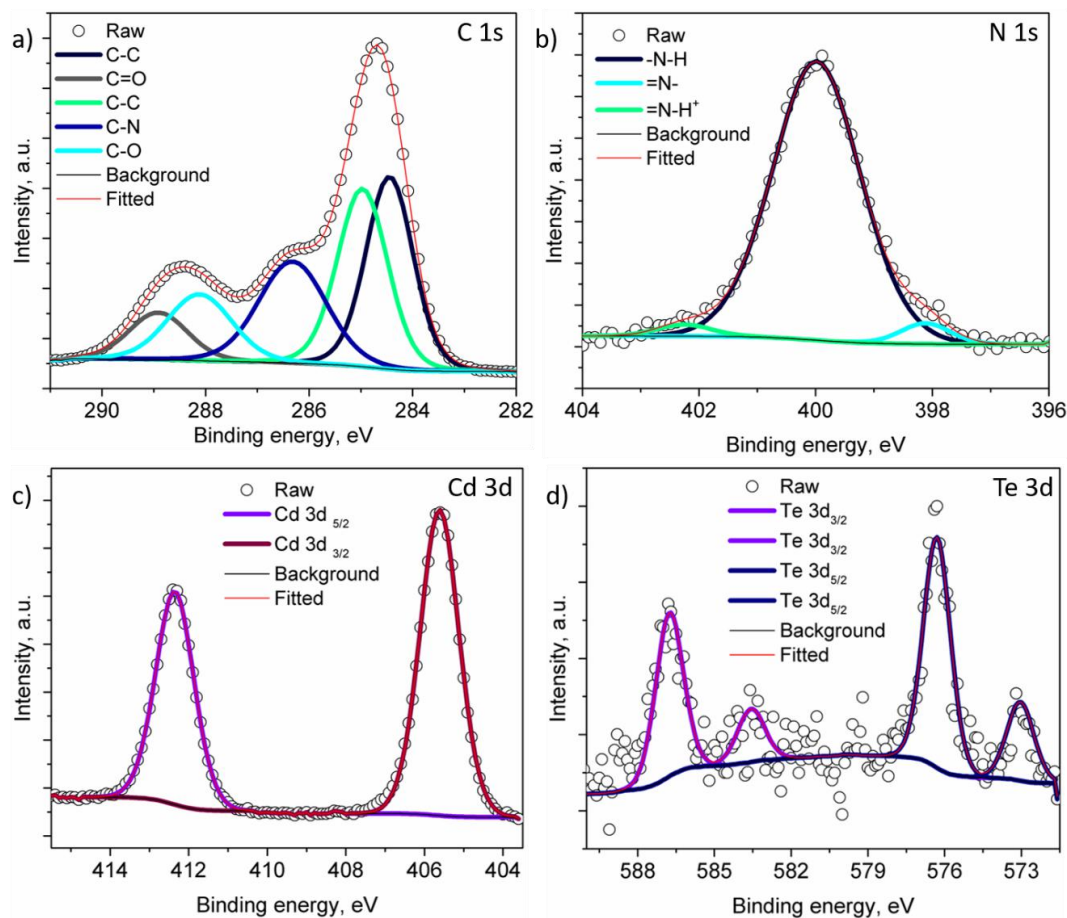


Figure 4. High-resolution XPS core level spectra of the (a) C 1s and (b) N 1s at the PPy layer, and the (c) Cd 3d and (d) Te 3d at the CdTe/PPy layer.

Electrical characterization of the PPy, CdTe/PPy (1:10) and CdTe/PPy (1:2) L SAW sensors were investigated by measuring their transmission scattering parameter (S_{21}). The magnitude of the insertion loss versus the resonant frequency of the sensors for the reference (i.e., with only SiO₂ guiding layer) and the L SAW sensors (with the second sensitive/guiding layer based on PPy or CdTe/PPy) is displayed in **Figure 5**. The results show the shift in the resonant frequency from 165.3 MHz (reference sensor) to 162.5 MHz for the PPy, 162.4 MHz for the CdTe/PPy (1:10), and 163.7 MHz for the CdTe/PPy (1:2) L SAW sensors. An increase of the insertion loss from -18 dB (reference sensor) to -22 dB (PPy and CdTe/PPy (1:10) sensors) and even to -32 dB in the case CdTe/PPy (1:2) sensors is also observed. The changes in operation frequency of the L SAW sensors may be attributed to the confinement of the acoustic energy by the second guiding/sensitive layer. However, the larger differences in frequency and insertion loss for the CdTe/PPy (1:2) compared to the other L SAW sensors could be caused in major degree by the parameters of the sensitive layer, including its thickness, density, or shear stiffness [42, 43]. Profilometry measurements corroborated this fact as the sensitive layers revealed more than two times higher thickness (250 nm) for the PPy and CdTe/PPy (1:10) L SAW sensors as compared to the CdTe/PPy (1:2) L SAW sensors (100 nm). Normally, L SAW sensors with thin sensitive/guiding layers (of the same nature) involve lower insertion loss compared to thick layers [42]. However, this is not the case for the CdTe/PPy (1:2) L SAW sensors, which despite the lower thickness respect to the CdTe/PPy (1:10) layer, register higher insertion loss due to the higher concentration of QDs and their tendency to agglomerate. AFM analysis (**Figure S5a** and **S5b**) confirmed this fact, showing the irregular agglomeration of QDs over the sensitive layer surface of the CdTe/PPy (1:2) L SAW sensor. This was not noticed in the case of CdTe/PPy (1:10) L SAW sensor.

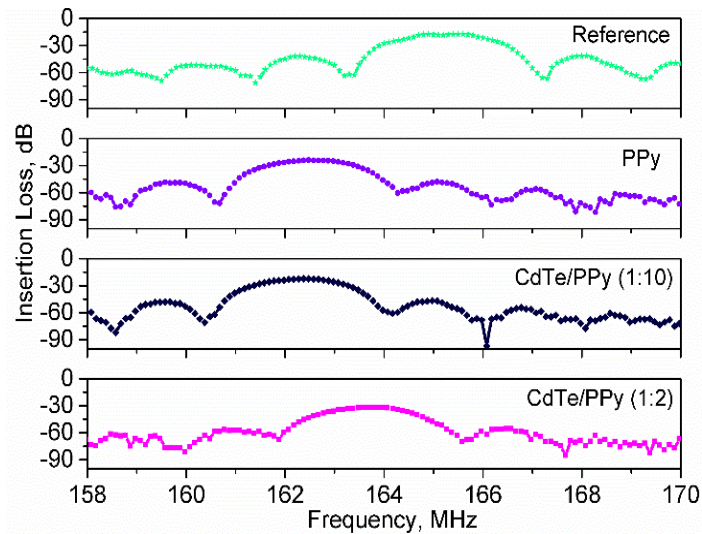


Figure 5. Transmission scattering parameter (S_{21}) for the reference, PPy, CdTe/PPy (1:10) and CdTe/PPy (1:2) L SAW sensors.

In summary, the morphological and chemical characterization techniques indicate a blend of PPy NPs with PVA after the oxidative chemical polymerization of pyrrole monomer. The results also prove the incorporation of CdTe QDs in the spin coated sensitive PPy layers. TEM, FTIR and/or XPS analysis identify both PPy and CdTe in the nanocomposites indicating no chemical interaction between them. Generally, the L SAW structure showed lower velocity and insertion loss (~ 4550 m/s and -22 dB) for the PPy and CdTe/PPy (1:10) samples compared to the CdTe/PPy (1:2) sensors (4584 m/s and -32 dB). The deviation in the properties of each L SAW sensor type is caused by the different thickness of the second guiding/sensitive layer. Despite the attempts to achieve layers of each material type with the same thickness, the tuning for the CdTe/PPy (1:2) material was not feasible due to the high insertion loss induced by the high amount of QDs and their agglomeration.

3.3. Gas sensing test of the L SAW sensors

The following studies were employed to characterize the PPy, CdTe/PPy (1:10) and CdTe/PPy (1:2) L SAW sensors and to examine the effects of the CdTe QDs in the gas sensing properties of PPy. To this end, the gas sensing test of the sensors toward acetone, ethanol and toluene were explored at room temperature. The frequency response of the sensors to 5 ppm of acetone is shown in **Figure 6**. Generally, the L SAW sensors with low QD loadings (CdTe/PPy (1:10)) displayed the highest response amongst the three type of sensors, whereas the sensors with the higher QD loadings (CdTe/PPy (1:2)) showed the lowest responses. Thus, the response amplitude of the CdTe/PPy (1:10) sensors to acetone was 1.2 and 2 fold higher than that of PPy and CdTe/PPy (1:2) sensors, respectively. The L SAW sensors responses to ethanol and toluene were in the same order as for acetone, with the highest and lowest frequency shifts with respect to the PPy sensors being observed for CdTe/PPy (1:10) and CdTe/PPy (1:2) sensors, respectively.

These results and, analogously, our previous studies on the modification of PPy with gold catalytic particles [44] prove the enhancement of PPy sensing properties by the incorporation of inorganic catalytic particles. Overall, we notice that the use of relatively low amounts of QDs (CdTe/PPy (1:10)) in the second/guiding PPy sensitive layer decreases the velocity of the acoustic wave without modifying significantly the total losses of the system. This allows for boosting the response and enhancing the functional properties of the whole sensor. Additionally, the operating frequencies of PPy and CdTe/PPy (1:10) sensors in the same range, indicate that the enhanced properties of the CdTe/PPy (1:10) samples are also connected to the incorporation of CdTe QDs in PPy. In contrast, the use of high amounts of QDs, which tend to agglomerate the CdTe/PPy (1:2) layers, increases the operating frequency and the total losses of the system and, in turn, influences negatively on the gas sensing performance of the sensors. This is in line with other systems, in which large amount of catalyst added to the sensitive material have shown to decrease the sensor sensitivity [45]. In this context, hereafter, the gas tests were focussed on the sensors with lower QD loadings (CdTe/PPy (1:10)) as representatives of the CdTe/PPy composite based sensors.

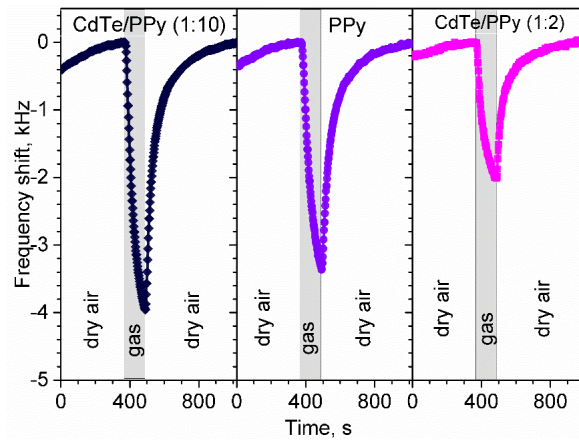


Figure 6. Response of CdTe/PPy (1:10) (black line), PPy (purple line) and CdTe/PPy (1:2) (pink line) L-SAW sensors to 5 ppm of acetone.

Figure 7 shows the variance of sensitivity (S) to acetone, ethanol, and toluene. The sensitivity was defined as the ratio between the change in sensor response for a fixed change in analyte concentration (between 1 and 5 ppm for this study). The mean sensitivity values to acetone, ethanol, and toluene are 652, 441, and 260 Hz/ppm for the PPy sensors and 771, 546, and 303 Hz/ppm for the CdTe/PPy (1:10) L SAW sensors. This shows that the sensitivity of the CdTe/PPy (1:10) sensors was improved by a factor of ~ 1.2 compared to the PPy L SAW sensors for all tested analytes. Moreover, the analysis of variance shows higher sensitivities to acetone for both the PPy and CdTe/PPy (1:10) L SAW sensors, with cross-sensitivities (ΔS) to ethanol and toluene of 211 and 392 Hz/ppm for PPy, respectively and 225 and 468 Hz/ppm for CdTe/PPy (1:10), respectively. This indicates a good sensitivity and a partial selectivity in both sensors to acetone.

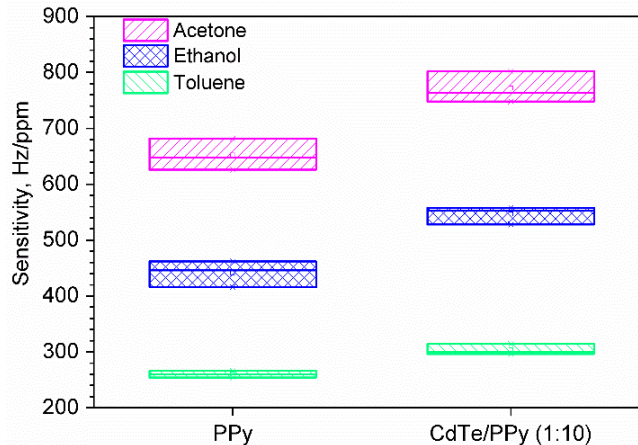


Figure 7. Plot box of the sensitivity to acetone, ethanol and toluene using PPy and CdTe/PPy (1:10) sensors.

Overall, these results show that the PPy and CdTe/PPy (1:10) L SAW sensors respond better to polar (acetone and ethanol) than to non-polar (toluene) gases. This behaviour could be caused by the polar nature of the sensitive layer (i.e., the PPy-PVA blend), which facilitates the dipole-dipole interaction with other polar molecule. Previously, it was also observed that the polar polymers (e.g., polythiophene) also showed an improved sensitivity to polar VOCs, including alcohols and ketones, compared to nonpolar analytes (e.g., aromatic hydrocarbons) [46]. Interestingly, the sensitivity order of the L SAW sensors to tested analytes is also correlated with the polarity of each analyte. For instance, the sensors show better response to analytes with higher dipole moments (i.e., higher molecular polarity) [47] than to those with lower dipole moments. Thus, the dipole moments of acetone (2.88 D), ethanol (1.69 D) and toluene (0.38 D) correspond with the order of sensitivity registered. In this context, the dipole-dipole interactions of the positively polarized side in pyrrole ($N^{\delta-}-H^{\delta+}$) and/or the hydroxyl group in PVA ($-O^{\delta-}-H^{\delta+}$) with

the negatively polarized side of functional groups in acetone ($>C^{\delta-}=O^{\delta-}$) or ethanol ($-O^{\delta-}-H^{\delta+}$) lead to the formation of hydrogen bond (see **Figure 8a**). This might lead to stronger interactions between PPy and the polar molecules compared to non-polar molecules [48-51] and, in turn, to better sensor responses to acetone and ethanol than to toluene. The FTIR analysis of the sensors before and after exposure to acetone-model analyte (**Figure 8b**) is also in line with this statement, as we observe a lowering of the O–H stretching band frequency in PPy from 3520 cm^{-1} to 3473 cm^{-1} after acetone exposure [35], which points out the formation of hydrogen bond between PPy and acetone molecules. The changes in shape, intensity and slightly in position of the bands between 1652 and 1462 cm^{-1} (stretching of C=N, C–N, C–N–H or C=C bonds) and the band at 1711 cm^{-1} (stretching of C=O bond) also suggest interactions between the N–H bond of PPy and the C=O bonds of acetone. This is also consistent with the adsorption of acetone at the PPy surface.

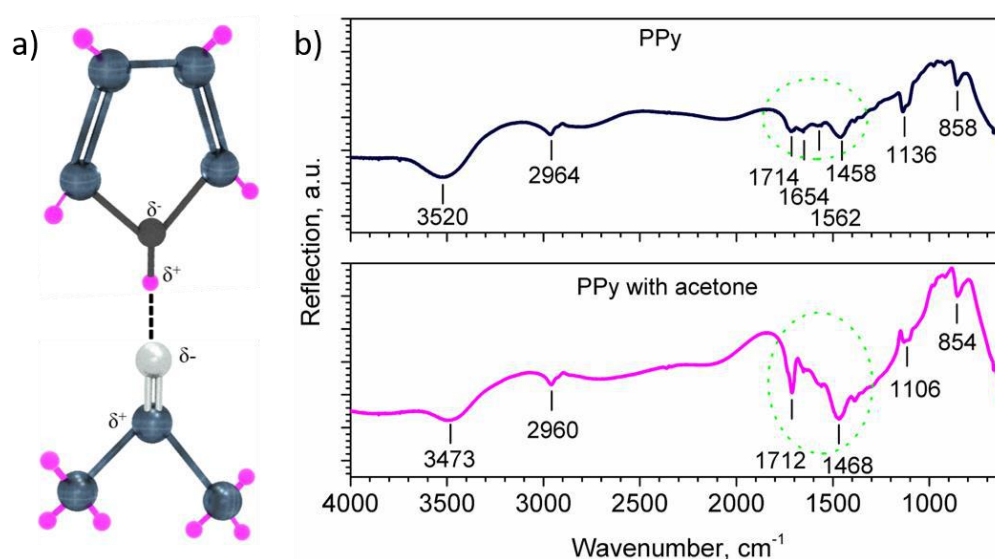


Figure 8. (a) Schematic illustration of dipole-dipole interaction (hydrogen bond) between pyrrole and acetone molecules. (b) FTIR spectra of PPy L SAW sensors before (black line) and after (pink line) exposure to acetone.

Apart from the sensitivity and selectivity, we also analysed and compared the response and recovery times of the PPy and CdTe/PPy (1:10) L-SAW sensors to the tested VOCs. Generally, the tests show faster responses to ethanol (134 and 112 s) than to acetone (165 and 155 s) and toluene (200 and 186 s) for the PPy and CdTe/PPy (1:10) sensors, respectively. In contrast to response time, the recovery times, oscillate in similar ranges for all three tested analytes between 290 and 320 s for PPy and 270 and 310 s for CdTe/PPy (1:10). The slight faster response and recovery time for the CdTe/PPy (1:10) sensors may be related to the presence of the catalytic particles. In summary, the response and recovery speed of the analytes is faster for ethanol than to acetone and toluene (i.e., ethanol < acetone < toluene). This order might be connected with the faster diffusion of smaller gas molecules into the sensing layer (kinetic diameters: for ethanol 0.45 nm, acetone 0.46 nm, and toluene 0.58 nm) [52].

Since the CdTe/PPy (1:10) L SAW sensors proved enhanced sensing performances (higher sensitivity and faster response/recovery time) over PPy sensors, we performed further analysis only for the CdTe/PPy (1:10) sensors. **Figure 9a** displays the dynamic response of the CdTe/PPy (1:10) sensors to various acetone concentrations (from 0.5 to 5 ppm). These tests show the proportional increase (**Figure 9b**) of the sensor response (frequency shifts from 705 Hz to 4 kHz) to the analyte concentration (from 0.5 to 5 ppm). The results also show the reproducibility of the response with the errors lower than 2% over three consecutive sensing cycles for each gas concentration. The response of the bare PPy sensors displayed similar reproducibility (**Figure S6, Supplementary information**). Overall, the sensors responded to all tested gases (acetone, ethanol and toluene) in the range of 0.5 to 5 ppm. The theoretical limit of detection (LOD) for the CdTe/PPy (1:10) L SAW sensors to acetone was estimated to be 5 ppb. Further details of the estimation of the LOD are described in section **S2, Supplementary information**.

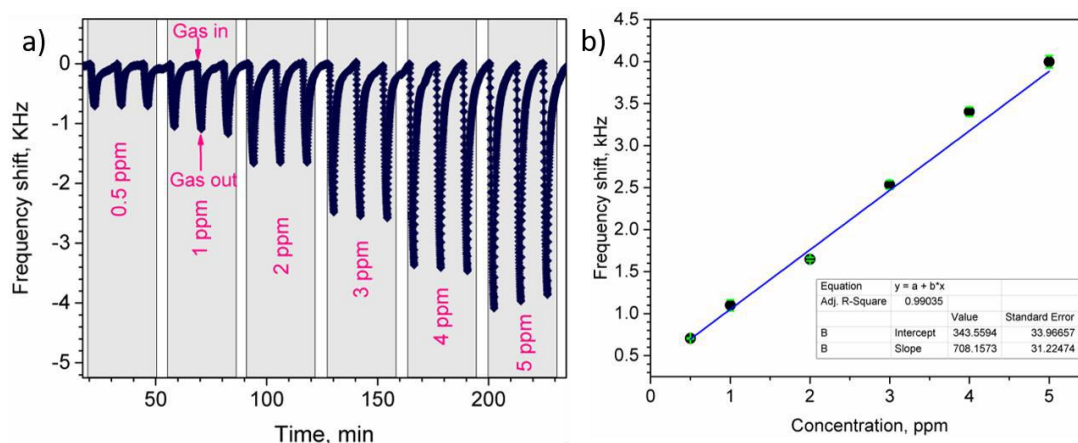


Figure 9. (a) Dynamic response of the CdTe/PPy (1:10) L SAW sensors to concentration of acetone varying from 0.5 to 5 ppm. (b) Calibration curve (concentration vs. response) of the CdTe/PPy (1:10) L SAW sensors.

In order to investigate the humidity influence on the gas sensing performances of CdTe/PPy (1:10) L SAW sensors during the acetone exposure, the sensor responses in dry and humid ambient (10 % and 30 % RH) were compared. **Figure 10** shows the decrease of the response as the humidity is increased. One can observe that the frequency shifts to 5 ppm of acetone change from 4 kHz in dry air to 1.8 and 0.9 kHz at 10 % and 30 % RH, respectively. This demonstrates that the humidity interferes with the absorption of acetone affecting significantly the response of the sensors. This effect can be attributed to the occupation of the sensitive material active sites by the adsorbed water molecules [9] as the polymer materials have an intrinsic affinity to water sorption [53, 54]. Hence, it is important to develop a humidity filtering and precondition elements to improve the gas sensing properties of the most CPs such as PPy.

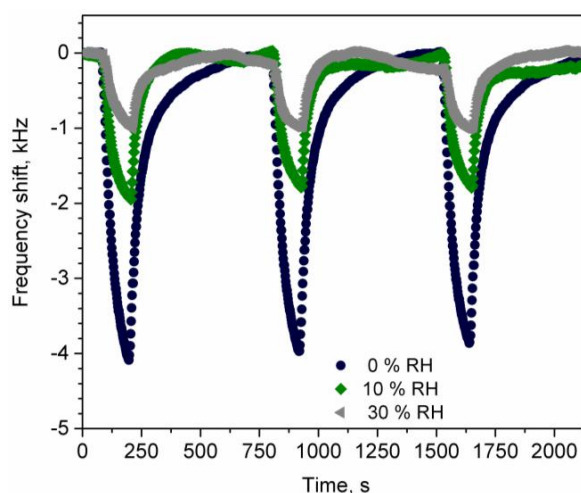


Figure 10. The CdTe/PPy (1:10) L SAW sensor responses to 5 ppm of acetone in dry and wet (10 % and 30 % of RH) ambient.

Table 3 summarizes the gas sensing properties of CdTe/PPy (1:10) L SAW sensors to acetone and compares our results with those reported for other SAW sensors and/or PPy based chemo-resistive sensors in the literature. These data suggest that the CdTe/PPy (1:10) L SAW sensors respond to low acetone concentration with an ultrahigh sensitivity and low theoretical LOD of 5 ppb, in contrast to other SAW sensors (based on different sensing materials). Additionally, one can see that PPy was also employed as a modifying material for semiconducting oxides in chemo-resistive sensors, showing a sensitivity to acetone in less degree than the most of the SAW sensors in **Table 3**. The use of CdTe QDs in gas sensing application is not commonly reported in the literature (neither in SAW or chemo-

resistive sensors), thus a comparison of the performance of the CdTe/PPy (1:10) L SAW sensors with other sensors containing CdTe is challenging. Similarly, the effect of humidity in the most of the polymer based sensors, including PPy, reported in the literature is rarely discussed and therefore a comparative evaluation of the humidity effect in our sensors and those previously developed is not viable.

Table 3. Comparison of gas sensing responses of the CdTe/PPy (1:10) L SAW sensors and other SAW or chemo-resistive sensors reported in the literature to acetone. The response of SAW sensors is shown as the frequency shift in KHz, while the response of chemo-resistive sensors is presented R_a/R_g , where R_a and R_g is resistance in air and gas, respectively.

| Acetone sensing | | | | | | | |
|--------------------------------------|-----|----|---------|-----|-----|-------|-----------|
| Material | TP | T | Ambient | C | R | LOD | Ref. |
| QDs/PPy (1:10) | SAW | RT | Dry air | 5 | 4 | 0.005 | This work |
| PPy | SAW | RT | - | 5.5 | 4 | - | [55] |
| PEI/WO ₃ | SAW | RT | - | 800 | 2.7 | 11 | [56] |
| Cu/SWCNT | SAW | RT | Dry air | 100 | 15 | - | [57] |
| ZIF8/Au | SAW | RT | Dry air | 10 | 0.3 | 1.1 | [58] |
| PPy/Zn ₂ SnO ₄ | CR | RT | Dry air | 1 | 0.9 | - | [59] |
| SnO ₂ -PPy | CR | RT | - | 100 | 1.1 | >10 | [17] |
| PPy/MnO ₂ | CR | RT | Dry air | 30 | 1.0 | - | [60] |

PEI - polyethyleneimine, Cu/SWCNT - copper nanoparticles/single wall carbon nanotube, ZIF8/Au - zeolitic imidazolate nanocrystals/gold nanoparticles, TP - transducing principle, CR - chemo-resistive, T - temperature, RT - room temperature, C - concentration, R - sensor response. The concentration and LOD are in parts per million (ppm).

4. CONCLUSION

Nanocomposite based on PPy NPs and CdTe QDs were synthesized and incorporated on L SAW structures as guiding/sensitive layers. Analysis (TEM, FTIR, XPS) of these sensitive layers corroborated the presence of both inorganic-organic components with no evidence of strong chemical interactions among them. Gas sensing test of the PPy, CdTe/PPy (1:10) or CdTe/PPy (1:2) L SAW sensors displayed responses to acetone, ethanol and toluene at room temperature. Systematic gas sensing tests of the L SAW sensors showed that the magnitude of responses to these vapors changes from the highest to the lowest in the following order: CdTe/PPy (1:10) > PPy > CdTe/PPy (1:2). Generally, the CdTe/PPy (1:10) L SAW sensors show better responses to acetone with a sensitivity of 771 Hz/ppm, estimated LOD of 5 ppb and low cross-sensitivities to ethanol and to toluene. The enhanced sensing performance of the CdTe/PPy (1:10) L SAW sensors to acetone was attributed in part to the catalytic activity of the QDs and the adsorption of acetone at PPy via dipole-dipole interaction. In contrast, the low responses of the CdTe/PPy (1:2) sensors are connected with the agglomeration of QDs on the PPy layer and, thus, a deviation in an operation frequency and insertion loss of these sensors compared to the PPy and CdTe/PPy (1:10) sensors. A comparison of the sensing properties of the CdTe/PPy (1:10) L SAW and other sensors in the literature confirm the improvements achieved by using guiding/sensitive layers based on organic-inorganic nanocomposite.

ACKNOWLEDGMENT

This work has been supported in part by the Czech Science Foundation (GAČR) via Grant No. 20-20123S, the Spanish Ministry of Economy and Competitiveness via projects TEC2015-74329-JIN-(AEI/FEDER, EU), and TEC2016-79898-C6-1-R (AEI/FEDER, EU) and by Universidad Nacional Autónoma de México via Grant DGAPA-UNAM-PAPIIT TA100118. The support of the Ramón y Cajal are also acknowledged. This research has made use of the infrastructures of the Spanish ICTS Network MICRONANOFABS, partially supported by MINECO, and Czech CEITEC Nano Research Infrastructure, supported by MEYS CR (LM2018110). We are grateful to Tomas Lednický for supporting us with the profilometry measurements.

REFERENCES

- [1] T. Zhang, S. Mubeen, N.V. Myung, M.A. Deshusses, Recent progress in carbon nanotube-based gas sensors, *Nanotechnology*, 19 (2008) 14.
- [2] S. Wang, Y. Kang, L. Wang, H. Zhang, Y. Wang, Y. Wang, Organic/inorganic hybrid sensors: A review, *Sensors and Actuators B: Chemical*, 182 (2013) 467-81.

- [3] A.A. Baharuddin, B.C. Ang, A.S.M.A. Haseeb, Y.C. Wong, Y.H. Wong, Advances in chemiresistive sensors for acetone gas detection, *Materials Science in Semiconductor Processing*, 103 (2019) 104616.
- [4] D.S. Calheiro, R.F. Bianchi, Tuning the detection limit in hybrid organic-inorganic materials for improving electrical performance of sensing devices, *Sensors and Actuators A: Physical*, 298 (2019) 111480.
- [5] C. Dong, R. Zhao, L. Yao, Y. Ran, X. Zhang, Y. Wang, A review on WO₃ based gas sensors: Morphology control and enhanced sensing properties, *Journal of Alloys and Compounds*, 820 (2020) 153194.
- [6] S. Nasirian, Enhanced carbon dioxide sensing performance of polyaniline/tin dioxide nanocomposite by ultraviolet light illumination, *Applied Surface Science*, 502 (2020) 144302.
- [7] M. Šetka, J. Drbohlavová, J. Hubálek, Nanostructured polypyrrole-based ammonia and volatile organic compound sensors, *Sensors* 17 (2017) 28.
- [8] Y. Hui, C. Bian, S.H. Xia, J.H. Tong, J.F. Wang, Synthesis and electrochemical sensing application of poly(3,4-ethylenedioxythiophene)-based materials: A review, *Analytica Chimica Acta*, 1022 (2018) 1-19.
- [9] M. Šetka, F.A. Bahos, D. Matatagui, M. Potoček, Z. Kral, J. Drbohlavová, et al., Love wave sensors based on gold nanoparticle-modified polypyrrole and their properties to ammonia and ethylene, *Sensors and Actuators B: Chemical*, 304 (2019) 127337.
- [10] S. Bagchi, R. Achla, S.K. Mondal, Electrospun polypyrrole-polyethylene oxide coated optical fiber sensor probe for detection of volatile compounds, *Sensors and Actuators B-Chemical*, 250 (2017) 52-60.
- [11] A. Beniwal, Sunny, Novel TPU/Fe₂O₃ and TPU/Fe₂O₃/PPy nanocomposites synthesized using electrospun nanofibers investigated for analyte sensing applications at room temperature, *Sensors and Actuators B: Chemical*, 304 (2020) 127384.
- [12] X.H. Tang, D. Lahem, J.P. Raskin, P. Gerard, X. Geng, N. Andre, et al., A Fast and Room-Temperature Operation Ammonia Sensor Based on Compound of Graphene With Polypyrrole, *Ieee Sensors Journal*, 18 (2018) 9088-96.
- [13] J. Sun, Z. Shen, L. Zhang, Y. Zhang, T. Zhang, Y. Lei, et al., Volatile organic compounds emissions from traditional and clean domestic heating appliances in Guanzhong Plain, China: Emission factors, source profiles, and effects on regional air quality, *Environment International*, 133 (2019) 105252.
- [14] N. Ramírez, A. Cuadras, E. Rovira, F. Borrull, R.M. Marcé, Chronic risk assessment of exposure to volatile organic compounds in the atmosphere near the largest Mediterranean industrial site, *Environment International*, 39 (2012) 200-9.
- [15] B. Uttara, A.V. Singh, P. Zamboni, R.T. Mahajan, Oxidative Stress and Neurodegenerative Diseases: A Review of Upstream and Downstream Antioxidant Therapeutic Options, *Current Neuropharmacology*, 7 (2009) 65-74.
- [16] J. Bai, S.M. Baker, R.M. Goodrich-Schneider, N. Montazeri, P.J. Sarnoski, Aroma Profile Characterization of Mahi-Mahi and Tuna for Determining Spoilage Using Purge and Trap Gas Chromatography-Mass Spectrometry, *Journal of Food Science*, 84 (2019) 481-9.
- [17] S. Bagchi, C. Ghanshyam, Understanding the gas sensing properties of polypyrrole coated tin oxide nanofiber mats, *Journal of Physics D-Applied Physics*, 50 (2017) 10.
- [18] Y. Guo, B. Li, Carbon dots-initiated luminol chemiluminescence in the absence of added oxidant, *Carbon*, 82 (2015) 459-69.
- [19] S. Jain, S. Bharti, G.K. Bhullar, S.K. Tripathi, I-III-VI core/shell QDs: Synthesis, characterizations and applications, *Journal of Luminescence*, 219 (2020) 28.
- [20] Y. Zhang, W.J. Pan, G.K. Dong, D.Z. Zhang, A high-performance room temperature methanol gas sensor based on alpha-iron oxide/polyaniline/PbS quantum dots nanofilm, *Journal of Materials Science-Materials in Electronics*, 30 (2019) 17907-15.
- [21] M. Cheng, Z. Wu, G. Liu, L. Zhao, Y. Gao, S. Li, et al., Carbon dots decorated hierarchical litchi-like In₂O₃ nanospheres for highly sensitive and selective NO₂ detection, *Sensors and Actuators B: Chemical*, 304 (2020) 127272.
- [22] M.S. Park, J.H. Lee, Y. Park, R. Yoo, S. Park, H. Jung, et al., Doping effects of ZnO quantum dots on the sensitive and selective detection of acetylene for dissolved-gas analysis applications of transformer oil, *Sensors and Actuators B: Chemical*, 299 (2019) 126992.
- [23] J. Jaiswal, A. Sanger, P. Tiwari, R. Chandra, MoS₂ hybrid heterostructure thin film decorated with CdTe quantum dots for room temperature NO₂ gas sensor, *Sensors and Actuators B: Chemical*, 305 (2020) 127437.
- [24] M. Dun, J. Tan, W. Tan, M. Tang, X. Huang, CdS quantum dots supported by ultrathin porous nanosheets assembled into hollowed-out Co₃O₄ microspheres: A room-temperature H₂S gas sensor with ultra-fast response and recovery, *Sensors and Actuators B: Chemical*, 298 (2019) 126839.
- [25] J. Devkota, P.R. Ohodnicki, D.W. Greve, SAW Sensors for Chemical Vapors and Gases, *Sensors*, 17 (2017) 28.
- [26] E. Mitrani, T. Callender, B. Orha, P. Dragnea, G. Botezatu, Neurotoxicity associated with occupational exposure to acetone, methyl ethyl ketone, and cyclohexanone, *Environmental Research*, 73 (1997) 181-8.
- [27] W.W. Li, Y. Liu, X.Y. Lu, Y.P. Huang, Y. Liu, S.Q. Cheng, et al., A cross-sectional study of breath acetone based on diabetic metabolic disorders, *Journal of Breath Research*, 9 (2015) 9.
- [28] J.Y. Hong, H. Yoon, J. Jang, Kinetic Study of the Formation of Polypyrrole Nanoparticles in Water-Soluble Polymer/Metal Cation Systems: A Light-Scattering Analysis, *Small*, 6 (2010) 679-86.
- [29] J.P. Simeunović, J. Pekárková, J. Žák, I. Chamradová, J. Hubálek, Studying of quantum dot luminescence quenching effect caused by covalent conjugation with protein, *Monatshefte für Chemie - Chemical Monthly*, 148 (2017) 1901-9.
- [30] D. Matatagui, F.A. Bahos, I. Gràcia, M.d.C. Horrillo, Portable Low-Cost Electronic Nose Based on Surface Acoustic Wave Sensors for the Detection of BTX Vapors in Air, *Sensors*, 19 (2019) 5406.

- [31] S. Vallejos, I. Gràcia, O. Chmela, E. Figueras, J. Hubálek, C. Cané, Chemoresistive micromachined gas sensors based on functionalized metal oxide nanowires: Performance and reliability, *Sensors and Actuators B: Chemical*, 235 (2016) 525-34.
- [32] G.R. Bhand, N.B. Chaure, Synthesis of CdTe, CdSe and CdTe/CdSe core/shell QDs from wet chemical colloidal method, *Materials Science in Semiconductor Processing*, 68 (2017) 279-87.
- [33] J. Gounder Thangamani, K. Deshmukh, K.K. Sadasivuni, D. Ponnamma, S. Goutham, K. Venkateswara Rao, et al., White graphene reinforced polypyrrole and poly(vinyl alcohol) blend nanocomposites as chemiresistive sensors for room temperature detection of liquid petroleum gases, *Microchimica Acta*, 184 (2017) 3977-87.
- [34] J.M. Thompson, *Infrared Spectroscopy*: Jenny Stanford Publishing; 2018.
- [35] D. Lin-Vien, N.B. Colthup, W.G. Fateley, J.G. Grasselli, *The Handbook of Infrared and Raman Characteristic Frequencies of Organic Molecules*: Elsevier Science; 1991.
- [36] M. Das, D. Sarkar, Development of room temperature ethanol sensor from polypyrrole (PPy) embedded in polyvinyl alcohol (PVA) matrix, *Polymer Bulletin*, 75 (2018) 3109-25.
- [37] Y. Zhou, P. Wang, M. Hu, X. Tian, Charge carrier related superior capacitance of the precisely size-controlled polypyrrole nanoparticles, *Electrochimica Acta*, 249 (2017) 290-300.
- [38] H.S. Mansur, C.M. Sadahira, A.N. Souza, A.A.P. Mansur, FTIR spectroscopy characterization of poly (vinyl alcohol) hydrogel with different hydrolysis degree and chemically crosslinked with glutaraldehyde, *Materials Science and Engineering: C*, 28 (2008) 539-48.
- [39] M. Makhlouki, J.C. Bernede, M. Morsli, A. Bonnet, A. Conan, S. Lefrant, XPS study of conducting polypyrrole-poly(vinyl alcohol) composites, *Synthetic Metals*, 62 (1994) 101-6.
- [40] M. Setka, R. Calavia, L. Vojkuvka, E. Llobet, J. Drbohlavova, S. Vallejos, Raman and XPS studies of ammonia sensitive polypyrrole nanorods and nanoparticles, *Scientific Reports*, 9 (2019) 10.
- [41] B.R.C. Vale, R.S. Mourao, J. Bettini, J.C.L. Sousa, J.L. Ferrari, P. Reiss, et al., Ligand induced switching of the band alignment in aqueous synthesized CdTe/CdS core/shell nanocrystals, *Scientific Reports*, 9 (2019) 12.
- [42] J.R. Fragoso-Mora, D. Matatagui, F.A. Bahos, J. Fontecha, M.J. Fernandez, J.P. Santos, et al., Gas sensors based on elasticity changes of nanoparticle layers, *Sensors and Actuators B: Chemical*, 268 (2018) 93-9.
- [43] J.S. Liu, L.J. Wang, Y.Y. Lu, S.T. He, Properties of Love waves in a piezoelectric layered structure with a viscoelastic guiding layer, *Smart Materials and Structures*, 22 (2013) 8.
- [44] M. Šetka, F.A. Bahos, D. Matatagui, Z. Kral, I. Gràcia, J. Drbohlavová, et al., Polypyrrole Based Love-Wave Gas Sensor Devices with Enhanced Properties to Ammonia, *Proceedings*, 2 (2018) 786.
- [45] H.-J. Cho, V.T. Chen, S. Qiao, W.-T. Koo, R.M. Penner, I.-D. Kim, Pt-Functionalized PdO Nanowires for Room Temperature Hydrogen Gas Sensors, *ACS Sensors*, 3 (2018) 2152-8.
- [46] B. Li, G. Sauve, M.C. Iovu, M. Jeffries-El, R. Zhang, J. Cooper, et al., Volatile organic compound detection using nanostructured copolymers, *Nano Lett*, 6 (2006) 1598-602.
- [47] W.C. Geng, S.B. Ge, X.W. He, S. Zhang, J.W. Gu, X.Y. Lai, et al., Volatile Organic Compound Gas-Sensing Properties of Bimodal Porous α -Fe₂O₃ with Ultrahigh Sensitivity and Fast Response, *Acs Applied Materials & Interfaces*, 10 (2018) 13702-11.
- [48] S. Hamilton, M.J. Hopher, J. Sommerville, Polypyrrole materials for detection and discrimination of volatile organic compounds, *Sensors and Actuators B: Chemical*, 107 (2005) 424-32.
- [49] L. Ruangchuay, A. Sirivat, J. Schwank, Electrical conductivity response of polypyrrole to acetone vapor: effect of dopant anions and interaction mechanisms, *Synthetic Metals*, 140 (2004) 15-21.
- [50] R.-J. Wu, Y.-C. Huang, M.-R. Yu, T.H. Lin, S.-L. Hung, Application of m-CNTs/NaClO₄/Ppy to a fast response, room working temperature ethanol sensor, *Sensors and Actuators B: Chemical*, 134 (2008) 213-8.
- [51] F. Müller-Plathe, W.F. van Gunsteren, Solvation of poly(vinyl alcohol) in water, ethanol and an equimolar water-ethanol mixture: structure and dynamics studied by molecular dynamics simulation, *Polymer*, 38 (1997) 2259-68.
- [52] R. Sankar ganesh, M. Navaneethan, G.K. Mani, S. Ponnusamy, K. Tsuchiya, C. Muthamizhchelvan, et al., Influence of Al doping on the structural, morphological, optical, and gas sensing properties of ZnO nanorods, *Journal of Alloys and Compounds*, 698 (2017) 555-64.
- [53] V.P. Anju, P.R. Jithesh, S.K. Narayanankutty, A novel humidity and ammonia sensor based on nanofibers/polyaniline/polyvinyl alcohol, *Sensors and Actuators A: Physical*, 285 (2019) 35-44.
- [54] M. Matsuguchi, A. Okamoto, Y. Sakai, Effect of humidity on NH₃ gas sensitivity of polyaniline blend films, *Sensors and Actuators B: Chemical*, 94 (2003) 46-52.
- [55] F. Li, H. Li, H. Jiang, K. Zhang, K. Chang, S. Jia, et al., Polypyrrole nanoparticles fabricated via Triton X-100 micelles template approach and their acetone gas sensing property, *Applied Surface Science*, 280 (2013) 212-8.
- [56] I. Constantinoiu, C. Viespe, Detection of Volatile Organic Compounds Using Surface Acoustic Wave Sensor Based on Nanoparticles Incorporated in Polymer, *Coatings*, 9 (2019) 9.
- [57] M. Asad, M.H. Sheikhi, Surface acoustic wave based H₂S gas sensors incorporating sensitive layers of single wall carbon nanotubes decorated with Cu nanoparticles, *Sensors and Actuators B: Chemical*, 198 (2014) 134-41.
- [58] F.A. Bahos, A. Sainz-Vidal, C. Sanchez-Perez, J.M. Saniger, I. Gracia, M.M. Saniger-Alba, et al., ZIF Nanocrystal-Based Surface Acoustic Wave (SAW) Electronic Nose to Detect Diabetes in Human Breath, *Biosensors-Basel*, 9 (2018) 13.
- [59] D. Zhang, Z. Wu, X. Zong, Y. Zhang, Fabrication of polypyrrole/Zn₂SnO₄ nanofilm for ultra-highly sensitive ammonia sensing application, *Sensors and Actuators B: Chemical*, 274 (2018) 575-86.

- [60] K. Malook, H. Khan, M. Shah, H. Ihsan Ul, Highly selective and sensitive response of Polypyrrole-MnO₂ based composites towards ammonia gas, *Polymer Composites*, 40 (2019) 1676-83.
- [61] M. Li, H. Kan, S. Chen, X. Feng, H. Li, C. Li, et al., Colloidal quantum dot-based surface acoustic wave sensors for NO₂-sensing behavior, *Sensors and Actuators B: Chemical*, 287 (2019) 241-9.

SUPPLEMENTARY INFORMATION

S1. Results

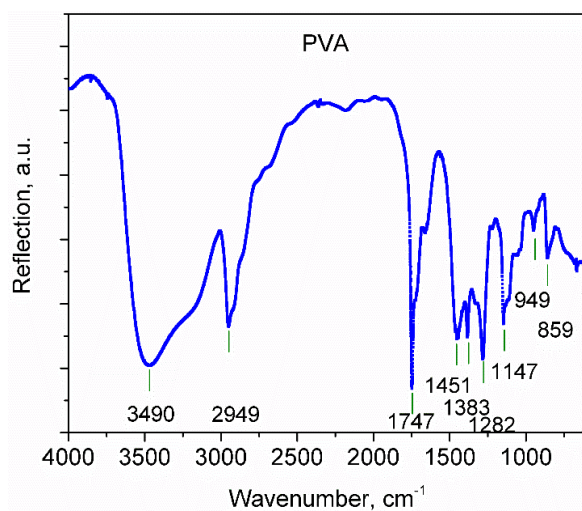


Figure S1. FTIR spectrum of polyvinyl alcohol (PVA).

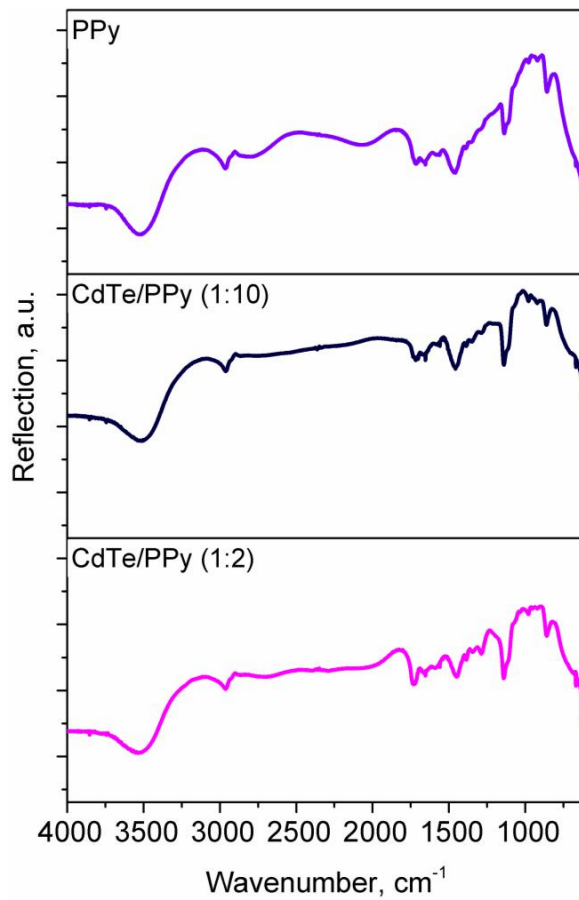


Figure S2. FTIR spectra of PPy, CdTe/PPy (1:10) and CdTe/PPy (1:2) layers.

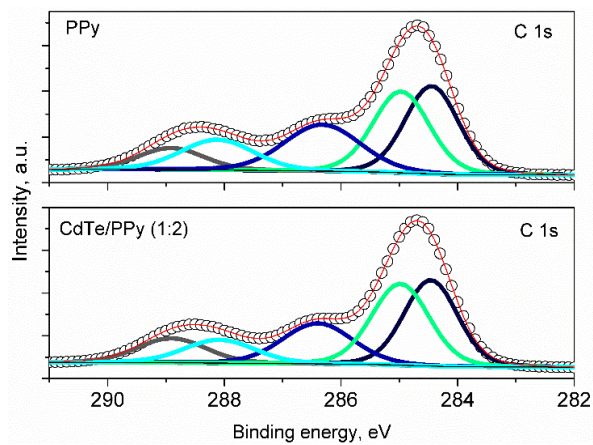


Figure S3. High resolution C 1s XPS core level spectra of PPy and CdTe/PPy (1:2) L SAW sensors. The spectra of CdTe/PPy (1:10) and CdTe/PPy (1:2) L SAW sensors displayed similar characteristics.

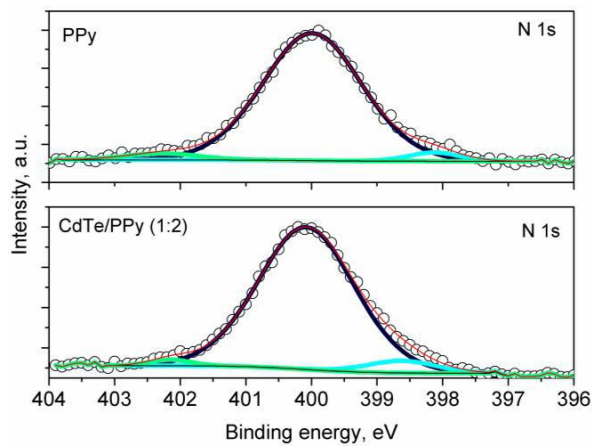


Figure S4. High resolution N 1s XPS core level spectra of PPy and CdTe/PPy (1:2) L SAW sensors. The spectra of CdTe/PPy (1:10) and CdTe/PPy (1:2) L SAW sensors displayed similar characteristics.

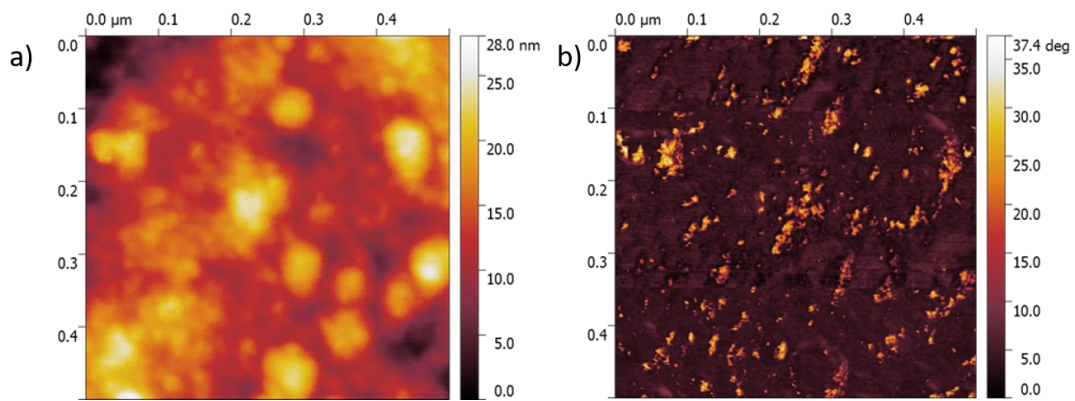


Figure S5. (a) Topography AFM image of CdTe/PPy (1:2) L SAW sensor. (b) Phase imaging of the CdTe/PPy (1:2) layers displayed visible contrast changes suggesting a variation in a surface composition due the presence of CdTe QDs clusters and PPy NPs at the surface.

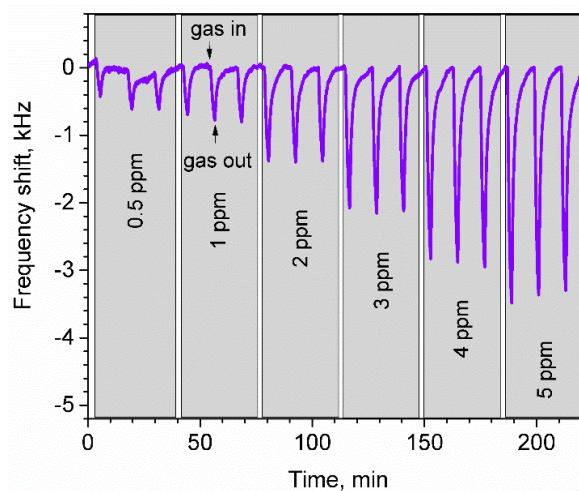


Figure S6. Dynamic response of the PPy L SAW sensors to acetone concentration from 0.5 to 5 ppm.

S2. Limit of detection

In order to calculate the limit of detection (LOD), we used following root-mean-square (RMS) deviation equation for sensors noise and the equation for theoretical LOD [61]:

$$RMS_{noise} = \sqrt{\frac{S^2}{N}}$$

where RMS is sensors noise, S is standard deviation of base line, N is number of data points (200 points used);

$$LOD (ppm) = 3 \times \frac{RMS_{noise}}{Slope}$$

where the slope value is extracted from the calibration curve presented in **Figure 9b** (refers to the main manuscript).

Chapter 7

Summary of results and conclusions

In this dissertation, the investigation of non-modified and modified PPy nanostructures and their integration into gas sensing devices was presented. The motivation behind this work was to examine the properties of PPy based materials and their sensing performances, in order to develop a cheap gas sensor which enables for the detection of specific gases and VOCs such as ammonia, acetone, ethanol, ethylene and toluene.

The work summarizes the development of five different PPy systems, including two non-modified in the form of NRs and NPs, and three modified based on functionalized PPy NPs with Au NPs, Ag NPs and CdTe QDs. Many complementary analytical techniques (microscopic and spectroscopic) were used for the determination of morphology and chemical composition of synthesized PPy nanostructures. Moreover, Raman and XPS spectroscopic techniques also showed to be an insightful tool for *in-situ* gas sensing test. Raman and XPS *in-situ* gas sensing test revealed the potential of PPy NRs and PPy NPs to sense ammonia and to be used as a gas sensitive material. However, beside the nature of material and chemical predisposition, the efficient integration of sensing material with a particular electronic system (a transducing platform) is the key factor for the accomplishment of the sensing capability (see Table 7.1). Accordingly, the complex design of PPy NRs chemo-resistive sensors and the extremely high resistance (in the range of G Ω) of PPy NPs based chemo-resistive sensors were the main reasons for their incapability. Nevertheless, the 'simple' design of L-SAW sensors based on PPy NPs resulted in the development of the gas sensors with outstanding performances.

Table 7.1: Comparison of gas sensing response of PPy based chemo-resistive and L-SAW sensors to ammonia (NH₃) and ethanol (C₂H₆O). The response of L-SAW sensors is showed as the frequency shift in kHz, while the response of chemo-resistive sensors is presented as R_a/R_g, where R_a and R_g is resistance in air and gas, respectively. The response of L-SAW sensors has negative value, as the frequency was decreased during the gas exposure.

| Material | Type of sensor | C (ppm) | Response | |
|---------------|-----------------|---------|-----------------|---------------------------------|
| | | | NH ₃ | C ₂ H ₆ O |
| PPy NRs | Chemo-resistive | 100 | 1 | Not tested |
| PPy NPs | Chemo-resistive | 80 | Not tested | 1 |
| PPy NPs | L-SAW | 5 | 0.4 | 2.9 |
| Au/PPy (1:10) | Chemo-resistive | 80 | Not tested | 1.6 |
| Au/PPy (1:10) | L-SAW | 5 | 1.4 | 3.8 |
| Ag/PPy | Chemo-resistive | 80 | Not tested | 1 |
| Ag/PPy | L-SAW | 5 | Not tested | 4.7 |

In order to create the L-SAW sensors with enhanced performances, various material combinations were investigated in this thesis. Also, the sensitive layers with different thickness were tested by changing the deposition conditions. In total, eight different PPy based multi-guiding L-SAW sensors were fabricated, and their properties and sensing abilities are summarized in Table 7.2. The results showed that the final sensing performances of the L-SAW sensors are dependent on the choice of the second guiding/sensitive

layer, but also the velocity of the propagated wave has a strong influence.

The propagation velocity and attenuation of Love wave are determined by the properties of the second guiding/sensitive layer such as thickness, stiffness, roughness, etc. Normally, as the thickness of the guiding/sensitive layer increases, the operation frequency of sensor should decrease, and the sensors with lower operation frequency (slower wave velocity) and appropriate insertion loss may provide higher mass sensitivity. Our results are in the line with those facts. The higher response and/or sensitivity of the non-modified PPy sensors to acetone, ethanol and toluene is observed for the sensor with the lower operation frequency (161.8 MHz) than by the one with higher frequency (162.5 MHz). This can be ascribed to slower velocity of the Love wave in the thicker PPy layer. The same observations are also noticed in the case of the sensors based on CdTe/PPy. Accordingly, the CdTe/PPy (1:2) sensor with higher operation frequency of 163.8 MHz showed the lower response and/or sensitivity to acetone, ethanol and toluene compared to CdTe/PPy (1:10) which had the operation frequency of 162.4 MHz. In both cases, the second/guiding layer is made of the material with the same chemical structure, thus, the differences in the response and/or sensitivity of two sensors could be caused by the different velocity of the wave in those layers. However, the higher sensitivity of Ag/PPy and Au/PPy sensors to acetone, ethanol and toluene compared to non-modified PPy sensor is caused by the presence of the catalytic nanoparticles rather than by the different operation frequency. Minimal variations of ± 0.3 MHz in the operation frequency are observed among those sensors. In the same line, the CdTe/PPy (1:10) sensors established higher response compared to non-modified PPy sensor. This improvement in response could be assigned to the presence of the hybrid material, as the difference in the operation frequency of those sensors is ± 0.1 MHz.

Table 7.2: Summary and comparison of the L-SAW sensor characteristics and their gas sensing performances to target analytes: acetone (C_3H_6O), ammonia (NH_3), ethanol (C_2H_6O), ethylene (C_2H_4) and toluene (C_7H_8). All developed sensors have multi-guiding layer concept, where the first guiding layer is made of SiO_2 (3 μm thick) and the second guiding layer is corresponding sensitive layer deposited with spin coating velocity of 2500 or 4000 rpm. The response of the sensors is presented for 5 ppm of the target gas. The sensitivity was defined as the ratio between the change in sensor response for a fixed change in analyte concentration (between 2 and 10 ppm for ammonia and ethylene, and between 1 and 5 ppm for acetone, ethanol and toluene). The insertion loss and response have negative value.

| SL | V (rpm) | d (nm) | f (MHz) | II (dB) | R (Hz) | | | S (Hz/ppm) | | | | | | |
|------------------|------------|-----------|------------|------------|--------------------|-----------|----------|------------|-----------|----------|------|-----|-----|-----|
| PPy | 4000 | 250 | 161.6 | 23 | NH_3 | C_2H_4 | NH_3 | C_2H_4 | | | | | | |
| | | | | | 374 | 360 | 50 | 84 | | | | | | |
| | | | | | 1380 | 652 | 89 | 152 | | | | | | |
| Au/PPy (1:10) | | 350 | 161.4 | 22 | | | | | | | | | | |
| Au/PPy (1:2) | | 400 | 161.2 | 22 | 513 | 1325 | 112 | 271 | | | | | | |
| PPy | 2500 | 260 | 161.8 | 22 | C_3H_6O | C_2H_6O | C_7H_8 | C_3H_6O | C_2H_6O | C_7H_8 | | | | |
| | | | | | 3456 | 3119 | 1573 | 670 | 551 | 260 | | | | |
| | | | | | 4700 | 4212 | 2143 | 876 | 738 | 340 | | | | |
| Ag/PPy (1:10) | | 260 | 161.5 | 19 | | | | | | | | | | |
| Au/PPy (1:10) | | 500 | 161.7 | 22 | 4156 | 3750 | 1915 | 776 | 656 | 302 | | | | |
| PPy | 4000 | 250 | 162.5 | 22 | 3374 | 2879 | 1554 | 652 | 441 | 250 | | | | |
| | | | | | CdTe/PPy (1:10) | 250 | 162.4 | 22 | 3967 | 3566 | 1859 | 771 | 546 | 308 |
| | | | | | CdTe/PPy (1:2) | 100 | 163.8 | 32 | 2029 | 1874 | 988 | 379 | 280 | 162 |

SL - second guiding/sensitive layer, V - velocity of spin coater, d - thickness of second guiding/sensitive layer (with errors of ± 10 nm), f - operation frequency of sensor, II - insertion loss of sensors, R - response of sensor, S - sensitivity.

In conclusion, the results achieved in this thesis, demonstrated the fabrication of L-SAW sensors with high mass sensitivity. This was achieved thanks to the choice of sensing material and slow transfer wave velocity presented in the multi-guiding layer concept where elastic layer of SiO₂ is combined with viscos-elastic layer based on PPy nanostructures. The objective of cost effective fabrication of simple micro-sensing elements with ability to sense all selected gases and VOCs was fulfilled. Among the tested sensing layers, modified PPy layer with Ag NPs and/or Au NPs deposited with spin coating velocity of 2500 rpm can be selected as the best technological solution for the fabrication of L-SAW sensors for the detection of acetone in dry and humid (at RH up to 30 %) environment. The improved sensing performances accomplish at RT operation, such as high sensitivity and low LOD, make these sensors a good candidate for the potential use in applications such as breath analysis for diagnostic purposes, as well as quality monitoring of air and food. However, before Ag/PPy and/or Au/PPy L-SAW sensors can be exploit in future consumer devices, the further technological solutions for the detection of acetone in the presence of large amount of moisture (RH > 30 %) remain to be investigated. Thus, the use of dehydration elements in the system or moisture filter with a specific pore channels which ensures that target gas molecules can easily pass through it, while it blocks the water molecules, could be helpful [215].

List of abbreviations

| | |
|--------------------------|---|
| <i>AAO</i> | Anodic aluminum oxide |
| <i>ACGHI</i> | American Conference of Governmental Industrial Hygienists |
| <i>AFM</i> | Atomic Force Microscopy |
| <i>Ag</i> | Silver |
| <i>Au</i> | Gold |
| <i>BAW</i> | Bulk acoustic wave |
| <i>BSE</i> | Backscattered electrons |
| <i>CdTe</i> | Cadmium-telluride |
| <i>CEITEC</i> | Central European Institute of Technology |
| <i>CPs</i> | Conductive polymer |
| <i>DC</i> | Direct current |
| <i>EDX</i> | Energy dispersive X-ray |
| <i>FTIR</i> | Fourier transform infrared spectrometry |
| <i>GaAs</i> | Gallium arsenate |
| <i>HOMO</i> | Highest occupied molecular orbital |
| <i>IDTs</i> | Interdigital transducers |
| <i>IMB – CNM, CSIC</i> | Institute de Microelectronica de Barcelona |
| K^2 | Electromechanical coupling coefficient |
| <i>L – SAW</i> | Love mode surface acoustic wave |
| <i>LiNbO₃</i> | Lithium niobate |
| <i>LiTaO₃</i> | Lithium tantalite |
| <i>LOD</i> | Limit of detection |
| <i>LUMO</i> | Lowest unoccupied molecular orbital |
| <i>MOX</i> | Metal oxides |
| <i>NPs</i> | Nanoparticle |
| <i>NRs</i> | Nanorods |
| <i>PA</i> | Polyacetylene |
| <i>PANI</i> | Polyaniline |
| <i>Pd</i> | Palladium |

| | |
|------------------------|--|
| <i>PEDOT</i> | Poly(3,4 ethylenedioxythiophe) |
| <i>ppb</i> | Parts per billion |
| <i>ppm</i> | Parts per million |
| <i>PPy</i> | Polypyrrole |
| <i>Pt</i> | Platinum |
| <i>PTh</i> | Polythiophene |
| <i>PVA</i> | Polyvinyl alcohol |
| <i>QCM</i> | Quartz crystal microbalance |
| <i>QDs</i> | Quantum dots |
| <i>RH</i> | Relative humidity |
| <i>RT</i> | Room temperature |
| <i>S₂₁</i> | Transmission scattering parameter |
| <i>SAW</i> | Surface acoustic wave |
| <i>SE</i> | Secondary electrons |
| <i>SEM</i> | Scanning Electron Microscopy |
| <i>SH</i> | Shear Horizontal |
| <i>SiO₂</i> | Silicon dioxide |
| <i>TCF</i> | Temperature coefficient of frequency |
| <i>TEM</i> | Transmission Electron Microscopy |
| <i>ToF – SIMS</i> | Time-of-Flight Secondary Ion Mass Spectrometry |
| <i>TVB – N</i> | Total volatile basic nitroge |
| <i>UNAM</i> | Universidad Nacional Autónoma de México |
| <i>UV – Vis</i> | Ultravioletvisible |
| <i>VOCs</i> | Volatile organic compounds |
| <i>XPS</i> | X-Ray Photoelectron Spectroscopy |
| <i>ZnO</i> | Zinc-oxide |

Bibliography

- [1] BARBRI, N. E. et al. An electronic nose system based on a micro-machined gas sensor array to assess the freshness of sardines. *Sensors and Actuators B: Chemical*, 2009, vol. 141, no. 2, pp. 538-543. ISSN 0925-4005.
- [2] PENG, G. et al. Detection of lung, breast, colorectal, and prostate cancers from exhaled breath using a single array of nanosensors. *British Journal of Cancer*, 2010, vol. 103, no. 4, pp. 542-551. ISSN 0007-0920.
- [3] MORANDI, S. et al. Operational functionalities of air-quality WSn metal-oxide sensors correlating semiconductor defect levels and surface potential barriers. *Science of The Total Environment*, 2020, vol. 706, pp. 135731. ISSN 0048-9697.
- [4] ZENG, Y. M. et al. Two-dimensional nanomaterials for gas sensing applications: the role of theoretical calculations. *Nanomaterials*, 2018, vol. 8, no. 10, pp. 16. ISSN 2079-4991.
- [5] JI, H. C. et al. Gas sensing mechanisms of metal oxide semiconductors: a focus review. *Nanoscale*, 2019, vol. 11, no. 47, pp. 22664-22684. ISSN 2040-3364.
- [6] MIRZAEI, A. et al. Nanostructured semiconducting metal oxide gas sensors for acetaldehyde detection. *Chemosensors*, 2019, vol. 7, no. 4, pp. 16.
- [7] SUN, Y. F. et al. Metal oxide nanostructures and their gas sensing properties: a review. *Sensors*, 2012, vol. 12, no. 3, pp. 2610-2631. ISSN 1424-8220.
- [8] KOO, W.-T. et al. Catalyst-decorated hollow WO₃ nanotubes using layer-by-layer self-assembly on polymeric nanofiber templates and their application in exhaled breath sensor. *Sensors and Actuators B: Chemical*, 2016, vol. 223, pp. 301-310. ISSN 0925-4005.
- [9] WANG, Y. et al. NH₃ gas sensing performance enhanced by Pt-loaded on mesoporous WO₃. *Sensors and Actuators B: Chemical*, 2017, vol. 238, pp. 473-481. ISSN 0925-4005.
- [10] ZHANG, S. et al. Self-assembled hierarchical Au-loaded In₂O₃ hollow microspheres with superior ethanol sensing properties. *Sensors and Actuators B: Chemical*, 2016, vol. 231, pp. 245-255. ISSN 0925-4005.
- [11] LI, M. et al. Ultrasensitive and highly selective detection of methoxy propanol based on Ag-decorated SnO₂ hollow nanospheres. *Sensors and Actuators B: Chemical*, 2016, vol. 232, pp. 545-556. ISSN 0925-4005.
- [12] LEE, S. W. et al. Recent advances in carbon material-based NO₂ gas sensors. *Sensors and Actuators B: Chemical*, 2018, vol. 255, pp. 1788-1804. ISSN 0925-4005.
- [13] LLOBET, E. Gas sensors using carbon nanomaterials: A review. *Sensors and Actuators B: Chemical*, 2013, vol. 179, pp. 32-45. ISSN 0925-4005.
- [14] WANG, Y. M. et al. Sensors based on conductive polymers and their composites: a review. *Polymer International*, 2019, vol. 69, no. 1, pp. 11. ISSN 0959-8103.
- [15] YOON, H. Current trends in sensors based on conducting polymer nanomaterials. *Nanomaterials*, 2013, vol. 3, no. 3, pp. 524-549. ISSN 2079-4991.
- [16] CHOUDHURY, A. Polyaniline/silver nanocomposites: dielectric properties and ethanol vapour sensitivity. *Sensors and Actuators B: Chemical*, 2009, vol. 138, no. 1, pp. 318-325. ISSN 0925-4005.

- [17] KABIR, L. et al. Humidity-sensing properties of conducting polypyrrole-silver nanocomposites. *Journal of Experimental Nanoscience*, 2008, vol. 3, no. 4, pp. 297-305. ISSN 1745-8080.
- [18] LEE, J.-S. et al. Au-polypyrrole framework nanostructures for improved localized surface plasmon resonance volatile organic compounds gas sensing. *Journal of Nanoscience and Nanotechnology*, 2015, vol. 15, no. 10, pp. 7738-7742. ISSN 1533-4880.
- [19] ATHAWALE, A. A. et al. Nanocomposite of Pd-polyaniline as a selective methanol sensor. *Sensors and Actuators B: Chemical*, 2006, vol. 114, no. 1, pp. 263-267. ISSN 0925-4005.
- [20] HUANG, J. et al. Gas sensing performance of polyaniline/ZnO organic-inorganic hybrids for detecting VOCs at low temperature. *Journal of Natural Gas Chemistry*, 2011, vol. 20, no. 5, pp. 515-519. ISSN 1003-9953.
- [21] JOULAZADEH, M. a NAVARCHIAN, A. H. Ammonia detection of one-dimensional nanostructured polypyrrole/metal oxide nanocomposites sensors. *Synthetic Metals*, 2015, vol. 210, pp. 404-411. ISSN 0379-6779.
- [22] BACHHAV, S. G. a PATIL, D. R. Study of polypyrrole-coated MWCNT nanocomposites for ammonia sensing at room temperature. *Journal of Materials Science and Chemical Engineering*, 2015, vol. 3, pp. 30-44.
- [23] DANESHKHAH, A. et al. Poly(vinylidene fluoride-hexafluoropropylene) composite sensors for volatile organic compounds detection in breath. *Sensors and Actuators B: Chemical*, 2015, vol. 221, pp. 635-643. ISSN 0925-4005.
- [24] TUNG, T. T. et al. Graphene-Fe₃O₄/PIL-PEDOT for the design of sensitive and stable quantum chemo-resistive VOC sensors. *Carbon*, 2014, vol. 74, pp. 104-112. ISSN 0008-6223.
- [25] FENG, X. M. et al. The synthesis of shape-controlled polypyrrole/graphene and the study of its capacitance properties. *Polymer Bulletin*, 2013, vol. 70, no. 8, pp. 2291-2304. ISSN 0170-0839.
- [26] GUERNION, N. et al. The fabrication and characterisation of a highly sensitive polypyrrole sensor and its electrical responses to amines of differing basicity at high humidities. *Synthetic Metals*, 2002, vol. 126, no. 2-3, pp. 301-310. ISSN 0379-6779.
- [27] ZHANG, L. et al. A novel ammonia sensor based on high density, small diameter polypyrrole nanowire arrays. *Sensors and Actuators B: Chemical*, 2009, vol. 142, no. 1, pp. 204-209. ISSN 0925-4005.
- [28] ATHAWALE, A. A. a KULKARNI, M. V. Polyaniline and its substituted derivatives as sensor for aliphatic alcohols. *Sensors and Actuators B-Chemical*, 2000, vol. 67, no. 1-2, pp. 173-177. ISSN 0925-4005.
- [29] KIM, J.-S. et al. Fabrication and sensing behavior of PVF₂ coated-polyaniline sensor for volatile organic compounds. *Sensors and Actuators B: Chemical*, 2005, vol. 108, no. 1-2, pp. 409-413. ISSN 0925-4005.
- [30] EAIDKONG, T. et al. Polydiacetylene paper-based colorimetric sensor array for vapor phase detection and identification of volatile organic compounds. *Journal of Materials Chemistry*, 2012, vol. 22, no. 13, pp. 5970-5977. ISSN 0959-9428.
- [31] YOON, J. et al. Colorimetric sensors for volatile organic compounds (VOCs) based on conjugated polymer-embedded electrospun fibers. *Journal of the American Chemical Society*, 2007, vol. 129, no. 11, pp. 3038-3039. ISSN 0002-7863.
- [32] MALKESHI, H. a MILANI MOGHADDAM, H. Ammonia gas-sensing based on polythiophene film prepared through electrophoretic deposition method. *Journal of Polymer Research*, 2016, vol. 23, no. 6, pp. 108. ISSN 1572-8935.
- [33] KIM, T. a KWAK, D. Flexible VOC sensors using conductive polymers and porous membranes for application to textiles. *Fibers and Polymers*, 2012, vol. 13, no. 4, pp. 471-474. ISSN 1229-9197.

- [34] PARK, E. et al. One-pot synthesis of silver nanoparticles decorated poly(3,4-ethylenedioxythiophene) nanotubes for chemical sensor application. *Journal of Materials Chemistry*, 2012, vol. 22, no. 4, pp. 1521-1526. ISSN 0959-9428.
- [35] KAISER, M. R. et al. Electro-polymerized polypyrrole film for fabrication of flexible and slurry-free polypyrrole-sulfur-polypyrrole sandwich electrode for the lithium-sulfur battery. *Journal of Power Sources*, 2019, vol. 437, pp. 226925. ISSN 0378-7753.
- [36] LUO, S. J. et al. Self-standing polypyrrole/black phosphorus laminated film: promising electrode for flexible supercapacitor with enhanced capacitance and cycling stability. *ACS Applied Materials & Interfaces*, 2018, vol. 10, no. 4, pp. 3538-3548. ISSN 1944-8244.
- [37] NOWICKA, A. M. et al. Polypyrrole-au nanoparticles composite as suitable platform for dna biosensor with electrochemical impedance spectroscopy detection. *Electrochimica Acta*, 2014, vol. 140, pp. 65-71. ISSN 0013-4686.
- [38] NAYAK, A. K. et al. Hierarchical nanostructured WO₃-SnO₂ for selective sensing of volatile organic compounds. *Nanoscale*, 2015, vol. 7, no. 29, pp. 12460-12473. ISSN 2040-3364.
- [39] DALAVI, D. S. et al. Nanoporous network of nickel oxide for ammonia gas detection. *Materials Letters*, 2015, vol. 146, pp. 103-107. ISSN 0167-577X.
- [40] LI, Y. S. et al. High-aspect-ratio single-crystalline porous In₂O₃ nanobelts with enhanced gas sensing properties. *Journal of Materials Chemistry*, 2011, vol. 21, no. 34, pp. 12852-12857. ISSN 0959-9428.
- [41] NA, C. W. et al. Transformation of ZnO nanobelts into single-crystalline Mn₃O₄ nanowires. *ACS Applied Materials & Interfaces*, 2012, vol. 4, no. 12, pp. 6565-6572. ISSN 1944-8244.
- [42] PETER MARTIN, L. et al. Effect of Cr₂O₃ electrode morphology on the nitric oxide response of a stabilized zirconia sensor. *Sensors and Actuators B: Chemical*, 2003, vol. 96, no. 1, pp. 53-60. ISSN 0925-4005.
- [43] WANG, S. et al. Organic/inorganic hybrid sensors: A review. *Sensors and Actuators B: Chemical*, 2013, vol. 182, pp. 467-481. ISSN 0925-4005.
- [44] HAKIM, M. et al. Volatile organic compounds of lung cancer and possible biochemical pathways. *Chemical Reviews*, 2012, vol. 112, no. 11, pp. 5949-5966. ISSN 0009-2665.
- [45] HAICK, H. a COHEN-KAMINSKY, S. Detecting lung infections in breathprints: empty promise or next generation diagnosis of infections. *European Respiratory Journal*, 2015, vol. 45, no. 1, pp. 21-24. ISSN 0903-1936.
- [46] VAN DE KANT, K. D. G. et al. Clinical use of exhaled volatile organic compounds in pulmonary diseases: a systematic review. *Respiratory Research*, 2012, vol. 13, pp. 1-23. ISSN 1465-993X.
- [47] PACHECO, J. G. et al. Molecularly imprinted electrochemical sensor for the point-of-care detection of a breast cancer biomarker (CA 15-3). *Sensors and Actuators B-Chemical*, 2018, vol. 256, pp. 905-912. ISSN 0925-4005.
- [48] ZONTA, G. et al. Detection of colorectal cancer biomarkers in the presence of interfering gases. *Sensors and Actuators B-Chemical*, 2015, vol. 218, pp. 289-295. ISSN 0925-4005.
- [49] DI FRANCESCO, F. et al. Breath analysis: trends in techniques and clinical applications. *Microchemical Journal*, 2005, vol. 79, no. 1, pp. 405-410. ISSN 0026-265X.
- [50] RAMÍREZ, N. et al. Chronic risk assessment of exposure to volatile organic compounds in the atmosphere near the largest Mediterranean industrial site. *Environment International*, 2012, vol. 39, no. 1, pp. 200-209. ISSN 0160-4120.
- [51] BAI, J. et al. Aroma profile characterization of Mahi-Mahi and tuna for determining spoilage using purge and trap gas chromatography-mass spectrometry. *Journal of Food Science*, 2019, vol. 84, no. 3, pp. 481-489. ISSN 0022-1147.
- [52] FINK, T. et al. Ion mobility spectrometry in breath research. *Journal of Breath Research*, 2014, vol. 8, no. 2, pp. 1-11. ISSN 1752-7155.

- [53] LIGOR, M. et al. Determination of volatile organic compounds in exhaled breath of patients with lung cancer using solid phase microextraction and gas chromatography mass spectrometry. *Clinical Chemistry and Laboratory Medicine*, 2009, vol. 47, no. 5, pp. 550-560. ISSN 1434-6621.
- [54] AHMED, W. M. et al. Exhaled volatile organic compounds of infection: A systematic review. *ACS Infectious Diseases*, 2017, vol. 3, no. 10, pp. 695-710. ISSN 2373-8227.
- [55] SUN, J. et al. Volatile organic compounds emissions from traditional and clean domestic heating appliances in Guanzhong Plain, China: Emission factors, source profiles, and effects on regional air quality. *Environment International*, 2019, vol. 133, pp. 105252. ISSN 0160-4120.
- [56] KIM, H.-J. a LEE, J.-H. Highly sensitive and selective gas sensors using p-type oxide semiconductors: Overview. *Sensors and Actuators B: Chemical*, 2014, vol. 192, pp. 607-627. ISSN 0925-4005.
- [57] STETTER, J. R. a LI, J. Amperometric gas sensors - A review. *Chemical Reviews*, 2008, vol. 108, no. 2, pp. 352-366. ISSN 0009-2665.
- [58] BAHARUDDIN, A. A. et al. Advances in chemiresistive sensors for acetone gas detection. *Materials Science in Semiconductor Processing*, 2019, vol. 103, pp. 104616. ISSN 1369-8001.
- [59] CALHEIRO, D. S. a BIANCHI, R. F. Tuning the detection limit in hybrid organic-inorganic materials for improving electrical performance of sensing devices. *Sensors and Actuators A: Physical*, 2019, vol. 298, pp. 111480. ISSN 0924-4247.
- [60] DONG, C. et al. A review on WO₃ based gas sensors: morphology control and enhanced sensing properties. *Journal of Alloys and Compounds*, 2020, vol. 820, pp. 153194. ISSN 0925-8388.
- [61] FENG, S. B. et al. Review on smart gas sensing technology. *Sensors*, 2019, vol. 19, no. 17, pp. 22.
- [62] GARDON, M. a GUILMANY, J. M. A review on fabrication, sensing mechanisms and performance of metal oxide gas sensors. *Journal of Materials Science: Materials in Electronics*, 2013, vol. 24, no. 5, pp. 1410-1421. ISSN 1573-482X.
- [63] AFZAL, A. et al. Advanced vapor recognition materials for selective and fast responsive surface acoustic wave sensors: a review. *Analytica Chimica Acta*, 2013, vol. 787, pp. 36-49. ISSN 0003-2670.
- [64] YAACOB, M. H. et al. Optical response of WO₃ nanostructured thin films sputtered on different transparent substrates towards hydrogen of low concentration. *Sensors and Actuators B: Chemical*, 2013, vol. 177, pp. 981-988. ISSN 0925-4005.
- [65] ARAFAT, M. M. et al. Gas sensors based on one dimensional nanostructured metal-oxides: a review. *Sensors*, 2012, vol. 12, no. 6, pp. 7207-7258. ISSN 1424-8220.
- [66] RIGHETTONI, M. et al. Breath analysis by nanostructured metal oxides as chemo-resistive gas sensors. *Materials Today*, 2015, vol. 18, no. 3, pp. 163-171. ISSN 1369-7021.
- [67] TOMIC, M. et al. Cerium oxide-tungsten oxide core-shell nanowire-based microsensors sensitive to acetone. *Biosensors-Basel*, 2018, vol. 8, no. 4, pp. 11.
- [68] MILLER, D. R. et al. Nanoscale metal oxide-based heterojunctions for gas sensing: a review. *Sensors and Actuators B: Chemical*, 2014, vol. 204, pp. 250-272. ISSN 0925-4005.
- [69] SKOTHEIM, T. A. a REYNOLDS, J. Conjugated polymers: theory, synthesis, properties, and characterization. CRC Press, 2006, ISBN 9781420043594.
- [70] CELIESIUTE, R. et al. Electrochromic sensors based on conducting polymers, metal oxides, and coordination complexes. *Critical Reviews in Analytical Chemistry*, 2019, vol. 49, no. 3, pp. 195-208. ISSN 1040-8347.
- [71] LONG, Y.-Z. et al. Recent advances in synthesis, physical properties and applications of conducting polymer nanotubes and nanofibers. *Progress in Polymer Science*, 2011, vol. 36, no. 10, pp. 1415-1442. ISSN 0079-6700.
- [72] WANG, Y. Q. et al. Conductive polymers for stretchable supercapacitors. *Nano Research*, 2019, vol. 12, no. 9, pp. 1978-1987. ISSN 1998-0124.

- [73] LE, T. H. et al. Electrical and electrochemical properties of conducting polymers. *Polymers*, 2017, vol. 9, no. 4, pp. 32. ISSN 2073-4360.
- [74] MA, Z. et al. Doping engineering of conductive polymer hydrogels and their application in advanced sensor technologies. *Chemical Science*, 2019, vol. 10, no. 25, pp. 6232-6244. ISSN 2041-6520.
- [75] BREDAS, J. L. a STREET, G. B. Polarons, bipolarons, and solitons in conducting polymers. *Accounts of Chemical Research*, 1985, vol. 18, no. 10, pp. 309-315. ISSN 0001-4842.
- [76] PARK, S. J. et al. Conducting polymer-based nanohybrid transducers: A potential route to high sensitivity and selectivity sensors. *Sensors*, 2014, vol. 14, no. 2, pp. 3604-3630. ISSN 1424-8220.
- [77] ZHANG, L. et al. Recent progress on nanostructured conducting polymers and composites: synthesis, application and future aspects. *Science China-Materials*, 2018, vol. 61, no. 3, pp. 303-352. ISSN 2095-8226.
- [78] JACKOWSKA, K. et al. Hard template synthesis of conducting polymers: a route to achieve nanostructures. *Journal of Solid State Electrochemistry*, 2008, vol. 12, no. 4, pp. 437-443. ISSN 1432-8488.
- [79] SHAH, K. W. et al. One-dimensional nanostructure engineering of conducting polymers for thermoelectric applications. *Applied Sciences-Basel*, 2019, vol. 9, no. 7, pp. 22.
- [80] JACKOWSKA, K. et al. Hard template synthesis of conducting polymers: a route to achieve nanostructures. *Journal of Solid State Electrochemistry*, 2008, vol. 12, no. 4, pp. 437-443. ISSN 1433-0768.
- [81] GHOSH, S. et al. Nanostructured conducting polymers for energy applications: towards a sustainable platform. *Nanoscale*, 2016, vol. 8, no. 13, pp. 6921-6947. ISSN 2040-3364.
- [82] ZHANG, X. et al. Controllable synthesis of conducting polypyrrole nanostructures. *The Journal of Physical Chemistry B*, 2006, vol. 110, no. 3, pp. 1158-1165. ISSN 1520-6106.
- [83] DIAZ-ORELLANA, K. P. a ROBERTS, M. E. Scalable, template-free synthesis of conducting polymer microtubes. *Rsc Advances*, 2015, vol. 5, no. 32, pp. 25504-25512. ISSN 2046-2069.
- [84] ZHOU, Y. et al. Charge carrier related superior capacitance of the precisely size-controlled polypyrrole nanoparticles. *Electrochimica Acta*, 2017, vol. 249, pp. 290-300. ISSN 0013-4686.
- [85] UPPALAPATI, D. et al. Conducting polymers with defined micro- or nanostructures for drug delivery. *Biomaterials*, 2016, vol. 111, pp. 149-162. ISSN 0142-9612.
- [86] WONG, Y. C. et al. Review-conducting polymers as chemiresistive gas sensing materials: a review. *Journal of the Electrochemical Society*, 2019, vol. 167, no. 1. ISSN 0013-4651.
- [87] GENG, L. a WU, S. Preparation, characterization and gas sensitivity of polypyrrole/ γ -Fe₂O₃ hybrid materials. *Materials Research Bulletin*, 2013, vol. 48, no. 10, pp. 4339-4343. ISSN 0025-5408.
- [88] HAMILTON, S. et al. Polypyrrole materials for detection and discrimination of volatile organic compounds. *Sensors and Actuators B: Chemical*, 2005, vol. 107, no. 1, pp. 424-432. ISSN 0925-4005.
- [89] BENIWAL, A. a SUNNY Electrospun SnO₂/PPy nanocomposite for ultra-low ammonia concentration detection at room temperature. *Sensors and Actuators B: Chemical*, 2019, vol. 296, pp. 126660. ISSN 0925-4005.
- [90] LI, S. et al. Room temperature gas sensor based on tin dioxide@ polyaniline nanocomposite assembled on flexible substrate: ppb-level detection of NH₃. *Sensors and Actuators B: Chemical*, 2019, vol. 299, pp. 126970. ISSN 0925-4005.
- [91] YU, X. et al. Digital ammonia gas sensor based on quartz resonator tuned by interdigital electrode coated with polyaniline film. *Organic Electronics*, 2020, vol. 76, pp. 105413. ISSN 1566-1199.
- [92] CHEN, X. et al. Gas sensing properties of surface acoustic wave NH₃ gas sensor based on Pt doped polypyrrole sensitive film. *Sensors and Actuators B: Chemical*, 2013, vol. 177, pp. 364-369. ISSN 0925-4005.

- [93] USMAN, F. et al. Enhanced sensitivity of surface plasmon resonance biosensor functionalized with doped polyaniline composites for the detection of low-concentration acetone vapour. *Journal of Sensors*, 2019, vol. 2019, pp. 13. ISSN 1687-725X.
- [94] BAGCHI, S. et al. Electrospun polypyrrole-polyethylene oxide coated optical fiber sensor probe for detection of volatile compounds. *Sensors and Actuators B-Chemical*, 2017, vol. 250, pp. 52-60.
- [95] LAKARD, B. et al. Gas sensors based on electrodeposited polymers. *Metals*, 2015, vol. 5, no. 3, pp. 1371-1386. ISSN 2075-4701.
- [96] PARK, S. J. et al. Chemo-electrical gas sensors based on conducting polymer hybrids. *Polymers*, 2017, vol. 9, no. 5, pp. 24.
- [97] SANJUÁN, A. M. et al. Recent developments in sensing devices based on polymeric systems. *Reactive and Functional Polymers*, 2018, vol. 133, pp. 103-125. ISSN 1381-5148.
- [98] BAI, H. a SHI, G. Q. Gas sensors based on conducting polymers. *Sensors*, 2007, vol. 7, no. 3, pp. 267-307. ISSN 1424-8220.
- [99] CHOUGULE, M. A. et al. Polypyrrole thin film: room temperature ammonia gas sensor. *IEEE Sensors Journal*, 2011, vol. 11, no. 9, pp. 2137-2141. ISSN 2379-9153.
- [100] YADAV, A. A. et al. Synthesis and characterization of polypyrrole thin film by MW-CBD method for NH₃ gas sensor. *Polymer Bulletin*, 2018, vol. 75, no. 10, pp. 4547-4553. ISSN 1436-2449.
- [101] TANG, X. et al. An ammonia sensor composed of polypyrrole synthesized on reduced graphene oxide by electropolymerization. *Sensors and Actuators B: Chemical*, 2020, vol. 305, pp. 127423. ISSN 0925-4005.
- [102] SHARMA, A. L. et al. Nanostructured polyaniline films on silicon for sensitive sensing of ammonia. *Sensors and Actuators A: Physical*, 2013, vol. 198, pp. 107-112. ISSN 0924-4247.
- [103] SUTAR, D. S. et al. Preparation of nanofibrous polyaniline films and their application as ammonia gas sensor. *Sensors and Actuators B: Chemical*, 2007, vol. 128, no. 1, pp. 286-292. ISSN 0925-4005.
- [104] WANG, H. et al. 3D Hollow quasi-graphite capsules/polyaniline hybrid with a high performance for room-temperature ammonia gas sensors. *ACS Sensors*, 2019, vol. 4, no. 9, pp. 2343-2350. ISSN 2379-3694.
- [105] NAVALE, S. T. et al. Room temperature NO₂ sensing properties of polythiophene films. *Synthetic Metals*, 2014, vol. 195, pp. 228-233. ISSN 0379-6779.
- [106] BAI, S. L. et al. Enhancement of NO₂-sensing performance at room temperature by graphene-modified polythiophene. *Industrial & Engineering Chemistry Research*, 2016, vol. 55, no. 19, pp. 5788-5794. ISSN 0888-5885.
- [107] SEEKAEW, Y. et al. Low-cost and flexible printed graphene-PEDOT:PSS gas sensor for ammonia detection. *Organic Electronics*, 2014, vol. 15, no. 11, pp. 2971-2981. ISSN 1566-1199.
- [108] KWON, O. S. et al. Novel flexible chemical gas sensor based on poly(3,4-ethylenedioxythiophene) nanotube membrane. *Talanta*, 2010, vol. 82, no. 4, pp. 1338-1343. ISSN 0039-9140.
- [109] LI, S. Y. et al. Flexible ammonia sensor based on PEDOT:PSS/silver nanowire composite film for meat freshness monitoring. *Ieee Electron Device Letters*, 2017, vol. 38, no. 7, pp. 975-978. ISSN 0741-3106.
- [110] LIU, X. et al. A survey on gas sensing technology. *Sensors*, 2012, vol. 12, no. 7, pp. 9635-9665. ISSN 1424-8220.
- [111] HANGARTER, C. M. et al. Hybridized conducting polymer chemiresistive nano-sensors. *Nano Today*, 2013, vol. 8, no. 1, pp. 39-55. ISSN 1748-0132.
- [112] CAPONE, S. et al. Solid state gas sensors: State of the art and future activities. *Journal of Optoelectronics and Advanced Materials*, 2003, vol. 5, no. 5, pp. 1335-1348. ISSN 1454-4164.

- [113] BALLANTINE, D. S. et al. Acoustic wave sensors: theory, design and physico-chemical applications. Elsevier Science, 1996, ISBN 9780080523330.
- [114] EGGINS, B. R. Chemical sensors and biosensors. Wiley, 2008, ISBN 9780470511312.
- [115] JANATA, J. Principles of chemical sensors. Springer Publishing Company, Incorporated, 2009, ISBN 0387699309, 9780387699301.
- [116] MOSELEY, P. T. Progress in the development of semiconducting metal oxide gas sensors: a review. Measurement Science and Technology, 2017, vol. 28, no. 8, pp. 15. ISSN 0957-0233.
- [117] WANG, W. Progresses in chemical sensor. IntechOpen, 2016, ISBN 9789535125327.
- [118] FANGET, S. et al. Gas sensors based on gravimetric detection—A review. Sensors and Actuators B: Chemical, 2011, vol. 160, no. 1, pp. 804-821. ISSN 0925-4005.
- [119] BRYANT, A. et al. A surface acoustic wave gas detector. Ieee Transactions on Sonics and Ultrasonics, 1982, vol. 29, no. 3, pp. 167-167. ISSN 0018-9537.
- [120] YANASE, Y. et al. Diagnosis of immediate-type allergy using surface plasmon resonance. Optical Materials Express, 2016, vol. 6, no. 4, pp. 1339-1348. ISSN 2159-3930.
- [121] WOHLTJEN, H. Mechanism of operation and design considerations for surface acoustic wave device vapour sensors. Sensors and Actuators, 1984, vol. 5, no. 4, pp. 307-325. ISSN 0250-6874.
- [122] ATHANASOPOULOS, G. A. et al. Effect of soil stiffness in the attenuation of Rayleigh-wave motions from field measurements. Soil Dynamics and Earthquake Engineering, 2000, vol. 19, no. 4, pp. 277-288. ISSN 0267-7261.
- [123] MORGAN, D. Surface acoustic wave filters: with applications to electronic communications and signal processing. Elsevier Science, 2010, ISBN 9780080550138.
- [124] LIU, J. a HE, S. Properties of Love waves in layered piezoelectric structures. International Journal of Solids and Structures, 2010, vol. 47, no. 2, pp. 169-174. ISSN 0020-7683.
- [125] IPPOLITO, S. J. et al. Acoustic wave gas and vapor sensors, Solid State Gas Sensing. Boston, MA: Springer US, 2009, pp. 1-44.
- [126] DEVKOTA, J. et al. SAW sensors for chemical vapors and gases. Sensors, 2017, vol. 17, no. 4, pp. 28. ISSN 1424-8220.
- [127] MATATAGUI, D. et al. Chemical warfare agents simulants detection with an optimized SAW sensor array. Sensors and Actuators B: Chemical, 2011, vol. 154, no. 2, pp. 199-205. ISSN 0925-4005.
- [128] JAKUBIK, W. P. Surface acoustic wave-based gas sensors. Thin Solid Films, 2011, vol. 520, no. 3, pp. 986-993. ISSN 0040-6090.
- [129] XU, Z. a YUAN, Y. J. Implementation of guiding layers of surface acoustic wave devices: A review. Biosensors and Bioelectronics, 2018, vol. 99, pp. 500-512. ISSN 0956-5663.
- [130] BRYANT, A. et al. Gas detection using surface acoustic wave delay lines. Sensors and Actuators, 1983, vol. 4, no. Supplement C, pp. 105-111. ISSN 0250-6874.
- [131] MATATAGUI, D. et al. Array of Love-wave sensors based on quartz/Novolac to detect CWA simulants. Talanta, 2011, vol. 85, no. 3, pp. 1442-1447. ISSN 0039-9140.
- [132] KOLANJIAPPAN, K. et al. Measurement of erythrocyte lipids, lipid peroxidation, antioxidants and osmotic fragility in cervical cancer patients. Clinica Chimica Acta, 2002, vol. 326, no. 1, pp. 143-149. ISSN 0009-8981.
- [133] NI, Z. et al. Analytical strategies to uncover the diversity of lipid peroxidation products and their biological effects. Free Radical Biology and Medicine, 2018, vol. 124, pp. 560-561. ISSN 0891-5849.
- [134] AMES, B. N. et al. Oxidants, antioxidants, and the degenerative disease of aging, Proceedings of the National Academy of Sciences of the United States of America, 1993, vol. 90, no. 17, pp. 7915-7922. ISSN 0027-8424.

- [135] DIX, T. A. a AIKENS, J. Mechanisms and biological relevance of lipid-peroxidation initiation. *Chemical Research in Toxicology*, 1993, vol. 6, no. 1, pp. 2-18. ISSN 0893-228X.
- [136] UTTARA, B. et al. Oxidative stress and neurodegenerative diseases: a review of upstream and downstream antioxidant therapeutic options. *Current Neuropharmacology*, 2009, vol. 7, no. 1, pp. 65-74. ISSN 1570-159X.
- [137] ARSLANOV, D. D. et al. Real-time, subsecond, multicomponent breath analysis by optical parametric oscillator based off-axis integrated cavity output spectroscopy. *Optics Express*, 2011, vol. 19, no. 24, pp. 24078-24089. ISSN 1094-4087.
- [138] BOOTS, A. W. et al. The versatile use of exhaled volatile organic compounds in human health and disease. *Journal of Breath Research*, 2012, vol. 6, no. 2, pp. 21. ISSN 1752-7155.
- [139] BRUDERER, T. et al. On-line analysis of exhaled breath. *Chemical Reviews*, 2019, vol. 119, no. 19, pp. 10803-10828. ISSN 0009-2665.
- [140] PLEIL, J. D. et al. Clinical breath analysis: discriminating between human endogenous compounds and exogenous (environmental) chemical confounders. *Journal of Breath Research*, 2013, vol. 7, no. 1, pp. 11. ISSN 1752-7155.
- [141] BOOTS, A. W. et al. Exhaled molecular fingerprinting in diagnosis and monitoring: validating volatile promises. *Trends in Molecular Medicine*, 2015, vol. 21, no. 10, pp. 633-644. ISSN 1471-4914.
- [142] COSTELLO, B. D. et al. A review of the volatiles from the healthy human body. *Journal of Breath Research*, 2014, vol. 8, no. 1, pp. 29. ISSN 1752-7155.
- [143] DAS, S. et al. Significance of exhaled breath test in clinical diagnosis: a special focus on the detection of diabetes mellitus. *Journal of Medical and Biological Engineering*, 2016, vol. 36, no. 5, pp. 605-624. ISSN 1609-0985.
- [144] MIEKISCH, W. et al. Diagnostic potential of breath analysis—focus on volatile organic compounds. *Clinica Chimica Acta*, 2004, vol. 347, no. 1, pp. 25-39. ISSN 0009-8981.
- [145] SCHUBERT, J. K. et al. Breath analysis in critically ill patients: potential and limitations. *Expert Review of Molecular Diagnostics*, 2004, vol. 4, no. 5, pp. 619-629. ISSN 1473-7159.
- [146] KUMAR, S. et al. Mass spectrometric analysis of exhaled breath for the identification of volatile organic compound biomarkers in esophageal and gastric adenocarcinoma. *Annals of Surgery*, 2015, vol. 262, no. 6, pp. 981-990. ISSN 0003-4932.
- [147] KANSAL, A. Sources and reactivity of NMHCs and VOCs in the atmosphere: A review. *Journal of Hazardous Materials*, 2009, vol. 166, no. 1, pp. 17-26. ISSN 0304-3894.
- [148] JONES, A. P. Indoor air quality and health. *Atmospheric Environment*, 1999, vol. 33, no. 28, pp. 4535-4564. ISSN 1352-2310.
- [149] FRANKE, C. a BEAUCHAMP, J. Real-time detection of volatiles released during meat spoilage: a case study of modified atmosphere-packaged chicken breast fillets inoculated with br. *thermosphacta*. *Food Analytical Methods*, 2017, vol. 10, no. 2, pp. 310-319. ISSN 1936-9751.
- [150] DUFLOS, G. et al. Determination of volatile compounds to characterize fish spoilage using headspace/mass spectrometry and solid-phase microextraction/gas chromatography/mass spectrometry. *Journal of the Science of Food and Agriculture*, 2006, vol. 86, no. 4, pp. 600-611. ISSN 0022-5142.
- [151] HONG, X. et al. Discrimination and prediction of multiple beef freshness indexes based on electronic nose. *Sensors and Actuators B: Chemical*, 2012, vol. 161, no. 1, pp. 381-389. ISSN 0925-4005.
- [152] LI, W. W. et al. A cross-sectional study of breath acetone based on diabetic metabolic disorders. *Journal of Breath Research*, 2015, vol. 9, no. 1, pp. 9. ISSN 1752-7155.
- [153] WANG, C. et al. A Study on breath acetone in diabetic patients using a cavity ringdown breath analyzer: exploring correlations of breath acetone with blood glucose and glycohemoglobin A1C. *IEEE Sensors Journal*, 2010, vol. 10, no. 1, pp. 54-63. ISSN 2379-9153.

- [154] ULANOWSKA, A. et al. The application of statistical methods using VOCs to identify patients with lung cancer. *Journal of Breath Research*, 2011, vol. 5, no. 4, pp. 11. ISSN 1752-7155.
- [155] RUZSANYI, V. a KALAIPOS, M. P. Breath acetone as a potential marker in clinical practice. *Journal of Breath Research*, 2017, vol. 11, no. 2, pp. 18. ISSN 1752-7155.
- [156] SPANEL, P. et al. Breath acetone concentration; biological variability and the influence of diet. *Physiological Measurement*, 2011, vol. 32, no. 8, pp. N23-N31. ISSN 0967-3334.
- [157] HUANG, Y. et al. Evaluation and characterization of volatile air toxics indoors in a heavy polluted city of northwestern China in wintertime. *Science of The Total Environment*, 2019, vol. 662, pp. 470-480. ISSN 0048-9697.
- [158] GOODMAN, N. B. et al. Indoor volatile organic compounds at an Australian university. *Building and Environment*, 2018, vol. 135, pp. 344-351. ISSN 0360-1323.
- [159] MITRAN, E. et al. Neurotoxicity associated with occupational exposure to acetone, methyl ethyl ketone, and cyclohexanone. *Environmental Research*, 1997, vol. 73, no. 1-2, pp. 181-188. ISSN 0013-9351.
- [160] EZHILAN, M. et al. An Electronic nose for royal delicious apple quality assessment – a tri-layer approach. *Food Research International*, 2018, vol. 109, pp. 44-51. ISSN 0963-9969.
- [161] DELAHOZ, R. E. et al. Chronic lung disease secondary to ammonia inhalation injury: A report on three cases. *American Journal of Industrial Medicine*, 1996, vol. 29, no. 2, pp. 209-214. ISSN 0271-3586.
- [162] TIMMER, B. et al. Ammonia sensors and their applications—a review. *Sensors and Actuators B: Chemical*, 2005, vol. 107, no. 2, pp. 666-677. ISSN 0925-4005.
- [163] LEDUC, D. et al. Acute and long-term respiratory damage following inhalation of ammonia. *Thorax*, 1992, vol. 47, no. 9, pp. 755-757. ISSN 0040-6376.
- [164] POPA, C. et al. Ethylene and ammonia traces measurements from the patients' breath with renal failure via LPAS method. *Applied Physics B-Lasers and Optics*, 2011, vol. 105, no. 3, pp. 669-674. ISSN 0946-2171.
- [165] OBERMEIER, J. et al. Exhaled volatile substances mirror clinical conditions in pediatric chronic kidney disease. *Plos One*, 2017, vol. 12, no. 6, pp. 18. ISSN 1932-6203.
- [166] IACUMIN, L. et al. A new cause of spoilage in goose sausages. *Food Microbiology*, 2016, vol. 58, pp. 56-62. ISSN 0740-0020.
- [167] ZHANG, B. et al. Identification of beef spoilage via the analysis of volatiles using long optical-path Fourier transform infrared spectroscopy. *Analytical Methods*, 2015, vol. 7, no. 14, pp. 5891-5897. ISSN 1759-9660.
- [168] CABALLERO, A. a SEGURA, A. The quest for lower alcoholic wines. *Microbial Biotechnology*, 2017, vol. 10, no. 2, pp. 238-241. ISSN 1751-7915.
- [169] CONTRERAS, M. D. M. et al. Usefulness of GC-IMS for rapid quantitative analysis without sample treatment: Focus on ethanol, one of the potential classification markers of olive oils. *LWT*, 2020, vol. 120, pp. 108897. ISSN 0023-6438.
- [170] MITSUBAYASHI, K. et al. Bioelectronic sniffers for ethanol and acetaldehyde in breath air after drinking. *Biosensors and Bioelectronics*, 2005, vol. 20, no. 8, pp. 1573-1579. ISSN 0956-5663.
- [171] GOLDNER, M. C. et al. Effect of ethanol level in the perception of aroma attributes and the detection of volatile compounds in red wine. *Journal of Sensory Studies*, 2009, vol. 24, no. 2, pp. 243-257. ISSN 0887-8250.
- [172] GUOHUA, H. et al. Study of peach freshness predictive method based on electronic nose. *Food Control*, 2012, vol. 28, no. 1, pp. 25-32. ISSN 0956-7135.

- [173] TURNER, C. et al. A longitudinal study of ethanol and acetaldehyde in the exhaled breath of healthy volunteers using selected-ion flow-tube mass spectrometry. *Rapid Communications in Mass Spectrometry*, 2006, vol. 20, no. 1, pp. 61-68. ISSN 0951-4198.
- [174] GOERL, T. et al. Volatile breath biomarkers for patient monitoring during haemodialysis. *Journal of Breath Research*, 2013, vol. 7, no. 1, pp. 8. ISSN 1752-7155.
- [175] MATTOO, A. K. *The Plant Hormone Ethylene*. CRC Press, 2018. pp. ISBN 9781351092661.
- [176] CAPRIOLI, F. a QUERCIA, L. Ethylene detection methods in post-harvest technology: A review. *Sensors and Actuators B: Chemical*, 2014, vol. 203, pp. 187-196. ISSN 0925-4005.
- [177] HU, B. et al. Recent advances in detecting and regulating ethylene concentrations for shelf-life extension and maturity control of fruit: A review. *Trends in Food Science & Technology*, 2019, vol. 91, pp. 66-82. ISSN 0924-2244.
- [178] SARAIVA, L. A. et al. Thap Maeo bananas: Fast ripening and full ethylene perception at low doses. *Food Research International*, 2018, vol. 105, pp. 384-392. ISSN 0963-9969.
- [179] LI, Y. et al. Continuous exposure to ethylene in the storage environment adversely affects 'Afourer' mandarin fruit quality. *Food Chemistry*, 2018, vol. 242, pp. 585-590. ISSN 0308-8146.
- [180] PAARDEKOOOPER, L. M. et al. Ethylene, an early marker of systemic inflammation in humans. *Scientific Reports*, 2017, vol. 7, pp. 10. ISSN 2045-2322.
- [181] PETRUS, M. et al. Spectroscopic analysis of breath ethylene and oxidative stress relation with glycaemic status in type 2 diabetes. *Optical and Quantum Electronics*, 2016, vol. 49, no. 1, pp. 2. ISSN 1572-817X.
- [182] CRISTESCU, S. M. et al. Real-time monitoring of endogenous lipid peroxidation by exhaled ethylene in patients undergoing cardiac surgery. *American Journal of Physiology-Lung Cellular and Molecular Physiology*, 2014, vol. 307, no. 7, pp. 509-515. ISSN 1040-0605.
- [183] POPA, C. et al. The level of ethylene biomarker in the renal failure of elderly patients analyzed by photoacoustic spectroscopy. *Laser Physics*, 2013, vol. 23, no. 12, pp. 4. ISSN 1054-660X.
- [184] FENG, R. et al. Ethylene, xylene, toluene and hexane are major contributors of atmospheric ozone in Hangzhou, China, prior to the 2022 Asian Games. *Environmental Chemistry Letters*, 2019, vol. 17, no. 2, pp. 1151-1160. ISSN 1610-3653.
- [185] KELLER, N. et al. Ethylene removal and fresh product storage: a challenge at the frontiers of chemistry. toward an approach by photocatalytic oxidation. *Chemical Reviews*, 2013, vol. 113, no. 7, pp. 5029-5070. ISSN 0009-2665.
- [186] GREENBERG, M. M. The central nervous system and exposure to toluene: A risk characterization. *Environmental Research*, 1997, vol. 72, no. 1, pp. 1-7. ISSN 0013-9351.
- [187] LOCK, E. A. et al. Solvents and Parkinson disease: A systematic review of toxicological and epidemiological evidence. *Toxicology and Applied Pharmacology*, 2013, vol. 266, no. 3, pp. 345-355. ISSN 0041-008X.
- [188] FILLEY, C. M. et al. The effects of toluene on the central nervous system. *Journal of Neuropathology and Experimental Neurology*, 2004, vol. 63, no. 1, pp. 1-12. ISSN 0022-3069.
- [189] ALONSO, M. et al. Evaluation of potential breath biomarkers for active smoking: assessment of smoking habits. *Analytical and Bioanalytical Chemistry*, 2010, vol. 396, no. 8, pp. 2987-2995. ISSN 1618-2642.
- [190] LIGOR, T. et al. The analysis of healthy volunteers' exhaled breath by the use of solid-phase microextraction and GC-MS. *Journal of Breath Research*, 2008, vol. 2, no. 4, pp. 8. ISSN 1752-7155.
- [191] OSTROVERKHOVA, O. *Handbook of Organic Materials for Electronic and Photonic Devices*. Elsevier Science, 2018, ISBN 9780081022849.

- [192] ZHOU, X. J. et al. Solar paint: from synthesis to printing. *Polymers*, 2014, vol. 6, no. 11, pp. 2832-2844.
- [193] CALLISTER, W. D. *Materials science and engineering: An Introduction*. Wiley, 1997, ISBN 9780471134596.
- [194] SHARMA, S. K. et al. *Handbook of materials characterization*. Springer International Publishing, 2018, ISBN 9783319929552.
- [195] ABD MUTALIB, M. et al. Chapter 9 - Scanning electron microscopy (SEM) and energy-dispersive x-ray (EDX) spectroscopy, In *Membrane Characterization*, Elsevier, 2017, pp. 161-179.
- [196] LÜTH, H. *Solid surfaces, interfaces and thin films*. Springer Berlin Heidelberg, 2010, ISBN 9783642135927.
- [197] INKSON, B. J. 2 - Scanning electron microscopy (SEM) and transmission electron microscopy (TEM) for materials characterization. In *Materials Characterization Using Nondestructive Evaluation (NDE) Methods*. Woodhead Publishing, 2016, pp. 17-43.
- [198] SONG, L. et al. Sr-doped cubic In₂O₃/Rhombohedral In₂O₃ homojunction nanowires for highly sensitive and selective breath ethanol sensing: experiment and dft simulation studies. *ACS Applied Materials & Interfaces*, 2020, vol. 12, no. 1, pp. 1270-1279. ISSN 1944-8244.
- [199] VOIGTLÄNDER, B. *Scanning probe microscopy: atomic force microscopy and scanning tunneling microscopy*. Springer Berlin Heidelberg, 2015, ISBN 9783662452400.
- [200] LTD., N. N. Benefits of atomic force microscopy (AFM). *AZoNano*, 2020, vol. 0.
- [201] VAN DER HEIDE, P. *X-ray photoelectron spectroscopy: an introduction to principles and practices*. Wiley, 2011, ISBN 9781118162903.
- [202] WAGNER, J. M. *X-ray photoelectron spectroscopy*. Nova Science Publishers, 2011, ISBN 9781617282409.
- [203] LIN-VIEN, D. *The handbook of infrared and raman characteristic frequencies of organic molecules*. Academic Press, 1991, ISBN 9780124511606.
- [204] LARKIN, P. *Infrared and raman spectroscopy: principles and spectral interpretation*. Elsevier Science, 2011, ISBN 9780123870186.
- [205] STEVIE, F. *Secondary ion mass spectrometry: applications for depth profiling and surface characterization*. Momentum Press, 2015, ISBN 9781606505892.
- [206] MATATAGUI, D. et al. Acoustic sensors based on amino-functionalized nanoparticles to detect volatile organic solvents. *Sensors*, 2017, vol. 17, no. 11, pp. 9. ISSN 1424-8220.
- [207] [online]. [cit. Available from: <laurell.com/literature/brochures/WS-650-23NPP-spin-coater-brochure.pdf>].
- [208] MATATAGUI, D. et al. Portable low-cost electronic nose based on surface acoustic wave sensors for the detection of BTX vapors in air. *Sensors*, 2019, vol. 19, no. 24, pp. 5406. ISSN 1424-8220.
- [209] FRAGOSO-MORA, J. R. et al. Gas sensors based on elasticity changes of nanoparticle layers. *Sensors and Actuators B: Chemical*, 2018, vol. 268, pp. 93-99. ISSN 0925-4005.
- [210] ŠETKA, M. et al. Nanostructured polypyrrole-based ammonia and volatile organic compound sensors. *Sensors*, 2017, vol. 17, no. 3, pp. 28.
- [211] SETKA, M. et al. Raman and XPS studies of ammonia sensitive polypyrrole nanorods and nanoparticles. *Scientific Reports*, 2019, vol. 9, pp. 10. ISSN 2045-2322.
- [212] ŠETKA, M. et al. Gold/polypyrrole nanorods for gas sensing application. *Proceedings of SPIE - The International Society for Optical Engineering*. Barcelona, Spain: Smart Sensors, Actuators, and MEMS VIII, 2018, vol. 10246.

- [213] ŠETKA, M. et al. Love wave sensors based on gold nanoparticle-modified polypyrrole and their properties to ammonia and ethylene. *Sensors and Actuators B: Chemical*, 2019, vol. 304, pp. 127337. ISSN 0925-4005.
- [214] ŠETKA, M. et al. Love wave sensors with silver modified polypyrrole nanoparticles for VOCs monitoring. *Sensors*, 2020, vol. 20, no. 5, pp. 1432. ISSN 1424-8220.
- [215] LIU, W. et al. A highly sensitive and moisture-resistant gas sensor for diabetes diagnosis with Pt@In₂O₃ nanowires and a molecular sieve for protection. *Npg Asia Materials*, 2018, vol. 10, pp. 293-308. ISSN 1884-4049.
- [216] CLAROS, M. et al. AACVD Synthesis and Characterization of Iron and Copper Oxides Modified ZnO Structured Films. *Nanomaterials*, 2020, vol. 10, no. 3, pp. 16.

List of publications

Journal Articles

1. **Šetka, M.**, Bahos, A.F., Chmela, O., Matatagui, D., Gràcia, I., Drbohlavová, J., Vallejos, S., Cadmium telluride/polypyrrole nanocomposite based Love wave sensors highly sensitive to acetone at room temperature. (under review in the Sensors and Actuators B: Chemical)
2. **Šetka, M.**, Bahos, F.A., Matatagui, D., Gràcia, I., Figueras, E., Drbohlavová, J., Vallejos, S., Love wave sensors with silver modified polypyrrole nanoparticles for VOCs monitoring, *Sensors*, 20, 2020, doi:10.3390/s20051432.
3. Claros, M., **Šetka, M.**, Jimenez, Y., Vallejos, S., AACVD synthesis and characterization of iron and copper oxides modified ZnO structured films, *Nanomaterials*, 10, 3, 2020, doi: 10.3390/nano10030471.
4. **Šetka, M.**, Bahos, F.A., Matatagui, D., Potoček, M., Kral, Z., Drbohlavová, J., Gràcia, I., Vallejos, S., Love wave sensors based on gold nanoparticle-modified polypyrrole and their properties to ammonia and ethylene. *Sensors and Actuators B: Chemical*, 304, 2019, doi:10.1016/j.snb.2019.127337.
5. **Šetka, M.**, Calavia, R., Vojkuvka, L., Llobet, E., Drbohlavova, J., Vallejos, S., Raman and XPS studies of ammonia sensitive polypyrrole nanorods and nanoparticles, *Scientific Reports*, 9, 2019, doi: 10.1038/s41598-019-44900-1.
6. Tomić, M., **Šetka, M.**, Chmela, O., Gràcia, I., Figueras, E., Cané, C., Vallejos, S., Cerium oxide-tungsten oxide core-shell nanowire-based microsensors sensitive to acetone, *Biosensors*, 8, 4, 2018, doi: 10.3390/bios8040116
7. **Šetka, M.**, Drbohlavová, J., Hubálek, J., Nanostructured polypyrrole-based ammonia and volatile organic compound sensors, *Sensors*, 17, 2017, doi: 10.3390/s17030562.

Conference Articles

1. **Šetka M.**, Calavia, R., Vojkuvka, L., Polčák, J., Llobet, E., Jana, D., Vallejos, S., Electrochemically deposited polypyrrole nanorods and study of their ammonia sensing properties, *Materials Today: Proceedings* 20, 2020, doi: 10.1016/j.matpr.2019.10.067.
2. **Šetka, M.**, Bahos, F.A., Matatagui, D., Kral, Z., Gràcia, I., Drbohlavová, J., Vallejos, S., Polypyrrole based love-wave gas sensor devices with enhanced properties to ammonia, *Proceedings*, 2, 2018, doi: 10.3390/proceedings2130786.
3. **Šetka, M.**, Drbohlavová, J., Vallejos, S., Márik, M., Llobet, E., Hubálek, J., Gold/polypyrrole nanorods for gas sensing application, *Proceedings of SPIE (Smart Sensors, Actuators, and MEMS VIII)*, 2017, doi: 10.1117/12.2265565.

Appendix A

Polypyrrole nanoparticles as chemo-resistive sensors

Polypyrrole nanoparticles based chemo-resistive sensors

1 Experimental

1.1 Fabrication of sensors

In this thesis, three chemo-resistive sensors based on PPy NPs and modified PPy with Au NPs (Au/PPy) and Ag NPs (Ag/PPy) were developed. The Au interdigital electrodes were integrated with the micro sensors platforms, and they were covered by the PPy based sensitive layers using spin coating technique. The velocity of spin coating was 4000 rpm.

1.2 Characterization of sensors

The sensors were tested in a continuous flow test chamber provided with mass flow controllers that allow the mixture of dry air and calibrated gaseous analyte (ethanol purchased from Praxair) to obtain the concentration of 80 ppm. The dc resistance measurements of the microsensor were achieved in a system provided with an electrometer (Keithley 6517A, Cleveland, OH, USA) and a multimeter (Keithley 2700, Cleveland, OH, USA) with switch system to monitor various sensors simultaneously. More details of the characterization systems were reported elsewhere [1]. The response of sensors is presented as R_a/R_g , where R_a and R_g is resistance in air and gas, respectively.

2 Results

The PPy chemo-resistive sensors showed the resistance higher than tens of $G\Omega$. The used characterization system was not able to record this high resistance. Therefore, the response of those sensors to ethanol was not measurable (see **Figure 1**).

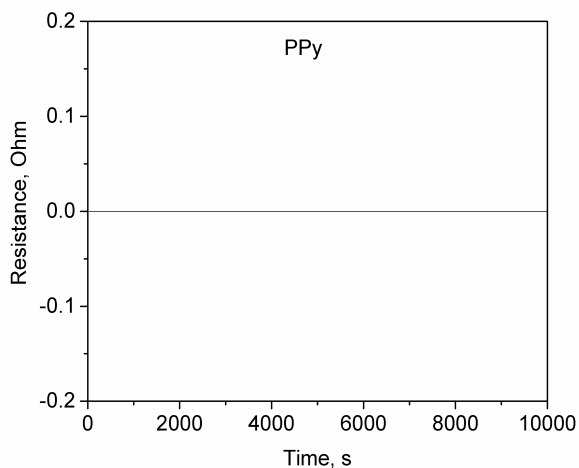


Figure 1: The response of PPy chemo-resistive sensor to 80 ppm of ethanol.

The Au/PPy sensors showed slightly lower resistance compared to PPy sensors. The sensors response to 80 ppm of ethanol was 1.6 and it is shown in **Figure 2**.

The Ag/PPy chemoresistive sensors showed oscillations in the resistance and similarly to PPy sensors, their response to ethanol was not clearly registered (see **Figure 3**).

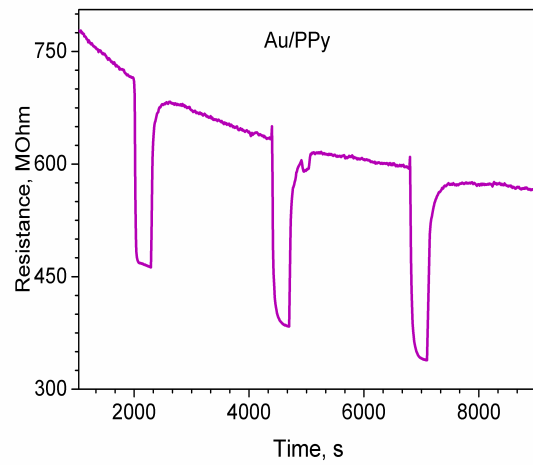


Figure 2: The response of Au/PPy chemo-resistive sensor to 80 ppm of ethanol.

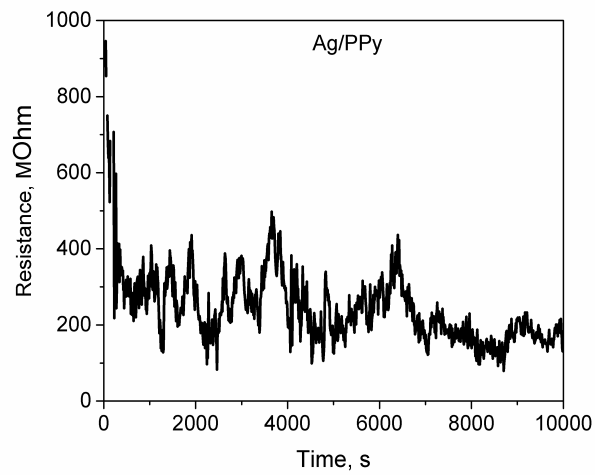


Figure 3: The response of Ag/PPy chemo-resistive sensor to 80 ppm of ethanol.

References

- [1] VALLEJOS, S. et al. Chemoresistive micromachined gas sensors based on functionalized metal oxide nanowires: Performance and reliability. *Sensors and Actuators B: Chemical*, 2016, vol. 235, pp. 525-534. ISSN 0925-4005.

Appendix B

Other collaborative journal papers

Article

AACVD Synthesis and Characterization of Iron and Copper Oxides Modified ZnO Structured Films

Martha Claros ^{1,*} , Milena Setka ¹, Yecid P. Jimenez ² and Stella Vallejos ^{1,3}

¹ CEITEC—Central European Institute of Technology, Brno University of Technology, 61200 Brno, Czech Republic; Milena.Setka@ceitec.vutbr.cz (M.S.); stella.vallejos@imb-cnm.csic.es (S.V.)

² Departamento de Ingeniería Química y Procesos de Minerales, Facultad de Ingeniería, Universidad de Antofagasta, 1270300 Antofagasta, Chile; yecid.jimenez@uantof.cl

³ Instituto de Microelectrónica de Barcelona (IMB-CNM, CSIC), Campus UAB, 08193 Cerdanyola del Vallès, Barcelona, Spain

* Correspondence: martha.claros@ceitec.vutbr.cz

Received: 17 January 2020; Accepted: 3 March 2020; Published: 5 March 2020



Abstract: Non-modified (ZnO) and modified (Fe₂O₃@ZnO and CuO@ZnO) structured films are deposited via aerosol assisted chemical vapor deposition. The surface modification of ZnO with iron or copper oxides is achieved in a second aerosol assisted chemical vapor deposition step and the characterization of morphology, structure, and surface of these new structured films is discussed. X-ray photoelectron spectrometry and X-ray diffraction corroborate the formation of ZnO, Fe₂O₃, and CuO and the electron microscopy images show the morphological and crystalline characteristics of these structured films. Static water contact angle measurements for these structured films indicate hydrophobic behavior with the modified structures showing higher contact angles compared to the non-modified films. Overall, results show that the modification of ZnO with iron or copper oxides enhances the hydrophobic behavior of the surface, increasing the contact angle of the water drops at the non-modified ZnO structures from 122° to 135° and 145° for Fe₂O₃@ZnO and CuO@ZnO, respectively. This is attributed to the different surface properties of the films including the morphology and chemical composition.

Keywords: AACVD; zinc oxide; iron oxide; copper oxide; structured films; water contact angle

1. Introduction

Zinc oxide (ZnO) is a well-known n-type semiconducting material that possesses a wide band gap (3.37 eV) and large exciton binding energy (60 meV), hence its relevance in optoelectronics, photonics, and semiconducting devices [1]. Additionally, the tunable wetting properties of ZnO [2] has proved also attractive in the field of smart surfaces (e.g., self-cleaning surfaces for windows, solar cells, automobile windshields), micro/nano-fluidic systems, and sensors among others [3–5].

Overall, the aforementioned usages are strongly dependent on the chemical and physical properties of ZnO. Thus, according to the targeted application, transition metals (e.g., Mn, Co, Fe, Cu) and transition metal oxides (e.g., Cu_xO_x, Co_xO_x, Fe_xO_x) have been introduced as second-phase modifier materials in ZnO films to tune its electrical, optical and magnetic properties [4,6–9]. Similarly, the modification of ZnO with organic agents such as octadecylphosphonic acid (ODP) or alkanolic acids, as well as inorganic metal oxides such as cuprous oxide (Cu₂O), has also been explored to improve its wettability [10–13] and sensing properties [14,15]. Hence, there is continuous interest in establishing new synthetic routes that allow tuning the properties of ZnO by the incorporation of second-phase materials.

Previously, several synthesis techniques have been employed to prepare non-modified and modified ZnO films with second-phase materials. Solution-based routes such as hydrothermal synthesis, sol-gel method, and chemical coprecipitation are among the most common procedures [16,17]. However, the integration of the materials synthesized by these techniques with silicon-based microfabrication processes (e.g., for electronics, sensors or microfluidics systems), is challenging and generally presents scalability issues. In contrast, chemical vapor deposition routes, including aerosol assisted chemical vapor deposition (AACVD), are good candidates to overcome this drawback, as these techniques are scalable and industrially attractive in silicon-based microfabrication processes. In particular, AACVD works at atmospheric pressure; therefore, the rates of deposition are typically magnitudes of orders higher than low-pressure processes, which impacts directly on the energy input required per gram of product. Moreover, AACVD is versatile and low-cost process, that allows the deposition of both thin films and micro/nanostructures via vapor-solid mechanism at moderated temperatures on different substrates [18,19]. A great variety of solvent precursor mixtures can be employed to change the morphology and size of the structures, since there is no need for the precursor to be volatile as in a regular CVD process [20]. At the same time, the process enables the modification of structures or thin films with second-phase materials in one or more subsequent steps [19,21,22].

AACVD has enabled previously the formation of ZnO structures via vapor-solid mechanism. Furthermore, it has been demonstrated that different ZnO morphologies (e.g., rods, needles, pyramids) may be deposited by simple changes in the AACVD operational parameters [5,18]. These morphological and therefore surface chemistry changes have shown to enhance properties such as wettability and gas sensing [5], hence the interest in tuning further the properties of AACVD ZnO structures and investigating its properties when modified with other metal oxides.

Therefore, here, it is presented the synthesis of ZnO structured films and their subsequent surface modification with Fe₂O₃ or CuO by AACVD. This work also evaluates and discusses the possible routes for AACVD deposition of Fe₂O₃ or CuO, as well as the morphological, chemical, and wetting properties of the synthesized structured films before and after surface modification.

2. Materials and Methods

2.1. Chemicals

Zinc (II) chloride of analytical grade (purity ≥ 0.98 in mass fraction) was purchased from Merck (KGaA, Darmstadt, Germany). Copper (II) nitrate hexahydrate and iron (III) chloride hexahydrate with a purity of >0.985 and >0.999 (mass fraction), respectively, were purchased from Sigma-Aldrich (GmbH, Albu, Germany). Ethanol and acetone with purity > 0.999 (mass fraction) were purchased from Penta Chemicals (Prague, Czech Republic). All the reagents were used without further purification.

2.2. AACVD Synthesis

The AACVD synthesis was carried out in a horizontal hot-walled reactor, using nitrogen flow (Linde, oxygen free) and piezoelectric ultrasonic atomizer (Liquifog, Johnson Matthey, Redwitz, Germany).

Columnar zinc oxide (ZnO) structures were obtained via AACVD following the procedure presented before by Vallejos et al. [23]. Briefly, zinc chloride (50 mg) was dissolved in 5 mL of ethanol. The solution was converted into fine aerosol with the aid of the ultrasonic atomizer operating at 16 MHz. The aerosol formed was transferred by a nitrogen flow of $200 \text{ cm}^3 \cdot \text{min}^{-1}$ into the hot-wall AACVD reactor, which remained at a constant temperature of 723.15 K. The time to transport completely the solution into the reactor was typically 45 min. Silicon wafers were cut in pieces of $1 \times 1 \text{ cm}$ and used as substrates. For all the experiments, the substrates were cleaned thoroughly with plenty-deionized water and sonicated for 5 min in isopropanol. Then, the substrates were dried under nitrogen flow before placing them into the reactor.

The AACVD ZnO structures were modified with iron and copper oxides in a second step deposition. The conditions for the AACVD of iron and copper oxide were chosen by performing

a systematic study of several parameters, including different solvents (acetone, methanol, ethanol) and temperatures (from 673.15 to 773.15 K). Hereafter, the optimized AACVD conditions used in this work are described. For the deposition of iron oxide, a solution of 3 mg of $\text{FeCl}_3 \cdot 6\text{H}_2\text{O}$ dissolved in 3 mL of acetone was prepared. This solution was placed in the aerosol generator and the mist was conducted by the nitrogen flow previously established to the reactor heated at a constant temperature of 723.15 K. The deposition lasted for 10 min until all the solution was completely consumed. Similar procedure was followed for the deposition of copper oxide. Typically, 3 mg of $\text{Cu}(\text{NO}_3)_2 \cdot 6\text{H}_2\text{O}$ was dissolved in 3 mL of ethanol and placed in the aerosol generator. The temperature of the reactor was set at 723.15 K and the deposition lasted 25 min until all the solution was completely consumed. All the solutions were prepared only a few minutes prior to the synthesis.

2.3. Characterization

The morphology of the obtained nanostructures was observed by scanning electron microscopy (SEM, Tescan FE Mira II LMU, Brno, Czech Republic). A solid-state EDX detector (Bruker AXS, Inc., AZtec software package released by Oxford Instruments, Abingdon, UK) installed on the SEM performed the elemental line scans and mapping. TEM images were obtained with a scanning transmission electron microscopy (FEI Tecnai F20, 200 kV, Hillsboro, OR, USA) after removing the structures from the substrate and redeposit them on Cu grids. X-ray diffraction measurements were performed with a Bruker-AXS (LinxEye XE-T detector, KFL Cu 2K, λ ($\text{CuK}\alpha$) = 1.541840 Å, Karlsruhe, Germany) operated at 40 KV and 40 mA. X-ray photoelectron spectroscopy (Kratos Axis Supra with monochromatic Al $\text{K}\alpha$ X-ray radiation, emission current of 15 mA and hybrid lens mode, Manchester, UK) was used for the analysis of the surface. Wide and narrow spectra were measured with pass energy of 80 eV and 20 eV, respectively. XPS spectra were analyzed using CasaXPS software version 2.3.22. All spectra were calibrated using C 1s peaks with a fixed value of 284.7 eV. The Shirley algorithm was used to establish the background of the spectra and the Gaussian–Lorentzian (GL) line shape was used to fit the XPS peaks. The Gibbs free energy for the proposed reactions were calculated by HSC chemistry 6 software (Outokumpu Research Oy, Pori, Finland).

Static water contact angle measurements were performed in a contact-angle measurement station (SEO Phoenix 300, Suwon City, Korea), with an automatic software controlled demi-water drop volume, set at 5 μL for each measure. The sample surfaces were gently cleaned with nitrogen flow before each measurement. Samples were tested in three different points, and the results presented here are an average of the three measures, each with 20 high-speed photographs. The static contact angle of the bare silicon substrates was examined before the AACVD of films. These tests registered a low water contact angle (52°) for the silicon surface. The drop photographs were acquired by a high-speed camera (Firewire digital camera) and the contact angles were analyzed by Surface-ware 8 contact angle analyzer software (Suwon City, Korea).

3. Results and Discussion

3.1. Zinc Oxide Films

The columnar ZnO structures deposited by AACVD are depicted in Figure 1a,b. SEM images indicate that the obtained structures have a well-defined rod-like morphology with spear-shape ending. The average length of the roads was of $\sim 1.2 \mu\text{m}$ and a mid-height diameter of $\sim 80 \text{ nm}$, the base of the structures is $\sim 300 \text{ nm}$, whereas the smallest diameter at the top is $\sim 22 \text{ nm}$. After the ZnO deposition, the silicon substrates presented a homogeneous grey to white opaque color, in contrast to the silver shining bare silicon substrate. The measured static water contact angle for the pure ZnO film was registered as 122° (see Figure 1c).

The chemical composition of the deposited products was analyzed by EDX and XPS. The EDX analysis indicated that the resulted nanostructures were composed by zinc and oxygen as major

components; additionally, the presence of chlorine was detected as a product of unreacted precursor (0.9 wt.%).

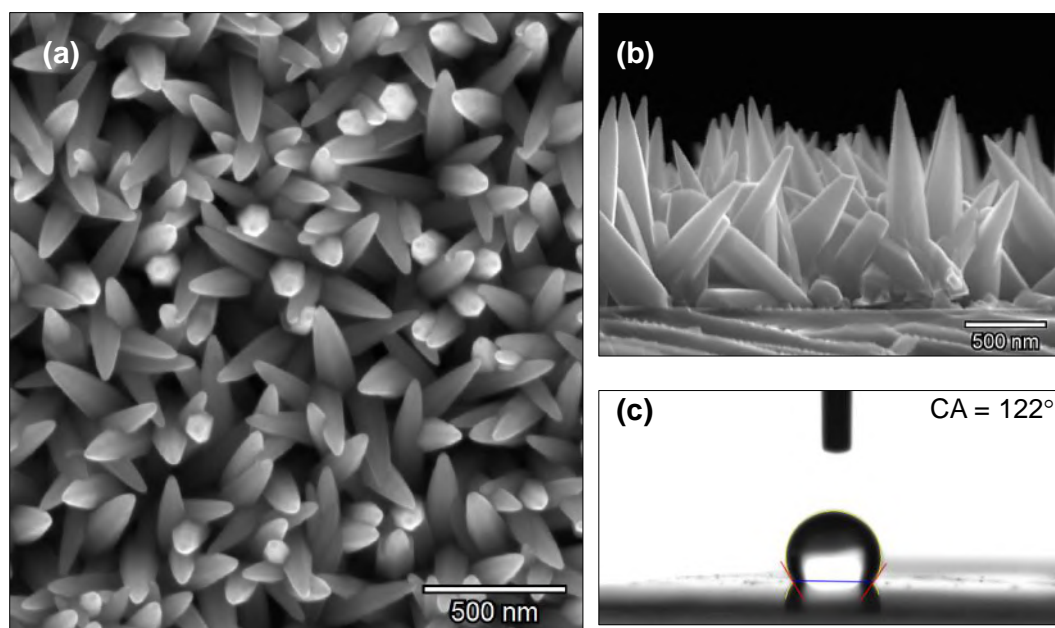


Figure 1. SEM images of the zinc oxide structures synthesized by AACVD on silicon substrate (a) top view; (b) cross section and (c) static water contact angle measurement.

Further studies of the ZnO deposited structures by XPS analysis in Figure 2a shows the characteristic Zn 2p doublet peaks corresponding to Zn²⁺ oxidation state [17,23,24]. The components centered at binding energies (BE) of 1021.8 eV and 1044.9 eV correspond to Zn 2p_{3/2} and 2p_{1/2}, respectively, while a shake-up is located at 1040.2 eV. These Zn 2p_{3/2} and 2p_{1/2} core level binding energies are slightly shifted compared to other reports [17,23–27], however, the separation between them is constant and equals to 23 eV, in agreement with the literature as shown in Table 1.

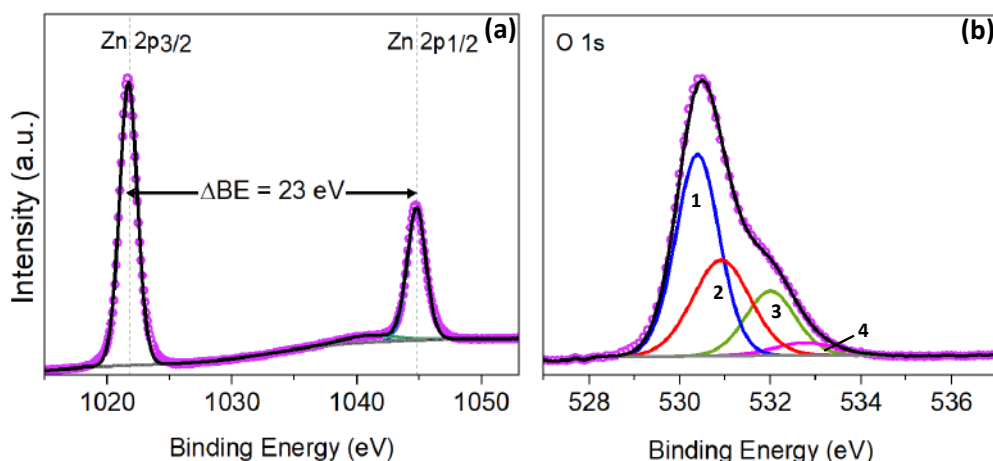


Figure 2. (a) Zn 2p and (b) O 1s core level XPS spectra of the non-modified ZnO films. Pink hollow dots show the XPS raw data, the black solid line corresponds to the envelope-fitting curve, and the colored solid lines to the components.

The XPS spectrum of the O 1s region present an asymmetric peak, indicating the presence of different oxygen species. The curve was fitted to four distinctively GL components (1, 2, 3 and 4, as shown in Figure 2b). The peak 1 centered at 530.4 eV is attributed to O²⁻ ions in the Zn-O bonding

of the wurtzite structure of Zn^{2+} [17,28,29], whereas the peak 2 situated at 530.9 eV is assigned to O^{2-} state of oxygen defects or vacancies, supporting the formation of the non-stoichiometric ZnO. Finally, the peaks 3 and 4 at 532.0 eV and 532.8 eV, respectively, are typically related to weak bonds of oxygen on the surface, such as OH groups [29–31].

Table 1. Comparative table showing the Zn $2p_{3/2}$ and Zn $2p_{1/2}$ binding energy values from the literature.

| Structure Type | Size (nm) | Binding Energy Zn $2p_{3/2}$ (eV) | Binding Energy Zn $2p_{1/2}$ (eV) | Zn $2p_{1/2}$ -Zn $2p_{3/2}$ Splitting (eV) | Ref |
|-----------------|----------------------|-----------------------------------|-----------------------------------|---|-----------|
| Nanoparticle | ~30 | 1020.7 | 1043.7 | 23.0 | [17] |
| Nanoflowers | 100–250 ^a | 1020.8 | 1043.8 | 23.0 | [17] |
| Nanorods | 45–96 ^b | 1021.2 | 1044.2 | 23.0 | [17] |
| Nanosheets | 10 ^c | 1022.0 | 1045.0 | 23.0 | [25] |
| Nanoplates | 10–15 ^c | 1021.1 | NR | NR | [24] |
| Rods | ~380 ^b | 1022.0 | 1045.0 | 23.0 | [23] |
| Bulk film | NR | 1021.0 | 1044.1 | 23.1 | [26] |
| Bulk film | NR | 1022.0 | 1045.0 | 23.0 | [27] |
| Spear-like rods | ~80 ^d | 1021.8 | 1044.8 | 23.0 | This work |

^a Tip-base relation; ^b Diameter; ^c Thickness; ^d Mid-height diameter, NR: not reported.

3.2. Iron Modified Zinc Oxide Films

The ZnO structures modified with iron oxide are depicted in Figure 3a,b. These SEM images show the morphology of the ZnO structured film and the iron oxide deposited in the second deposition step. The cross-section SEM image in Figure 3b displays the irregular iron oxide layer of aggregated particles with sharp edges, resembling a nanoflake-like morphology. The total thickness of these structures formed over the ZnO rods is about 200 nm. This corresponds with the thickness measured for an AACVD deposited iron oxide on bare silicon substrate. The static water contact angle of these samples is 135° as displayed in Figure 3c.

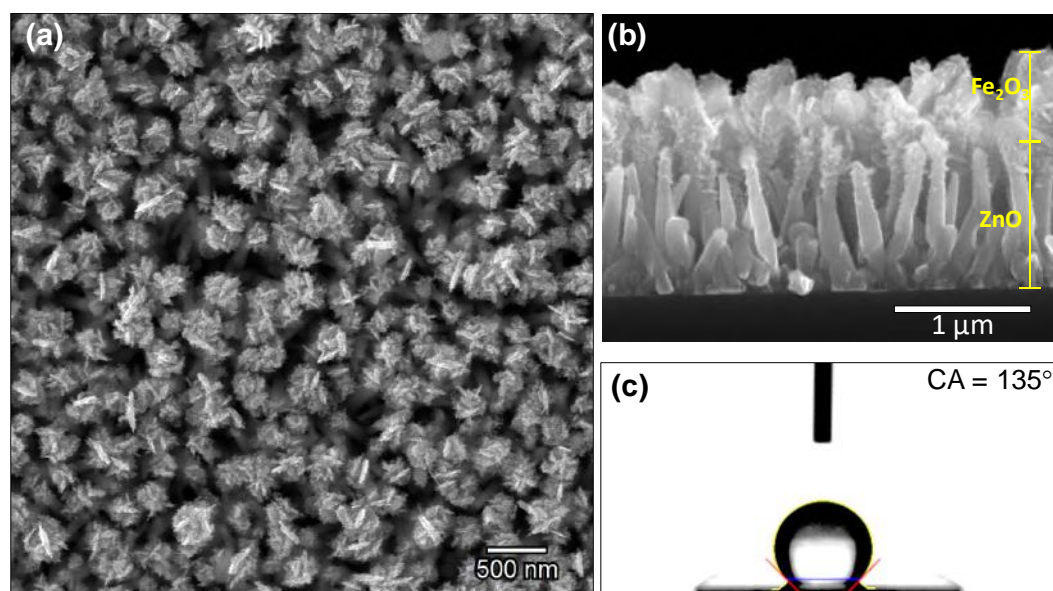


Figure 3. SEM images of $\text{Fe}_2\text{O}_3@ZnO$ structures (a) top view; (b) cross section and (c) static water angle measurement.

The XRD diffraction pattern of the $\text{Fe}_2\text{O}_3@ZnO$ nanostructured surfaces is displayed in Figure 4. The pattern shows the presence of a hexagonal ZnO phase, with a high intensity peak at $34.4^\circ 2\theta$, that indicate a preferred orientation in the (002) direction (P63mc space group, ICDD card No. 50664); this

is in good agreement with our previous results for bare ZnO deposited via AACVD [23]. In addition, the pattern indicates the presence of three other phases, represented by diffractions with less intensity as they may be related to smaller amounts of particles compared to the ZnO. Thus, the (222) plane of the cubic Fe_2O_3 (Ia-3 space group, ICSD Card No. 108905) is visible at $33.0^\circ 2\theta$, in agreement with previous Fe_2O_3 structures deposited by AACVD [32]. The patterns also suggest the presence of other planes related to cubic $\text{Fe}_2\text{O}_4\text{Zn}$ (Fd-3m space group, ICSD Card No. 91940) and rhombohedral ZnSiO_3 (R-3 space group, ICSD Card No. 340575) most likely present at the interfaces of $\text{Fe}_2\text{O}_3/\text{ZnO}$ and ZnO/Si (from substrate), respectively.

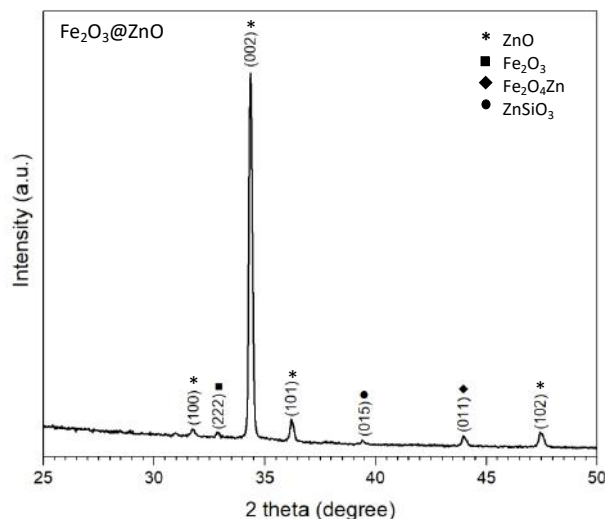


Figure 4. XRD diffraction pattern of the $\text{Fe}_2\text{O}_3@\text{ZnO}$ films.

The structured films were also analysed by TEM after the deposition of iron oxide over the zinc oxide structures (Figure 5a). The TEM images reveal the zinc oxide rod surface, covered by agglomerated iron oxide particles. The HRTEM image of this particle displays well-ordered atomic array (Figure 5b) with the planar spacing of 0.26 nm approximately; this is consistent with the (002) internal lattice spacing of the hexagonal ZnO, also found in the XRD diffraction pattern ($d = 0.2602$ nm, ICSD card No. 50664). The HRTEM image also shows the presence of a second phase with a planar spacing of approximately 0.28 nm, that is in agreement with the internal lattice spacing of the (222) plane of the cubic phase of Fe_2O_3 ($d = 0.271$ nm, ICSD card No. 108905) identified in the XRD pattern shown above.

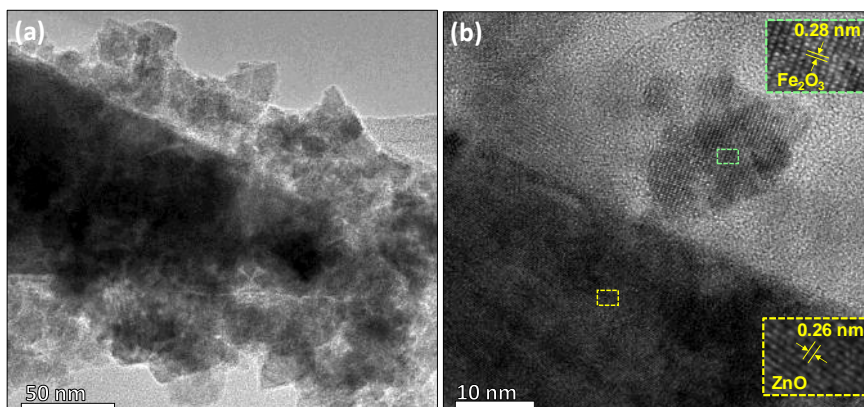


Figure 5. (a) Low and (b) high resolution TEM image for the $\text{Fe}_2\text{O}_3@\text{ZnO}$ structures. The insets display the plane spacing of Fe_2O_3 and ZnO. The colour code corresponds to the areas indicated in the TEM image from which the insets were taken.

To determine the surface chemical composition, EDX analysis was performed. This analysis showed as a result zinc and iron as major components, as well as the presence of chlorine traces (0.8 wt.%), which might be related to unreacted precursor from zinc and/or iron during deposition.

Detailed chemical composition was studied by XPS analysis. The Zn 2p core level spectrum is depicted in Figure 6a. As seen above for the non-modified ZnO structures (Figure 2a), the characteristic Zn 2p doublet is also present, although it shows a slight shift to higher binding energies. Thus, the Zn 2p core level peaks appear at 1021.9 eV for Zn 2p_{3/2} and 1045.1 eV for Zn 2p_{1/2}, the separation between both peaks is equals to 23.1 eV, in agreement with the literature [26] and the results shown for the bare ZnO.

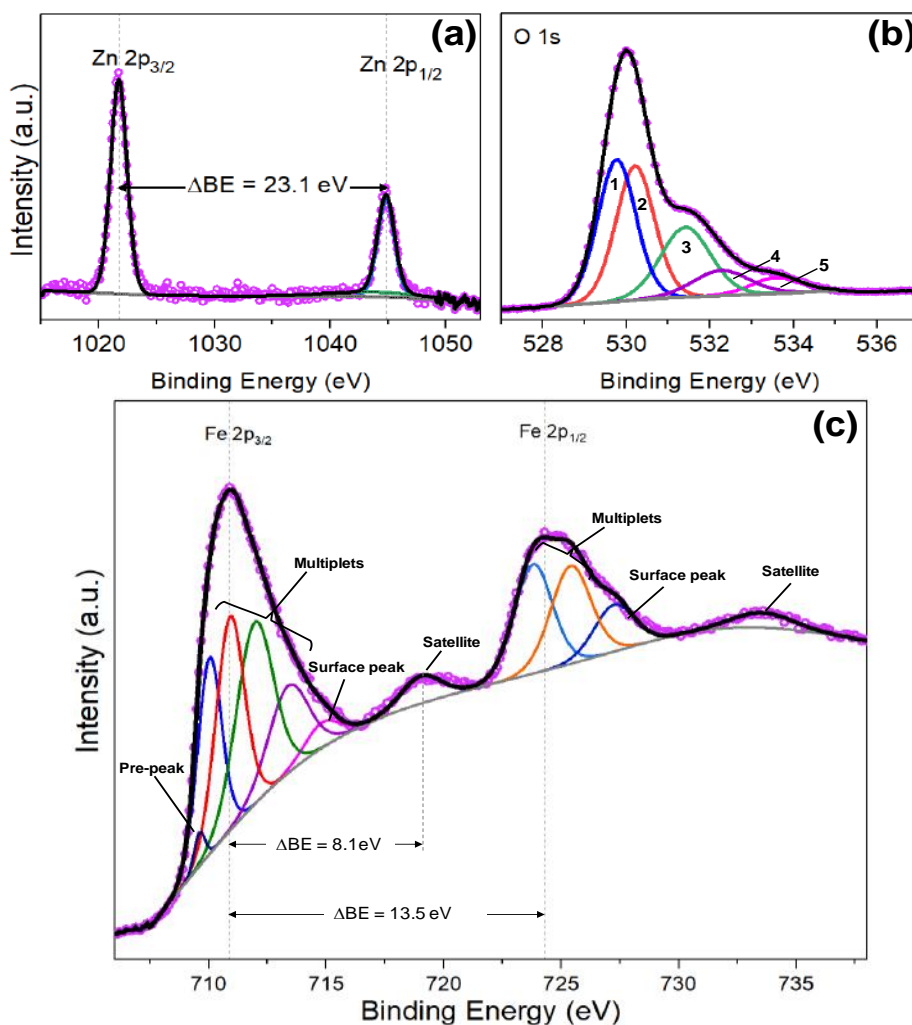


Figure 6. (a) Zn 2p, (b) O1s and (c) Fe 2p core levels XPS spectra of the Fe₂O₃@ZnO films. Pink hollow dots represent the raw data, the black solid line corresponds to the envelope/fitting curve, and the colored curves to the deconvoluted components.

The O 1s and Fe 2p core level spectra are depicted in Figure 6b,c, respectively. An asymmetric peak is observed for O 1s spectrum, and after deconvolution, five GL components are determined. Peaks 1 at 529.7 eV and peak 2 at 530.1 eV are usually related to the O²⁻ bonding with metals [17], i.e., Fe-O and Zn-O for the present study, whereas peak 3 at 531.4 eV is associated with the oxygen vacancies as noticed above for the non-modified ZnO structures. Peak 4 situated at 532.5 eV is connected with the contribution of surface OH groups and possible Zn-Fe-O bond [33], and peak 5 at 533.6 eV is associated with the presence of iron oxide-hydroxide (FeO(OH)) and H₂O adsorbed in the surface of the nanostructures, as reported in literature [34–36].

The Fe 2p core level spectrum shown in Figure 6c, contains two main peaks at 710.8 and 724.4 eV corresponding to Fe 2p_{3/2} and Fe 2p_{1/2}, respectively and two satellite peaks at 718.9 eV and 733.4 eV. The difference binding energy between Fe 2p_{3/2} and Fe 2p_{1/2} peaks is 13.5 eV, which results from spin-orbit (j-j) coupling and is in accordance with literature values [31,37]. The Fe 2p_{3/2} peak was deconvoluted and fitted to six GL peaks. The distribution of these peaks show a characteristic pre-peak at 709.6 eV, followed by multiple splitting of the four peaks and finally a surface peak at 714.8 eV, which is consistent with the data found in literature for the Fe³⁺ ion oxidation state [35,38], and rules out the presence of Fe²⁺ species. This is also corroborated by the satellite peak typically associated with Fe₂O₃, which is located at a higher binding energy (8.1 eV) than the main Fe 2p_{3/2} peak, as reported previously in literature (8 eV) [35–40].

3.3. Copper Modified Zinc Oxide Films

Figure 7a,b, show the SEM images of the Cu-modified ZnO structures. These images show the copper oxide deposited as spherical-like particles (as shown in Figure 7b) that tend to aggregate on the top of the columnar ZnO structures and disperse evenly along their side walls. The contact angle determined for these films is 145° as displayed in Figure 7c.

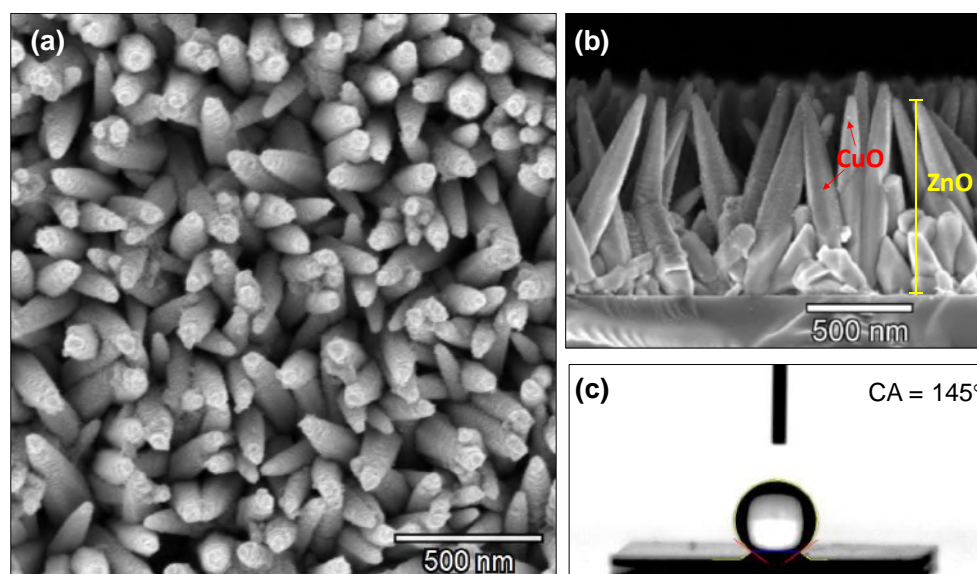


Figure 7. SEM images of CuO@ZnO structures (a) top view; (b) cross section and (c) static water contact angle.

The XRD diffraction pattern of the CuO@ZnO films is presented in Figure 8. Similar to previous case (i.e., Fe₂O₃@ZnO), the pattern shows intense diffraction peaks that correspond to the hexagonal zinc oxide phase and indicate a preferential orientation in the (002) plane. In addition, the pattern shows three other phases. The first connected with the monoclinic copper (II) oxide phase (C12/c1 space group, ICSD Card No. 160630) in which the (200) plane and (202) plane are observed, the later overlapped with the (102) plane of hexagonal ZnO. The second and third attributed to the cubic ZnCuO (0.85/0.15/1) compound (Fm-3m space group, ICSD Card No. 181023) and the ZnSiO₃ (R-3 space group, ICSD Card No. 340575), as in previous case, most likely present at the interfaces of CuO/ZnO and ZnO/Si (from substrate), respectively.

To get better insight into the structures formed by AACVD, TEM images were carried out. Figure 9, shows the columnar zinc oxide structure covered by the copper oxide particles. As can be seen, the particles with spherical morphologies are well-distributed over the rod surface. The size of the particles is between 8 and 20 nm (recorded for a total population 25 particles). The HRTEM images show a well-ordered planar atomic array with planar spacing of approximately 0.26 nm and 0.23 nm.

The first corresponds to the internal lattice spacing of the (0020) plane of the hexagonal ZnO phase ($d = 0.2602$ nm, ICSD card No. 50664) identified by XRD, whereas the second is associated to the (200) plane of the monoclinic CuO phase ($d = 0.2362$ nm, ICSD Card No. 160630), also determined in the XRD analysis.

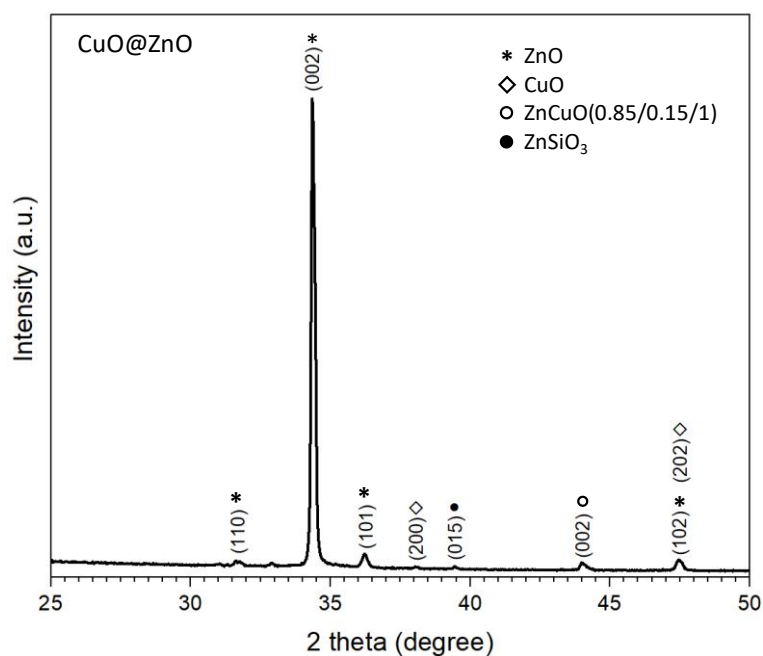


Figure 8. XRD diffraction pattern of the CuO@ZnO films.

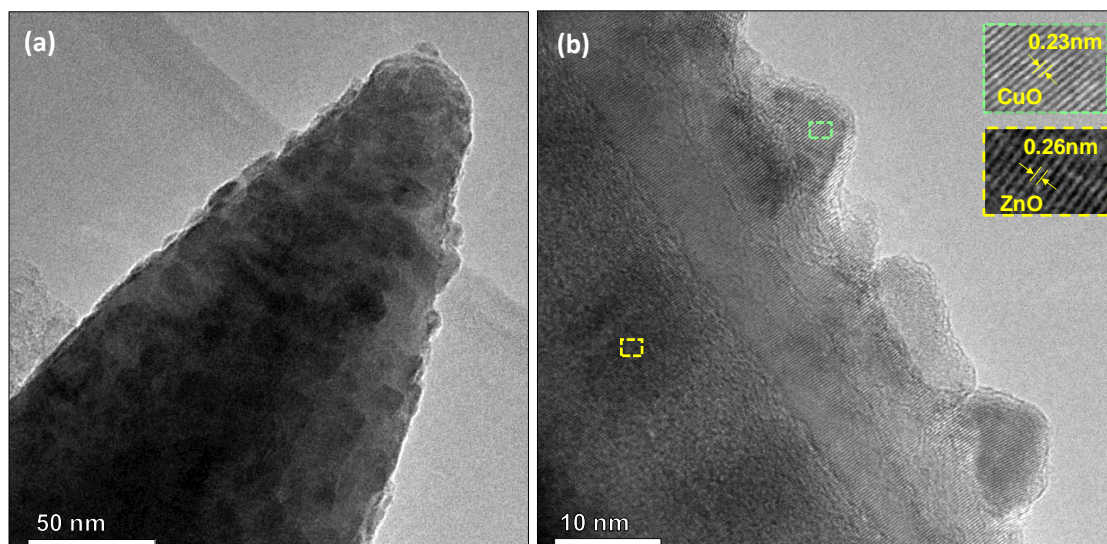


Figure 9. (a) Low and (b) high resolution TEM images for the copper oxide modified zinc oxide rods. The insets display the plane spacing of CuO and ZnO. The colour code corresponds to the areas indicated in the TEM image from which the insets were taken.

The chemical composition of the film was first evaluated by EDX analysis. This analysis revealed the presence of copper along with zinc as the major component. Similar to the previous cases, for ZnO and Fe_2O_3 @ZnO, chlorine traces (0.7 wt.%) were also detected.

A more detailed chemical composition was performed by XPS analysis. The XPS spectrum for the Zn 2p is shown in Figure 10a. The Zn 2p characteristic doublet peaks are slightly shifted to higher

binding energies (1021.9 eV for Zn 2p_{3/2} and 1045.0 eV for Zn 2p_{1/2}) as compared to the Zn 2p peaks in the bare ZnO (Figure 2a). As seen before, the separation between these two main peaks remains at 23.1 eV, consistent with the literature [26].

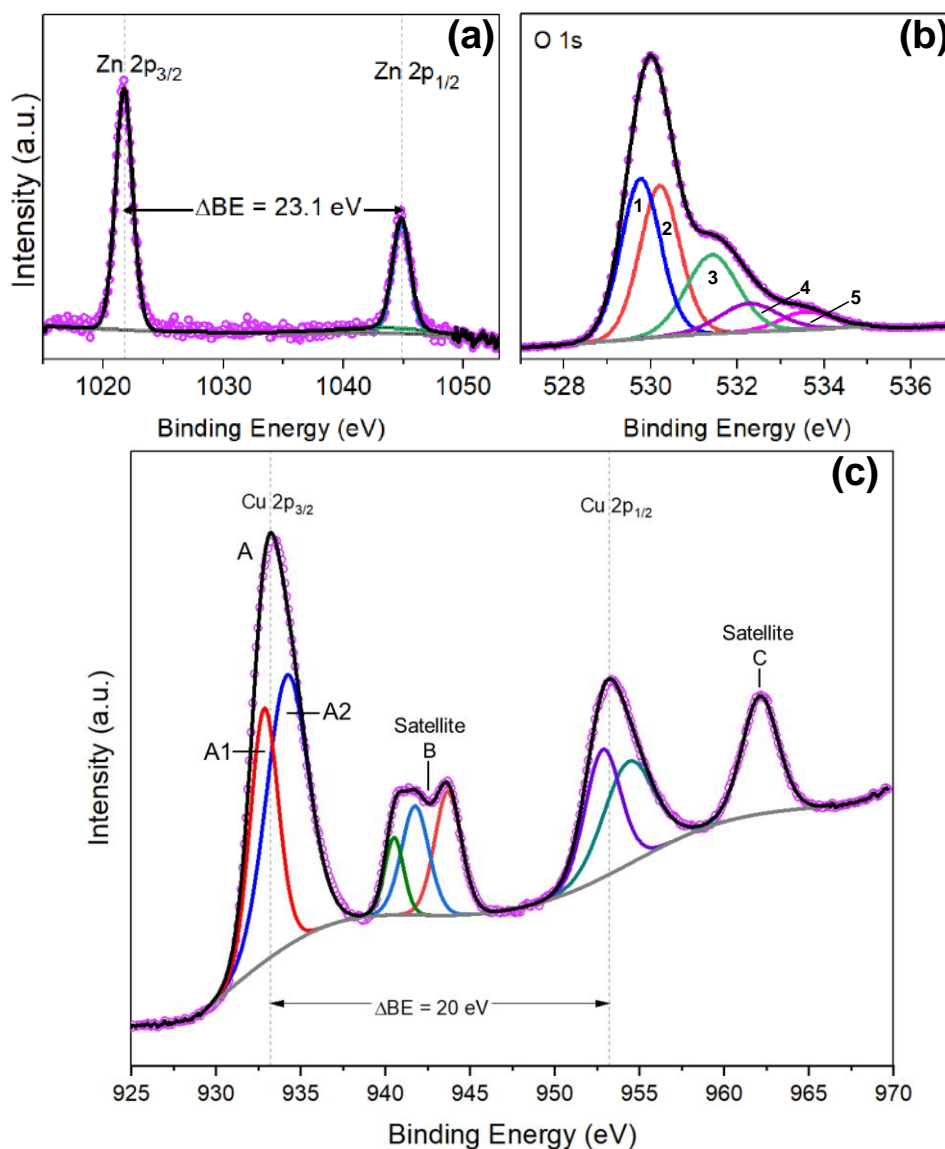


Figure 10. (a) Zn 2p, (b) O 1s and (c) Cu 2p core levels XPS spectra for CuO@ZnO films. Pink hollow dots represent the raw data, the black solid line corresponds to the envelope/fitting curve, and the colored curves to the deconvoluted components.

The O 1s XPS spectrum presents an asymmetric curve as in the afore cases. Five distinguishable curves after deconvolution were determined, as depicted in Figure 10b. In agreement with the literature [41], peak 1 at 529.5 eV is associated with the bonding between copper and O²⁻ (Cu-O), whereas peak 2 located at 530.7 eV is related to the Zn-O wurtzite lattice bond, as established above. Peak 3 at a binding energy of 531.7 eV is assigned to the oxygen deficiency regions, i.e., oxygen vacancies. Finally, peak 4 at 532.7 eV, and peak 5 at 533.9 eV may be associated with chemisorbed oxygen, hydroxides, and H₂O on the surface of the Cu-modified ZnO structures [33,42].

The Cu 2p core level spectrum show the characteristic peaks at binding energies of 933.2 eV for Cu 2p_{3/2} and 953.2 eV for Cu 2p_{1/2}, with a difference between both peaks of 20 eV (Figure 10c). Along the main peaks, two satellite peaks, B and C, are found. The peak B consists of three components

at 940.5 eV, 941.1 eV and 943.5 eV (B peaks), whereas the peak C is described by one component at 962.1 eV.

3.4. Discussion

Results show the formation of ZnO structures via aerosol assisted chemical vapor deposition, and the surface modification of these structures by Fe₂O₃ and CuO in a second step using the same synthetic method. These structured films demonstrated visible morphological and chemical composition changes respect to the bare ZnO structures as well as changes in the surface properties including the wettability properties.

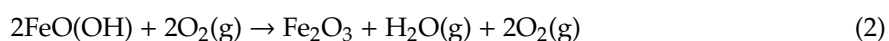
The surface chemical composition of the synthesized films was studied using EDX and XPS analysis. EDX analysis showed a similar content of chlorine in the films (0.9 wt.%, 0.8 wt.%, and 0.7 wt.%, for bare the ZnO, Fe₂O₃@ZnO, and CuO@ZnO, respectively). Although this low chlorine contents can influence the functional properties of the surface in certain applications (e.g., chemical sensing), to the best of our knowledge, there is no evidence in which these traces have shown significant effects on the contact angle of demi-water drops. In this context and due to the similar chlorine contents in the tested samples, we rule out the influence of this ion on the wetting properties of the structured films. For the bare ZnO rods, the XPS analysis showed the characteristic peaks for the Zn²⁺ state, i.e., Zn 2p_{3/2} and 2p_{1/2} core level binding energies. Previous reports have found that for a stoichiometric ZnO compound, the 2p_{3/2} and 2p_{1/2} core level XPS peaks are located at 1022.0 eV and 1045 eV, respectively [23,25,27]. However, the XPS records of the AACVD structures presented an overall shift to lower binding energies, which is usually related to the formation of nonstoichiometric ZnO due to oxygen vacancies induced by the structural size reduction [43]. This oxygen deficit is supported by the O 1s spectrum, which after the deconvolution presents a component linked to the oxygen vacancies (component 2 in Figure 2b).

After the second deposition step by AACVD, the spear pointing ending structures of the bare ZnO are covered by the Fe₂O flake-like structure, as evidenced in the SEM and TEM images (Figures 3 and 5). The incorporation of these iron compound also altered the chemical surface composition. XPS spectra analysis indicate that Zn 2p doublet are shifted to higher binding energy compared to bare ZnO; this may be related to the incorporation of Fe³⁺ ion into the ZnO lattice, as noticed previously in the literature [31]. In addition, the deconvolution of O 1s spectra shows a component situated at 532.5 eV that is not only related to surface OH groups, but also to a possible Zn-Fe-O bond [33]. This is consistent with the XRD diffractions, in which it was registered diffractions liked to the Franklinite (Fe₂O₄Zn) compound (Figure 4).

The results obtained from the XPS analysis through deconvolution and fitting, suggest the complete oxidation of the precursor into Fe₂O₃ during the AACVD synthesis. Usually the chemical reactions involved in the synthesis process are not well defined, and in an attempt to understand this process, two consecutive chemical reactions are proposed as possible routes for the AACVD formation of Fe₂O₃ from the iron precursor dissolved in acetone at a temperature of 723.15 K. The estimation of the Gibbs free energy (ΔG) for the following reactions were calculated by HSC chemistry software (see materials and methods section). The first reaction (1) may involve the formation of FeO(OH) and the release of gaseous species such as chloromethane, hydrogen, and carbon dioxide, whereas the subsequent second reaction (2) may involve the formation of Fe₂O₃ and release of water and oxygen.



$$\Delta G = -97.18 \text{ kcal at } 723.15 \text{ K}$$



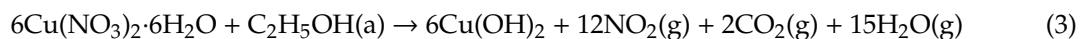
$$\Delta G = -13.05 \text{ kcal at } 723.15 \text{ K}$$

Notice that for both reactions the calculated ΔG is negative (-97.18 kcal and -13.05 kcal for the first and second reaction, respectively), indicating that the reaction enthalpy (ΔH) is lower than the entropy (ΔS) (i.e., the ΔS of the products is greater than the reactants ΔS) therefore the proposed reactions are thermodynamically feasible.

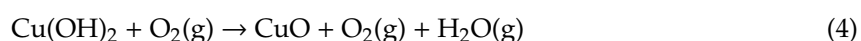
Similar to this analysis, the incorporation of copper oxide in the ZnO structures was studied. As seen in the SEM and TEM images, the deposition of the copper oxide in a AACVD second step, modifies the morphology of the bare ZnO, as well as the surface chemical composition. XPS analysis showed the Zn 2p characteristic doublet peaks are slightly shifted to higher binding energies (1021.9 eV and 1045.0 eV for Zn 2p_{3/2} and Zn 2p_{1/2}, respectively) as compared to the Zn 2p peaks in the bare ZnO (Figure 2a). This shifting of the binding energy could be related to the Zn-O bond length change, which is likely connected with the incorporation and/or substitution of Cu²⁺ ion into the ZnO lattice [14,33,44]. The diffraction connected with the ZnCuO compound (Figure 8) also corroborate the presence of Zn-Cu bonding. The component at 529.5 eV (peak 1, Figure 10b) in the O 1s spectra of the CuO@ZnO films also suggest the presence of the Cu-O bond in the film [45].

Due to typical formation of different copper oxidation states, i.e. Cu⁰, Cu⁺ and Cu²⁺, during oxidation, the Cu 2p XPS spectrum was analyzed to determine the main specie in the structured film. To this end, it was employed the method described by Jasieniak and Gerson [26], which relates the deconvoluted fitted areas of the Cu 2p_{3/2} peak and its closest satellite peak. To calculate the percentage of the components, the fitted areas of Cu 2p_{3/2} peak (components A1 and A2) and the nearest shake-up peak (satellite B) were considered, as described elsewhere [45]. Shake-up peaks are typically generated when the outgoing photoelectron interacts simultaneously with a valence electron and excites it to a higher-energy level. In this process, the kinetic energy of the photoelectrons is slightly reduced giving a satellite structure in a lower energy (higher in the binding energy scale) than the core level position [14,39,45]. For the present results, the deconvolution of the Cu 2p_{3/2} XPS peak (Figure 10c), indicate the co-existence of a mixed oxidation states, and thus the peak A1 at 932.8 eV might be related to Cu²⁺, and peak A2 at 934.3 eV might be related to Cu⁰ and Cu⁺ contribution. The presence of satellites shake-up peaks in B (components at 940.5 eV, 941.1 eV and 943.5 eV), are associated with Cu²⁺ oxidation state since these peak is characteristic of a partially filled d-orbital (d⁹) and is not present in the d¹⁰ Cu⁺ spectra. Therefore, the estimation of the content of (Cu⁰ + Cu⁺) and Cu²⁺ is approximately 17% and 83%, respectively. These suggest that the compound deposited on the ZnO structures corresponds mainly to CuO.

In a like manner to the former case, it is proposed that the AACVD formation of CuO occurs through two consecutive chemical reactions (Equations (3) and (4)), that are possible routes for copper nitrate oxidation in the presence of ethanol at high temperature ($T = 723.15$ K). Under these temperature conditions, it was found that the Gibbs free energy is negative for both possible reactions (-531.20 kcal and -8.31 kcal for reactions 3 and 4, respectively). This is related to enthalpy reactions (ΔH) that are lower than the entropy (ΔS), and thus the entropy of the products is greater than the reactants entropy making the reactions thermodynamically possible.



$$\Delta G = -531.20 \text{ kcal}$$



$$\Delta G = -8.31 \text{ kcal}$$

The oxidation of the Cu(OH)₂ in air (proposed in Equation (4)) is experimentally observed when the reactor chamber is open (immediately after deposition without temperature alteration) as the color of the film change instantaneously from dark orange to dark brown-black.

The alterations in morphology and surface composition of the ZnO structures also showed an effect in the wetting properties of the structured films. We noticed that the static water CA of the

films increased from 122° (bare ZnO) to 134° (Fe₂O₃@ZnO) and 145° (CuO@ZnO). These results are consistent with the literature, which showed previously the possibility of tuning the wetting capability of a surface towards more hydrophobic (CA > 90°) or hydrophilic (CA < 90°) characteristics [46] by modifying the surface morphology and chemical composition of a surface [47,48].

The different wetting properties of the modified films (Fe₂O₃@ZnO and CuO@ZnO) could be attributed in part to the surface morphology, which suggests a favorable Cassie-Baxter regime with a CA exceeding the 120° [49]. In addition, the wetting properties could also be attributed to the surface chemistry of the films, in particular to the oxygen vacancies as noticed previously in the literature [50]. The results obtained from the deconvolution of the O 1s XPS spectrum made through conventional fitting procedure indicate that all samples (i.e., ZnO, Fe₂O₃@ZnO and CuO@ZnO) present a component associated with O⁻ and O₂⁻ ions in the oxygen deficient regions –oxygen vacancies– (O_V). A comparison of the atomic percentage concentration (at.%) of these species (that generally is the representation in percentage of the intensity of a type of oxygen respect to the other oxygen species at the surface) indicates that the O_V at the non-modified ZnO is higher (30.2 at.%) compared to Fe₂O₃@ZnO (20.7 at.%) and CuO@ZnO (18.6 at.%). Also, it is noticed that the O_V concentration of Fe₂O₃@ZnO is higher compared to CuO@ZnO, this could be related to the ion size and charge of the iron ion, as Fe³⁺ (0.63 Å) ion is smaller than Cu²⁺ (0.73 Å) ion, and the extra positive charge of Fe³⁺ compared with Cu²⁺ attracts more oxygen to the lattice, and consequently the incorporation of Fe³⁺ in ZnO structures reduces the surface oxygen compared to Cu²⁺ [44,51].

Previously, it has been suggested that a preferred dissociation adsorption of water molecules takes place, with the formation of hydroxyl groups (OH⁻) in surfaces with oxygen vacancies. Therefore, when the oxygen vacancies concentration at the surface is low is expected that the film surface became more hydrophobic [50,52]. As a result of the analysis, the oxygen vacancies decrease in the following order ZnO > Fe₂O₃@ZnO > CuO@ZnO and water CA increases correspondingly 122° < 135° < 145°. Therefore, the decrease in oxygen vacancies concentration that is achieved with the deposition of Fe₂O₃ and CuO in the ZnO structured films increases the contact angle. Overall, these results demonstrate that the modification of ZnO with iron and copper oxides modifies the wetting properties, increasing the hydrophobicity of the films. This behavior is correlated in part with the surface morphology and the oxygen deficiency at the surface of each film.

4. Conclusions

The synthesis of ZnO structures in one step, and their surface modification with either Fe₂O₃ or CuO in a second step was achieved using the AACVD method. The AACVD conditions employed proved to be reliable and repeatable. SEM and TEM images of the non-modified ZnO films revealed an initial spear-ending like morphology, which after the deposition of Fe₂O₃ or CuO was covered by flake-like structures or spherical nanoparticles, respectively. The formation of crystalline ZnO, Fe₂O₃, and CuO structures was determined by X-ray diffraction and HRTEM analysis. Deconvolution and fitting of the XPS spectra recorded on the Fe₂O₃@ZnO films showed the presence of Fe³⁺ oxidation state, indicating the formation of Fe₂O₃. Similarly, the XPS of the CuO@ZnO films showed the presence of (Cu⁰ + Cu⁺) and Cu²⁺ co-existing oxidation states, with Cu²⁺ as the major component, indicating that the particles formed are composed mainly of CuO. Wettability studies by static water contact angle of these films show that the modification of the ZnO surface with iron and copper oxides increases the hydrophobicity of the ZnO surfaces, from 122° for bare ZnO to 135° and 145° for Fe₂O₃@ZnO and CuO@ZnO, respectively. Results lead to the conclusion that this behavior is related to both morphological changes and chemical surface alterations.

Author Contributions: M.C.; synthesis of structured films and contact angle measurements, M.S., M.C. and S.V.; XPS analysis. M.C. and Y.P.J.; chemical reactions and thermodynamic analysis. S.V. and M.C.; morphological characterization. M.C., S.V., M.S. and Y.P.Y.; writing, review and editing. S.V.; funding acquisition. All authors have read and agreed to the published version of the manuscript.

Funding: The authors acknowledge the support of the Czech Science Foundation (GAČR) via Grant no. 20-20123S, Becas Chile (CONICYT) and the Ramón y Cajal programme. This research was made using the infrastructures of the SIX Research Centre and CEITEC Nano Research Infrastructure supported by MEYS CR (LM2018110).

Acknowledgments: The authors acknowledge the support of the Czech Science Foundation (GAČR) via Grant no. 20-20123S, Becas Chile (CONICYT) and the Ramón y Cajal programme. This research was made using the infrastructures of the SIX Research Centre and CEITEC Nano Research Infrastructure supported by MEYS CR (LM2018110).

Conflicts of Interest: The authors declare no conflict of interest.

References

1. Wang, Z.L. Splendid one-dimensional nanostructures of zinc oxide: A new nanomaterial family for nanotechnology. *ACS Nano* **2008**, *2*, 1987–1992. [[CrossRef](#)]
2. Dave, P.Y.; Patel, K.H.; Chauhan, K.V.; Chawla, A.K.; Rawal, S.K. Examination of Zinc Oxide Films Prepared by Magnetron Sputtering. *Procedia Technol.* **2016**, *23*, 328–335. [[CrossRef](#)]
3. Stratakis, E.; Ranella, A.; Fotakis, C. Biomimetic micro/nanostructured functional surfaces for microfluidic and tissue engineering applications. *Biomicrofluidics* **2011**, *5*, 13411. [[CrossRef](#)]
4. Srivastava, A.; Kumar, N.; Khare, S. Enhancement in UV emission and band gap by Fe doping in ZnO thin films. *Opto Electron. Rev.* **2014**, *22*, 68–76. [[CrossRef](#)]
5. Vallejos, S.; Gràcia, I.; Pizúrová, N.; Figueras, E.; Čechal, J.; Hubálek, J.; Cané, C. Gas sensitive ZnO structures with reduced humidity-interference. *Sens. Actuators B Chem.* **2019**, *301*, 127054. [[CrossRef](#)]
6. Sharma, D.; Jha, R. Transition metal (Co, Mn) co-doped ZnO nanoparticles: Effect on structural and optical properties. *J. Alloy. Compd.* **2017**, *698*, 532–538. [[CrossRef](#)]
7. Yulizar, Y.; Bakri, R.; Apriandanu, D.O.B.; Hidayat, T. ZnO/CuO nanocomposite prepared in one-pot green synthesis using seed bark extract of Theobroma cacao. *Nano Struct. Nano Objects* **2018**, *16*, 300–305. [[CrossRef](#)]
8. Irshad, K.; Khan, M.T.; Murtaza, A. Synthesis and characterization of transition-metals-doped ZnO nanoparticles by sol-gel auto-combustion method. *Phys. B Condens. Matter* **2018**, *543*, 1–6. [[CrossRef](#)]
9. Kumaresan, N.; Sinthiya, M.M.A.; Ramamurthi, K.; Ramesh Babu, R.; Sethuraman, K. Visible light driven photocatalytic activity of ZnO/CuO nanocomposites coupled with rGO heterostructures synthesized by solid-state method for RhB dye degradation. *Arab. J. Chem.* **2019**, *13*, 3910–3928. [[CrossRef](#)]
10. Suryani, S.E.I.; Sa'Adah, U.; Amini, W.N.L.; Suprayogi, T.; Mustikasari, A.A.; Taufiq, A.; Sunaryono; Diantoro, M.; Nur, H. Effect of ZnO and Annealing on the Hydrophobic Performance of x(ZnO)-CA-PLA. *J. Phys. Conf. Ser.* **2018**, *1093*, 12003. [[CrossRef](#)]
11. Charinpanitkul, T.; Suthabanditpong, W.; Watanabe, H.; Shirai, T.; Faungnawakij, K.; Viriya-empikul, N.; Fuji, M. Improved hydrophilicity of zinc oxide-incorporated layer-by-layer polyelectrolyte film fabricated by dip coating method. *J. Ind. Eng. Chem.* **2012**, *18*, 1441–1445. [[CrossRef](#)]
12. Boyer, Q.; Duluard, S.; Tenaillieu, C.; Ansart, F.; Turq, V.; Bonino, J.P. Functionalized superhydrophobic coatings with micro-/nanostructured ZnO particles in a sol-gel matrix. *J. Mater. Sci.* **2017**, *52*, 12677–12688. [[CrossRef](#)]
13. Ennaceri, H.; Wang, L.; Erfurt, D.; Riedel, W.; Mangalgiri, G.; Khaldoun, A.; El Kenz, A.; Benyoussef, A.; Ennaoui, A. Water-resistant surfaces using zinc oxide structured nanorod arrays with switchable wetting property. *Surf. Coat. Technol.* **2016**, *299*, 169–176. [[CrossRef](#)]
14. Vuong, N.M.; Chinh, N.D.; Huy, B.T.; Lee, Y.I. CuO-decorated ZnO hierarchical nanostructures as efficient and established sensing materials for H₂S Gas Sensors. *Sci. Rep.* **2016**, *6*, 1–13. [[CrossRef](#)] [[PubMed](#)]
15. Ramgir, N.S.; Sharma, P.K.; Datta, N.; Kaur, M.; Debnath, A.K.; Aswal, D.K.; Gupta, S.K. Room temperature H₂S sensor based on Au modified ZnO nanowires. *Sens. Actuators B Chem.* **2013**, *186*, 718–726. [[CrossRef](#)]
16. Ghorbani, H.R.; Mehr, F.P.; Pazoki, H.; Rahmani, B.M. Synthesis of ZnO nanoparticles by precipitation method. *Orient J. Chem.* **2015**, *31*, 1219–1221. [[CrossRef](#)]
17. Al-Gaashani, R.; Radiman, S.; Daud, A.R.; Tabet, N.; Al-Douri, Y. XPS and optical studies of different morphologies of ZnO nanostructures prepared by microwave methods. *Ceram. Int.* **2013**, *39*, 2283–2292. [[CrossRef](#)]
18. Chen, S.; Wilson, R.M.; Binions, R. Synthesis of highly surface-textured ZnO thin films by aerosol assisted chemical vapour deposition. *J. Mater. Chem. A* **2015**, *3*, 5794–5797. [[CrossRef](#)]

19. Palgrave, R.G.; Parkin, I.P. Aerosol assisted chemical vapor deposition using nanoparticle precursors: A route to nanocomposite thin films. *J. Am. Chem. Soc.* **2006**, *128*, 1587–1597. [[CrossRef](#)]
20. Powell, M.J.; Potter, D.B.; Wilson, R.L.; Darr, J.A.; Parkin, I.P.; Carmalt, C.J. Scaling aerosol assisted chemical vapour deposition: Exploring the relationship between growth rate and film properties. *Mater. Des.* **2017**, *129*, 116–124. [[CrossRef](#)]
21. Vallejos, S.; Stoycheva, T.; Umek, P.; Navio, C.; Snyders, R.; Bittencourt, C.; Llobet, E.; Blackman, C.; Moniz, S.; Correig, X. Au nanoparticle-functionalised WO₃ nanoneedles and their application in high sensitivity gas sensor devices. *Chem. Commun.* **2011**, *47*, 565–567. [[CrossRef](#)]
22. Annanouch, F.E.; Haddi, Z.; Ling, M.; Di Maggio, F.; Vallejos, S.; Vilic, T.; Zhu, Y.; Shujah, T.; Umek, P.; Bittencourt, C.; et al. Aerosol-Assisted CVD-Grown PdO Nanoparticle-Decorated Tungsten Oxide Nanoneedles Extremely Sensitive and Selective to Hydrogen. *ACS Appl. Mater. Interfaces* **2016**, *8*, 10413–10421. [[CrossRef](#)] [[PubMed](#)]
23. Vallejos, S.; Pizúrová, N.; Gràcia, I.; Sotelo-Vazquez, C.; Čechal, J.; Blackman, C.; Parkin, I.; Cané, C. ZnO Rods with Exposed {100} Facets Grown via a Self-Catalyzed Vapor-Solid Mechanism and Their Photocatalytic and Gas Sensing Properties. *ACS Appl. Mater. Interfaces* **2016**, *8*, 33335–33342. [[CrossRef](#)]
24. Wang, X.; Cai, W.; Lin, Y.; Wang, G.; Liang, C. Mass production of micro/nanostructured porous ZnO plates and their strong structurally enhanced and selective adsorption performance for environmental remediation. *J. Mater. Chem.* **2010**, *20*, 8582–8590. [[CrossRef](#)]
25. Khan, S.B.; Rahman, M.M.; Marwani, H.M.; Asiri, A.M.; Alamry, K.A. An assessment of zinc oxide nanosheets as a selective adsorbent for cadmium. *Nanoscale Res. Lett.* **2013**, *8*, 1–8. [[CrossRef](#)] [[PubMed](#)]
26. Biesinger, M.C.; Payne, B.P.; Grosvenor, A.P.; Lau, L.W.M.; Gerson, A.R.; Smart, R.S.C. Resolving surface chemical states in XPS analysis of first row transition metals, oxides and hydroxides: Cr, Mn, Fe, Co and Ni. *Appl. Surf. Sci.* **2011**, *257*, 2717–2730. [[CrossRef](#)]
27. Available online: <https://srdata.nist.gov/xps/> (accessed on 12 June 2019).
28. Das, J.; Pradhan, S.K.; Sahu, D.R.; Mishra, D.K.; Sarangi, S.N.; Nayak, B.B.; Verma, S.; Roul, B.K. Micro-Raman and XPS studies of pure ZnO ceramics. *Phys. B Condens. Matter* **2010**, *405*, 2492–2497. [[CrossRef](#)]
29. Zheng, J.H.; Jiang, Q.; Lian, J.S. Synthesis and optical properties of flower-like ZnO nanorods by thermal evaporation method. *Appl. Surf. Sci.* **2011**, *257*, 5083–5087. [[CrossRef](#)]
30. Tam, K.H.; Cheung, C.K.; Leung, Y.H.; Djurišić, A.B.; Ling, C.C.; Beling, C.D.; Fung, S.; Kwok, W.M.; Chan, W.K.; Phillips, D.L.; et al. Defects in ZnO nanorods prepared by a hydrothermal method. *J. Phys. Chem. B* **2006**, *110*, 20865–20871. [[CrossRef](#)]
31. Karamat, S.; Rawat, R.S.; Lee, P.; Tan, T.L.; Ramanujan, R.V. Structural, elemental, optical and magnetic study of Fe doped ZnO and impurity phase formation. *Prog. Nat. Sci. Mater. Int.* **2014**, *24*, 142–149. [[CrossRef](#)]
32. Vallejos, S.; Gràcia, I.; Figueras, E.; Cané, C. Nanoscale Heterostructures Based on Fe₂O₃@WO_{3-x} Nanoneedles and Their Direct Integration into Flexible Transducing Platforms for Toluene Sensing. *ACS Appl. Mater. Interfaces* **2015**, *7*, 18638–18649. [[CrossRef](#)] [[PubMed](#)]
33. Karamat, S.; Rawat, R.S.; Tan, T.L.; Lee, P.; Springham, S.V.; Anis-Ur-Rehman; Chen, R.; Sun, H.D. Exciting dilute magnetic semiconductor: Copper-doped ZnO. *J. Supercond. Nov. Magn.* **2013**, *26*, 187–195. [[CrossRef](#)]
34. Lee, S.H.; Sridhar, V.; Jung, J.H.; Karthikeyan, K.; Lee, Y.S.; Mukherjee, R.; Koratkar, N.; Oh, I.K. Graphene-nanotube-iron hierarchical nanostructure as lithium ion battery anode. *ACS Nano* **2013**, *7*, 4242–4251. [[CrossRef](#)] [[PubMed](#)]
35. McIntyre, N.S.; Zetaruk, D.G. X-ray Photoelectron Spectroscopic Studies of Iron Oxides. *Anal. Chem.* **1977**, *49*, 1521–1529. [[CrossRef](#)]
36. Mullet, M.; Khare, V.; Ruby, C. XPS study of Fe(II)-Fe(III) (oxy)hydroxycarbonate green rust compounds. *Surf. Interface Anal.* **2008**, *40*, 323–328. [[CrossRef](#)]
37. Yamashita, T.; Hayes, P. Analysis of XPS spectra of Fe²⁺ and Fe³⁺ ions in oxide materials. *Appl. Surf. Sci.* **2008**, *254*, 2441–2449. [[CrossRef](#)]
38. Wang, M.; Hu, H.P.; Chen, Q.Y.; Ji, G.F. FT-IR, XPS, and DFT study of adsorption mechanism of sodium acetohydroxamate onto goethite or hematite. *Chin. J. Chem. Phys.* **2016**, *29*, 308–318. [[CrossRef](#)]
39. Grosvenor, A.P.; Kobe, B.A.; Biesinger, M.C.; McIntyre, N.S. Investigation of multiplet splitting of Fe 2p XPS spectra and bonding in iron compounds. *Surf. Interface Anal.* **2004**, *36*, 1564–1574. [[CrossRef](#)]

40. Liu, Y.; Yu, L.; Hu, Y.; Guo, C.; Zhang, F.; Wen, L.X. A magnetically separable photocatalyst based on nest-like γ -Fe₂O₃/ZnO double-shelled hollow structures with enhanced photocatalytic activity. *Nanoscale* **2012**, *4*, 183–187. [[CrossRef](#)]
41. Zhu, L.; Li, H.; Liu, Z.; Xia, P.; Xie, Y.; Xiong, D. Synthesis of the 0D/3D CuO/ZnO Heterojunction with Enhanced Photocatalytic Activity. *J. Phys. Chem. C* **2018**, *122*, 9531–9539. [[CrossRef](#)]
42. Wang, Y.; Lü, Y.; Zhan, W.; Xie, Z.; Kuang, Q.; Zheng, L. Synthesis of porous Cu₂O/CuO cages using Cu-based metal-organic frameworks as templates and their gas-sensing properties. *J. Mater. Chem. A* **2015**, *3*, 12796–12803. [[CrossRef](#)]
43. Tay, Y.Y.; Li, S.; Sun, C.Q.; Chen, P. Size dependence of Zn 2p 3/2 binding energy in nanocrystalline ZnO. *Appl. Phys. Lett.* **2006**, *88*, 173118. [[CrossRef](#)]
44. Shannon, R.D. Revised effective ionic radii and systematic studies of interatomic distances in halides and chalcogenides. *Acta Crystallogr. Sect. A* **1976**, *32*, 751–767. [[CrossRef](#)]
45. Biesinger, M.C. Advanced analysis of copper X-ray photoelectron spectra. *Surf. Interface Anal.* **2017**, *49*, 1325–1334. [[CrossRef](#)]
46. Shirtcliffe, N.J.; McHale, G.; Atherton, S.; Newton, M.I. An introduction to superhydrophobicity. *Adv. Colloid Interface Sci.* **2010**, *161*, 124–138. [[CrossRef](#)]
47. Wang, G.; Zhang, T.Y. Oxygen adsorption induced superhydrophilic-to-superhydrophobic transition on hierarchical nanostructured CuO surface. *J. Colloid Interface Sci.* **2012**, *377*, 438–441. [[CrossRef](#)]
48. Saini, C.P.; Barman, A.; Das, D.; Satpati, B.; Bhattacharyya, S.R.; Kanjilal, D.; Ponomaryov, A.; Zvyagin, S.; Kanjilal, A. Role of oxygen vacancy on the hydrophobic behavior of TiO₂ nanorods on chemically etched Si pyramids. *J. Phys. Chem. C* **2017**, *121*, 278–283. [[CrossRef](#)]
49. Celia, E.; Darmanin, T.; de Givenchy, E.T.; Amigoni, S.; Guittard, F. Recent advances in designing superhydrophobic surfaces. *J. Colloid Interface Sci.* **2013**, *402*, 1–18. [[CrossRef](#)]
50. Hu, H.; Ji, H.F.; Sun, Y. The effect of oxygen vacancies on water wettability of a ZnO surface. *Phys. Chem. Chem. Phys.* **2013**, *15*, 16557–16565. [[CrossRef](#)]
51. Bajpai, G.; Srivastava, T.; Patra, N.; Moirangthem, I.; Jha, S.N.; Bhattacharyya, D.; Riyajuddin, S.; Ghosh, K.; Basaula, D.R.; Khan, M.; et al. Effect of ionic size compensation by Ag⁺ incorporation in homogeneous Fe-substituted ZnO: Studies on structural, mechanical, optical, and magnetic properties. *RSC Adv.* **2018**, *8*, 24355–24369. [[CrossRef](#)]
52. Mrabet, C.; Mahdhi, N.; Boukhachem, A.; Amlouk, M.; Manoubi, T. Effects of surface oxygen vacancies content on wettability of zinc oxide nanorods doped with lanthanum. *J. Alloy. Compd.* **2016**, *688*, 122–132. [[CrossRef](#)]





Article

Cerium Oxide-Tungsten Oxide Core-Shell Nanowire-Based Microsensors Sensitive to Acetone

Milena Tomić ¹, Milena Šetka ², Ondřej Chmela ² , Isabel Gràcia ¹ , Eduard Figueras ¹, Carles Cané ¹ and Stella Vallejos ^{1,2,*}

¹ Instituto de Microelectrónica de Barcelona (IMB-CNM, CSIC), Campus UAB, 08193 Bellaterra, Spain; milena.tomic@imb-cnm.csic.es (M.T.); isabel.gracia@imb-cnm.csic.es (I.G.); Eduard.Figueras@imb-cnm.csic.es (E.F.); carles.cane@imb-cnm.csic.es (C.C.)

² CEITEC-Central European Institute of Technology, Brno University of Technology, 61200 Brno, Czech Republic; milena.setka@ceitec.vutbr.cz (M.Š.); Ondrej.Chmela@ceitec.vutbr.cz (O.C.)

* Correspondence: stella.vallejos@imb-cnm.csic.es; Tel.: +34-935-947700

Received: 31 October 2018; Accepted: 19 November 2018; Published: 23 November 2018



Abstract: Gas sensitive cerium oxide-tungsten oxide core-shell nanowires are synthesized and integrated directly into micromachined platforms via aerosol assisted chemical vapor deposition. Tests to various volatile organic compounds (acetone, ethanol, and toluene) involved in early disease diagnosis demonstrate enhanced sensitivity to acetone for the core-shell structures in contrast to the non-modified materials (i.e., only tungsten oxide or cerium oxide). This is attributed to the high density of oxygen vacancy defects at the shell, as well as the formation of heterojunctions at the core-shell interface, which provide the modified nanowires with ‘extra’ chemical and electronic sensitization as compared to the non-modified materials.

Keywords: gas sensors; volatile organic compounds (VOCs); acetone; metal oxides; heterojunctions

1. Introduction

Odor (gas, vapor, aroma) detection systems are of high interest as they are non-invasive key-enabling technologies, which are relevant in both traditional (e.g., environment, industry) and innovative applications such as the early detection of diseases from exhaled breath [1,2]. The literature related to exhaled breath as bio information for disease diagnosis has shown previously that human breath contains more than two hundred different gases and volatile organic compounds (VOCs) species that vary from person to person [3]. In the midst of a wide range of analytes, acetone, toluene, and ethanol are within the most relevant VOCs that are typically involved in various diseases, including diabetes and cancer. Thus, for instance, high acetone concentrations (~21 ppm) have been identified in the exhaled breath of diabetic patients, as compared to healthy patients (~2.7 ppm) and oppositely to patients with lung cancer, who showed lower acetone concentrations (~0.9 ppm). Similarly, the ethanol concentration in breath has shown an increase (~2.1 ppm) in patients with lung/breast cancer and diabetes with respect to healthy patients (~0.2 ppm) [4–6].

Currently, the analysis of breath is still an emerging diagnosis technology that uses large and expensive laboratory equipment such as gas-chromatograph, ion-mobility and/or mass spectrometers [7]. In the future, however, miniaturized, portable, and wearable systems with enhanced functionality (sensitivity, selectivity, and stability) and high autonomy at a low cost could substitute this equipment; a fact that demands the innovation of current odor detection systems. In this context, metal oxide (MOX) gas sensors based on the chemoresistive principle represent an alternative to bulky equipment providing simpler architecture and fabrication processes compatible with ‘standard’ MEMS and CMOS technologies [2]. Chemoresistive gas sensors devices generally consist of a transducing

platform (microscale) and a gas sensitive MOX optimized to interact with specific groups of gaseous or vapor analytes. However, among the diverse issues that may potentially be addressed to improve the functionality of these monitoring systems (e.g., optimization of sensing modes and control electronics or the integration of smart systems with new micro/nano fabrication concepts), the focus on nanoscaled sensitive materials is still essential to radically improve their performance. Thus, several studies have demonstrated that MOXs modified with second-phase constituents, either nanosized noble metals or other MOXs, have a positive effect on the sensing properties of both the host MOX and the second-phase constituent, particularly when the size of both materials is within the Debye length of the surface (typically on the order of 2–100 nm) [8]. Moreover, recently, it has been pointed out that the modification of a MOX with noble metals or other MOXs allows for the formation of nanoscale heterojunctions and, in turn, sensing mechanisms dominated not only by the surface, but also the interface, which has proved to improve the sensing properties of these materials [9].

In recent years, tungsten oxide has demonstrated high potential in gas sensing among traditional gas sensitive MOXs such as SnO₂ and ZnO (Figure 1), showing a strong sensitivity to oxidizing gases including nitrogen dioxide and ozone [10]. Moreover, the modification of tungsten oxide with second-phase constituents such as platinum, copper oxide, or iron oxide has shown an improved sensitivity and selectivity to reducing species including hydrogen [11], hydrogen sulfide [12] or toluene [13], respectively. As far as cerium oxide is concerned, the peculiarity that makes this oxide also attractive in gas sensors reside overall in the defect sites caused by the valence state changes between Ce⁴⁺ and Ce³⁺, which considerably alter the concentration of oxygen vacancies, and provides a good redox behavior and catalytic activity [14–16]. However, and despite these favorable surface properties the use of cerium oxide in gas sensing is still infrequent (Figure 1) and its sensing properties upon VOCs have not been fully explored in the literature related to gas sensors.

Optimized gas sensitive MOXs need synthetic methods able to produce well defined and even structures. Additive (bottom-up) synthetic methods, as opposed to subtractive (top-down) methods, are ideal for this task and industrially attractive as they provide the ability to generate films in a continuous mode with high purities and high throughput. Aerosol assisted (AA) chemical vapor deposition (CVD) is a versatile additive synthetic method used previously to obtain non-modified (e.g., WO₃) or metal/MOX modified MOXs (e.g., Pt/WO₃, Fe₂O₃/WO₃) [11,13]. Additionally, recently, the AACVD of cerium oxide from Ce (dbm)₄ has been proved as a strategy to overcome the low volatility of traditional cerium CVD precursors [17]. In this work, however, we achieve the AACVD of cerium oxide from Ce (acac)₃ precursor and use this route to synthesize cerium oxide-tungsten oxide core-shell nanowires in a two-step process performed directly on silicon-based micromachined platforms. In addition, we validate the sensing properties of these systems to acetone, and other relevant VOCs monitored in early disease diagnosis.

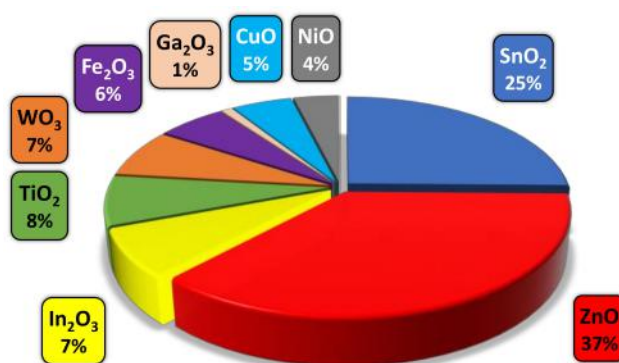


Figure 1. A survey of the most applicable gas sensitive MOXs reported in the literature (Web of Science database from 1998 to 2018).

2. Materials and Methods

Tungsten oxide (non-modified nanowires), cerium oxide (non-modified porous films), and cerium oxide-tungsten oxide core-shell nanowires were grown directly onto micromachined transducing platforms (Figure 2a) [18] using the AACVD system described previously [19]. AACVD is a variant of the conventional CVD technique, which uses aerosol to transport dissolved precursors to a heated reaction zone. Here, the non-modified tungsten oxide nanowires films were deposited at 350 °C from a solution of tungsten hexacarbonyl (30 mg, $W(CO)_6$, Sigma-Aldrich, St. Louis, MO, USA, $\geq 97\%$) and methanol (5 mL Sigma-Aldrich, $\geq 99.6\%$), whereas the non-modified cerium oxide films were deposited at 500 °C from cerium (III) acetylacetonate hydrate (28 mg, $Ce(acac)_3 \cdot xH_2O$, Sigma-Aldrich) dissolved in methanol (2 ml, Sigma-Aldrich). On the other hand, the cerium oxide-tungsten oxide core-shell nanowires were achieved using a two-step AACVD process [20], in which the tungsten oxide nanowire cores were deposited at 350 °C in the first step and the cerium oxide shell film at 500 °C in the second step employing the same protocols described above for the non-modified films. Finally, the non-modified and modified films were annealed at 500 °C in air.

The morphology of the films was examined using scanning electron microscopy (SEM— Auriga Series, 3 KV, Carl Zeiss, Jena, Germany) and the phase using X-ray Diffraction (XRD—Bruker-AXS, model A25 D8 Discover, Cu $K\alpha$ radiation, Billerica, MA, USA). Further analysis of the material was carried out using X-ray photoelectron spectroscopy (XPS—Kratos Axis Supra with monochromatic Al $K\alpha$ X-ray radiation, an emission current of 15 mA and hybrid lens mode, Manchester, UK). The survey and detailed spectra were measured using pass energy of 80 eV and 20 eV, respectively. The band gap of the films was estimated by measuring the diffuse reflectance (AvaSpec-UV/VIS/NIR, Avantes, Apeldoorn, the Netherlands) of the films and performing Kubelka–Munk transformation.

The microsensors were tested in a continuous flow test chamber provided with mass flow controllers that allow the mixture of dry/humid air and calibrated gaseous analytes (ethanol, acetone, toluene, carbon monoxide and hydrogen purchased from Praxair, Danbury, CT, USA) to obtain the desired concentration. To have a proper control of the relative humidity (RH) inside the gas test chamber, an evaluation kit (EK-H4, Sensirion AG, Stäfa, Switzerland) with a humidity sensor was also used. The dc resistance measurements of the microsensor were achieved in a system provided with an electrometer (Keithley 6517A, Cleveland, OH, USA) and a multimeter (Keithley 2700, Cleveland, OH, USA) with switch system to monitor various sensors simultaneously. More details of the characterization systems were reported elsewhere [18]. The sensor response was defined as R_a/R_g , where R_a and R_g are the resistance in dry/humid air and the resistance after 600 s of analyte exposure, respectively. The sensors were tested for a period of one month during which each sensor accumulated 180 h of operation under the different conditions (analytes, temperatures, humidity) employed.

3. Results

3.1. Gas Sensitive Films

SEM imaging of the microsensors after AACVD of the gas sensitive structures showed uniform deposited films that covered the electrodes integrated into the micromachined membrane (Figure 2a). A close view of the non-modified tungsten oxide wires (W) showed bare and even surfaces as noticed previously for other AACVD tungsten oxide structures [21]. In contrast, a close view of the cerium oxide-tungsten oxide core-shell wires (Ce/W) displayed the presence of a rugged thin film covering the wire surface (Figure 2b,c), similarly to that observed when depositing non-modified cerium-based films (Ce) from a $Ce(acac)_3$ methanolic solution via AACVD (Figure 2d).

Generally, AACVD of the non-modified (W and Ce) and modified (Ce/W) films showed a good adherence to the substrate, with the wire-like morphology films (i.e., W and Ce/W) forming a mat-like network of non-aligned nanowires with diameters below 100 nm, and the particle-like morphology films (i.e., Ce) displaying a porous surface composed of grains with diameters below 40 nm. The as-deposited non-modified W films displayed a bluish color, whereas the Ce/W films

displayed a dark yellowish to dark green color, similarly to the color observed on the *Ce* films. However, after annealing the non-modified *W* and modified *Ce/W* films became whitish and pale yellowish, respectively. Figure 3 displays the diffuse reflectance spectra of the films deposited without modification (i.e., only tungsten oxide or only cerium oxide) via AACVD. These measurements and their corresponding Kubelka–Munk transformation indicated optical band gaps at ~ 3.2 eV for the tungsten oxide films and ~ 3.1 eV for the cerium oxide films, in agreement with the literature band gap values of tungsten oxide (2.6–3.7 eV) [22] and cerium oxide (2.7–3.4 eV) [15].

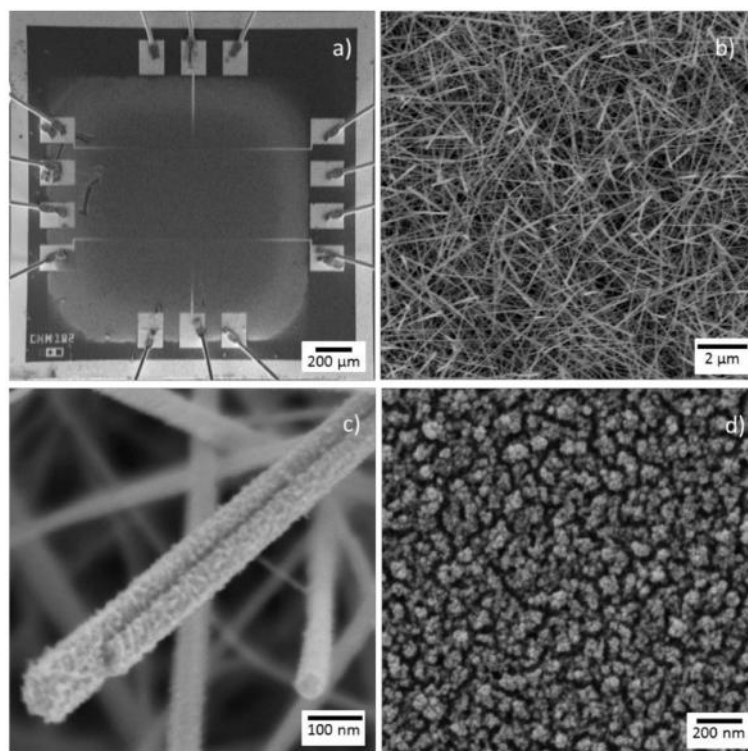


Figure 2. The SEM imaging of a (a) gas sensor device, the *Ce/W* nanowires at (b) low and (c) high magnification, and (d) the non-modified *Ce* films integrated on the micromachined membrane.

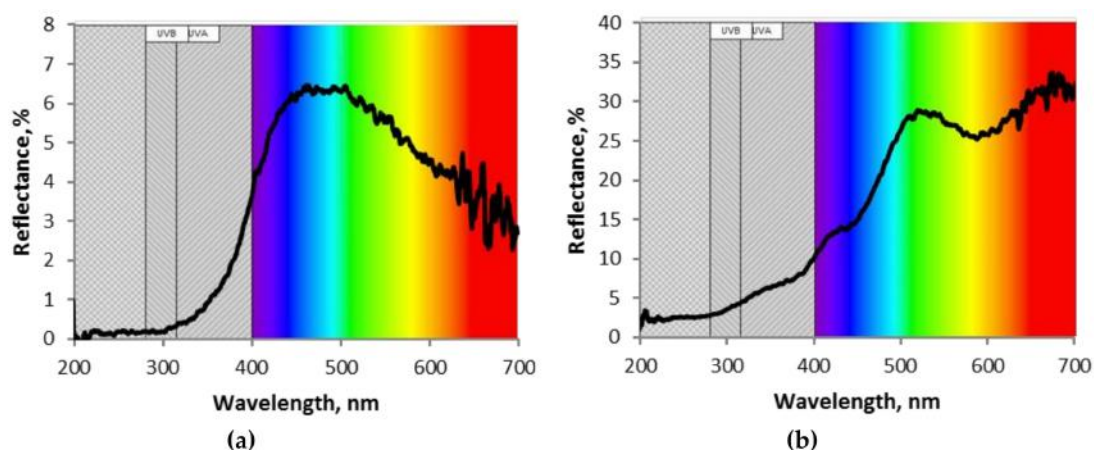


Figure 3. The diffuse reflectance spectra of the aerosol assisted chemical vapor deposited (a) tungsten oxide and (b) cerium oxide films without modification.

XRD analysis of the films revealed the presence of a monoclinic-phase (International Centre of Diffraction Data–ICDD card no. 72-0677) in the *W* and *Ce/W* films with greatly enhanced intensity (preferred orientation) in the [001] direction, consistent with our previous results for AACVD of tungsten oxide [13]. A weak diffraction peak was also noticed at 47.8° 2θ for the *Ce/W* films

(Figure 4). This diffraction peak is in line with the pattern identified on the non-modified *Ce* based films corresponding to cerium dioxide (Crystallography Open Database–COD ID card no. 7217887).

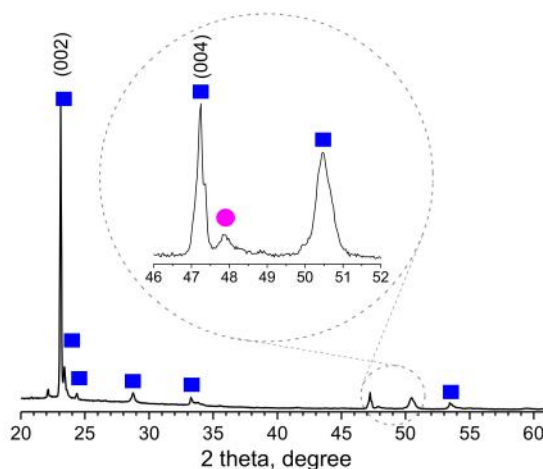


Figure 4. The XRD pattern of the *Ce/W* films. The diffraction peak at 47.8° 2θ (full pink circle) corresponds to cerium dioxide cubic phase (P1), COD ID card no. 7217887, the rest of the diffraction peaks (full blue squares) in the data can be indexed to a monoclinic phase (P21/n), ICDD card no. 72-0677, with only peaks of greatly enhanced intensity (preferred orientation), specifically indexed.

The XPS of both *W* and *Ce/W* films exhibited typical *W* 4 $f_{7/2}$, *W* 4 $f_{5/2}$ and *W* 5 $p_{3/2}$ XPS core level peaks (Figure 5a), consistent with the literature and previous tungsten oxide nanowires synthesized via AACVD [13]. XPS narrow scan spectra of the *Ce* 3d core level peaks at the *Ce* and *Ce/W* wires displayed multiplet splitting between 875 and 920 eV in agreement with the standard binding energies for *Ce* 3d peaks and partially reduced cerium oxide [23,24]. Figure 5b displays the experimental data and the corresponding deconvolution of the *Ce* 3d spectrum recorded on the *Ce/W* wires. The peaks v , v'' and v''' are attributed to the main and satellite peaks of the Ce^{4+} state, whereas the peaks v_0 , v' correspond to the peaks of Ce^{3+} state. The relative contribution of Ce^{4+} and Ce^{3+} species at the *Ce/W* films was estimated from the ratio of integrated Ce^{4+} peaks to the total Ce^{4+} and Ce^{3+} peaks, finding a value of $\sim 42\%$ for Ce^{4+} and 58% Ce^{3+} species. The relatively high amount of Ce^{3+} species indicate a charge imbalance with oxygen vacancy defects and an unsaturated chemical bond at the *Ce/W* film suggesting a high redox nature of the film.

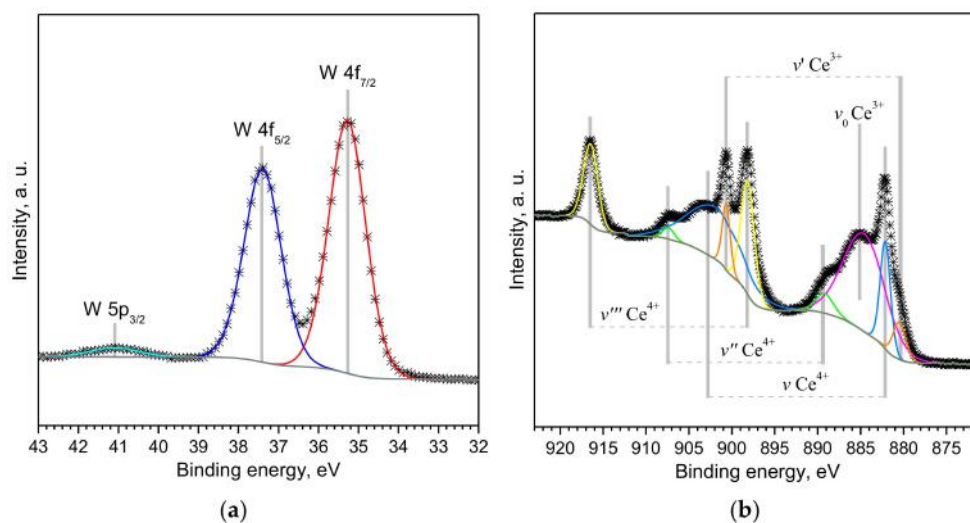


Figure 5. (a) The *W* 4 f and (b) *Ce* 3d spectra recorded on the cerium-modified wires. The *W* 4 f spectrum recorded on the non-modified tungsten oxide wires showed similar characteristics.

Linear extrapolation of the valence band (VB) leading edge on the XPS spectra recorded on the *Ce/W* film near the Fermi level ($E_B = 0$) indicates the simultaneous presence of both cerium oxide and tungsten oxide induced VB (Figure 6a). One can notice that the VB onset for cerium oxide occurs ~ 0.5 eV (ΔE_V) above the VB onset for tungsten oxide. Therefore, according to the band gap estimated by diffuse reflectance for each non-modified material in the position of the conduction band (CB) of cerium oxide is ~ 0.4 eV (ΔE_C) above the CB of tungsten oxide, consequently suggesting a staggered type of heterojunction at the interface of the *Ce/W* core-shell structures (Figure 6b). In contrast, the linear extrapolation of VB leading edge on the XPS spectra of the *W* and *Ce* films showed only the presence of tungsten oxide induced VB at 2.9 eV in agreement with previous reports [13].

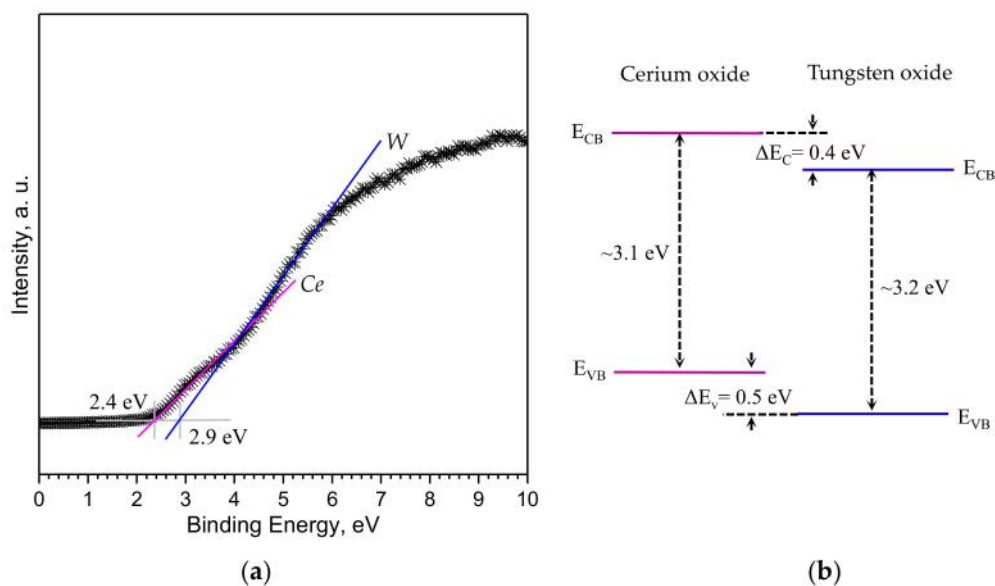


Figure 6. (a) The XPS valence band spectra of the cerium-modified tungsten oxide nanowires, and (b) schematic of the estimated energy level diagram at the interface. E_{CB} and E_{VB} represent the conduction band minimum and the valence band maximum (not to scale).

In brief, the characterization of the films deposited via AACVD demonstrates the formation of crystalline cerium oxide-tungsten oxide core-shell wires with a relatively high amount of Ce^{3+} species at the surface and the presence of the characteristic valence band onsets for cerium oxide and tungsten oxide.

3.2. Gas Sensing Tests

Overall, the sensors displayed an n-type response with a good reproducibility to the target gaseous analytes (acetone, ethanol, toluene, carbon monoxide, and hydrogen) and relatively low variations of the baseline resistance along the testing period. Gas sensing tests of the microsensors were carried out at various operating temperatures from 150 °C to 400 °C by DC resistance measurements of the films integrated via AACVD. These tests proved a better sensor functionality to 80 ppm of acetone at 300 °C for the sensors based on *W* and *Ce/W* films and 400 °C for the sensors based on *Ce* films. As the *Ce* based sensors registered comparatively higher baseline resistances (~ 40 G Ω at 400 °C) than *W* (13 k Ω at 300 °C) and *Ce/W* (65 k Ω at 300 °C) sensors, additionally requiring higher temperatures to achieve the maximum responses (e.g., response to acetone 4.9 at 400 °C for the *Ce* sensors and 5.6 at 300 °C for the *Ce/W* sensors), further analyses related to the analyte concentration and humidity dependence of the sensor response were performed only for the *W* and *Ce/W* based sensors at 300 °C.

Figure 7a displays the sensor response to 80 ppm of each analyte and type of sensor at 300 °C. These results show the improved responses registered for the *Ce/W* sensors, as opposed to the *W* sensors, as well as the higher responses to acetone compared to the rest of the analytes. Results in

Figure 7a also suggests an improved selectivity for the *Ce/W* films with lower cross-responses among the analytes; for instance, the difference of the response to acetone in relation to ethanol is 1.6 for the *Ce/W* films and 1 for the *W* films. The low cross response registered on the *Ce/W* sensor is noticed in more detail in Figure 7b, in which is displayed the analysis of variance (ANOVA) realized for a data set comprising four replicates for each type of sensor and analyte. Additionally, the principal component (PC) analysis performed using replicated responses of both sensors (i.e., *W* and *Ce/W*) to each analyte is represented in Figure 8. These results, specifically the scores, which correspond to the projections of the measurements in an orthogonal base of PCs, indicate the possibility to improve the discrimination of the analytes by using an array of *W* and *Ce/W* based sensors.

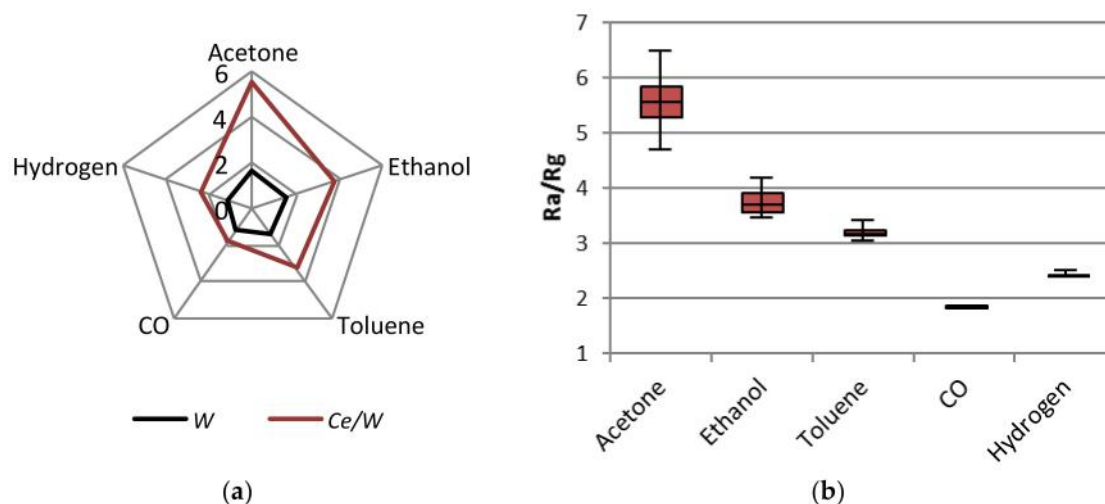


Figure 7. (a) The radial plot of the sensor response to 80 ppm of acetone, ethanol, toluene, carbon monoxide, and hydrogen using the *W* and *Ce/W* based sensors. (b) Box plots of the sensor response to each analyte recorded by the *Ce/W* based sensors. Each box displays the median and upper and lower quartiles (first and third) of the respective distribution. Box whiskers indicate the dispersion of the measurements.

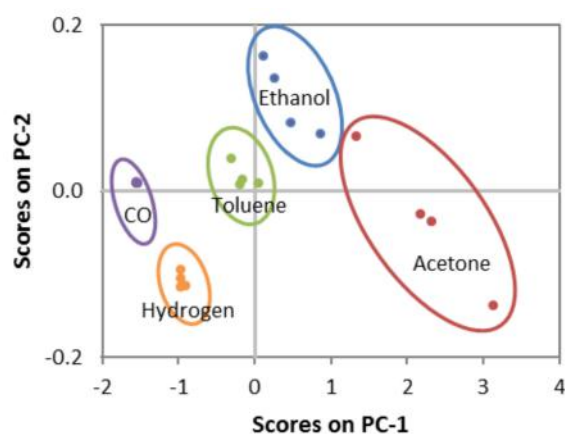


Figure 8. Principal component analysis applied to discriminate the tested VOCs by using an array of non-modified tungsten oxide wires and the cerium oxide-tungsten oxide core-shell wire-based sensors.

Further tests of the sensors to various concentrations of each analyte showed direct proportional changes in the response to concentration. An example of the response registered with both types of sensors to acetone is shown in Figure 9. For these conditions, the limit of detection corresponding to three times the noise level [25] was estimated at 1 ppm for *W* and 0.2 ppm for *Ce/W* sensors. Overall, the changes respect to concentration for the *W* sensors proved a lower sensitivity compared to the *W/Ce* sensors, which demonstrates a better sensitivity to the analytes. The sensitivity (*S*), defined as the

ratio between the change in response (ΔR) and a fixed change in analyte concentration (ΔC) for each sensor and analyte, was registered to be nearly five times higher for acetone and three times higher for ethanol when using the cerium-modified sensors (found $\Delta R/\Delta C_{\text{acetone}}$ for W sensors 0.8%, Ce/W sensors 4.7%; $\Delta R/\Delta C_{\text{ethanol}}$ for W sensors 0.8%, Ce/W sensors 2.2%).

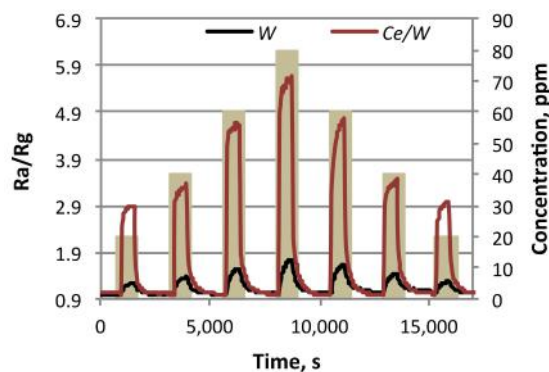


Figure 9. The sensor response to various concentrations (from 20 to 80 ppm) of acetone recorded with the W and Ce/W based sensors.

Additional tests of the sensors in a controlled humid ambient (10 and 20% RH), consistent with those reported after preconditioning the relative humidity in breath samples [26], registered lower sensor response to the analytes. The loss of response in humid ambient is a consequence of the proportional drop of the baseline resistance to relative humidity. This proportional change is usually present in metal oxides exposed to humidity due to the formation of hydroxyl groups at temperatures above 100 °C [18]. Currently, most of the strategies to attenuate further the humidity interference from the material point of view are connected with the fine tune of the MOX morphology [27] and/or the incorporation of humidity-insensitive additives (e.g., NiO [28], CuO [12], or SiO₂ [29]). Figure 10 displays the typical resistance changes for the W and Ce/W sensors to each mixture of RH and acetone tested and their replicates.

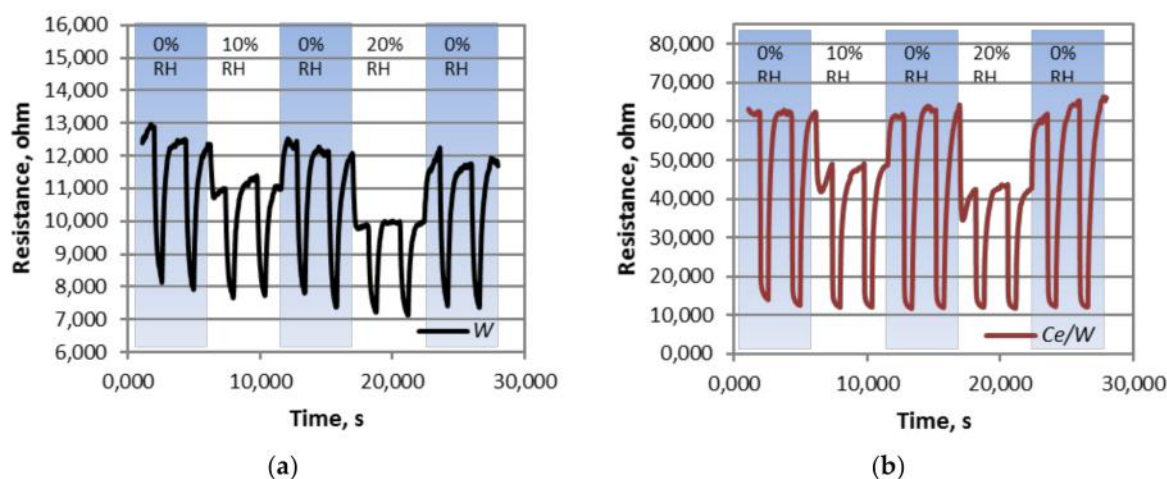


Figure 10. The resistance changes registered for (a) W and (b) Ce/W to acetone in dry and humid ambient (RH: relative humidity).

Previous reports in the literature related to acetone sensing using modified tungsten oxide films (with Au, Pd, AuPd) suggest the functionality of tungsten oxide at 300 °C for relatively high acetone concentrations (200–1000 ppm) [30]. Further tests, also performed on tungsten oxide, modified with TiO₂ [31] or Si [32] show the functionality of the sensors at similar (30 ppm) or lower (100–600 ppb) acetone concentrations, respectively, although requiring higher operating temperatures (400–500 °C),

than those needed in this work. On the other hand, the use of cerium oxide as the gas sensitive element has been rarely reported in the literature, with the performance of this material having indicated the potential for sensing VOCs including acetone [33,34]. In general, the responses of the above mentioned non-miniaturized acetone sensors in the literature [30–34] are in the same order of magnitude than our micromachined sensors based on the cerium oxide-tungsten oxide core-shell wires, which suggests the viability of sensor miniaturization without losing the sensitivity of the system when optimizing the sensitive material. In addition, the good reproducibility of the responses during the testing period and the analysis (SEM, XRD) of the samples after the gas sensing experiments (which showed unchanged properties of the material with respect to the properties recorded initially) indicated a good stability of the sensors.

The enhanced functionality recorded on the *Ce/W* sensors is connected with the formation of heterojunctions at the interface of the tungsten oxide wires and the cerium oxide porous films. These heterojunctions are present due to the different band energies in both MOXs (Figure 6b), which facilitate electron migration from the cerium oxide film to the tungsten oxide wire. Generally, as oxygen is preadsorbed at the sensitive film during air exposure, the surface depletion region (L_D) and, in turn, the conduction channel along the wires are narrowed, which leads to lower conductivity along the film (Figure 11a). Alternatively, when a reducing analyte (i.e., VOCs) reacts with the preadsorbed oxygen, electrons are released back to the conduction band, and the depth of the surface depletion is narrowed, increasing the conduction channel along the wire and, in turn, its conductivity (Figure 11b). This mechanism controlled by the pre-adsorbed oxygen is similar for the non-modified and modified films, with the peculiarity that the charge transfer process (electron migration) occurring at the junction of the cerium oxide film and tungsten oxide wire provides larger electron density to the wires (accumulation layer) in the pre-adsorption cycle (as opposed to the non-modified *W* or *Ce* films). This allows for larger changes of the depletion layer and an enhanced modulation of the wire conduction channel, which is reflected finally on the sensor response.

In the same line, the lowering of the baseline resistance upon humidity implies a diminution of the chemically active oxygen species at the surface and, in turn, a narrow surface depletion in the air (pre-adsorption). Thus, as the conduction channel in humid ambient is wider than in dry ambient (Figure 11), the conduction changes induced by the reducing gas are less significant, and thus the sensor response is as well.

Summarizing, the gas sensing tests showed improved acetone sensing properties for *Ce/W* based microsensors showing a higher response, and better sensitivity and selectivity to the analytes tested in relation to the *W* or *Ce* based microsensors.



Figure 11. The schematic view of the heterojunction formed at the surface of the cerium oxide (*Ce*) core-shell tungsten oxide (*W*) wires and the possible mechanism (a) after exposure to air and (b) reducing gases such as acetone. L_D is the Debye length or depth of the depletion region from the surface (not at scale).

4. Conclusions

These results demonstrate the formation of cerium oxide-tungsten oxide core-shell nanowires with improved response and sensitivity to acetone as compared to non-modified tungsten oxide wires or cerium oxide porous films. Tests of these sensors to acetone in humid ambient showed a drop of the responses as a consequence of the lowering of the baseline resistance due to humidity. Principal

component analysis of the responses obtained for each analytes using an array the non-modified and modified sensitive films indicated the possibility to enhance the selectivity of the microsensors by improving the discrimination of analytes. The improved sensitivity is attributed to the formation of heterojunctions at the interface of both oxides (i.e., tungsten oxide and cerium oxide) which leads to an 'extra' chemical and electronic sensitization to the modified films as compared to the non-modified films.

Author Contributions: M.T.; synthesis and integration of gas sensitive films, M.S. and S.V.; XPS analysis, M.T. and I.G. diffuse reflectance tests, I.G., E.F. and C.C.; Si-based micromachined platforms; I.G., E.F. and O.C. gas sensing characterization, M.T., M.S. and O.C., literature search, M.T., I.G. and S.V.; writing review and editing, S.V. and C.C.; funding acquisition.

Funding: This work has been supported by the Czech Science Foundation (GAČR) via Grant no. 17-16531S, and the Spanish Ministry of Science and Innovation via the Ramón y Cajal Programme and Grants TEC2015-74329-JIN-(AEI/FEDER,EU) and TEC2016-79898-C6-(AEI/FEDER,EU). This research has used the Spanish ICTS Network MICRONANOFABS (partially funded by MINECO). CEITEC Nano Research Infrastructure (IDL2015041, MEYS CR, 2016–2019) is also acknowledged.

Conflicts of Interest: The authors declare no conflict of interest.

References

1. Brattoli, M.; de Gennaro, G.; de Pinto, V.; Loiotile, A.D.; Lovascio, S.; Penza, M. Odour detection methods: Olfactometry and chemical sensors. *Sensors* **2011**, *11*, 5290–5322. [[CrossRef](#)] [[PubMed](#)]
2. Di Natale, C.; Paolesse, R.; Martinelli, E.; Capuano, R. Solid-state gas sensors for breath analysis: A review. *Anal. Chim. Acta* **2014**, *824*, 1–17. [[CrossRef](#)] [[PubMed](#)]
3. Phillips, M.; Herrera, J.; Krishnan, S.; Zain, M.; Greenberg, J.; Cataneo, R.N. Variation in volatile organic compounds in the breath of normal humans. *J. Chromatogr. B Biomed. Sci. Appl.* **1999**, *729*, 75–88. [[CrossRef](#)]
4. Das, S.; Pal, S.; Mitra, M. Significance of Exhaled Breath Test in Clinical Diagnosis: A Special Focus on the Detection of Diabetes Mellitus. *J. Med. Biol. Eng.* **2016**, *36*, 605–624. [[CrossRef](#)] [[PubMed](#)]
5. Dent, A.G.; Sutudja, T.G.; Zimmerman, P.V. Exhaled breath analysis for lung cancer. *J. Thorac. Dis.* **2013**, *5*, S540–S550. [[CrossRef](#)] [[PubMed](#)]
6. Li, J.; Peng, Y.; Liu, Y.; Li, W.; Jin, Y.; Tang, Z.; Duan, Y. Investigation of potential breath biomarkers for the early diagnosis of breast cancer using gas chromatography–mass spectrometry. *Clin. Chim. Acta* **2014**, *436*, 59–67. [[CrossRef](#)] [[PubMed](#)]
7. Van de Kant, K.D.; van der Sande, L.J.; Jöbsis, Q.; van Schayck, O.C.; Dompeling, E. Clinical use of exhaled volatile organic compounds in pulmonary diseases: A systematic review. *Respir. Res.* **2012**, *13*. [[CrossRef](#)] [[PubMed](#)]
8. Yamazoe, N. New approaches for improving semiconductor gas sensors. *Sens. Actuator B Chem.* **1991**, *5*, 7–19. [[CrossRef](#)]
9. Miller, D.R.; Akbar, S.A.; Morris, P.A. Nanoscale metal oxide-based heterojunctions for gas sensing: A review. *Sens. Actuator B Chem.* **2014**, *204*, 250–272. [[CrossRef](#)]
10. Vallejos, S.; Khatko, V.; Calderer, J.; Gracia, I.; Canè, C.; Llobet, E.; Correig, X. Micro-machined WO₃-based sensors selective to oxidizing gases. *Sens. Actuator B Chem.* **2008**, *132*, 209–215. [[CrossRef](#)]
11. Vallejos, S.; Umek, P.; Stoycheva, T.; Annanouch, F.; Llobet, E.; Correig, X.; De Marco, P.; Bittencourt, C.; Blackman, C. Single-step deposition of Au- and Pt-nanoparticle-functionalized tungsten oxide nanoneedles synthesized via aerosol-assisted CVD, and used for fabrication of selective gas microsensor arrays. *Adv. Funct. Mater.* **2013**, *23*, 1313–1322. [[CrossRef](#)]
12. Annanouch, F.E.; Haddi, Z.; Vallejos, S.; Umek, P.; Guttman, P.; Bittencourt, C.; Llobet, E. Aerosol-assisted CVD-grown WO₃ nanoneedles decorated with copper oxide nanoparticles for the selective and humidity-resilient detection of H₂S. *ACS Appl. Mater. Interfaces* **2015**, *7*, 6842–6851. [[CrossRef](#)] [[PubMed](#)]
13. Vallejos, S.; Gràcia, I.; Figueras, E.; Canè, C. Nanoscale heterostructures based on Fe₂O₃@WO_{3-x} nanoneedles and their direct integration into flexible transducing platforms for toluene sensing. *ACS Appl. Mater. Interfaces* **2015**, *7*, 18638–18649. [[CrossRef](#)] [[PubMed](#)]

14. Ma, R.; Jahurul Islam, M.; Amaranatha Reddy, D.; Kim, T.K. Transformation of CeO₂ into a mixed phase CeO₂/Ce₂O₃ nanohybrid by liquid phase pulsed laser ablation for enhanced photocatalytic activity through Z-scheme pattern. *Ceram. Int.* **2016**, *42*, 18495–18502. [[CrossRef](#)]
15. Montini, T.; Melchionna, M.; Monai, M.; Fornasiero, P. Fundamentals and Catalytic Applications of CeO₂-Based Materials. *Chem. Rev.* **2016**, *116*, 5987–6041. [[CrossRef](#)] [[PubMed](#)]
16. Magesh, G.; Viswanathan, B.; Viswanath, R.P.; Varadarajan, T.K. Photocatalytic behavior of CeO₂-TiO₂ system for the degradation of methylene blue. *Indian J. Chem. Sect. A* **2009**, *48A*, 480–488.
17. Evans, M.; Di Maggio, F.; Blackman, C.; Sankar, G. AACVD synthesis of catalytic gold nanoparticle-modified cerium(IV) oxide thin films. *Phys. Status Solidi C* **2015**, *12*, 996–1000. [[CrossRef](#)]
18. Vallejos, S.; Gràcia, I.; Chmela, O.; Figueras, E.; Hubálek, J.; Cané, C. Chemoresistive micromachined gas sensors based on functionalized metal oxide nanowires: Performance and reliability. *Sens. Actuator B Chem.* **2016**, *235*, 525–534. [[CrossRef](#)]
19. Vallejos, S.; Pizúrová, N.; Čechal, J.; Gràcia, I.; Cané, C. Aerosol-assisted chemical vapor deposition of metal oxide structures: Zinc oxide rods. *J. Vis. Exp.* **2017**, *127*, 56127. [[CrossRef](#)] [[PubMed](#)]
20. Annanouch, F.E.; Haddi, Z.; Ling, M.; Di Maggio, F.; Vallejos, S.; Vilic, T.; Zhu, Y.; Shujah, T.; Umek, P.; Bittencourt, C.; et al. Aerosol-Assisted CVD-Grown PdO Nanoparticle-Decorated Tungsten Oxide Nanoneedles Extremely Sensitive and Selective to Hydrogen. *ACS Appl. Mater. Interfaces* **2016**, *8*, 10413–10421. [[CrossRef](#)] [[PubMed](#)]
21. Vallejos, S.; Gràcia, I.; Figueras, E.; Cané, C. Catalyst-free vapor-phase method for direct integration of gas sensing nanostructures with polymeric transducing platforms. *J. Nanomaterials* **2014**, *2014*. [[CrossRef](#)]
22. Watanabe, H.; Fujikata, K.; Oaki, Y.; Imai, H. Band-gap expansion of tungsten oxide quantum dots synthesized in sub-nano porous silica. *Chem. Comm.* **2013**, *49*, 8477–8479. [[CrossRef](#)] [[PubMed](#)]
23. Mysliveček, J.; Matolín, V.; Matolínová, I. Heteroepitaxy of Cerium Oxide Thin Films on Cu(111). *Materials* **2015**, *8*, 6346–6359. [[CrossRef](#)] [[PubMed](#)]
24. Naganuma, T.; Traversa, E. Stability of the Ce³⁺ valence state in cerium oxide nanoparticle layers. *Nanoscale* **2012**, *4*, 4950–4953. [[CrossRef](#)] [[PubMed](#)]
25. Nicolas, J.; Romain, A.-C. Establishing the limit of detection and the resolution limits of odorous sources in the environment for an array of metal oxide gas sensors. *Sens. Actuator B Chem.* **2004**, *99*, 384–392. [[CrossRef](#)]
26. Prabhakar, A.; Iglesias, R.A.; Shan, X.; Xian, X.; Zhang, L.; Tsow, F.; Forzani, E.S.; Tao, N. Online Sample Conditioning for Portable Breath Analyzers. *Anal. Chem.* **2012**, *84*, 7172–7178. [[CrossRef](#)] [[PubMed](#)]
27. Vallejos, S.; Gràcia, I.; Pizúrová, N.; Figueras, E.; Hubálek, J.; Cané, C. Tuning of the Humidity-Interference in Gas Sensitive Columnar ZnO Structures. *Proceedings* **2017**, *1*. [[CrossRef](#)]
28. Wang, J.; Yang, P.; Wei, X. High-Performance, Room-Temperature, and No-Humidity-Impact Ammonia Sensor Based on Heterogeneous Nickel Oxide and Zinc Oxide Nanocrystals. *ACS Appl. Mater. Interfaces* **2015**, *7*, 3816–3824. [[CrossRef](#)] [[PubMed](#)]
29. Niarchos, G.; Dubourg, G.; Afroudakis, G.; Georgopoulos, M.; Tsouti, V.; Makarona, E.; Crnojevic-Bengin, V.; Tsamis, C. Humidity Sensing Properties of Paper Substrates and Their Passivation with ZnO Nanoparticles for Sensor Applications. *Sensors* **2017**, *17*. [[CrossRef](#)] [[PubMed](#)]
30. Kim, S.; Park, S.; Park, S.; Lee, C. Acetone sensing of Au and Pd-decorated WO₃ nanorod sensors. *Sens. Actuator B Chem.* **2015**, *209*, 180–185. [[CrossRef](#)]
31. Bertuna, A.; Comini, E.; Poli, N.; Zappa, D.; Sberveglieri, G. Acetone Detection by Chemical Sensors Based on Tungsten and Titanium Oxide Nanowires. *Proceedings* **2017**, *1*. [[CrossRef](#)]
32. Righettoni, M.; Tricoli, A.; Pratsinis, S.E. Si:WO₃ Sensors for Highly Selective Detection of Acetone for Easy Diagnosis of Diabetes by Breath Analysis. *Anal. Chem.* **2010**, *82*, 3581–3587. [[CrossRef](#)] [[PubMed](#)]
33. Pandeewari, R.; Jeyaprakash, B.G. CeO₂ thin film as a low-temperature formaldehyde sensor in mixed vapour environment. *Bull. Mater. Sci.* **2014**, *37*, 1293–1299. [[CrossRef](#)]
34. Nagaraju, P.; Vijayakumar, Y.; Choudhary, R.J.; Ramana Reddy, M.V. Preparation and characterization of nanostructured Gd doped cerium oxide thin films by pulsed laser deposition for acetone sensor application. *Mater. Sci. Eng., B* **2017**, *226*, 99–106. [[CrossRef](#)]

